An audiomagnetotelluric investigation of the Southern Upland Fault: novel instrumentation, field procedures and 3D modelling.

Oliver Ritter

Doctor of Philosophy
University of Edinburgh
1995

Contents

List of Figures

List of Tables

Declaration

This thesis has been composed by me and has not been submitted for any other degree. Except where acknowledgement is made, the work is original.

Oliver Ritter

Abstract

The feasibility of the magnetic variation field for electromagnetic investigations in the audiomagnetotelluric frequency range is tested at two separate locations in southeastern Scotland in the vicinity of the Southern Upland Fault complex (Lammermuir Fault). The Lammermuir Fault represents a lateral conductivity contrast in that it separates conductive Carboniferous sediments from resistive Ordovician meta-sediments.

For one of the experiments and for the first time, a new generation of instruments (S.P.A.M. MkIII) could be used for data acquisition. The instrument is operated as a network of geophysical sensors, it uses digital data communication between sites and provides on-line data quality control of all connected channels. For the experiment, we installed a 15-channel configuration of three synchronous AMT sites.

All recorded data were re-processed off-line, with a newly developed S.P.A.M. MkIII-compatible data processing package. The software is based on robust statistics and an integrated database helps to organise all relevant information. Despite some problems with noise, the overall quality of the data is satisfying. Both locations reveal strong vertical magnetic field anomalies. The anomalies are resolved convincingly in frequency and space.

Contrary to our original assumptions, the observed anomalies at neither location can be modelled using two-dimensional techniques. However, three-dimensional thin sheet models show that strong current channelling into a surface conductor can explain very large induction arrows. Full three-dimensional modelling of the data is necessary to fit both, real and imaginary parts of the observed induction arrows. The modelling results indicate that a SE/NW striking conductive feature at the surface is duplicated at greater depth and dips towards the south.

S.P.A.M. MkIII is ideally suited to collect data of densely spaced sites for such electromagnetic mapping experiments or possibly three-dimensional data sets in future projects. Vertical magnetic field anomalies can be detected over the whole AMT frequency range and they are more robust against noise than the electric fields. A further development of the geomagnetic variation mapping method at high frequencies is therefore highly recommended.

1 Introduction

The magnetotelluric method is applied to determine the electrical conductivity structure beneath the Earth's surface. The method is based on measurements of electric- (telluric) and magnetic field variations at the surface of the Earth. Fluctuations with time of the Earth's magnetic field – which at the surface have orders of magnitude smaller amplitudes than the main field – can be observed over a wide range of periods. Long period variations ($>1\,s$) are caused mainly by current systems created by the solar wind in the high atmosphere, while variations of shorter periods are predominantly generated by electromagnetic emissions from lightning discharges [Volland, 1986; Brasse, 1993]. The study of those short period signals, in the range between $10^{-4}\,s$ and $1\,s$, has become known as Audiomagnetotellurics.

The investigation of the vertical magnetic variation field, normalized by the horizontal fields, is the oldest of the electromagnetic methods. Its roots can be traced back to the last century, but the pioneering work which provided the first insights into the Earth's deep conductivity structure was carried out by Chapman and Price, [Chapman, 1919; Lahiri and Price, 1939]. This early work was based upon observations of field fluctuations with periods typically in the order of a few hours or longer. The electromagnetic response of the Earth to a particular input can be determined if the magnetic variations are separated into parts of internal and external origin. The external parts arise from transient current systems in the Earth's ionosphere or magnetosphere. The internal parts are from secondary eddy currents which are induced electromagnetically within the conductive layers of the Earth.

The magnetotelluric method (MT) was developed in the 1950's, independently by Tikhonov and Cagniard [Cagniard, 1953; Tikhonov, 1950]. It uses the surface impedance of the incident variation field, i.e. the ratio of horizontal electric to orthogonal horizontal magnetic fields. Magnetotelluric soundings utilize the skin-effect of electromagetic waves under the assumption that the primary field is of great lateral uniformity in comparison with its depth of penetration. For such a uniform source field, a vertical magnetic field component arises solely from lateral changes of the conductivity within the depth range of penetration.

Initially, the period range of the observations was dictated by the limitations of the instruments. Until the mid 1970's, magnetotelluric data were recorded in analogue form, typically in a period range between $50\,s$ and $5000\,s$. Only with the introduction of digital technology, did the audiomagnetotelluric (AMT) period range become accessible to investigation [Strangway et al., 1973]. The depth of penetration of electromagnetic waves into the Earth depends on their frequency; the penetration depth increases with decreasing frequency. Therefore, AMT soundings are usually carried out to investigate shallower features of the Earth's crust, e.g. for mineral exploration or in geothermal areas. A good example of such an AMT survey is the high resolution mapping of a geothermal anomaly on the island of Milos (Greece), where data from over 100 densely spaced sites were gathered by 4 European research institutions [Haak et al., 1989; Hutton et al., 1989].

However, the information from the vertical magnetic fields has hardly ever been considered for the interpretation of AMT data. The reasons were obvious in the days when researchers had to rely on 1D-modelling, which implies the exclusion of lateral changes in conductivity. Today, 2D and some 3D modelling programs are widely available and it appears that lack of interest is more because of inadequate equipment, insufficient care during the field work, or idleness of the observer than for scientific reasons. It is therefore one of the main interests of this thesis to explore the possibilities and limitations of vertical magnetic field variations in the AMT frequency range. This is documented in two field experiments from the south of Scotland, in geologically complex environments. The experiments were designed and carried out in connection with the development of a completely new generation of AMT instruments (S.P.A.M. MkIII).

S.P.A.M. MkIII is a highly portable real time AMT system which is operated as a network of geophysical sensors. The number and spatial distribution of the sensors is virtually arbitrary, as the processing power of the instrument increases with the number of network nodes. While S.P.A.M. MkIII facilitates field experiments with very dense site/sensor spacing, it can also handle larger distances between sites because all network nodes are inter-connected using digital data communication. The instrument with its hardware and software components is described in chapter 5.

In chapter 2 the basic concepts of the electromagnetic methods are introduced. The physical principles are summarized, important quantities of magnetotelluric and geomagnetic depth sounding methods are explained, and the interpretation of electromagnetic data is discussed. In particular, the meaning of induction arrows is highlighted, as they are most useful for the examination of the results from the field experiments.

In the framework of this thesis I undertook two field experiments, crossing the Southern Upland Fault (Lammermuir Fault) at different locations in the southeast of Scotland. At both locations, I observed surprisingly strong anomalies of the vertical magnetic variation field which cannot be explained by (standard) two-dimensional interpretation methods. However, many aspects of these complicated data can be explained if three dimensional modelling techniques are applied. A detailed description of the experiments with an assessment of the data quality and the modelling results is given in chapters 4 and 7, respectively.

In view of S.P.A.M. MkIII's extended facilities it became necessary to develop new data processing schemes that could cope with an arbitrary number of channels and sites. Chapter 3 overviews statistical methods, explains how electromagnetic response functions of the Earth and their confidence limits are computed, and describes a robust procedure for an automatic and reliable processing of data affected by noise. Because S.P.A.M. MkIII can be configured much more flexibly than existing instruments, we also had to find new ways to organise our data. In chapter 6, I develop a solution based on a database to store together all information on instruments, site configurations and recorded data.

2 Basic concept of the geoelectromagnetic method

2.1 Physical principles

The theory behind induction studies in geophysics is based upon Maxwell's equations. Electric currents in the Earth's ionosphere and magnetosphere give rise to time varying magnetic fields which induce electric currents in the Earth. Measurements of the electric and magnetic fields at the Earth's surface contain frequency dependent information about both the spatial variation of the Earth's conductivity and about the external sources. Electric and magnetic fields are connected by Maxwell's field equations:

$$\nabla \times \mathbf{H} = \frac{\partial \mathbf{D}}{\partial t} + \mathbf{J} \quad (1a) \qquad \nabla \cdot \mathbf{B} = 0 \quad (1b)$$

$$\nabla \times \mathbf{E} = -\frac{\partial \mathbf{B}}{\partial \mathbf{t}} \quad (1c) \qquad \nabla \cdot \mathbf{D} = q \quad (1d)$$

All of the above fields are functions of position $\mathbf{r} = (x, y, z)$ in $[m]$ and of time t in $[s]$; ω denotes the angular frequency $[\frac{1}{s}]$. $\mathbf{H}$ and $\mathbf{E}$ are the magnetic and electric field strengths in $[\frac{A}{m}]$ and $[\frac{V}{m}]$, respectively. $\mathbf{B}$ is the magnetic induction in $[\frac{Vs}{m^2}]$, $\mathbf{D}$ is the displacement in $[\frac{C}{m^2}]$, $\mathbf{J}$ is the electric current density in $[\frac{A}{m^2}]$, and q is the electric charge density in $[\frac{C}{m^3}]$. Throughout the text, we assume Cartesian coordinate systems and x, y, and z are defined to be positive when pointing towards the North, the East and downwards, respectively.

Ohm's law defines the scalar electrical conductivity σ in $[\frac{S}{m}]$ and the electrical resistivity ρ in $[\Omega m]$:

$$\mathbf{J} = \sigma \mathbf{E} = \frac{\mathbf{E}}{\rho} \quad (2)$$

The relation between magnetic field and induction and electric field and displacement is given by the constitutive equations:

$$\mathbf{B} = \mu\mu_0\mathbf{H} \quad (3a)$$
$$\mathbf{D} = \varepsilon\varepsilon_0\mathbf{E} \quad (3b)$$

where μ is the magnetic permeability and ε is the electrical permittivity. Both μ and ε are assumed to be constant and frequency independent. The free space constants are $\mu_0 = 4\pi 10^{-7}\,[\frac{Vs}{Am}]$ and $\varepsilon_0 = (\mu_0 c^2)^{-1} \approx 8.85 \cdot 10^{-12}\,[\frac{C}{Vm}]$, where c is the speed of light. μ can be regarded as a scalar value ≈ 1 in geophysical induction studies ince hardly any of the natural material of interest is ferromagnetic [Keller and Frischknecht, 1966].

In rock physics, where the conductivity of samples is measured for frequencies as high as $100MHz$, σ is usually given as a frequency dependent, complex quantity.

However, for most rocks this frequency dependency of σ appears only for frequencies of about $1kHz$ and above [e.g. Duba, 1977; Olhoeft, 1985; Jödicke, 1991, 240ff]. For the experiments discussed in this thesis the range of observation frequencies is limited by the instrumentation to a band between $100\,Hz$ and $100\,s$. Hence, we consider the conductivity to be a real function of position, only, and we also neglect the effect known as induced polarisation, which affects many sediments and sedimentary rocks with a high clay content [Telford et al., 1976].

At this point, it is useful to assume harmonic time dependence of the electromagnetic fields $\mathbf{F}$.

$$\mathbf{F} \sim e^{i\omega t} \tag{4}$$

The time - frequency domain relation can be written using a Fourier integral representation:

$$\mathbf{F}(\mathbf{r},t) = \int \mathbf{F}(\mathbf{r},\omega)\, e^{-i\omega t} d\omega \tag{5}$$

$\mathbf{F}$ denotes either the magnetic field $\mathbf{B}$ or the electric field $\mathbf{E}$. Assuming $\nabla \cdot \mathbf{F} = 0$ and $\sigma = constant$, elimination of $\mathbf{E}$ or $\mathbf{H}$ in 1a and 1c, using 2,3a and 3b results in a second order differential equation:

$$\nabla^2 \mathbf{F} = \mu_0 \left(\sigma \frac{\partial \mathbf{F}}{\partial t} - \varepsilon\varepsilon_0 \frac{\partial^2 \mathbf{F}}{\partial t^2} \right) \tag{6}$$

Using equation 4 we re-write equation 6 for the electric field $\mathbf{E}$:

$$\nabla^2 \mathbf{E} = \mu_0 \left(i\omega\sigma \mathbf{E} - \varepsilon\varepsilon_0 \omega^2 \mathbf{E} \right) \tag{7}$$

The way we interpret equation 7 is determined by the relative importance of the terms on the right hand side of the equation. The second term in equation 7 is equivalent to Maxwell's displacement current $(\partial \mathbf{D}/\partial t)$ in equation 1a. For most natural geological settings we can assume rock resistivies $< 10^4 \Omega m$ and $\varepsilon < 20$ [Beblo, 1982]. If our observations are furthermore electromagnetic waves of $f < 1kHz$, the induction current $\sigma\mathbf{E}$ within the conducting layers of the Earth exceeds the displacement current $\varepsilon\varepsilon_0\omega\mathbf{E}$ 100 times. Hence, we usually discard the displacement (equation 3b) in geo-electromagnetic induction studies.

Discarding displacement currents, but for general conductivity structures, we can transform Maxwell's equations into the induction equations:

$$\nabla^2 \mathbf{B} = i\omega\mu_0\sigma\mathbf{B} - \frac{1}{\sigma}\nabla\sigma \times (\nabla \times \mathbf{B}) \tag{8a}$$

$$\nabla^2 \mathbf{E} = i\omega\mu_0\sigma\mathbf{E} + \nabla(\mathbf{E} \cdot \frac{1}{\sigma}\nabla\sigma) \tag{8b}$$

For constant σ or partly homogeneous volumes with $\nabla\sigma = 0$, the induction equations reduce to the Helmholtz equations:

$$\nabla^2 \mathbf{F} = i\omega\mu_0\sigma\mathbf{F} = K_0^2 \mathbf{F} \tag{9}$$

Again, $\mathbf{F}$ denotes either the magnetic field $\mathbf{B}$ or the electric field $\mathbf{E}$. $K_0 = \sqrt{i\omega\mu_0\sigma}$ can formally be regarded as the complex wave number of a medium.

Suppose we consider a field of the form $\mathbf{F}(\mathbf{r}) = F_0(z)e^{i(k_x\hat{\mathbf{x}}+k_y\hat{\mathbf{y}}+\omega t)}$, $\mathbf{k} = (k_x, k_y)$ is the horizontal wave vector with magnitude $|k| = \sqrt{k_x^2 + k_y^2}$. Such a field with an attenuation term in the z - direction is a solution of the differential equation in (9):

$$F_0(z) = F_0(z_0 = 0)e^{-\frac{z}{c}} \tag{10}$$

c is a complex scale length for the depth of penetration of the field into the uniform domain [Schmucker, 1987].

$$c(\omega, |k|) = \sqrt{\frac{2i}{p^2} + |k|^2} \tag{11}$$

The skin depth p, at which the field's amplitude is attenuated to the $\frac{1}{e}$-part of its value at the surface ($\frac{|\mathbf{F}(z=p)|}{|\mathbf{F}(z=0)|} = \frac{1}{e}$), is defined as:

$$p = \sqrt{\frac{2\rho}{\omega\mu_0}} \tag{12}$$

If the horizontal wavelength $\frac{1}{|k|}$ of the source field is much smaller than the skin depth i.e. $\frac{2}{p^2} \ll |k|^2$, c is dominated by the geometry of the source. For $\frac{2}{p^2} \gg |k|^2$ the wavelengths of the inducing electromagnetic fields are large compared to their penetration depths into the Earth, and the c-response is dominated by the sub-surface conductivity and almost independent of the source geometry.

Weaver [1973] pointed out that the induction problem cannot be solved mathematically for source fields of $|k| = 0$. It is furthermore physically useless to assume truly uniform source fields ($|k| = 0$) since only a vertical magnetic field component induces [Schmucker and Weidelt, 1975]. However, to formally set $|k| \to 0$ simplifies considerably the mathematical description of the source; the source field is then called *quasi-uniform.*

For quasi-uniform source fields we can use equation (11) to derive the resistivity ρ_0 of the uniform halfspace [Cagniard, 1953]:

$$\rho_0 = \omega\mu_0|c|^2 \tag{13}$$

Considering a 2-dimensional conductivity structure $\sigma = \sigma(z, y)$ for which all partial derivatives with respect to x are zero ($\frac{\partial}{\partial x} = 0$), Maxwell's equations can be written as two sets of de-coupled equations:

$$\begin{aligned} \frac{\partial B_z}{\partial y} - \frac{\partial B_y}{\partial z} &= \mu_0\sigma E_x \\ -\frac{\partial E_x}{\partial z} &= i\omega B_y \\ \frac{\partial E_x}{\partial y} &= i\omega B_z \end{aligned} \qquad \begin{aligned} \frac{\partial E_y}{\partial z} - \frac{\partial E_z}{\partial y} &= i\omega B_x \\ \frac{\partial B_x}{\partial z} &= \mu_0\sigma E_y \\ -\frac{\partial B_x}{\partial y} &= \mu_0\sigma E_z \end{aligned} \tag{14}$$

E-polarisation B-polarisation

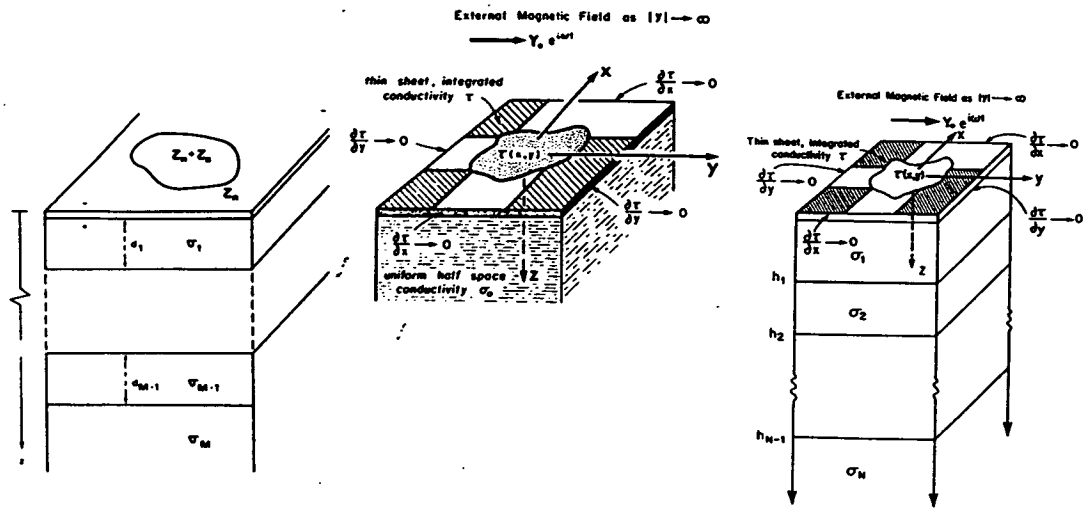

Figure 1: *The type of thin sheet models, that can be calculated with the methods described by Vasseur and Weidelt [1977], Dawson and Weaver [1979] and McKirdy, Dawson and Weaver [1985].*

The E-polarisation set describes the electric field E_x parallel to the direction of constant conductivity. This direction is called the electrical strike. The B-polarisation describes an electric field perpendicular to the strike, which has been induced by a magnetic field parallel to the strike (B_x). The E-polarisation has no vertical electric field, the B-Polarisation no vertical magnetic field. The terms E- and B-polarisation follow the naming conventions suggested by Hobbs [1992].

The system of differential equations to be solved for the two-dimensional case (equations 14 and 9) is [e.g. Haak, 1978]:

$$\frac{\partial}{\partial y}\left(\frac{1}{\sigma}\frac{\partial B_x}{\partial y}\right) + \frac{\partial}{\partial z}\left(\frac{1}{\sigma}\frac{\partial B_x}{\partial z}\right) = i\omega\mu_0 B_x \tag{15a}$$

$$\frac{\partial^2 E_x}{\partial y^2} + \frac{\partial^2 E_x}{\partial z^2} = i\omega\mu_0\sigma E_x \tag{15b}$$

This is usually accomplished numerically, applying the finite differences technique [e.g. Jones and Price, 1970; Jones, 1973; Brewitt-Taylor and Weaver, 1977] or the finite element method [e.g. Coggon, 1971; Reddy and Rankin, 1971; Wannamaker et al., 1987].

Mathematically, everything becomes much more complicated if σ varies in three dimensions. Now, a separation into E-polarisation and B-polarisation modes is no longer possible, and the differential equations of a vector field instead of a scalar field must be solved:

$$\nabla^2\mathbf{F}(\mathbf{r}) = i\omega\mu_0\sigma(\mathbf{r})\mathbf{F}(\mathbf{r}) \tag{16}$$

Typically, an integral equation solution is applied to tackle the problem [e.g. Hobbs, 1971; Weidelt, 1975; Hohmann, 1975].

For a special class of three-dimensional models, called thin sheet models, the Earth consists of an inhomogeneous thin conductive layer at the surface (oceans, seas, sedimentary rocks) over a thick, resistive lithosphere [e.g. Price, 1949; Schmucker, 1970]. For the thin sheet any vertical current inflow or outflow is suppressed by the insulating layer immediately below it. A layered substratum underneath it will produce only horizontal current loops. The field equations can be solved analytically above and below the thin sheet leaving only the sheet itself as the region where numerical methods must be applied. Figure 1 shows the types of model that can be computed with the methods developed by [Vasseur and Weidelt, 1977], [Dawson and Weaver, 1979] and [McKirdy et al., 1985], respectively.

2.2 Magnetotelluric (MT) sounding

The impedance is defined as the ratio of the electric to the magnetic fields $Z(\omega) = \frac{E(\omega)}{H(\omega)}$, with $E(\omega) \perp H(\omega)$. For general spatial structures of the conductivity the scalar impedance Z must be expanded into a matrix which contains complex elements. Considering furthermore that the magnetic induction B rather than the magnetic field H is the measured quantity, the relation between the horizontal components of the electromagnetic fields becomes:

$$\begin{pmatrix} E_x \\ E_y \end{pmatrix} = \frac{1}{\mu_0} \begin{pmatrix} Z_{xx} & Z_{xy} \\ Z_{yx} & Z_{yy} \end{pmatrix} \begin{pmatrix} B_x \\ B_y \end{pmatrix} \tag{17}$$

The frequency dependent impedance tensor $\mathbf{Z}$ contains the information about the conductivity distribution of the sub-surface. The Magnetotelluric (MT) method is applied to estimate the impedance tensor by measurements of orthogonal components of electric- and magnetic fields at the surface of the Earth. $\mathbf{Z}$ is also called a *response function* of the Earth and generally, any frequency dependent linear relation between components of the Earth's electric and magnetic fields is a response function. In practice, the aim of any electromagnetic method is to estimate these response functions as accurately as possible.

The expression for the uniform subsurface resistivity ρ_0 in equation 13 can be formulated for the scalar impedance: $\rho_0 = \frac{1}{\omega\mu_0}|Z|^2$. For general conductivity distributions this expression must be extended and we define the apparent resistivity ρ_a as:

$$\rho_{a\,ij}(\omega) = \frac{1}{\omega\mu_0}|Z_{ij}(\omega)|^2 \tag{18}$$

The indices i, j are substitutes for the indices x and y, referring to the horizontal field components, respectively. The apparent resistivities at a given skin depth ($\rho_a(\omega)$) yield the specific electric resistivities of a uniform halfspace [Cagniard, 1953].

Since the elements of $\mathbf{Z}$ are complex quantities we obtain the phase of the impedance tensor as:

$$\Phi_{ij}(\omega) = \arctan\left(\frac{\mathcal{I}m\{Z_{ij}(\omega)\}}{\mathcal{R}e\{Z_{ij}(\omega)\}}\right) \tag{19}$$

If the conductivity varies only with depth, the elements of the impedence tensor are $Z_{xx} = Z_{yy} = 0$, $Z_{xy} = -Z_{yx}$, and apparent resistivity and phase are connected by a dispersion relation[1] [Weidelt, 1972]:

$$\Phi(\omega) \approx \frac{\pi}{4}\left(1 - \frac{d\,log\rho_a(\omega)}{d\,log(\frac{2\pi}{\omega})}\right) \tag{20}$$

A two-dimensional conductivity structure can be described in a coordinate system in which the x direction is perpendicular and the y direction is parallel to the electrical strike: $Z_{xx} = Z_{yy} = 0$ and $Z_{xy} = Z_{\perp}$, $Z_{yx} = Z_{||}$. With real data however, the best one can hope to find is an optimum coordinate-system which fulfills the condition $|Z_{xx}|^2 + |Z_{yy}|^2 = min.$ After Swift, [1986] the rotation angle for this coordinate system is:

$$\theta = \frac{1}{4}\arctan\left[\frac{2\mathcal{R}e\{(Z_{xx} - Z_{yy})\,(Z_{xy} - Z_{yx})\}}{|Z_{xx} - Z_{yy}|^2 - |Z_{xy} + Z_{yx}|^2}\right] \tag{21}$$

The angle θ is estimated with a $\pm 90°$ ambiguity, which can be resolved if additional magnetic or geological information is available. Swift defined the skewness of the impedance tensor as a measure of the complexity of the underlying geology:

$$S = \frac{|Z_{xx} + Z_{yy}|}{|Z_{xy} - Z_{yx}|} \tag{22}$$

The skewness is invariant to rotation and is 0 or at least small (< 0.2) for one- and two-dimensional structures and over symmetrical 3D bodies.

In recent years Bahr [1988] and Groom and Bailey [1989] have stressed that Swift's criteria can lead to significantly wrong results if the regional (two-dimensional) electric fields are distorted by small scale local anomalies. They suggest more reliable undistorted skew and strike paramters. Following Bahr's notation, we define:

$$S_1 = Z_{xx} + Z_{yy} \qquad S_2 = Z_{xy} + Z_{yx} \tag{23a}$$

$$D_1 = Z_{xx} - Z_{yy} \qquad D_2 = Z_{xy} - Z_{yx} \tag{23b}$$

In the following equations, the phase differences between two complex numbers and the corresponding amplitude products are abbreviated by the commutators:

$$[C_1, C_2] = \mathcal{I}m\{C_2 C_1^*\} = \mathcal{R}e\{C_1\}\mathcal{I}m\{C_2\} - \mathcal{R}e\{C_2\}\mathcal{I}m\{C_1\} \tag{24}$$

The angle α of the direction of the regional strike is

$$\alpha = \frac{1}{2}\arctan\left(\frac{[S_1, S_2] - [D_1, D_2]}{[S_1, D_1] + [S_2, D_2]}\right) \tag{25}$$

and we define as the *phase-sensitive* skew η:

$$\eta = \frac{\sqrt{[D_1, S_2] - [S_1, D_2]}}{|D_2|} \tag{26}$$

[1] ρ_a must be given in Ωm and the angular frequency in s^{-1}.

Skew values $\eta > 0.3$ indicate that $\mathbf{Z}$ describes a regional 3D anomaly, which cannot be interpreted with two-dimensional models. Smaller values for η indicate that the data can be regarded as a superposition of small scale three-dimensional and regional two-dimensional models. In his paper Bahr [1991] demonstrates how data can be categorized into seven grades of distortion, and the method is applied in [Eisel and Bahr, 1993].

The usual way to present magnetotelluric data is to plot the apparent resistivity ρ_a and the phase versus period, possibly in a rotated coordinate system. Alternatively, the data can be presented in ρ^*-z^*-diagrams [Schmucker, 1987], which convey the conductivity versus depth structure more clearly:

$$\rho^*(\omega) = \rho_a(\omega) \cdot \begin{cases} 1/\left(2\sin^2\Phi(\omega)\right); & for\ \Phi \leq 45° \\ 2\cos^2\Phi(\omega); & for\ \Phi > 45° \end{cases} \tag{27a}$$

$$z^*(\omega) = \frac{1}{\mu_0\omega}\mathcal{I}m\{Z(\omega)\} \tag{27b}$$

The ρ^*-z^*-transformation is based on plane 2-layer models with two adjustable parameters: an h-model for a very poorly conducting top layer ($\Phi > 45°$) above a uniform halfspace and a τ-model ($\Phi \leq 45°$) for which the top layer is a very good conductor [Schmucker, 1987]. In the original concept [Schmucker, 1970] h-models were used in both cases, the τ-model was added later [Schmucker, 1971, Sec. 3.2].

2.3 Geomagnetic depth sounding (GDS)

The method in which geomagnetic observations are analysed depends on the period range of the data and hence, whether or not the source field can be regarded as uniform. Historically, the magnetic variation field was recorded globally at observatories. The data were derived from hourly mean values and show fluctuations of the geomagnetic field in the frequency range between 10^{-3} to 0.5 *cycles per day.* If these observations are used for vertical geomagnetic soundings, the source field wave number structure must be known. The spatial geometry of the source can be separated using spherical harmonic analysis (SHA); then, the total field is separated into inducing external parts and induced internal parts. The Earth is considered to consist of concentric spherical shells of uniform conductivity. The ratio of the parts of the magnetic field of internal and external origin is dependent on both the external current system and the distribution of the electrical conductivity within the Earth.

The source field geometry can be estimated for variations of the ring current in the magnetosphere, for which the corresponding primary magnetic source field can be described by associated Legendre polynomials of the first kind $P_1^0(\cos\theta)$ [Rokitiansky, 1982, p.36]. In another approach the daily changes of the geomagnetic field on quiet, undisturbed days (S_q variations) are examined. S_q-variations are depending on the local time and the location of their recording. Taking the data from many observatories world - wide, the wave numbers of the diurnal S_q variations can be estimated using the symmetry of the equinoxes of the S_q fields to the magnetic equator [Schmucker and Weidelt, 1975].

Although the method has been improved since the 1970's with the help of more accurate instruments, data in machine readable form and by enhanced mathematical skills [e.g. Banks, 1969; Schmucker, 1970; Larsen, 1975; Schultz and Larsen, 1983; Schultz and Larsen, 1987; Egbert, 1989; Olsen, 1991] it is still very difficult to obtain response functions with high accuracy. Nevertheless, global GDS provides one rare opportunity to *look* into the Earth's mantle. It is one of the few methods to obtain estimates about temperatures at several hundred kilometers depth c.f. [Schmucker and Weidelt, 1975; Rokitiansky, 1982, ch.4.6; Constable, 1993a; Constable, 1993b].

The analysis of S_q-variations has regained popularity as a method to estimate the amount of static shift on MT soundings [Larsen, 1977; Junge, 1988; Junge, 1995]. Non-inductive galvanic distortion of electric and magnetic fields is caused by surface structures which are small in comparison to the background induction scale. The distortion is caused by electric charges at discontinuities or gradients in electrical conductivity. The electric fields are affected at all periods, whereas magnetic distortion is frequency dependent. Therefore, long period magnetic observations are usually less influenced by small bodies at the surface. However, magnetic distortion as a result of deflection of regional current systems can be observed at long periods [Zhang et al., 1993; Chave and Smith, 1994; Ritter and Ritter, 1995; Ritter, 1995].

Most of the data discussed in this thesis are recorded in the audiomagnetotelluric frequency range between $100\,Hz$ and $0.01\,Hz$. For these data we can assume quasi-uniform source fields ($|k| \rightarrow 0$). Primary and secondary vertical magnetic fields compensate each other at the surface of the Earth, both, for a uniform and for a horizontally-layered substratum. The vertical magnetic component arises solely if a lateral resistivity contrast is present in the range of the penetration depth of the electromagnetic fields:

$$B_z(\omega) = Z_H\, B_x(\omega) + Z_D\, B_y(\omega) \tag{28}$$

The vector (Z_H, Z_D) is sometimes called *tipper*[2], and the response functions Z_H and Z_D are often presented as induction arrows. For historic reasons two definitions of the induction arrows are common. In the Parkinson convention [Parkinson, 1959] the arrows tend to point towards areas of higher conductivity (increased current density), whereas the Wiese arrows [Wiese, 1962] tend to point away from areas of higher conductivity. The original definitions of the induction arrows are based on time-domain observations, while the commonly used formula based on response function estimates was introduced by Schmucker [1970] . Setting $A_R = \mathcal{R}e\{Z_H\}$, $A_I = \mathcal{I}m\{Z_H\}$, $B_R = \mathcal{R}e\{Z_D\}$, and $B_I = \mathcal{I}m\{Z_D\}$, table 1 gives the definitions of the induction vectors.

Weaver [1990] pointed out that many authors avoid the word *induction vector* and prefer to use *induction arrow* instead because vectorial addition is not meaningful in a physical sense. It is appropriate however, to call the ordered pairs $[A_R, B_R]$ and $[A_I, B_I]$ vectors in the horizontal plane because they satisfy *the well-known*

[2] *...sometimes called "tipper" by those trying to confuse people,* John Booker, Working Group I.2 of IAGA - Electromagnetic Induction in the Earth, Electronic Newsletter #10: 1995, A. Jones

convention	real arrow		imaginary arrow	
	magnitude	angle	magnitude	angle
Parkinson	$\sqrt{A_R^2 + B_R^2}$	$\arctan\left[\frac{-B_R}{-A_R}\right]$	$\sqrt{A_I^2 + B_I^2}$	$\arctan\left[\frac{B_I}{A_I}\right]$
Wiese		$\arctan\left[\frac{B_R}{A_R}\right]$		

Table 1: *The definition of induction arrows in Parkinson and Wiese conventions.*

transformation definition of a vector under a rotation of the coordinate system about the z-axis.

The visual display of the induction arrows in maps is a comprehensive presentation of changes in vertical magnetic field anomalies, both, as a function of frequency and location. In Wiese convention, the real arrows point away from zones of high and towards zones of low conductivity. For two-dimensional conductivity structures, real and imaginary arrows point either parallel or anti-parallel to each other. If the induction anomaly is not in the range of the skin depth, both induction arrows are zero. The imaginary arrows point into opposite directions of the real arrows if the induction anomaly is within the range of the skin depth. An anomaly at the surface, which is small in comparison to the skin depth causes the imaginary arrows to point into the directions of the real arrows. The largest real induction arrows are observed close to a conductivity contrast, they become smaller with increasing distance from that boundary. Although vertical magnetic field response functions do not contain direct information about the underlying conductivity structure ($\sigma(z)$), they are extremely valuable in detecting the lateral extension of conductivity anomalies.

A lateral resistivity anomaly $\rho' = \rho(z) + \rho_a(x, y, z)$ gives also rise to anomalous horizontal magnetic fields. We define $\mathbf{B}$ as the reference field, $\mathbf{B}'$ as the observed total field at one site, and $\mathbf{B_a}$ as the anomalous field generated by the induction anomaly:

$$\mathbf{B_a} = \mathbf{B}' - \mathbf{B} = \begin{pmatrix} W'_{xx} & W'_{xy} \\ W'_{yx} & W'_{yy} \\ W'_{zx} & W'_{zy} \end{pmatrix} \begin{pmatrix} B_x \\ B_y \end{pmatrix} \tag{29}$$

The perturbation tensor $\mathbf{W}$ yields linear relations between the normal fields at the reference site and the anomalous fields at a mobile site. Synchronous recordings of the magnetic field components are necessary, in order to calculate inter-site response functions.

The response functions Z_H and Z_D in equation 28 are normalized to the total horizontal fields of a local site. The influence of the anomalous horizontal field depends for each site on the location relative to the anomaly and will differ between sites. Hence, single site response functions should not be compared directly, when

investigating anomalies of a regional or global scale. After Banks [1986] the influence of the anomalous response functions can be estimated as follows:

$$B'_z = Z'_H B'_x + Z'_D B'_y \quad (30a)$$
$$B_z = Z_H B_x + Z_D B_y \quad (30b)$$

The above two equations and 29 are used to generate a prediction of the vertical fields in terms of the horizontal field B_x and B_y at the reference site

$$B'_z = (Z'_H + Z'_H W'_{xx} + Z'_D W'_{yx}) B_x + (Z'_D + Z'_D W'_{yy} + Z'_H W'_{xy}) B_y \quad (31)$$

and for the anomalous vertical magnetic field response functions in equation 29 follows:

$$W'_{zx} = (Z'_H - Z_H) + (Z'_H W'_{xx} + Z'_D W'_{yx}) \quad (32a)$$
$$W'_{zy} = (Z'_D - Z_D) + (Z'_D W'_{xy} + Z'_H W'_{yy}) \quad (32b)$$

The expressions in the second bracketed terms in equations 32a and 32b correct the first bracketed terms for the effects of the anomalous horizontal fields. Banks [1986] develops the method further using the Laplace equations to obtain B_x and B_y from B_z and eventually, to derive estimates for the regional anomalous magnetic field.

Like the impedance tensor $\mathbf{Z}$ in equation 17, the perturbation tensor $\mathbf{W}$ can be rotated to a coordinate system parallel and perpendicular to the strike if the conductivity anomaly is two-dimensional. If the local site is situated close to the anomaly while the reference site is remote and not influenced by it, then the only non-zero elements of $\mathbf{W}$ are[3]: $W'_{xx} = W'_{\|}$ and $W'_{zx} = Z'_H$. The elements of the perturbation tensor can be combined columnwise and presented as perturbation arrows similar to the induction arrows in table 1 [Schmucker, 1970].

The perturbation tensor yields important information about the conductivity distribution of the sub-surface and/or the geometry of the source field. However, it is rather difficult to reconstruct the normal fields accurately and therefore the perturbation tensor has rarely been used to interpret electromagnetic data. Exceptions are [Weidelt, 1978; Banks, 1986; Siemon, 1991; Junge, 1995]

[3]assuming $(\frac{\partial}{\partial x} = 0)$.

3 Processing of electromagnetic data

"One of the main reasons for introducing probabilistic considerations in a variety of applications is the problem of noise. In this chapter, we discuss various ways of reducing it. We assume that the noise is additive, the processing linear, and the optimality criterion the minimization of the mean-square error." [4]

3.1 Analysis of linear systems

The relation between two linearly time dependent quantities $x(t)$ and $z(t)$ can be formulated by an integral expression [Jenkins and Watts, 1968, p.34ff]:

$$z(t) = \int_{-\infty}^{+\infty} h(u)x(t-u)du \tag{33}$$

The above equation describes a system's output $z(t)$ as a convolution of the system's input $x(t)$ with a weighting function $h(u)$. Since a physical system cannot respond to inputs it has not yet received, $h(u)$ is zero for negative values of u. Then, $h(u)$ is called the impulse response function.

Equation 33 can be transformed to the frequency domain:

$$Z(\omega) = H(\omega)X(\omega) \tag{34}$$

where $Z(\omega)$, $H(\omega)$, and $X(\omega)$ are the Fourier transformed $z(t)$, $h(t)$, and $x(t)$, respectively. Thus, convolution in the time domain transforms to multiplication in the frequency domain. $H(\omega)$ is called a frequency response function or transfer function. The frequency domain presentation is mathematically and – more importantly – computationally simpler. Furthermore, the direct calculation of the impulse response function, by cross-correlation methods, is unsatisfactory, because the estimates have bad statistical properties [Jenkins and Watts, 1968, p.422ff]. The frequency separation has also physical relevance as the information content of most electromagnetic parameters is frequency dependent (see chapter 2). Hence, electromagnetic data are usually analysed in the frequency domain.

In the MT case (equation 17) the horizontal magnetic field components B_x and B_y are regarded as the input signals to a linear system, described by the impedance tensor $\mathbf{Z}$, while the horizontal electric field components E_x and E_y are considered to be the outputs of the system. For the GDS case, B_x and B_y are the input signals, but now the vertical magnetic field component B_z is the only output from the system described by the response functions Z_H and Z_D (cf. equation 28).

In the real world, where we conduct our experiments, we always find our measurements disturbed by electromagnetic signals other than those generated by nature. Even naturally produced signals violate sometimes our mathematical presumptions,

[4] E. Parzen, "Time Series Analysis Papers", Holden-Day, Publisher, San Francisco, 1967.

e.g.near field effects by lightning or strongly polarized source fields in regions near the equator (equatorial electrojet). Since we furthermore record our data in finite time intervals, using instruments of limited accuracy, we must add noise components to the electromagnetic signals in order to fully describe the process.

The noise is always associated with the output components, while the input channels are assumed to be free of noise:

$$Z(\omega) = a(\omega)X(\omega) + b(\omega)Y(\omega) + \delta Z(\omega) \tag{35}$$

Here, the output component $Z(\omega)$ can be substituted by the horizontal electric- or the vertical magnetic field. $X(\omega)$ and $Y(\omega)$ are the horizontal magnetic field components; $a(\omega)$ and $b(\omega)$ are the corresponding response functions. $\delta Z(\omega)$ is the uncorrelated noise in $Z(\omega)$. In practice, noise-free input channels cannot be guaranteed. However, we have to make the assumption in order to develop a statistical working model of the noise.

Now, a bivariate linear regression problem must be solved. The best fitting response functions are the ones with mimimum noise $|\delta Z|^2$ in the statistical average. The average is to be taken over individual spectral estimates of many events or/and over frequency bands consisting of many adjacent spectral lines. If the δZ are Normally distributed, the response functions calculated with the least squares method are maximum likelyhood estimators and hence unbiased and efficient solutions[5]: [Jenkins and Watts, 1968]:

$$a = \frac{\langle ZX^* \rangle \langle YY^* \rangle - \langle ZY^* \rangle \langle YX^* \rangle}{\langle XX^* \rangle \langle YY^* \rangle - \langle XY^* \rangle \langle YX^* \rangle} \tag{36a}$$

$$b = \frac{\langle ZY^* \rangle \langle XX^* \rangle - \langle ZX^* \rangle \langle XY^* \rangle}{\langle XX^* \rangle \langle YY^* \rangle - \langle XY^* \rangle \langle YX^* \rangle} \tag{36b}$$

X^* denotes the complex conjungate of X and the terms enclosed in angular brackets are cross- and auto spectra.

3.2 Computation of EM response functions

The components of the electromagnetic fields are recorded at discrete values of time t. The data are given as time series x_i, y_i and z_i with the time increment Δt, synchronously recorded in L- sets of $i = 1 \ldots N + 1$ data samples. Consequently, the length of each data set is $T = N\Delta t$.

Before the data can be Fourier transformed, it is useful to apply some preparatory measures to the time series. First, the influence of long period offsets must be removed by subtraction of a linear trend from the time series data[6]. A second correction is necessary because the time series do not vanish outside the chosen interval. This causes transients at both ends of the time segment, which will lead

[5] dependence on frequency is assumed.

[6] This is usually not necessary for audiomagnetotelluric data, as the time series are recorded band-pass filtered in relatively narrow frequency bands.

to biased estimates of the spectra. To smooth down these amplitude steps, the first and last sections of the data samples – $\approx 10\%$ of the whole time series – are weighted with a window function, e.g. the cosine taper function. Suitable window functions can be found in Papoulis [1987, p.234-243].

The Fourier transform of a time series of length T results in a frequency spectrum with the resolution $\Delta f = 1/T$. Since the electromagnetic response functions vary only slowly with frequency, it is sensible to reduce the frequency resolution by averaging over adjacent spectral values. The widths of the frequency bands are chosen to produce centre frequencies which are distributed equi-distantly on a logarithmic scale. This means that the band widths and the number of contained Fourier coefficients increase towards higher frequencies. There is no general rule how to divide the frequency axis exactly, but $5-10$ frequency bands per decade are usually considered to be sufficient.

Averaging over individual spectral values results in a smoothed spectral estimate for a particular center frequency [Jenkins and Watts, 1968, p.239ff]. Simply taking the average is equivalent to applying a rectangular window to the spectrum. The variance of the spectrum estimator can be reduced if a Parzen or Bartlett window is used, instead. With all statistical estimators, however, one is forced to compromise between variance and bias. The bias can only be made small by a narrow spectral window or as close to a delta function as possible. On the other hand, a narrow spectral window results in a large variance [Jenkins and Watts, 1968, p.239ff].

To compute response functions, the smoothed cross- and auto spectra are inserted into equations 36a and 36b for each time segment. Summing up all these single event spectra is the simplest way to analyse all available data-sets:

$$\overline{\langle XY^* \rangle} = \sum_{l=1}^{L} \langle XY^* \rangle_l \tag{37}$$

Here, the $\langle XY^* \rangle$ can denote both cross- or auto spectra.

The averages taken this way are very sensitive to non-Normal distributions of the noise. A few outliers in the data are sufficient to destroy a Normal distribution, causing strongly biased results of the response functions. Outliers can be removed from the data with methods based on robust statistics, which are explained in chapter 3.5.

3.3 Multi-site response functions

The least squares method can be applied provided that the noise is Normally distributed and the input components are free of noise. If uncorrelated noise is on the magnetic field components, we will obtain downwards biased estimates of the response functions.

It can be shown, that the bias is caused only by the auto spectra of the input components, while cross spectra deliver noise free contributions. Assuming that all components are a mixture of signal and noise: $X = X_S + X_N$, we can write for the

cross-spectrum of X with $Y = Y_S + Y_N$:

$$\langle XY^* \rangle = \langle X_S Y_S^* \rangle + \underbrace{\langle X_S Y_N^* \rangle + \langle X_N Y_S^* \rangle + \langle X_N Y_N^* \rangle}_{=0} \tag{38}$$

The equation above defines the noise terms X_N and Y_N as uncorrelated. Therefore, all the mixed terms of signal and noise components are zero. For an auto spectrum $Y = X$ however, the noise power $\langle X_N X_N^* \rangle$ does not vanish and causes the biased estimate of the spectrum.

The relation between $\mathbf{E}$ and $\mathbf{B}$ can be explained equally well by a system that has the electric fields as inputs and the magnetic fields as outputs. This linear system is described by the complex, frequency dependent admittance tensor $\mathbf{A}$:

$$\begin{pmatrix} B_x \\ B_y \end{pmatrix} = \mu_0 \begin{pmatrix} A_{xx} & A_{xy} \\ A_{yx} & A_{yy} \end{pmatrix} \begin{pmatrix} E_x \\ E_y \end{pmatrix} = \mu_0 \mathbf{Z}^{-1} \begin{pmatrix} E_x \\ E_y \end{pmatrix} \tag{39}$$

This time, an unbiased estimate of the admittance tensor can only be achieved if the horizontal electric field components are free of noise. Otherwise we will get an upwards biased estimate of $\mathbf{Z} = \mathbf{A}^{-1}$. The upwards- and downwards biased solutions together should give an envelope within which the correct response functions should lie [Sims et al., 1971].

For MT data processing the bias problem can be addressed with the remote reference technique [Goubau et al., 1978; Gamble et al., 1979b; Larsen, 1989]. The method is based on the assumption that magnetic fields recorded at two different sites have only uncorrelated noise components. Using the input components from two sites, the impedance tensor can be calculated as:

$$\mathbf{Z} = \mu_0 \left(\mathbf{E}\mathbf{B}_r^*\right) \left(\mathbf{B}\mathbf{B}_r^*\right)^{-1}; \qquad \mathbf{E}\mathbf{B}^* := \begin{pmatrix} \langle E_x B_x^* \rangle & \langle E_x B_y^* \rangle \\ \langle E_y B_x^* \rangle & \langle E_y B_y^* \rangle \end{pmatrix} \tag{40}$$

where the subscript r denotes the fields of a remote site. Now, only cross-spectra of horizontal magnetic field components of local and remote sites appear in the solution of $\mathbf{Z}$. If the noise between the two sites is uncorrelated, the estimation of $\mathbf{Z}$ is unbiased.

The remote reference method is not to be confused with the difference fields method, used to compute response functions between a base and a local site (cf. equation 29):

$$\mathbf{W} = \left(\left(\mathbf{B} - \mathbf{B}_b\right) \mathbf{B}_b^*\right) \left(\mathbf{B}_b \mathbf{B}_b^*\right)^{-1} = \left(\mathbf{B}\mathbf{B}_b^* - \mathbf{B}_b \mathbf{B}_b^*\right) \left(\mathbf{B}_b \mathbf{B}_b^*\right)^{-1} \tag{41}$$

Here, the subscript b denotes the base site, in contrast to a local site. Obviously, the result can be biased again by noise powers in $\mathbf{B}_b$ and hence, we could use the remote reference technique to estimate the elements of the perturbation tensor:

$$\mathbf{W} = \left(\left(\mathbf{B} - \mathbf{B}_b\right) \mathbf{B}_r^*\right) \left(\mathbf{B}_b \mathbf{B}_r^*\right)^{-1} = \left(\mathbf{B}\mathbf{B}_r^* - \mathbf{B}_b \mathbf{B}_r^*\right) \left(\mathbf{B}_b \mathbf{B}_r^*\right)^{-1} \tag{42}$$

3.4 Confidence limits for EM response functions

The construction of confidence intervals is one of the most important aspects of the estimation procedure. The method described here is a parametric estimation of the statistical errors of measured random variables, which depends on the assumptions of independent input channels and Normally distributed noise. It is based on the ideas given in Schumucker and Weidelt [1975] and in an annotation to a lecture given by Schmucker in 1989. Since the topic is not covered by many publications (e.g. [Walden, 1986]), the introduction given here is rather detailed.

In order to estimate the errors of the observed electromagnetic response functions a and b, we must compare them with α and β, the expectations of an ideal linear system:

$$Z' = \alpha X + \beta Y + \delta Z' \tag{43a}$$

$$Z = \underbrace{aX + bY}_{Z_p} + \delta Z \tag{43b}$$

X and Y denote the input channels of the linear systems and Z and Z' their outputs, respectively. While the noise $\delta Z'$ in equation 43a is entirely based on Z', δZ in equation 43b is additionally afflicted with the errors of a and b.

In chapter 3.2 we defined the best fitting response functions as the ones that minimize the noise δZ:

$$S = |\delta Z|^2 = \langle \delta Z \delta Z^* \rangle = min! \tag{44}$$

The solution in a least squares sense is found by setting the derivatives of S with respect to the real and imaginary parts of the response functions a and b to zero. The results are the normal equations [Jenkins and Watts, 1968]

$$\langle \delta Z X^* \rangle = 0 \quad \text{and} \quad \langle \delta Z Y^* \rangle = 0 \tag{45}$$

which, together with $\delta Z = Z - aX - bY$ (eqn. 43b), lead to the solutions for the response functions in equations 36a, 36b. With regard to the sum-of-squares of the errors on the other hand, using equations 44 and 45, we obtain:

$$S = \langle \delta Z Z^* \rangle - \underbrace{a^* \langle \delta Z X^* \rangle - b^* \langle \delta Z Y^* \rangle}_{=0} = \langle Z Z^* \rangle - a \langle X Z^* \rangle - b \langle Y Z^* \rangle \tag{46}$$

The errors of the response functions are defined as the differences of the observed values to their expectations:

$$\Delta a = a - \alpha; \qquad \Delta b = b - \beta \tag{47}$$

Δa and Δb are assumed to be Normally distributed with zero means and variances σ_Z^2 ($var(\delta Z) = \sigma_Z^2$).

$\delta Z'$ can be determined from equations 43a and 43b as $\delta Z' = \delta Z + \Delta a X + \Delta b Y$. Then the $\delta Z'$ are also Normally distributed and hence

$$\begin{aligned} S' &= \langle \delta Z' \delta Z'^* \rangle \\ &= \langle \delta Z \delta Z^* \rangle + |\Delta a|^2 \langle X X^* \rangle + 2\mathcal{R}e\{\Delta a \Delta b^* \langle X Y^* \rangle\} + |\Delta b|^2 \langle Y Y^* \rangle \end{aligned} \tag{48}$$

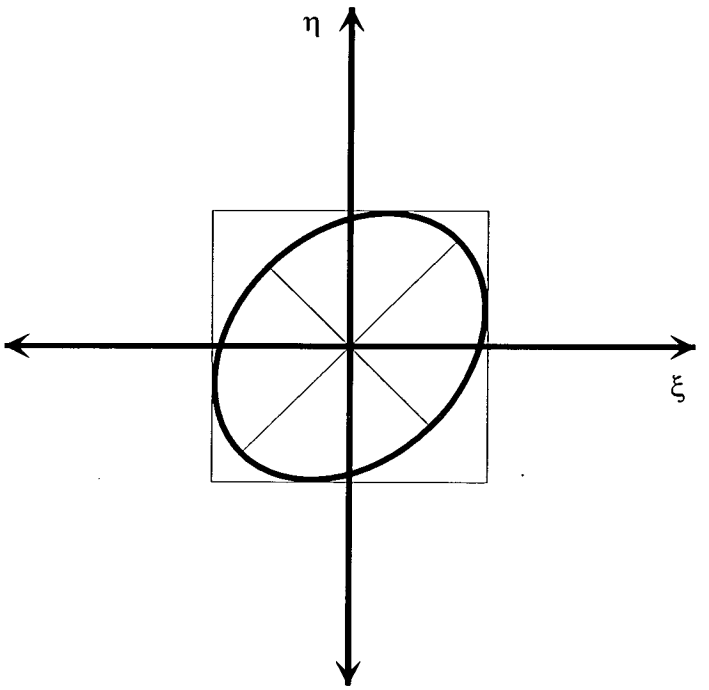

Figure 2: The geometrical construction of the error ellipses

So far the errors Δa and Δb can not be dealt with separately. Therefore, we define $\xi = |\Delta a|$, $\eta = |\Delta b|$ and rewrite equation 48:

$$S' = S + \xi^2 A + 2\xi\eta B + \eta^2 C \tag{49}$$

where $A = \langle XX^* \rangle$, $B = |\langle XY^* \rangle|$, and $C = \langle YY^* \rangle$. Equation 49 describes an ellipse whose axes are defined by linear combinations of Δa and Δb. The following relations, derived from the ellipse's tangents,

$$\xi = -\frac{B}{A}\eta \quad \text{and} \quad \eta = -\frac{B}{C}\xi \tag{50}$$

define a rectangle which encloses the error ellipse in the ξ-η-axes system (see figure 2). Now, ξ and η are inserted into equation 49 and we obtain two equations which depend on $|\Delta a|^2$ and $|\Delta b|^2$, respectively:

$$S' = (1 - r^2)\langle ZZ^* \rangle + |\Delta b|^2 \langle YY^* \rangle (1 - r_{xy}^2) \tag{51a}$$

$$S' = \underbrace{(1 - r^2)\langle ZZ^* \rangle}_{\Sigma_1} + \underbrace{|\Delta a|^2 \langle XX^* \rangle (1 - r_{xy}^2)}_{\Sigma_2} \tag{51b}$$

The multiple coherency r^2 is the ratio of predicted to measured signal energy (cf. equations 43b and 46):

$$r^2 = \frac{a\langle XZ^* \rangle + b\langle YZ^* \rangle}{\langle ZZ^* \rangle} = 1 - \frac{S}{\langle ZZ^* \rangle} = \frac{\langle Z_p Z_p^* \rangle}{\langle ZZ^* \rangle} \tag{52}$$

The coherency r_{xy}^2 measures, to which extent two random variables are linearly dependent[7]:

$$r_{xy}^2 = \frac{|\langle XY^* \rangle|^2}{\langle XX^* \rangle \langle YY^* \rangle} \tag{53}$$

If both equations 51a and 51b are normalized by σ_Z^2, the quotients S/σ_Z^2 on the left sides of the equations are χ^2- distributed quantities with ν degrees of freedom [cf. Jenkins and Watts, 1968, p.96ff]. It follows from equation 50 that the summands Σ_2 contain the errors of both, Δa and Δb[8], which means Σ_2 is χ^2- distributed with 4 degrees of freedom (real- and imaginary parts of both errors). Then, Σ_1 must be χ^2-distributed with $\nu - 4$ degrees of freedom. This consideration permits us to derive the quotients of the variances from equations 51a and 51b:

$$U_a = \frac{\frac{|\Delta a|^2 \langle XX^* \rangle (1-r_{xy}^2)}{4}}{\frac{(1-r^2)\langle ZZ^* \rangle}{(\nu-4)}} \quad \text{and} \quad U_b = \frac{\frac{|\Delta b|^2 \langle YY^* \rangle (1-r_{xy}^2)}{4}}{\frac{(1-r^2)\langle ZZ^* \rangle}{(\nu-4)}} \tag{54}$$

U_a and U_b are FISCHER distributed quantities with $\nu_1 = 4$ and $\nu_2 = \nu - 4$ degrees of freedom. Eventually, we can give estimates (upper limits) for the errors of the electromagnetic response functions:

$$|\Delta a|^2 < \frac{(1-r^2)\langle ZZ^* \rangle}{(1-r_{xy}^2)\langle XX^* \rangle} \frac{4}{\nu - 4} F_{4,\nu-4} \tag{55a}$$

$$|\Delta b|^2 < \frac{(1-r^2)\langle ZZ^* \rangle}{(1-r_{xy}^2)\langle YY^* \rangle} \frac{4}{\nu - 4} F_{4,\nu-4} \tag{55b}$$

F_{ν_1,ν_2} is called Fischer's F distribution with ν_1 (numerator) and ν_2 (denominator) degrees of freedom.

This error estimation procedure cannot easily be extended for the remote reference case, because the expressions for the auto spectra in equation 48 must be replaced with cross spectra of local and remote sites, and consequently S' becomes a complex quantity. Hence, we suggest to use the remote reference technique in an attempt to obtain unbiased estimates of the response functions, but we calculate the errors using the input components of the local sites, only. Alternatively, one could compare the electric fields of the local sites solely with the magnetic fields of the remote sites:

$$\mathbf{Z}' = \mu_0 \left(\mathbf{E}\mathbf{B}_r^*\right) \left(\mathbf{B}_r\mathbf{B}_r^*\right)^{-1} \tag{56}$$

More information on error estimation for the remote reference method can be found in Gamble et al. [1979a].

It follows from equations 55a and 55b that for given auto spectra and noise in Z, the response functions are estimated more accurately, if the number of degrees of freedom increases (many independent observations) and if the linear dependency

[7]The result for the coherency can be biased due to the noise in the auto spectra in the denominator

[8]from eqn. 50: $C = -B\frac{\xi}{\eta}$; insertion into 51a: $\Sigma_2 = -|\Delta b||\Delta a|\langle XY \rangle|(1 - r_{xy}^2)$.

between the two input channels is small ($r^2_{xy} \rightarrow 0$). The application of data windows (cf. chapter 3.2) increases the statistical dependencies between spectral estimates and therefore causes a decrease in the number of degrees of freedom.

It should be pointed out, that Chave et al. [1987] propose a non-parametric method[9] to estimate the confidence limits of the response functions. However, this method is not discussed here.

3.5 Robust methods

Generally, we have no knowledge of the true noise distribution in our observations; however, we would like the noise to be Normally distributed. Robust methods aim to single out data that belong to an unknown noise distribution of outliers. In that respect, response functions estimated with robust methods are less sensitive to a moderate amount of bad data or to an inadequately chosen statistical model. However, the amount of outliers must be less than 50% as robust methods do not perform any magic. If the majority of the data are bad, the results will be bad. Furthermore will robust methods not repair systematic instrumentation errors.

It is not the aim to review or compare the various robust procedures available, nor to have another discussion about the diverse advantages of robust statistics. Suggestions for further reading are [Huber, 1981; Hampel et al., 1986; Egbert and Booker, 1986; Chave et al., 1987; Ritter, 1988; Jones et al., 1989]. In this context I concentrate on the description of a method developed by Junge [Junge, 1990; 1992; 1994].

Junge's method combines two parts: the χ^2-criterion and the consistency criterion. The χ^2-criterion examines whether a single event spectrum fits into the global view of the majority of all data. Accordingly, the influence of a single event spectrum is increased or decreased by a robust weighting scheme. Furthermore, by comparison of the noise distribution of the observations with a theoretical χ^2-distribution, a more reliable estimate for the number of degrees of freedom is obtained. A trustworthy estimation of the number degrees of freedom is essential for meaningful error bars (chapter 3.4). The consistency criterion reduces non-stationary contributions in the response functions by iteratively replacing a certain amount of the *bad* data with predicted values.

I intend to illustrate the functioning of the algorithms. For a more detailed discussion of the statistical background see Junge [1994].

3.5.1 The χ^2 criterion

First step: Initial guess of response function estimates

The frequency domain observations of the electromagnetic field components X,Y and Z are recorded in $l = 1 \ldots L$ events. Z shall be expressed as a linear combination

[9] known as the jackknife method.

of the components X and Y, plus an additional noise term δZ.

$$Z_l = aX_l + bY_l + \delta Z_l \tag{57}$$

The response functions a and b are obtained as the solution of equation 57 by solving the normal equations. Let a^0 and b^0 be the response functions calculated by the Least Squares method (cf. equations 36a and 36b). Then, we derive for the errors δZ_l^0:

$$\delta Z_l^0 = Z_l - a^0 X_l - b^0 Y_l \tag{58}$$

Second step: Initial guess of variance

$\hat{\sigma}_Z^M$ is the initial guess for the variance[10] of the solution:

$$\hat{\sigma}_Z^M = 1.483\, med\left[\left|\delta Z_l^0 - med(\delta Z_l^0)\right|\right] \tag{59}$$

The median of a distribution is estimated from a sample of values $x_1, \ldots, x_N$ by finding that value x_i which has equal numbers of values above it and below it. If the values $x_{j,j=1,\ldots,N}$ are sorted into ascending order, then the formula for the median is [Press et al., 1988]:

$$x_{med} = \begin{cases} x_{\frac{N+1}{2}} & ; \text{ for N odd} \\ \frac{1}{2}\left(x_{\frac{N}{2}} + x_{\frac{N}{2}+1}\right) & ; \text{ for N even} \end{cases} \tag{60}$$

The median is preferred over the average mean because it is more robust against outliers [Junge, 1994]. We use $\hat{\sigma}_Z^M$ to define an upper limit c^M for a permitted variance of a single event:

$$c^M = 1.5\,\hat{\sigma}_Z^M \tag{61}$$

The value 1.5 in the above equation is an empirically established figure. The c^M-values must be adjusted if the assumed amount of bad data is smaller or larger than $\approx 20\%$ outliers. c^M is used to calculate HUBER-weights w_l for each event l [Huber, 1981]

$$w_l^M = \begin{cases} 1 & ; \text{ for } \delta Z_l^0 \le c^M \\ \frac{c^M}{|\delta Z_l^0|} & ; \text{ for } |\delta Z_l^0| > c^M \end{cases} \tag{62}$$

Reasoning similarly to equations 37, we formulate

$$\overline{\langle XY^* \rangle}^M = \sum_{l=1}^{L} \left(w_l^M \langle XY^* \rangle_l^0\right) \tag{63}$$

and the response functions a^M and b^M and the errors δZ_l^M are calculated according to equations 36a and 36b.

[10] For clarity, we write the variances without the squares: $\hat{\sigma}_Z^M = \hat{\sigma}_Z^{M^2}$.

Third step: Robust estimation of response functions and confidence limits

To estimate the variance of the robust solution above, we must take into account the weights w_l. Using the HUBER-weights, the variance $\hat{\sigma}_Z^H$ becomes:

$$\hat{\sigma}_Z^H = \frac{L}{L_c^2} \sum_{l=1}^{L} \left(w_l^M \delta Z_l^M \right) \tag{64}$$

L_c is the number of fully weighted events, which fullfill the condition $|\delta Z| \leq C$ in equation 62.

To proceed, we replace c^M in equation 61 with $c^H = 1.5\hat{\sigma}_Z^H$ and calculate the weights w_l^H in accordance to equation 62. Together with the HUBER-weights and using equation 63, we obtain new estimates for the response functions (a^H and b^H, respectively).

For the estimation of the variance in the second step we use the median because it is more robust than the average mean, but it merely serves as the initial guess for the HUBER weighting scheme (third step). The HUBER function, used to compute the weights, is guaranteed to converge, but it cannot always sufficiently eliminate the effects of extreme outliers [Junge, 1994].

Forth step: TUKEY weights (reduction of extreme outliers)

To get rid of these exteme values, the data are weighted again. This time, the weights w_l^T are calculated using Tukey's biweight function [Beaton and Tukey, 1974]. First we compute the variance $\hat{\sigma}_Z^T$ [Junge, 1994; app.A.1]:

$$\hat{\sigma}_Z^T = \frac{\frac{1}{L} \sum_l^L \left(w_l^H \delta Z_l^H \right)^2}{\frac{1}{L_c} \sum_l^L \left(1 - \left(\frac{\delta Z_l^H}{c^H} \right)^2 \right) \left(1 - 5 \left(\frac{\delta Z_l^H}{c^H} \right)^2 \right)} \tag{65}$$

and with the limit $c^T = 6\,\hat{\sigma}_Z^T$ we obtain TUKEY-weights w_l^T:

$$w_l^T = \begin{cases} \left(1 - \left(\frac{\delta Z_l^0}{c^T} \right)^2 \right)^2 & \text{for} \quad \delta Z_l^0 \leq c^T \\ 0 & \text{for} \quad \delta Z_l^0 > c^T \end{cases} \tag{66}$$

If the assumption was correct that – exept for a few outliers, which had to be removed – the δZ are Normally distributed with variance σ_Z^2, then $\langle \delta Z \delta Z^* \rangle / \sigma_Z^2$ is a χ^2-distributed quantity with ν degrees of freedom (cf. chapter 3.4). The number of degrees of freedom of a χ^2 distributed quantity can be estimated from the observations, as the ratio of the expected value to its variance (e.g.[Bronstein and Semendjajew, 1981; p.717ff]:

$$\nu = \frac{2E\{\langle \delta Z \delta Z^* \rangle\}^2}{var\{\langle \delta Z \delta Z^* \rangle\}} \approx \frac{2\left(\frac{1}{L} \sum_l \langle \delta Z \delta Z^* \rangle \right)^2}{\frac{1}{L-1} \sum_l \left(\langle \delta Z \delta Z^* \rangle_l - \overline{\langle \delta Z \delta Z^* \rangle} \right)^2} \tag{67}$$

Junge [1994] obtains consistently better agreements between the noise distributions of the observations and their theoretical expectations if the number of degrees of freedom is computed after equation 67, instead of being derived directly from the equivalent bandwidth of the spectral smoother (chapter 3.2). The latter method usually leads to systematically over-estimated values for ν and hence to under-estimated error bars.

3.5.2 Consistency criterion

In the last chapter we declared single event spectra data as *bad* if they had large errors compared to the rest of the data. The influence of these outliers was reduced by down-weighting (removing) the whole event. The algorithm is founded on the assumption that the distributions of the derived response functions are constant in time. However, the response functions could be non stationary due to changing quality (inhomogeneity) of the source fields or due to varying amounts of correlated noise which cannot be removed by the data processing procedures.

The algorithm works iteratively, the superscript $j = 0 \ldots J$ denotes the iterations. The following abbreviations are used: $S_{xx} = \langle XX^* \rangle$, $S_{zx} = \langle ZX^* \rangle$ and $S_{zy} = \langle ZY^* \rangle$:

First step: Calculation of response functions

The response functions a and b and their related errors δZ_l are calculated from the $l = 1 \ldots L$ single event spectra, e.g.using the χ^2-method of the last chapter. For each event, we define a limit $c^{(j)}$:

$$c^{(j)} = 1.5 \sqrt{\mathrm{var}\{S^{(j)}_{\delta Z,l}\}} \tag{68}$$

Second step: Calculation of weights

For the next iteration, weights less than 1 are calculated for events with errors greater than $c^{(j)}$:

$$\left(w_l^{(j+1)}\right)^2 = \begin{cases} 1 & ; \text{for} \quad S^{(j)}_{\delta Z,l} < c^{(j)} \\ \dfrac{c^{(j)}}{S^{(j)}_{\delta Z,l}} & ; \text{otherwise} \end{cases} \tag{69}$$

Third step: Prediction of new spectra

In order to compute better response function values, we calculate new estimates for the cross- and auto spectra. A similarly working algorithm was developed by Egbert and Booker [1986]. It can be shown to be similar to a Gauss-Newton scheme for solving non-linear systems. New estimates – or predictions – for single event spectra are obtained by comparing them with the stacked results from all events.

The results for the $(j+1)^{th}$-iteration are:

$$\langle \mid S_{zz,l}^{(j+1)} \mid^2 \rangle_l = (w_l^{(j)})^2 \langle \mid S_{zz,l}^{(j)} \mid^2 \rangle_l + 2w_l^{(j)}(1-w_l^{(j)}) Re\{\langle S_{zz,l}^{(j)} \hat{S}_{zz,l}^{(j)*} \rangle_l\} + (1-w_l^{(j)})^2 \langle \mid \hat{S}_{zz,l}^{(j)} \mid^2 \rangle_l \quad (70a)$$

$$\langle S_{zx,l}^{(j+1)} \rangle_l = w^{(j)} \langle S_{zx,l}^{(j)} \rangle_l + (1-w_l^{(j)}) \langle \hat{S}_{zx,l}^{(j)} \rangle_l \quad (70b)$$

$$\langle S_{zy,l}^{(j+1)} \rangle_l = w^{(j)} \langle S_{zy,l}^{(j)} \rangle_l + (1-w_l^{(j)}) \langle \hat{S}_{zy,l}^{(j)} \rangle_l \quad (70c)$$

The previous j^{th}-iteration cross- and auto spectra are calculated from the stacked results, using equations 36a and 36b:

$$\hat{S}_{zx}^{(j)} = a^{(j)} S_{xx}^{(j)} + b^{(j)} S_{xy}^{(j)} \quad (71a)$$

$$\hat{S}_{zy}^{(j)} = a^{(j)} S_{xy}^{(j)} + b^{(j)} S_{yy}^{(j)} \quad (71b)$$

$$\hat{S}_{zz}^{(j)} = |a^{(j)}| S_{xx}^{(j)} + |b^{(j)}| S_{yy}^{(j)} + 2Re\left\{a^{(j)} (a^{(j)})^* S_{xy}^{(j)}\right\} \quad (71c)$$

Steps 1 to 3 are repeated until the changes of $a^{(j)}$ and $b^{(j)}$ are less than a certain limit, e.g. $< 5\%$. The algorithm works in a way that the smaller the weigths $c^{(j)}$, the more a single event spectrum is replaced by the value predicted from the response function (averaged over all spectra). For $w^{(j)} = 1$ the observed spectra in equations 70a-70c are taken over to the next iteration unchanged, while for $w^{(j)} = 0$ they are entirely replaced by the ones calculated in equations 71a-71c.

The number of degrees of freedom is reduced to the same extent as the result of an event is replaced by its prediction:

$$\nu_l^{(j+1)} = \nu_l^{(j)} w_l^{(j)} \quad (72)$$

The consistency criterion is computationally more costly than the χ^2 procedure because it is based on an iterative algorithm. In practice, it is more often than not sufficient to run solely the χ^2-criterion. The application of the consistency criterion afterwards has usually no great effect on the results.

4 The Magnetic Variation Mapping experiment at Middleton

4.1 Objectives

Magnetic variation mapping (MVM) was one of the earliest tools to locate electrical conductivity contrasts. The vertical component of the time variations is particulary sensitive to the position of lateral conductivity boundaries because it is normally zero in their absence (chapter 2.3).

Magnetic variation anomalies have been mapped, typically at long periods between $30s$ and $6000s$ using suspended magnet and fluxgate magnetometers. Anomalous fields have been detected across the whole of the period range, and our ability to map them and identify their origins has been limited by the sampling rate of the observations (typically $10\,s$ or more), and by the sensitivity of the magnetic detectors ($0.2\,nT$ or worse). For that period range, the spatial scale of the anomalies is generally $10km$ or more, suggesting sources at least a few kilometers deep.

It is likely, however, that at least some anomalies are generated by boundaries visible at the surface, e.g.the faulted margins of sedimentary basins. But the spatial density of audiomagnetotelluric observations has rarely been sufficient to give us confidence that anomalies of shorter wave lengths were resolved adequately. Most of the early audiomagnetotelluric work was focused on the observation of the telluric field at higher frequencies. Often, the vertical magnetic field component was not recorded at all, sometimes the induction coils were simply not installed carefully enough in the field.

This chapter is about an experiment to map the spatial structure of the magnetic variations with sufficiently dense site spacing, and at sufficiently high frequencies to be able to interpret the anomalies in terms of conductive boundaries that can directly be correlated with the surface geology.

Further information on the application of high frequency geomagnetic variations to interpret AMT data can be found in Takasugi et al. [1992a, 1992b] and Zhang et al. [1995].

4.1.1 Site location and geological background

For the experiment's location we aimed to find a site close to Edinburgh, with a two-dimensional conductivity contrast of at least 10 to 1 at the surface, with easy access to work along a profile and – hardest to achieve – without any artifical electromagnetic noise sources. Obviously, those locations rarely ever exist in reality. Nevertheless, from previous and recent EM work, we considered the area around the Southern Upland Fault to be a suitable test site [Sule, 1985; Livelybrooks et al., 1993].

The ENE-WSW trending Southern Upland Fault (SUF) complex is a prominent geological feature that separates the Midland Valley and the Southern Uplands in the South of Scotland. Tectonically it is probably partly associated with the closure

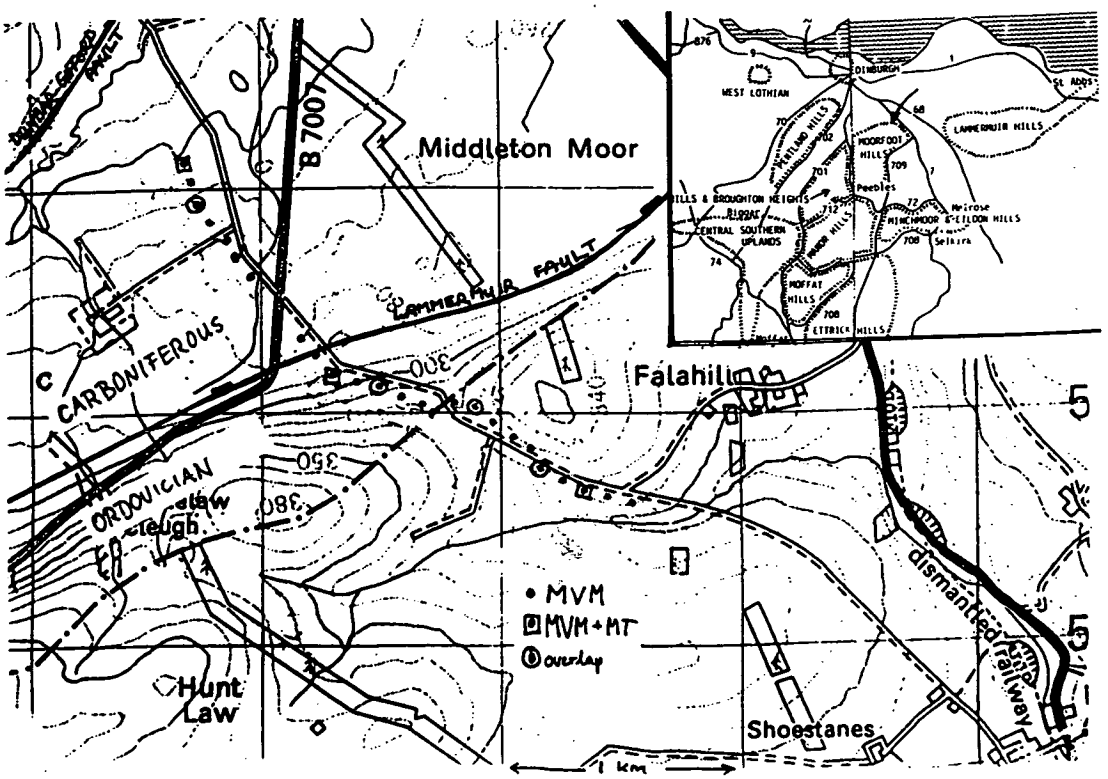

Figure 3: *The map shows the locations of 24 MVM and 3 MT sites; the gridlines on the map are plotted in a 1km raster.*

of a proto-Atlantic ocean in the Upper Paleozoic time. In Lower Palaeozoic times up to several hundred kilometers of deep sea – the Iapetus ocean – separated the North of Scotland, then part of the (American) Laurentian plate, from the Scottish Borders and England, being parts of the (European) Avalonia plate [Cocks and Fortey, 1982; Leggett et al., 1983]. Beginning in the Cambrian and continuing into the Devonian, this ocean was consumed by subduction to the north under Laurentia [McKerrow and Cocks, 1988].

Today, the Iapetus Suture Zone is covered by younger, Carboniferous sediments and is thought to be concealed beneath and possibly to the north of the Northumberland Trough in the UK [Livelybrooks et al., 1993]. The Iapetus Suture Zone has been and still is a prime target for geoscience research. Electromagnetic work has been undertaken since the late 1970's: [Jones, 1977; Hutton et al., 1979, Hutton et al., 1980, Hutton and Jones, 1980; Banks et al., 1983, Banks, 1986, Banks et al., 1993; Beamish, 1986, Beamish and Smythe, 1986; Parr and Hutton, 1993; Sule et al., 1993]

The profile we chose crosses the Southern Upland Fault 15 *km* SSE of Edinburgh (see figure 3). The fault, locally known as the Lammermuir Fault, throws down Carboniferous sedimentary rocks to the northwest against Ordovician meta-sedimentary rocks to the southeast. The throw is uncertain, though gravity data suggest that it

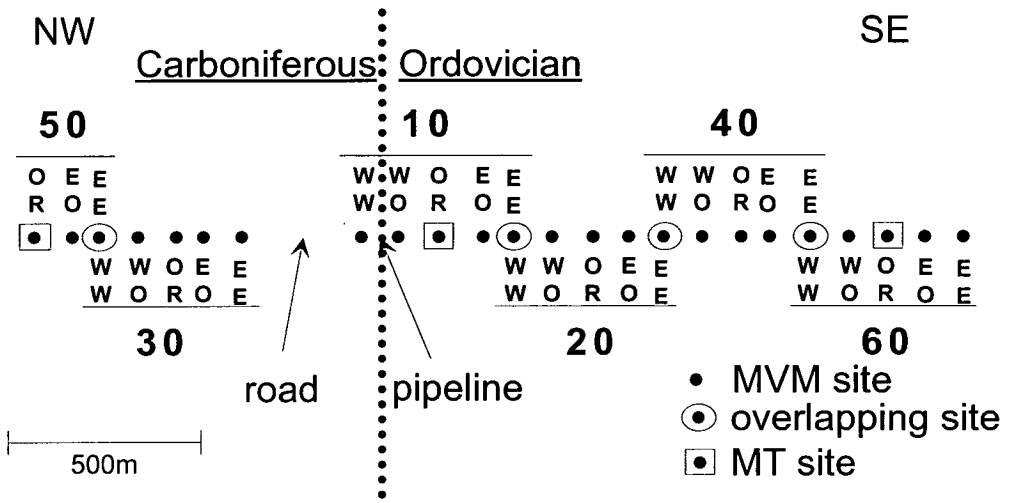

Figure 4: *Projection of the sites onto a profile. The data were recorded in clusters of site-sets* (10-60)*. Indicated are the locations of a road (B7007), the Lammermuir Fault (dotted line), and a gas pipeline.*

varies along the fault from $200 - 2000m$ [Lagios, 1979]. The Ordovician (Caradoc - Ashgill) rocks are mainly greywacke with conglomeratic bands, in places siltstone, shale and mudstone, with beds of chert and graptolite shale. The Calciferous Sandstone measures of the Carboniferous Limestone Series (Dinantian) are composed of an upper, predominantly sandy subdivision, and a lower sandstone, shale and cement stone subdivision [BGS, 1983b; Greig, 1971; MacGregor and MacGregor, 1948]. Judging from the previous investigations, we expected a conductivity contrast in the order of 10:1 for the fault. The Carboniferous sediments are known to be conductive with resistivities of less than $100\,\Omega m$, while the Ordovician rocks can reach resistivities of $1000\,\Omega m$ or more.

Figure 3 shows the locations of the 24 MVM sites (black dots) and 3 MT sites (hollow squares). Since the recording equipment had to be deployed in a trailer, we required road access to the sites. Therefore the profile follows a field track towards the southeast and goes along a minor road towards the northwest. To avoid the effects of traffic on the B7007, the profile had to be discontinued for ca. $300m$.

Shown in figure 4 is a projection of the sites onto a profile and the sites' naming convention is given. The whole of the data were recorded in clusters of six site-sets (10 - 60) in September and October 1992. Magnetotelluric data are available from sites 50OR, 60OR at both ends of the profile and from site 10OR in the centre of the profile. Also indicated in the figure are the road-gap and a gas pipeline that runs almost exactly on top of the presumed fault line. The location of the fault is marked as a dotted line between sites 10WW and 10WO.

To explain the idea of overlap-sites (circled dots in figure 4), it is necessary to have a more detailed look at the available instrumentation.

4.1.2 Instrumentation and equipment layout

In the past dense MVM arrays have been limited by the requirement for acquisition systems with higher sampling rates and magnetic detectors with enough sensitivity to cope with the so-called *dead band* around $1Hz$. At the time we carried out the experiment, the first was available in the form of a departmental S.P.A.M. MkIIb[11] [Dawes, 1984; 1987], and the second in the shape of CM11E induction coils, supplied by the NERC geophysical equipment pool. This combination of hardware facilitates observations of up to 7 channels of electromagnetic time series data, in short, non-continuous segments of 256 samples, in the frequency range $100\,Hz$ to $100\,s$.

The time series data are recorded in 4 frequency bands (see table 2), one of which can be selected at a time. The band limiting filters are realised in hardware

	low pass		high pass		sampling rate	
Band 0:	128	*Hz*	16	*Hz*	512	*Hz*
Band 1:	16	*Hz*	2	*Hz*	64	*Hz*
Band 2:	2	*Hz*	4	*s*	8	*Hz*
Band 3:	4	*s*	32	*s*	1	*s*

Table 2: *The four frequency bands of S.P.A.M. MkIIb.*

as active Butterworth filters, with 5-pole low-passes and 2-pole high-passes. For frequency bands 0 and 1, the instrument is equipped with $50\,Hz$ and $150\,Hz$ notch filter modules. Notch filter are necessary to suppress signals generated by the mains power supplies with much larger amplitudes than any of the natural signals. These signals do not carry useful geological information, but reduce the dynamic range of the instruments.

The overall signal amplification of the system after preconditioning[12] is selected in two stages in the range between $2^1 \ldots 2^{16}$. The first stage is pre-set by the user and remains fixed, while the second stage is automatically adjusted by the instrument. This ensures optimum usage of the dynamic range, which is mainly determined by the analogue-to-digital converter resolution (12 bits/channel).

For our experiment and to take full advantage of the 7 channels, we configured the instruments as shown in figure 5. Each site configuration consists of two orthogonal horizontal magnetic field sensors plus 5 vertical ones. The vertical induction coils are separated by approximately $100m$, covering a total of $400m$ on the profile by 5 MVM sites. The horizontal magnetic fields at the centre of a spread are recorded as reference signals for each of the 5 vertical magnetic field sites.

The last magnetometer of each site-spread is recycled as the first one of the next configuration (figure 5). The vertical magnetic field response functions for these

[11] By then, the new generation of the instruments (S.P.A.M. MkIII) was still at the planning stages (chapter 5).

[12] gains of 40 and 50 for the telluric and magnetic channels, respectively.

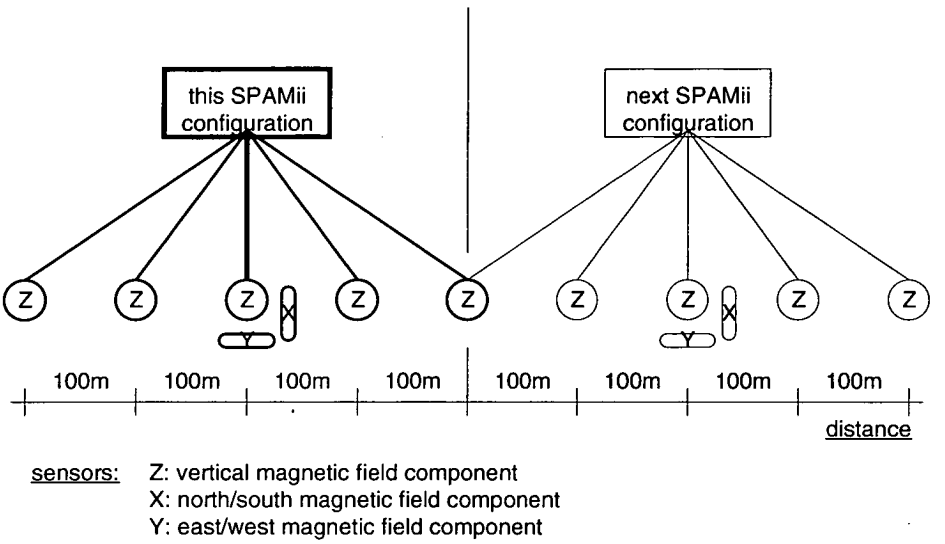

Figure 5: *S.P.A.M. MkIIb equipment layout for the MVM experiment.*

magnetometers are calculated twice, but each time with reference to a different centre site with its respective set of horizontal magnetic fields. We assume that the inducing fields are homogenous and that the response functions depend solely on position. Then, differing vertical magnetic field response functions at one site would indicate the presence of anomalous horizontal fields and we can obtain some information about their spatial variation. Anomalous horizontal fields occur in the vicinity of lateral resistivity boundaries and may bias the single site vertical response function results (chapter 2.3).

S.P.A.M. MkIIb is a real-time system, originally designed to process data from standard 5 component MT sites or 5 component sites with 2 remote telluric channels. In the course of this, the data of a whole time segment are rejected if a certain amount does not fulfill the minimum requirements for coherency and signal power. The thresholds are set by the user in accordance to the prevailing noise conditions. Because all S.P.A.M. MkIIb data are stored on floppy disks (720kb), only those time segments are saved that pass the on-line data quality criteria. Unfortunately, S.P.A.M. MkIIb's internal processing software could not be altered in time to adopt to this special MVM set-up. Consequently, it was only the quality of the (standard) site at the centre of each spread which decided if the data of the whole set was recorded or rejected. Appendix A.1 gives a complete listing of the total amount of recorded data together with the exact locations of the sites.

4.2 Results and data evaluation

4.2.1 Time series and data processing

To get a feeling for the pecularities of a specific field area and to examine the data quality it is always useful to look at the time series data first. Figure 6 shows time

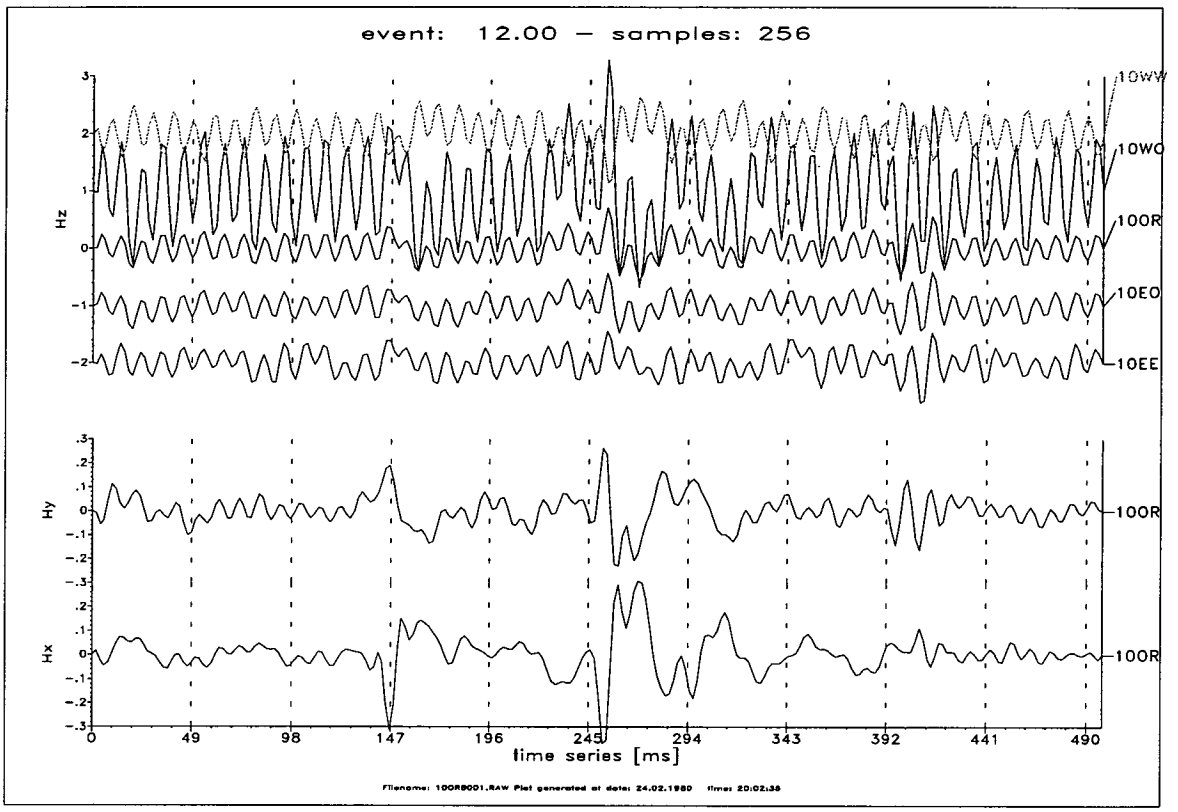

Figure 6: *High frequency (band 0) time series example from the sites close to the assumed fault line.*

series recorded in the high frequency band 0 ($128\,Hz$-$16\,Hz$) for the sites of set 10, that crosses the assumed fault line. What catches the eye immedeately are *(i)* strong sinusoidal $100\,Hz$ signals, *(ii)* a reversal of sign between sites 10WO and 10WW, and *(iii)* vertical magnetic field (H_z) amplitudes much larger than those of the horizontal magnetic fields (H_x, H_y). All time series data are scaled approximately to nT, as the induction coils have flat response curves of $50mV/nT$ over most of the frequency range. Only the effects of the band-limiting low- and high-pass filters are not taken into account.

$100\,Hz$ signals are usually generated by AC/DC conversion devices (rectifiers) and just like the $50\,Hz$ signals they do not carry any geological information. Although these signals appear to be dominating the time series, as they are not filtered by S.P.A.M. MkIIb, they are well within the dynamic range of the instrument. This guarantees that the far smaller natural signals of the frequency band are still resolved with sufficiently high resolution. Transformed into the frequency domain, the $100\,Hz$ signals affect only a very narrow range of the spectrum which can be omitted during data processing.

At a first glance, the reversal of sign in the time series between sites 10WO and 10WW seems to agree nicely with the mapped geological boundary, but it also coincides with the location of a gas pipeline, that runs almost exactly on top of the

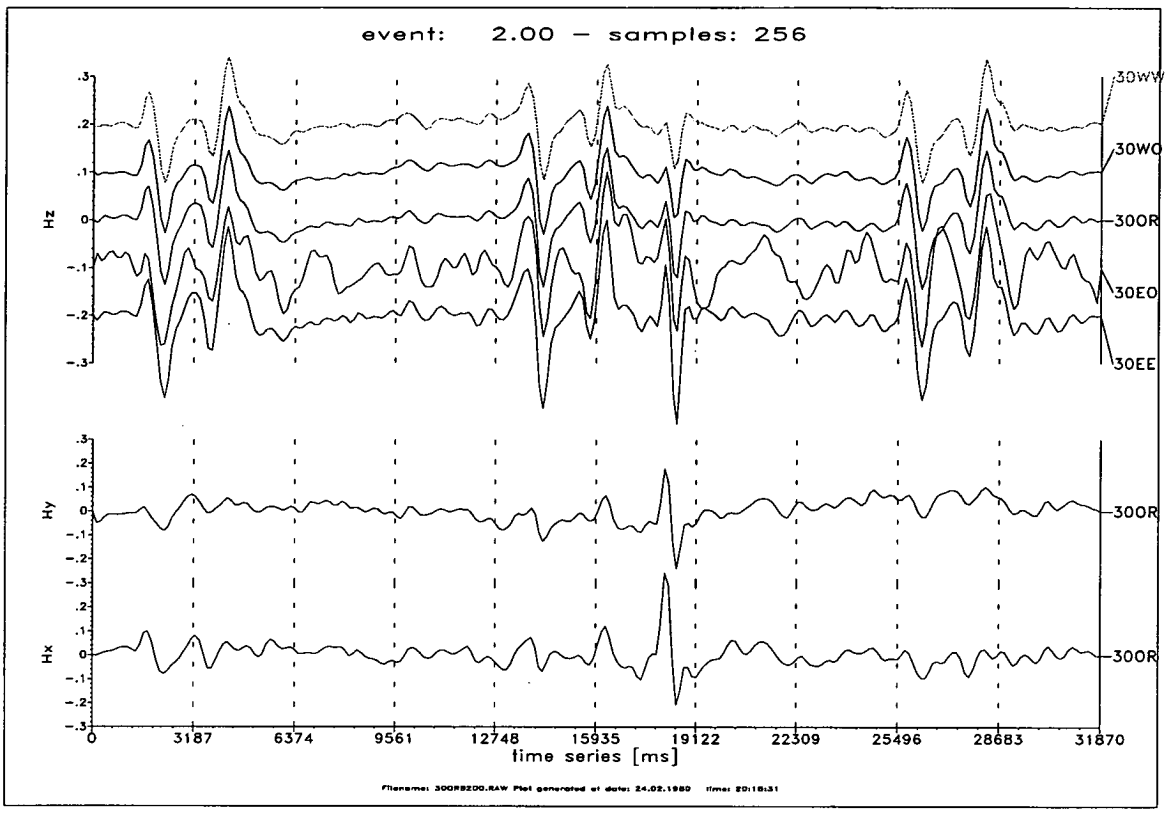

Figure 7: *Band 2 time series example of the sites on the Carboniferous sediments.*

fault line. Pipelines and electric fences are known to be potential noise sources, and therefore, it is important to discuss their possible influence on the final response function estimates.

Figure 7 shows a time series example of frequency band 2, with some odd looking signals, generated periodically every 11.5 s. The signals dominate the vertical magnetic field components (H_z) of all 5 sites, while they seemingly have smaller effects on the horizontal fields. This noise and the 100 Hz signals are presumably generated by electric fences and their underground supply lines, which were widely used in the area. Visible in the time series are the band-pass-filtered results of an originally more spike-like signal, produced by a switching device. Usually, impulsive phenomena are the most damaging forms of noise, as they contaminate a wide range of the frequency spectrum ([Fontes et al., 1988]). The situation is even worse since the H_z signals are coherent with the horizontal magnetic field components. However, what matters is that in comparison with the vertical component the horizontal fields seem to be much less affected by noise. Nevertheless, signal coherency is the key factor when estimating the quality criterion during data acquisition and therefore windows containing contaminated time series are not always rejected. Leakage of that kind of noise towards higher frequencies can futhermore not always be suppressed efficiently by the robust processing procedures.

There is one effect, near the middle of figure 7, which is clearly expressed on all

components. It is remarkable to see the energy of that event (and of the background signals) decreasing to one third in amplitude over a range of only 400m between sites 30EE and 30WO. This could well reflect the geological situation as all sites are located on the Carboniferous strata, with 30EE being closest to the conductivity boundary. Vertical magnetic fields are linked to lateral conductivity changes and the anomaly diminishes more rapidly over conductive strata (figure 9).

Since problems with noise are also noticable at sites located on the Ordovician side and because it is generally extremely difficult to get good quality data in the frequency range 10 Hz-0.1 Hz[13], one must expect less reliable results for that frequency range.

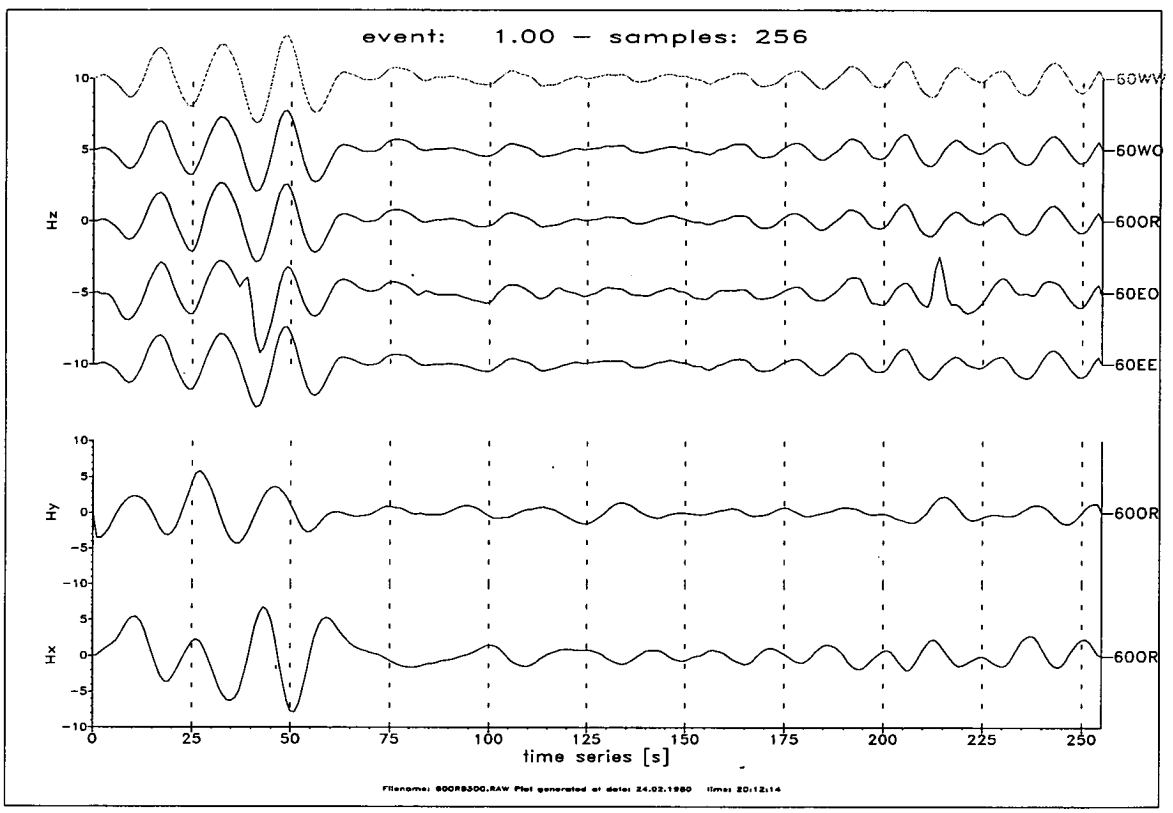

Figure 8: *Long period (band 3) time series example from the sites of the southeastern end of the profile.*

The last example of time series (figure 8) shows long period data (band 3) from the southeastern end of the profile (site-set 60). Typically for the long period data, the channels in this segment are well correlated. However, towards the shorter periods of that frequency band and in the absence of strong natural events, the influence of noise becomes more evident again. Consequently, the resulting response functions of band 3 are often disturbed towards the shorter periods, while the quality for the longest periods is generally very good. The vertical magnetic fields and their

[13]the so called *dead band*, where the natural electromagnetic activity is minimal.

respective response functions are much smaller in comparison to the other frequency bands.

4.2.2 Response functions and modelling

Following the survey, all available S.P.A.M. MkIIb pre-selected data sets were subjected to re-processing. For the re-processing I used the newly developed software (chapter 6.3), which is based on robust statistics (chapter 3). Below I give a brief recapitulation of the steps involved.

First the fixed length data segments (256 samples) are tapered with the cosine bell function and then they are Fourier transformed. The frequency domain data are corrected for the influence of the instrument response functions (induction coils and telluric signal pre-conditioning). The calibrated Fourier coefficients are divided into 8 bands per decade, with centre frequencies equally distributed on a logarithmic scale. For each band and all channels, auto- and cross spectra estimates are computed, applying Parzen smoothing windows. The final response functions are calculated by stacking the smoothed spectra from many time segments with Junge's robust algorithm. The total volume of data records is usually split into several runs, because S.P.A.M. MkIIb acquires data in 4 separate, sequentially activated frequency bands. Hence, each run is first processed individually and its quality is evaluated. Eventually, only the most consistent runs are stacked, to form the final response function results.

Since such a dense mapping of the vertical magnetic field response functions has never been tried before, it will be useful to establish the type of results one expects for such an experiment. Before we examine our field results in more detail, we therefore start with a discussion of a simple two-dimensional forward model. The model, illustrated in figure 9, serves as a first electromagnetic approximation to the suggested geological situation. The model is plotted in the lower part of the figure. It consists of a thin ($1km$) conductive surface layer of $10\,\Omega m$ in a less conductive $1000\,\Omega m$ surrounding. The horizontal extent of the model is $5km$, with 14 model sites - labelled *s001* to *s014* - distributed over the model. The distribution of the sites is not related to the observations, but in order to resolve the inductive anomaly, the sites close to the conductive boundary are arranged in a denser spacing. The smaller diagrams on the upper left and right show respectively contour plots of the real and imaginary parts of the Z_H vertical magnetic field response functions[14]. The contours are plotted as pseudo-depth sections with the locations of the model-sites on the horizontal axes and the logarithm of frequency on the vertical axes. The model responses and the contour plots are produced with the Geotools software package, which is based upon Wannamaker's 2D code [Wannamaker et al., 1987].

The real parts of the transfer functions (upper left graph in figure 9) have zero (light grey) to negative (dark) values. The edge of the conductive boundary is indicated by the transition from slightly negative values (< -0.4) to large negative values ($-0.8 \ldots -1.0$). The anomaly is clearly expressed over a wide frequency

[14]The Z_D response function equals zero in the 2D case (in a strike coordinates).

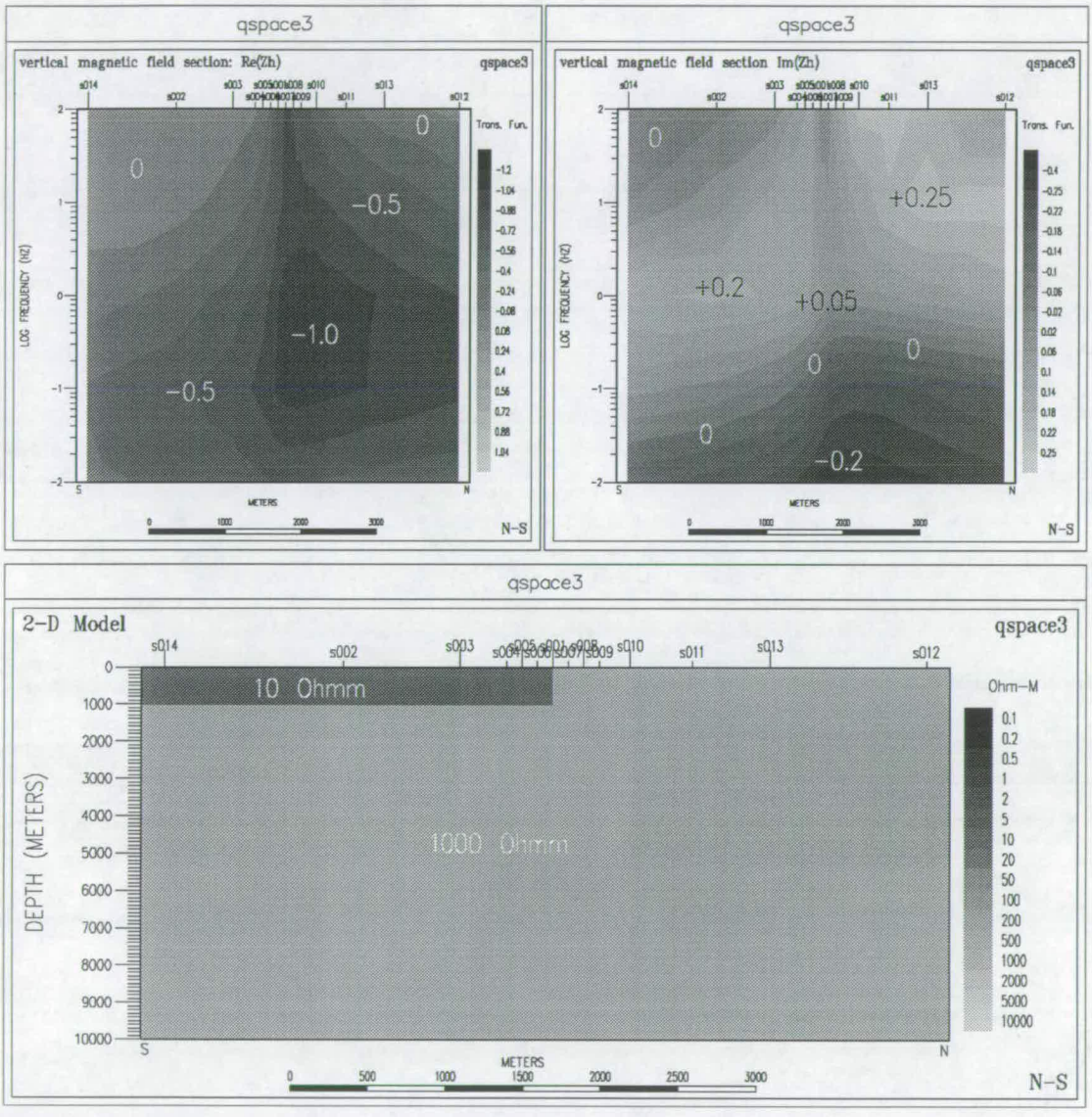

Figure 9: *A two-dimensional forward model as a preliminary electromagnetic approximation to the expected geological situation.*

range ($100\,Hz$ - $100\,s$), with the lateral boundary of the conductor being the most significant feature. At the highest frequencies, the horizontal extent of the anomaly is limited to an area underneath the very densely spaced sites, while the maximum broadens with greater penetration depths. The conductive boundary is also indicated by the imaginary part (upper right in figure 9). The imaginary parts change from positive to negative values with decreasing frequencies. This change of sign occurs asymetrically on opposite sides of the conductive boundary at a period of approximately $1\,s$. In the period range $1\,s$ to $10\,s$ we see a transition zone of small (≈ 0) imaginary parts, which correspond to a region of maximum real parts (≈ -1). The imaginary parts are generally smaller than the real parts. They reach maximum values around ± 0.3.

This characteristic effect in the response functions is a reflection of the underlying physical processes. They let us determine the origins of the anomalous currents. For the smaller penetration depths (high frequencies) induction is the dominant feature. The anomalous currents are created within the conductive layer. Maximum anomalous currents occur, when the anomalous fields are just in-phase with the inducing fields. For the longer periods, currents are produced outside the anomaly and deflected towards the surface conductor.

Figure (10) shows contour plots of the observed, north/south-orientated (unrotated) vertical magnetic field response functions[15]. The contouring is performed without further smoothing the data. The graphs in the upper left and right contain the real parts of Z_H and Z_D, while the imaginary parts are plotted in the bottom half of the figure. If we compare these contours with the modelling results (figure 9), we find that sites (10-60) show Z_H-response functions with the expected pattern. These south-eastern sites indicate the resistive side of the profile with a negative anomaly. Maximum negative values are reached at the sites closest to the expected conductivity contrast in the frequency range $1\,Hz$ - $10\,Hz$. With increasing distance from the fault line the anomaly flattens gradually towards the southeast, while it disappears more abruptly in the northwest. The imaginary parts of Z_H also show the expected pattern, with the reversal of sign in the frequency range of the maximum real parts.

However, just before the unfortunate gap in the profile, we see a change from negative to positive values in the real parts of Z_H. This change occurs very abruptly, between two neighbouring sites and this cannot be explained by the forward model. The gap in the data prohibits the continuation of this effect towards the north, and the anomaly on the conductive side of the profile is expressed less perceptible. It is only site 10WW that clearly indicates the change in sign, while the other northern sites 30EE-50OR show only neutral – zero to slightly positive – $\mathcal{R}e\{Z_H\}$ values.

In comparison with the Z_H-results, the Z_D response functions in figure 10 are consistently smaller and less uniform. In fact, the imaginary parts of Z_D appear to change their orientation twice. Attempts to minimise Z_D by rotation of the coordinate system result in greatly varying rotation angles, both between sites and over the frequency range. Even then, the Z_D values are considerably different from 0.

[15] all MVM sites, except site 10WO.

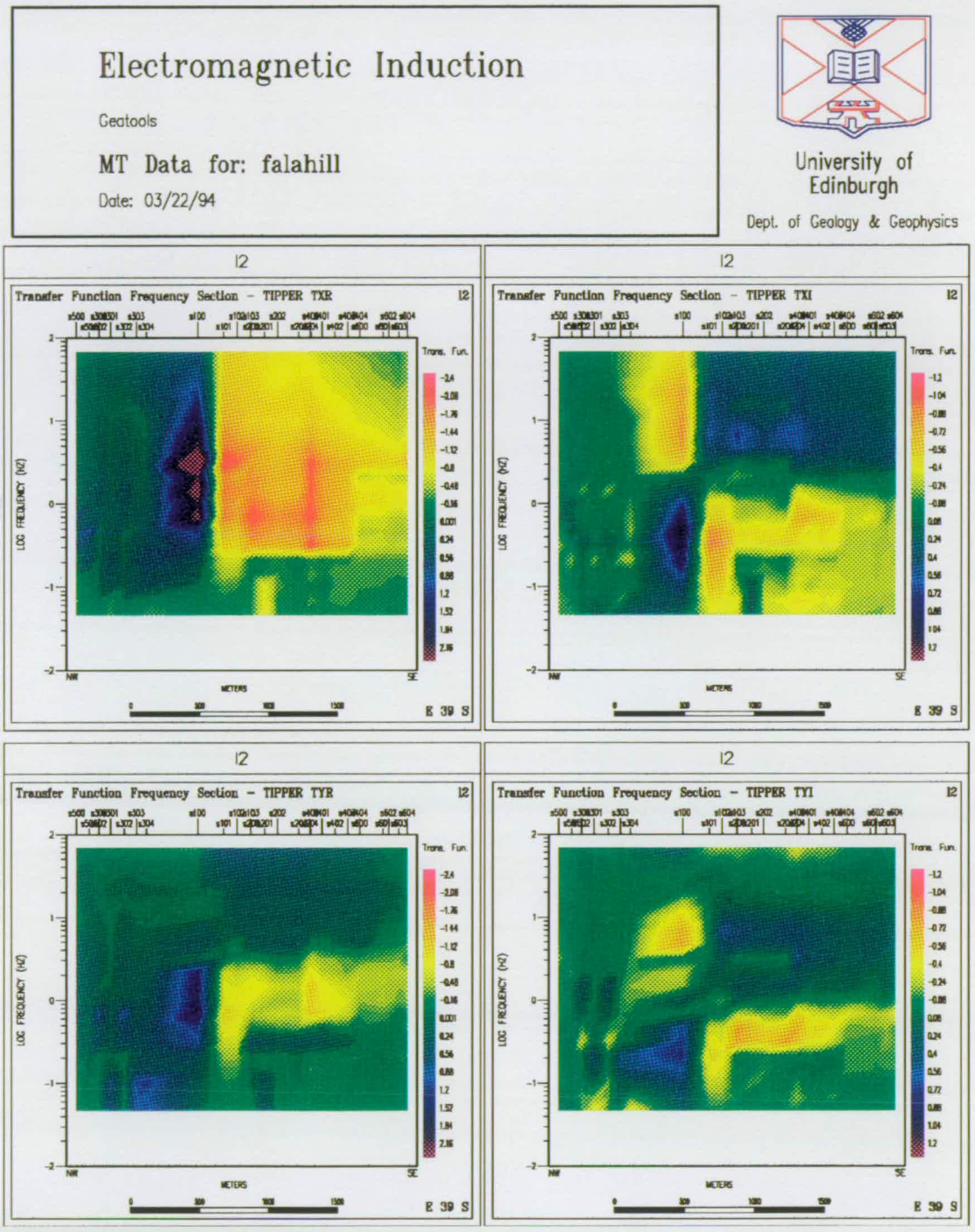

Figure 10: *Contour plot of the unrotated real and imaginary parts of the experiment's Z_H and Z_D response functions. In the diagrams the following notation is used: TXR=$\mathcal{R}e\{Z_H\}$, TXI=$\mathcal{I}m\{Z_H\}$, TYR=$\mathcal{R}e\{Z_D\}$, TYI=$\mathcal{I}m\{Z_D\}$*

As a consequence, we continue to use our data in the unrotated coordinate system, as our profile was oriented roughly perpendicular to the assumed electrical strike direction.

Neither the existence of a Z_D anomaly, nor the size of the anomalous values for Z_H, can be explained by a two-dimensional model. All my 2D modelling studies – even with the inclusion of extreme conductivity contrasts – show maximum anomalous values of around -1 for the real parts and ± 0.5 for the imaginary parts, while they easily exceed ± 2.0 in the observations.

The inclusion of site 10WW is crucial for the way the contouring is performed and for the kind of model we are seeking. Without it, the whole appearance of the response functions would be much more compatible with the results of the previously discussed 2D model in figure 9. It is therefore necessary to look at these MVM data in more detail, to get a better impression of the overall data quality.

The next two figures 11 and 12 show the Z_H and Z_D response functions presented versus frequency for site-sets 10 and 60. The distance between the two site-sets is approximately $1.2km$, and the individual sites are separated by ca. $100m$ (see figure 4). From the last site of the 60-set to the first of the 10-sites, the $\mathcal{R}e\{Z_H\}$ anomaly has almost doubled from around -1 to values of approximately -2. Note the different scales on the vertical axes! While the response functions vary only little between the 60-sites, the changes are drastic among the 10-sites. First we notice a moderate but steady increase of the anomaly between sites 10EE, 10EO and 10OR, then an enormous change at 10WO with maximum values exceeding -6. Only $100m$ further at site 10WW the response functions show reversed orientation. The result for site 10WO is very exceptional indeed, but the curves have compatible shapes and only because of the sheer magnitude we omitted the site from the contour plots in figure 10.

With the exception of the two highest frequencies of the 10-set, the Z_D response function data seem to be very consistent, too (figure 12). Looking from the highest to the lowest frequencies, the $\mathcal{R}e\{Z_D\}$ response functions start with positive values, they become negative towards lower frequencies ($10\,Hz$-$1\,Hz$) and eventually return to positive values for the longest periods. The imaginary parts of Z_D begin negative, then they take on positive values in the frequency range where the real parts are negative and they remain positive. This pattern is more distinctive at the sites close to the conductive boundary.

Figure 13 gives a more detailed impression of the spatial resolution of the anomaly. Now, the response functions are plotted for discrete frequencies at all sites along the profile. Again, the response functions vary quite smoothly and consistently. On the right side of the profile ($0km$ to $-1.5km$) and for the three highest frequencies the negative $\mathcal{R}e\{Z_H\}$ anomaly is widening steadily, both, towards the conductive boundary and with inreasing penetration depths. The response functions reach maximum negative values[16] at $2.2\,Hz$. At the same time, the $\mathcal{I}m\{Z_H\}$ values are reduced from slightly positive values ($68.1\,Hz$, $14.68\,Hz$) to values around 0 ($2.15\,Hz$). The frequency of maximum real parts corresponds to minimum imaginary parts, consis-

[16]The vertical axis is scaled differently at $2.2\,Hz$!

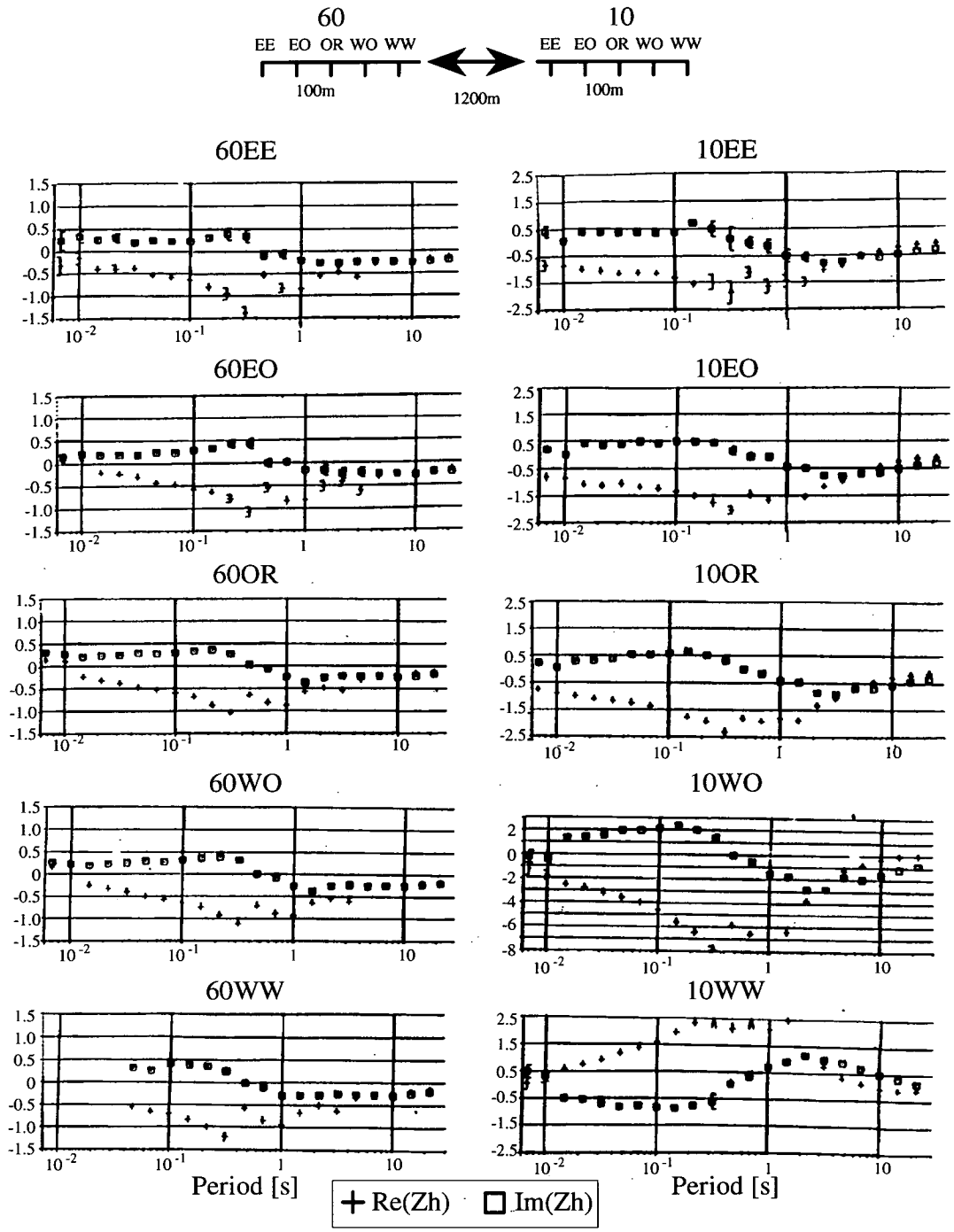

Figure 11: *Real and imaginary parts of the Z_H response functions versus period.*

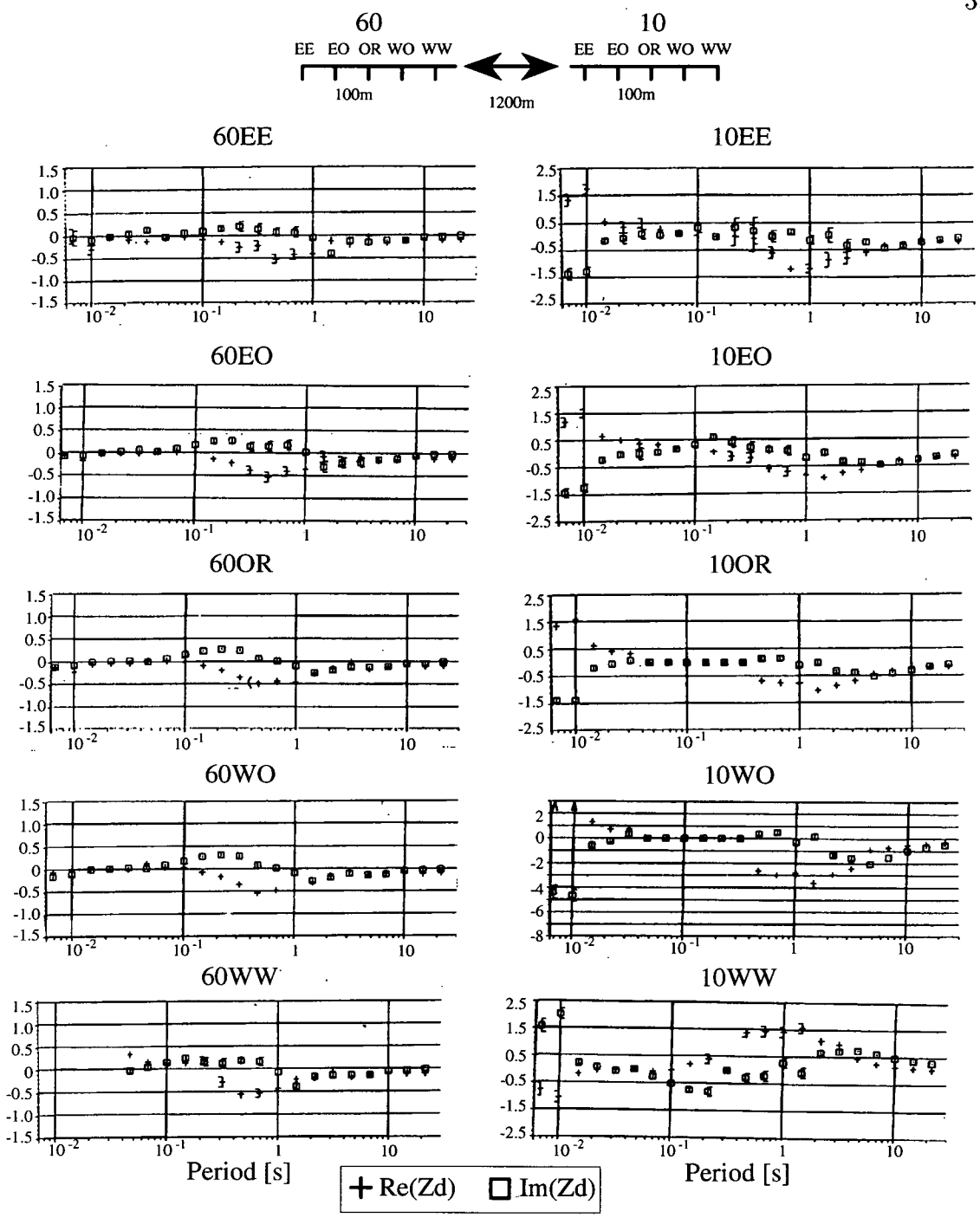

Figure 12: *Real and imaginary parts of the Z_D response functions versus period.*

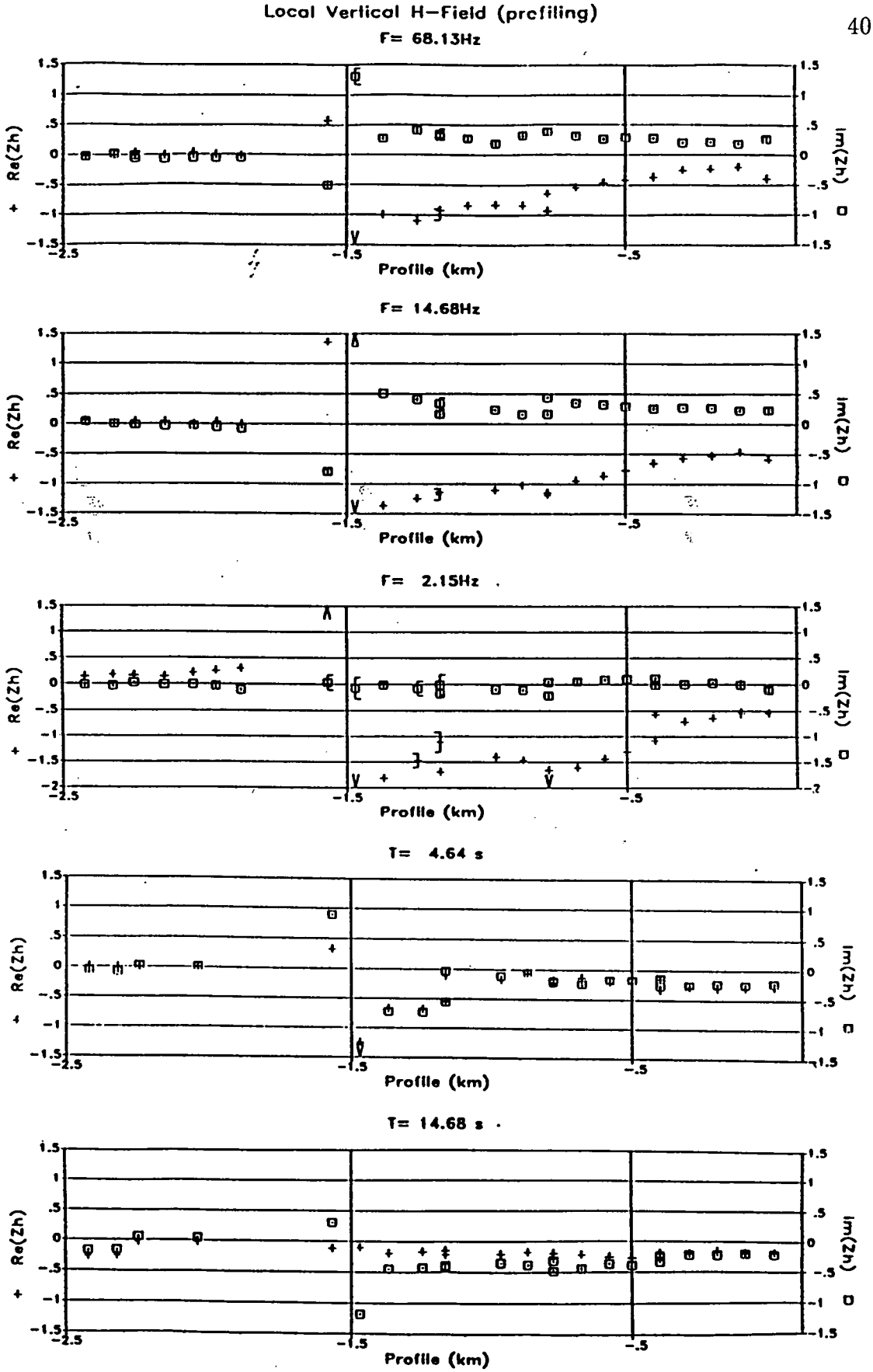

Figure 13: *Real and imaginary parts of the Z_H response functions plotted along the profile at discrete frequencies.*

tently at all sites on the profile. The response function values on the Carboniferous side of the profile ($-1.5km$ to $-2.5km$) are much smaller. For the most part, they vary around 0. However, this is to be expected as the anomaly must disappear quicker over conductive sediments. We find response function values significantly different from 0 only at $2.2\,Hz$, where the $\mathcal{R}e\{Z_H\}$ values are positive, and they increase towards the fault line. Thus, they seem to support the kind of reversed anomaly as indicated by the results of 10WW.

What sort of models can produce such reversed response functions? Figure 14 shows a 2D-model, featuring a shallow conductive channel instead of a conductive layer (figure 9) and its results. Most noticably, the $\mathcal{R}e\{Z_H\}$ values now change from positive to negative, indicating changes in conductivity on the left and right of the channel. The width of the conductor is expressed as a transition zone of neutral values. The imaginary parts show a *quadrantal*-type pattern with a change from positive to negative values, at both edges of the conductor and at the frequency of maximum real parts. While the overall shape of the anomaly seems to be more in agreement with the field observations, it is still unclear, why the changes in resistivity should occur over a distance of only $100m$.

The sites of the overlapping magnetometers are marked in figure 13 with two data values at one location. While some of these sites show significant differences in the response functions, this is not always the case and equally often the two results are indistinguishable. However, one would expect a conductivity anomaly of that size to be clearly expressed in the anomalous horizontal magnetic fields (chapters 2.3 and 3.3). But all in all, the data show not a consistent enough pattern that would allow satisfactory examination of the anomalous horizontal magnetic fields in greater deatail. Anomalous magnetic fields are very small quantities and good estimates for their respective response functions are difficult to measure. The usual way to obtain perturbation tensor estimates is to record the time series data synchronously at two or many sites and proceed as explained in chapter 3.3. However this was not possible with the S.P.A.M. MkIIb hardware.

The results of the three MT sites are presented in figures 15,16, and 17. The upper parts of the figures show the Swift-rotated apparent resistivity and phase curves, the lower parts contain graphs of the ρ^*-z^*-transformation, the bivariate coherencies, and the Swift and Bahr versions of the rotation angles and skews[17]. If we compare the apparent resistivity curves, we can clearly spot the expected change from conductive to resistive material between the Carboniferous (50OR) and the Ordovician sites (10OR, 60OR), respectively. Judging from the bivariate coherencies and from the scattering in the apparent resistivities and phase curves, however, we must conclude that data of reasonable quality is limited to the frequency range $100\,Hz$ to $5\,Hz$ and to the last two or three longest period values.

For the higher frequencies we observe fairly consistent rotation angles (Swift) in the range between 0° to 10°. This situation is less clear towards the longer period end, with rotation angles more likely around 45°. These long period rotation angles are very questionable though, as they coincide with large $(0.2\ldots1)$ skew

[17]see chapter 2.2 for more information on these parameters.

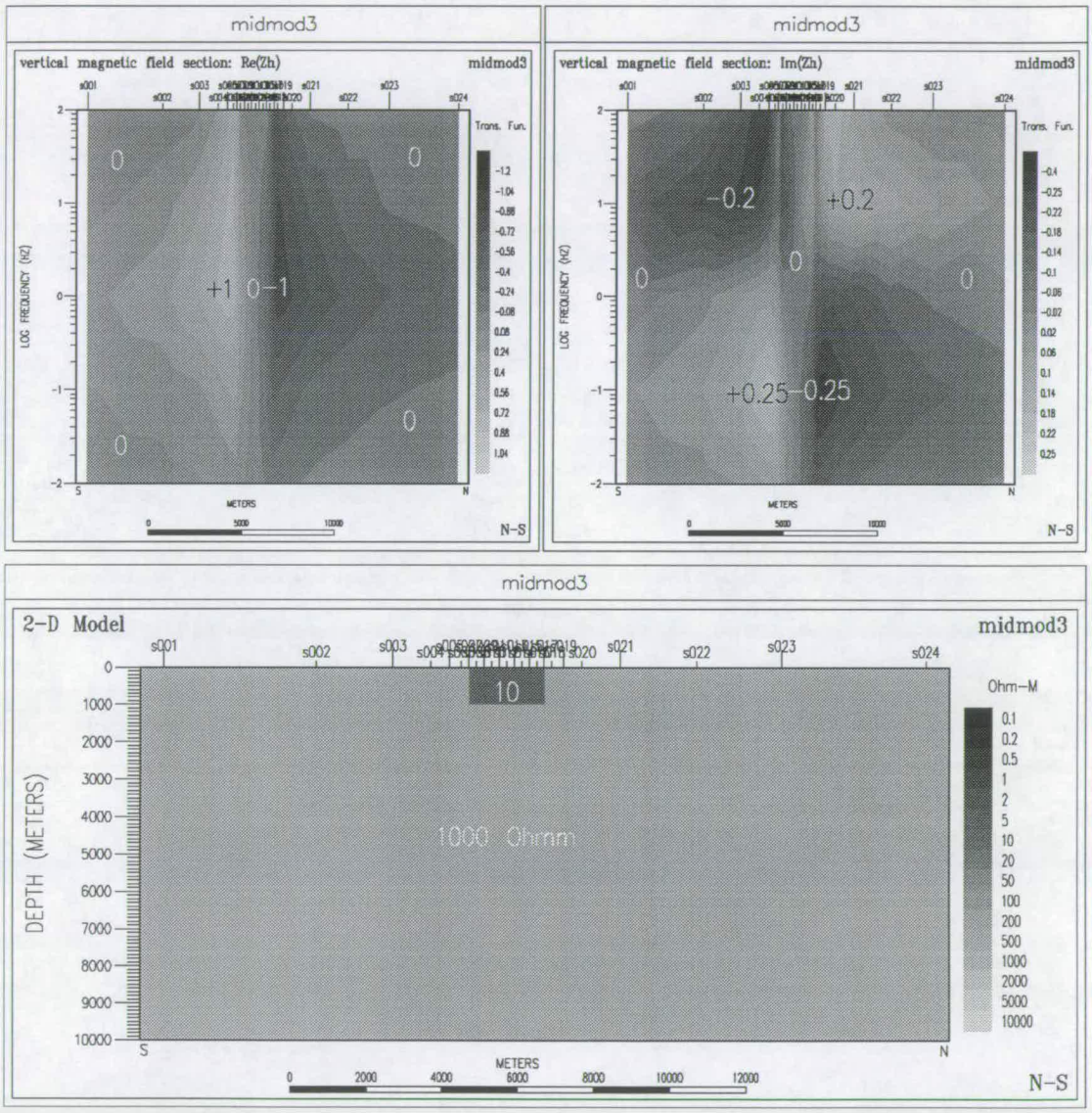

Figure 14: *2D-model featuring a conductive channel.*

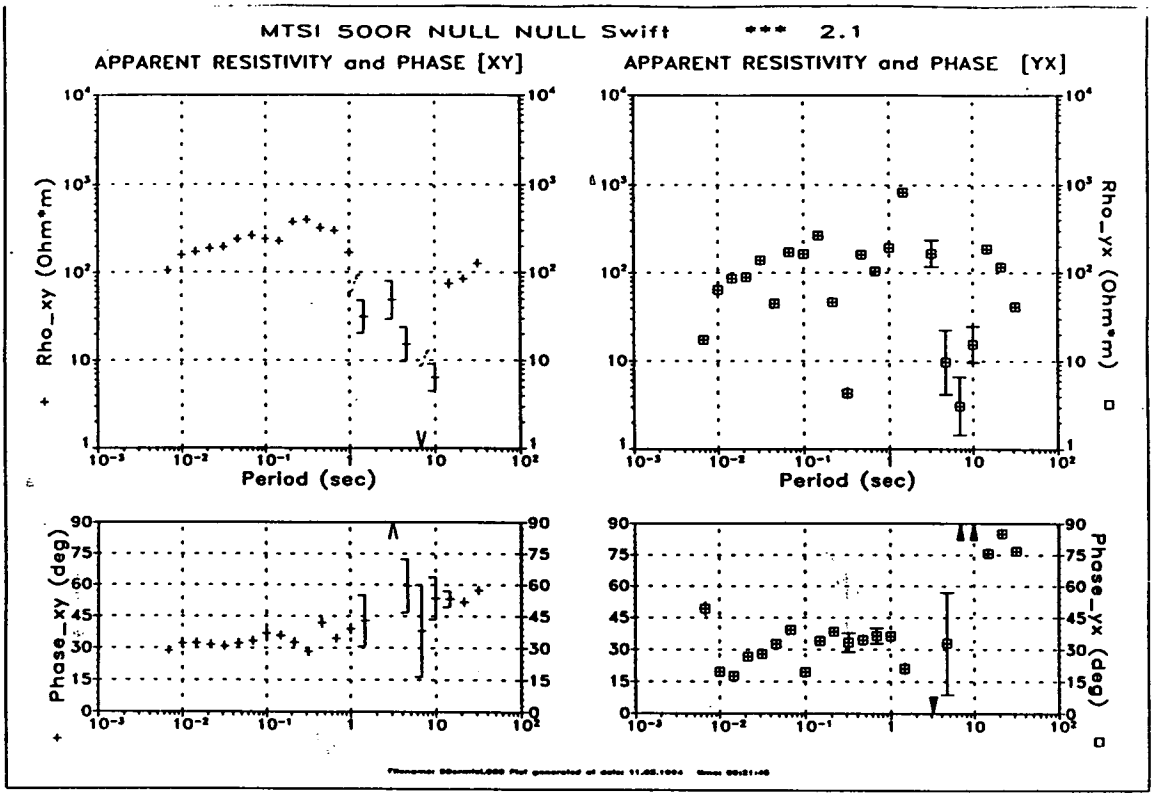

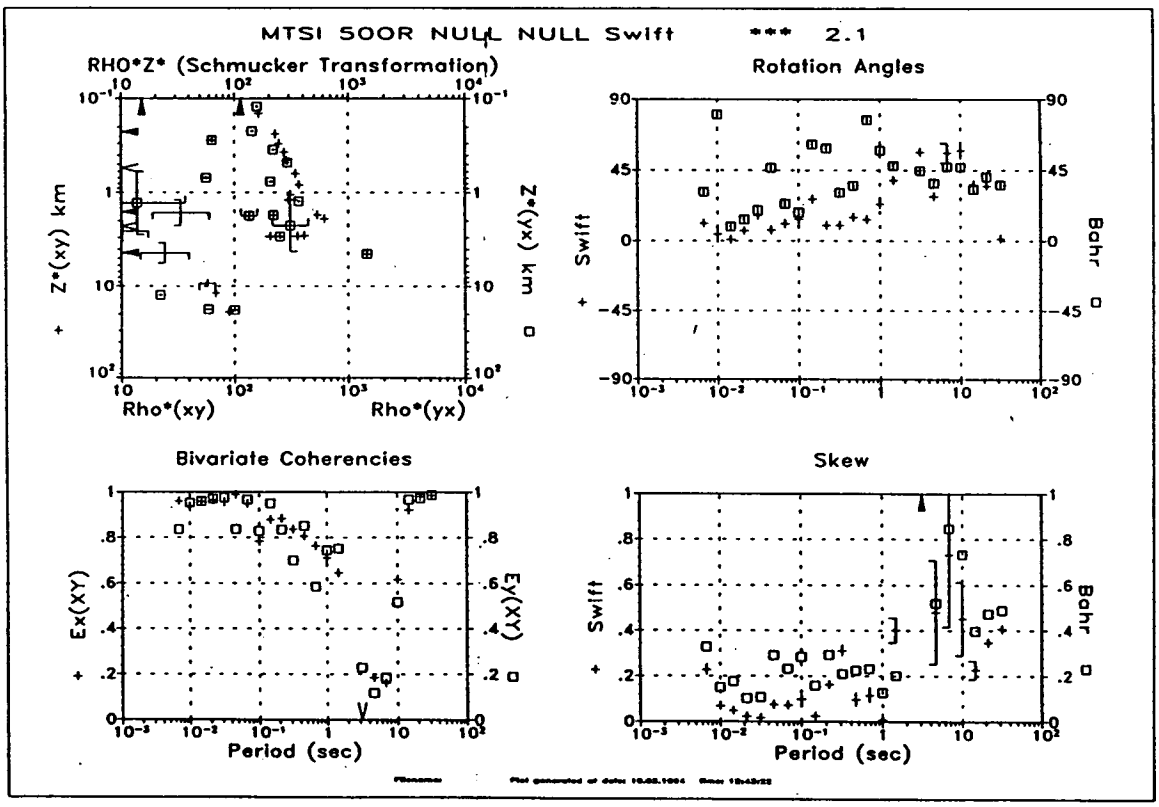

Figure 15: *MT results from site* 50OR.

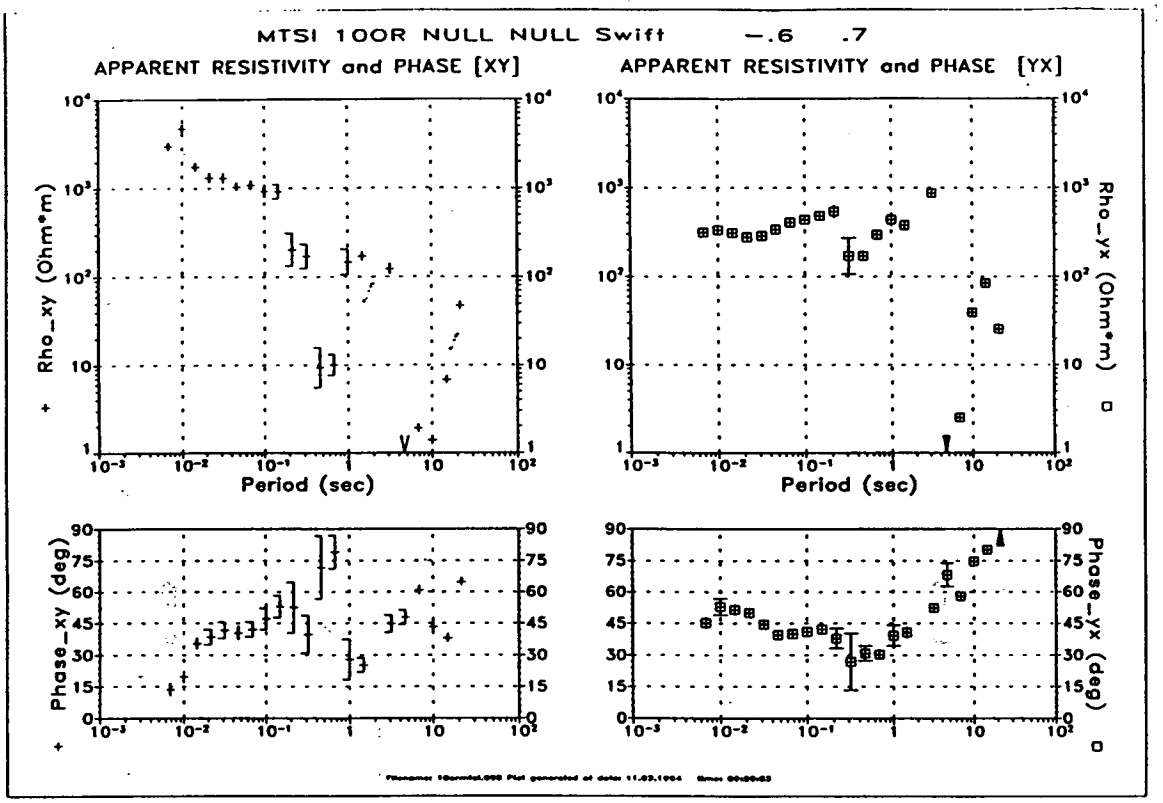

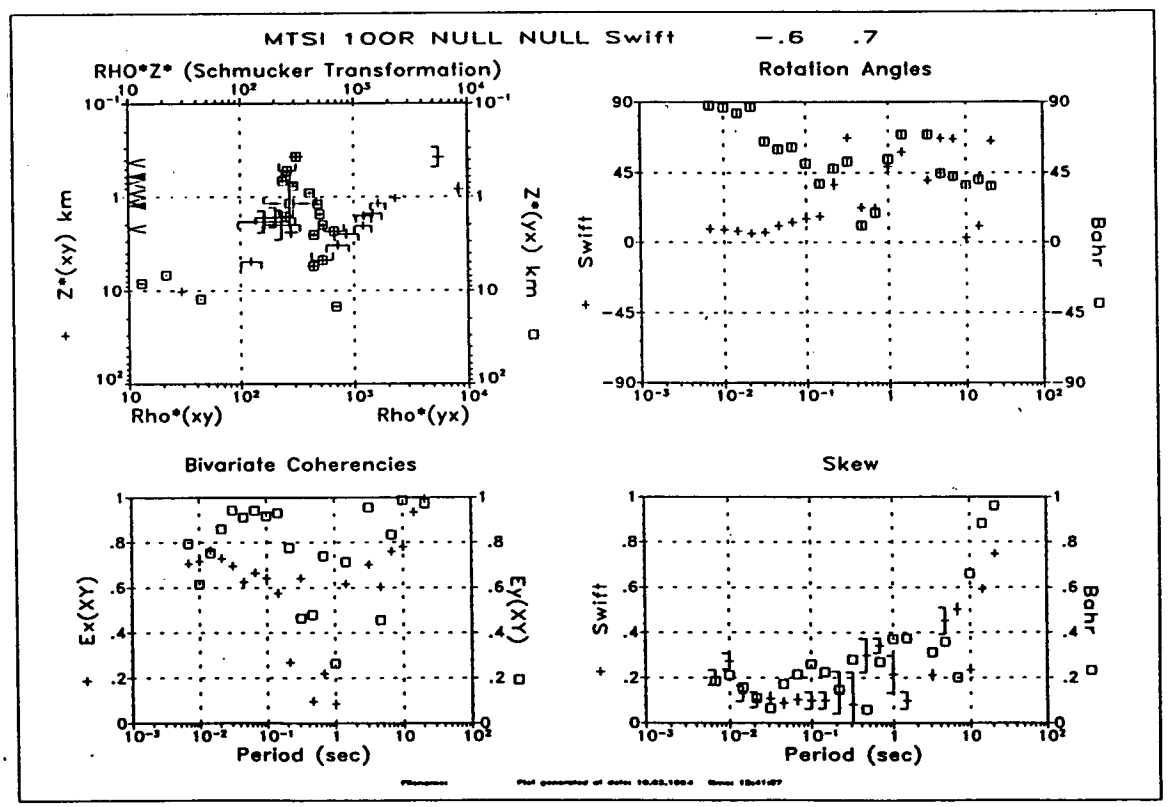

Figure 16: *MT results from site* 10OR.

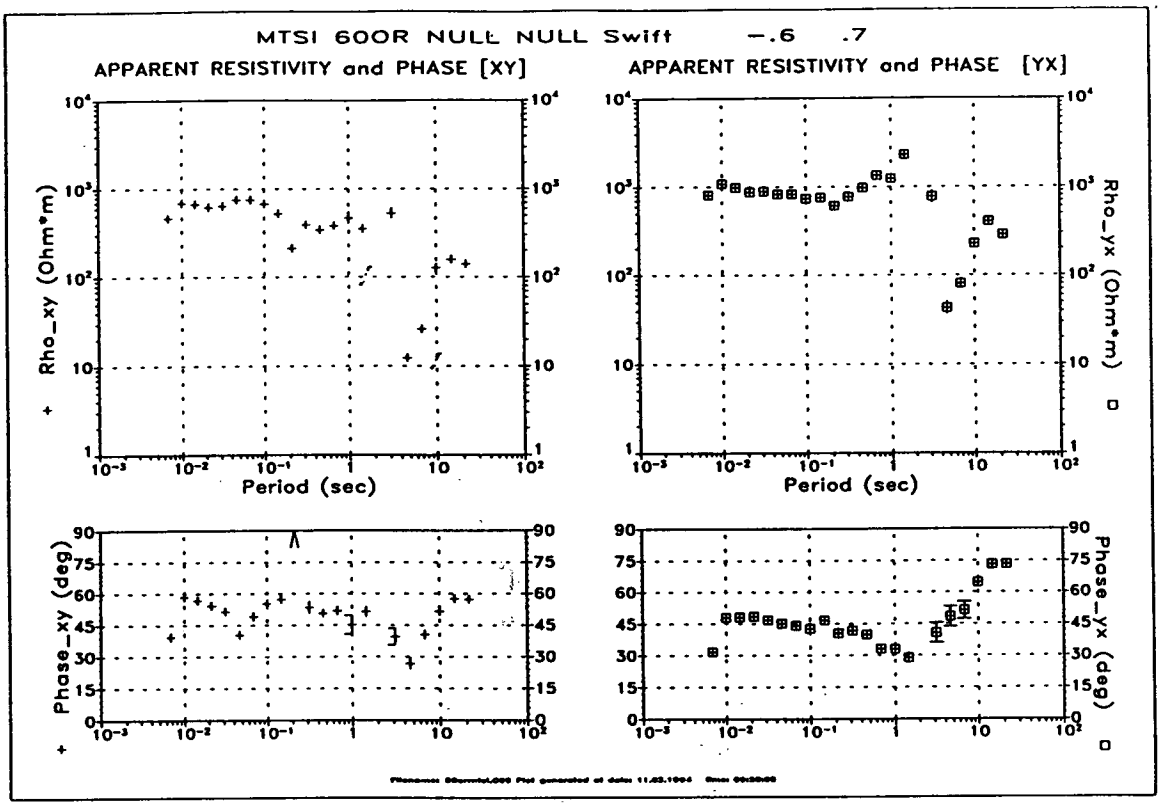

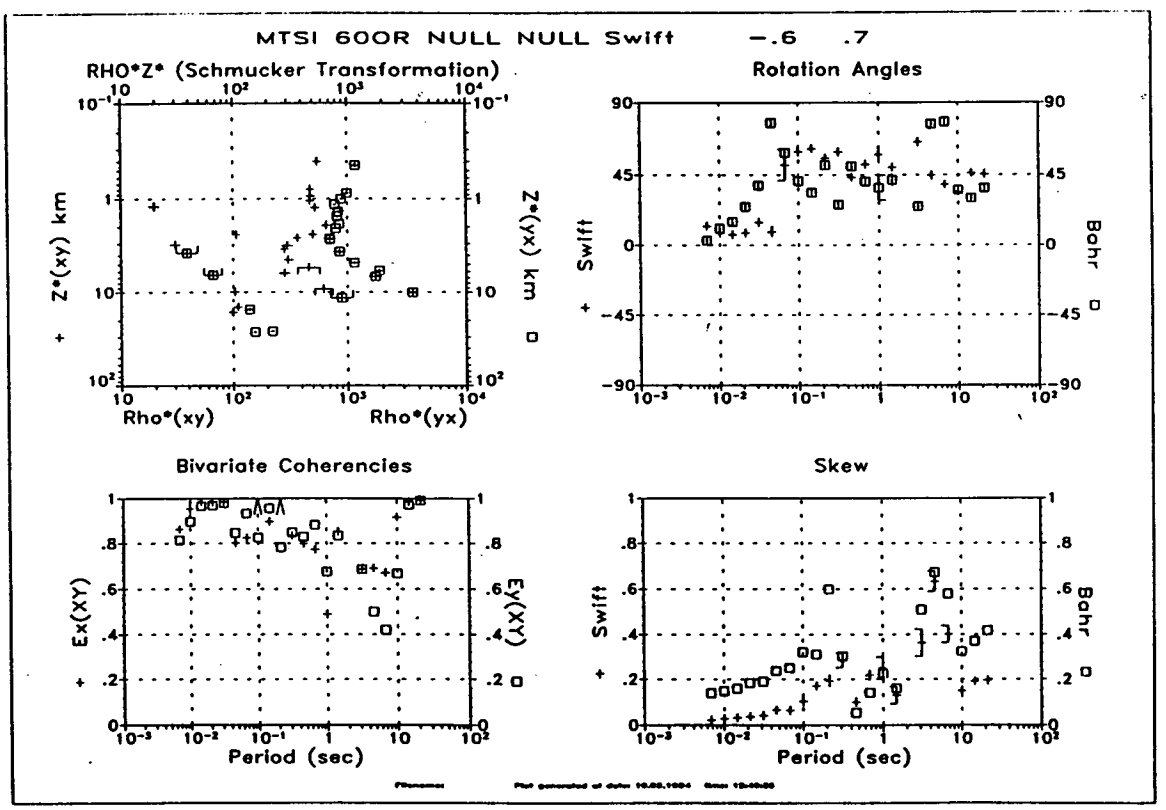

Figure 17: *MT results from site* 600R.

values. Large skews indicate three-dimensional conductivity structures without any preferences in the electrical strike directions. This result is reaffirmed by Bahr's skews, which are consistently higher than Swift's. If there is any hidden regional 2D structure in the data, Bahr's skews will be smaller than or equal to Swift's and usually < 0.1 [Bahr, 1991]. Bahr's rotation angles are scattered even more, because no regional 2D strike direction is detectable in the data.

4.3 Three-dimensional thin sheet modelling

From the magnitude of the Z_H-anomaly, from the fact that we cannot convincingly minimize the Z_D anomaly, and because of large MT-skew values, we drew the conclusion (chapter 4.2) that these data represent a three-dimensional substructure. It is always difficult to fit data with 3D-modelling, though. The forward solutions are computationally very time consuming and the sizes of the model grids are very limited. Hence, we must concentrate our efforts on certain aspects of the problem. One obvious target is to find an explanation for the size of the Z_H anomaly. In our observations Z_H exceeds -2, while the best we can achieve with 2D models are values around -1.

The modelling program is based on McKirdy's [McKirdy et al., 1985] thin sheet algorithm[18], the software and the plotting routines were installed by P. Jones on a departmental SUN Sparc workstation [Jones, 1992]. In this version of the program, the maximum grid size of the thin sheet is limited to 22 by 22 cells. As pointed out by Weaver [1994, p.251ff] proper grid design is extremely important for valid numerical results.

The most basic condition requires – as the name implies – the thickness of the thin sheet layer at the surface to be very much less than the inductive scale length in the structure [Weaver, 1994, p.86]. Furthermore the sheet must be much thinner than the inductive scale length in the structure underneath. The conductivity of the first layer beneath the thin sheet plays a dominant physical role, *because it largely controls the leakage of poloidal currents from the thin sheet into the underlying half-space and vice versa.* The overall size of the grid should be such *that all conductance gradients perpendicular to the nearest grid boundary are at least a distance* δ_1 *removed from the edge.* δ_1 is the skin depth of the layer beneath the thin sheet. *In addition, the node separations should only be a small fraction of the skin depth and certainly not greater than* $\delta_1/3$. Hence, for a particular model either the valid period range is very limited or the model grid must be altered to account for varying skin depths.

For our study, we chose the latter approach. Our model design carries on with the principle of a conductive feature at the surface in a resistive host. The thin sheet model is shown in figure 18. It is made of a conductive ($10\Omega m$) and a resistive ($1000\Omega m$) block, with a narrow channel of conductive material cutting through the resistive part. The thickness of the thin sheet is $500m$. The layer underneath is $25km$ thick, with a resistivity of $1000\Omega m$. To ensure valid numerical results, however, the model has variable extensions in both horizontal directions. These are summarized

[18] see also chapter 2.1.

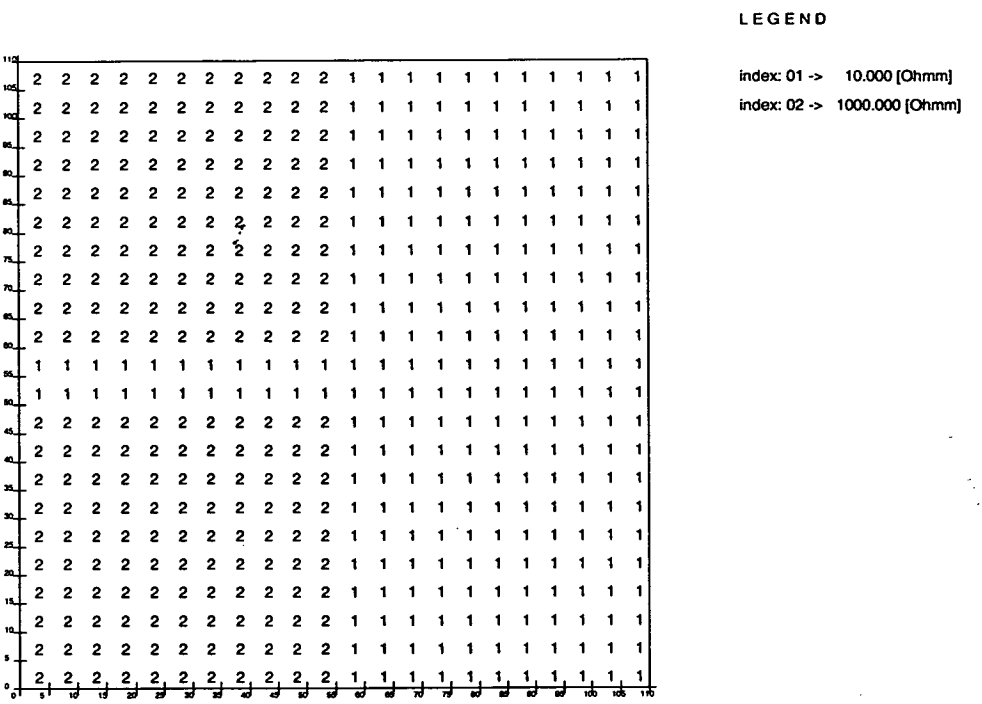

Figure 18: *The thin sheet model.*

in table 3. While the overall geometry of the models remains unchanged, the widths of the conductive channels range from $1km$ in the $10\,Hz$-case to $30km$ for the longest period of $100\,s$.

The way they are designed, these models force a strong channelling of the induced currents into the surface conductor, and the consequences on the Parkinson[19] induction arrows are shown in figure 19. The real and imaginary induction arrows are presented at four different frequencies ($10\,Hz$ - $0.01\,s$).

As expected, induction arrows of a significant size exist chiefly near conductivity boundaries. Over the conductive stratum the arrows are always close to 0, while they diminish more gradually on the resistive blocks. At the highest frequency ($10\,Hz$), the maximum magnitudes of the real arrows are in the order of 0.5 and they point to the nearest conductive zone. The $10\,Hz$-results must be treated with some care, though, as the thin sheet condition is not quite satisfied. For the conductive parts of the model the skin depth just equals the thickness of the sheet. With increasing skin depths ($1\,s$ and $10\,s$), the real arrows do not change their directions, but they become larger and actually, values of up to 2 can be reached. At $100\,s$ the lengths of the real parts decrease (0.5), as the induced currents are less affected by the surface anomaly. With the exception of the cells close to the joint of the channel and the conductive block, the real arrows show either the channel or the block as the nearest

[19]The real induction arrows in Parkinson convention tend to point towards a counductor, while the Wiese arrows point away from it. The imaginary arrows are the same in both conventions. See also chapter 2.3, table 1.

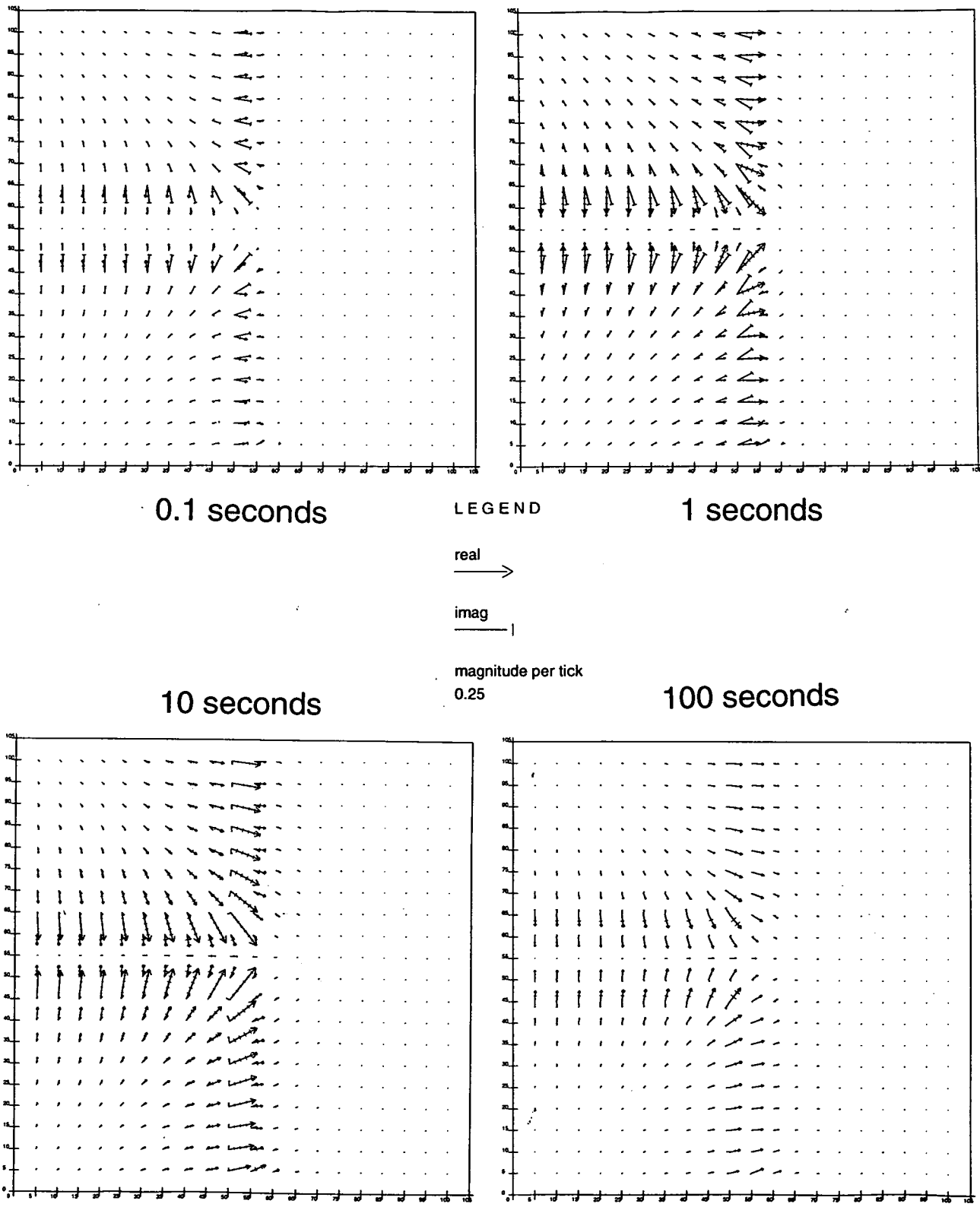

Figure 19: *Parkinson inductions arrows of a thin sheet model in the frequency range* $10\,Hz$ *to* $100\,s$.

period	conditions for cell sizes		chosen cell size for 22x22 grid
	distance δ_1 to conductance gradients	maximum node separation $< \delta_1/3$	
$0.1\,s$	$5.0\,km$	$1.7\,km$	$0.5\,km$
$1\,s$	$15.8\,km$	$5.3\,km$	$1.5\,km$
$10\,s$	$50\,km$	$16.7\,km$	$5.0\,km$
$100\,s$	$158\,km$	$52.7\,km$	$15\,km$

Table 3: *Construction of the thin sheet grid cells for a layer of* $1000\,\Omega m$ *beneath the sheet.*

conductor; they hardly indicate any inductive coupling between the two features.

In that case, one would expect the real and imaginary arrows to point, as in 2D, parallel to one another. However, even at $10\,Hz$, only the cells very close to the edges of the model show that kind of pattern. Most imaginary arrows point obliquely to the real parts, to a position between the two conductive features. At $10\,s$ the imaginary arrows become very small, as we find maximum real parts at this period. It is interesting to see all imaginary arrows apparently pointing into the same direction, the joint of the two conductors. This is the location of maximum current concentration and the most inhomogeneous part of the model. The imaginary arrows at $100\,s$ are still small, but clearly their orientation is reversed, as they now point approximately anti-parallel to the real arrows.

The real and imaginary inductions arrows of our observations are shown in figure 20. The arrows are plotted in Wiese convention in an unrotated coordinate system. For the overlapping sites, the arrows are drawn at the same x-coordinate, but offset towards the north. The chosen frequencies are the same as for the profile presentation of the response functions in figure 13. Note, that real and imaginary arrows always have same length scale at a particular frequency, but the scales differ between graphs!

Most noticably, the profile splits into three parts, one with large induction arrows, one with no data and a part with very small arrows. Comparison of these results with the geological map in figure 3 shows that all the sites with the large and better determined induction arrows are located on the Ordovician meta-sedimentary rocks. For the Ordovician sites, the induction arrows also become smaller with increasing distance from the anomaly.

At the highest frequency of $68\,Hz$, the real arrows indicate – as expected – a conductive zone towards the NE. The real arrows become larger with increasing penetration depths. At $2.2\,Hz$, they reach maximum values of the order of 2 or more. The largest arrows are located close to the assumed fault line. Initially, real and imaginary arrows point approximately anti-parallel. With increasing periods ($14.7\,Hz$), the imaginary arrows become smaller and they reach minimum values

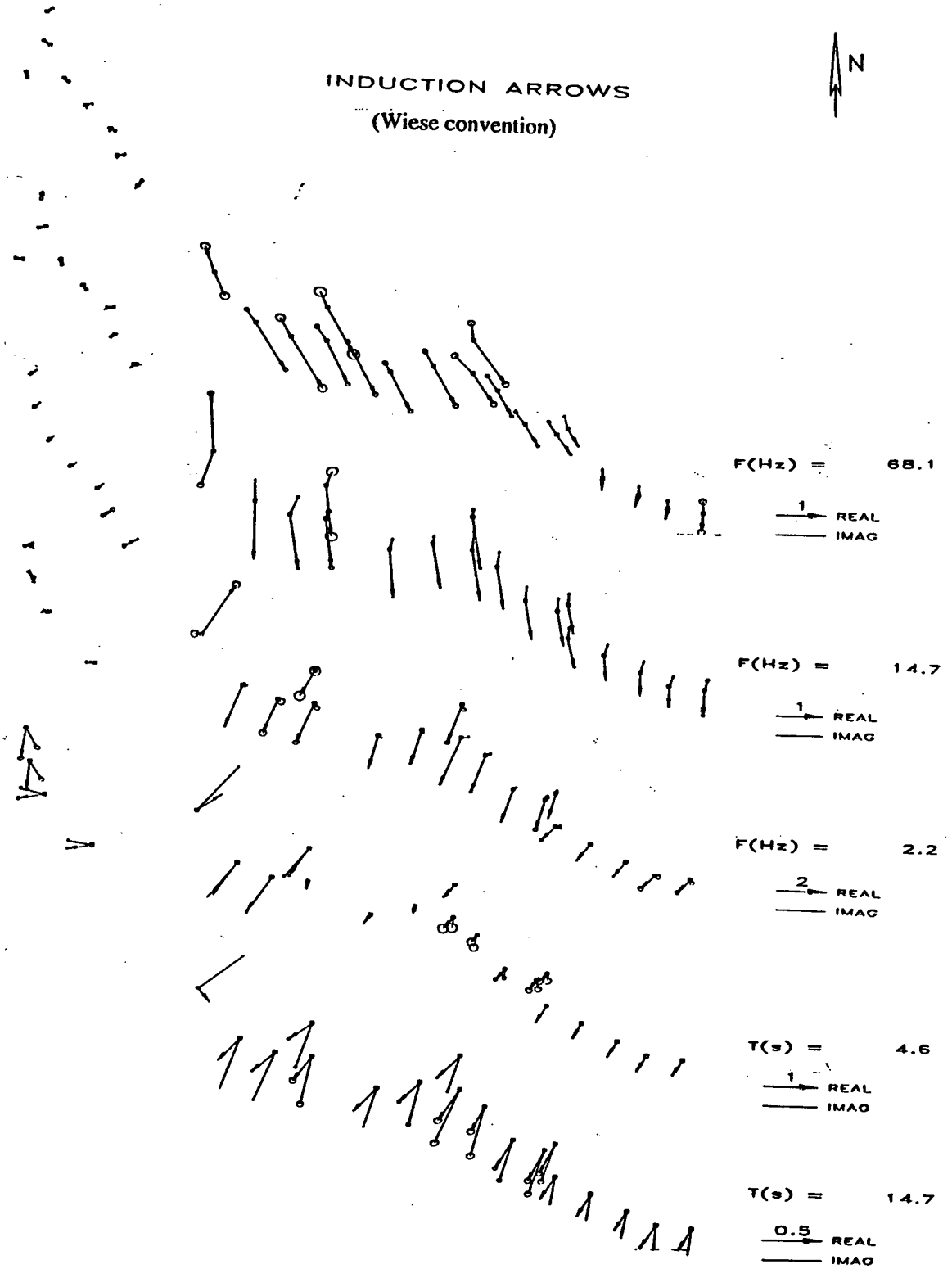

Figure 20: *Observed real and imaginary inductions arrows in Wiese convention. The ellipsoids represent the errors.*

at the frequency of maximum real parts ($2.2\,Hz$). With even greater penetration depths ($4.6\,s$), the real arrows are decreasing too, while the imaginary parts reverse their orientation. They now point parallel to the real arrows.

The results so far, are roughly in agreement with the modelling results[20] (see figure 19). The lack of an exact match is not a difficulty. Our intention was only to demonstrate that the spatial patterns, the frequency characteristics and the magnitudes could be reproduced. However, contrary to the thin sheet models, the real induction arrows also change their directions over the period range. The real arrows at $68.1\,Hz$ point towards south-eastern directions, while the arrows at $4.6\,s$ stand almost perpendicular to them, pointing towards the southwest. At the longest obsevation period of $14.7\,s$, real and imaginary arrows separate, with angular differences between 30° and 45°. The real parts continue to point towards the southwest, while the imaginary arrows show southern directions.

The induction arrows on the Carboniferous side are very small and less perceptible. At $2.2\,Hz$, however, they seem to point towards the northeast, indicating a conductive area towards the southwest. Thus, they actually point the same way as that ominous site 10WW and, clearly, this cannot be explained at all by the models.

As mentioned earlier, we found a gas pipeline running almost parallel to the fault line. Direct modelling of such a metal conductor is problematic because the lateral extensions are extremely small compared to any geological material and the conductivity is extremely high. Nevertheless, the effects of these man-made conductors have been studied recently [Hanstein, 1994; Qian and Boerner, 1995].

Hanstein models the pipeline as a thin conductor of infinite length, which can be approximated as a line current. The conductor is embedded in a homogeneous half space. How strongly apparent resistivity, phase and tipper are affected depends mainly on the conductivity contrast between the pipeline and the surrounding material, and the distance of the observations from the pipeline. If we assume $100\,\Omega m$ for the half space and for metal $10^7 \frac{S}{m}$, we yield case 2 in figure 21 (bottom graph). The real parts of the vertical magnetic field response functions (tipper) show maximum effects at a distance of 0.05 of the skindepth. This results suggests, that we observe the tipper anomaly centered around $100\,Hz$ for a site $250m$ away from the pipeline, while at a period of $100\,s$, an identical effect occurs at a location in a distance of $25km$. Presented as induction arrows, the real parts always point away from the pipeline, while the imaginary parts change their orientation.

We observe a pattern like this at $68.1\,Hz$ in figure 20 between sites 10WW and 10OR, which are separated by $200m$. However, since the induction arrows change their directions with increasing periods, they finally point almost perpendicular to the pipeline. It is furthermore questionable, whether the pipeline can be regarded as infinite in length, as real pipelines are usually electrically interrupted. Smaller segments of the conductive material would probably cause much reduced effects, at least towards longer periods. Clearly, we do not observe a dependency of maximum vertical magnetic field values with distance of the sites from the pipeline, as pre-

[20]Note, that observed and model arrows are plotted in different conventions!

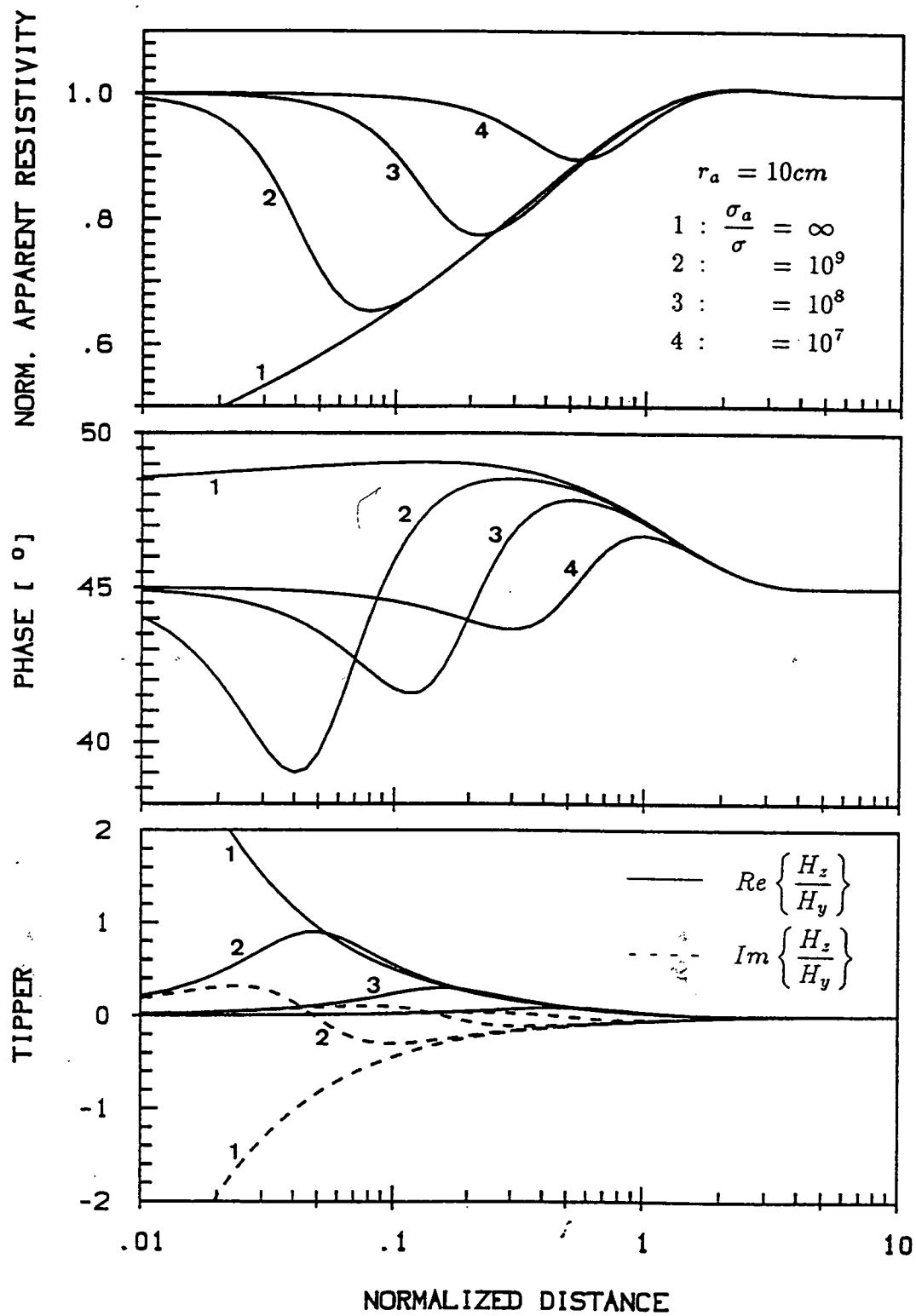

Figure 21: *Effects of ideal or metallic conductors* ($10^7 \frac{S}{m}$), *hosted in a* $100\,\Omega m$, $10\,\Omega m$, *and* $1\,\Omega m$ *half space, on apparent resistivity, phase and tipper curves. The results are plotted as functions of distance normalised to the skin depth* $r/p = (\omega\mu_0\sigma r^2/2)^{\frac{1}{2}}$ *(Hanstein [1994]).*

dicted by the modelling study. The data indicate gradually decreasing amplitudes over the whole frequency range with increasing distance from the fault. The geological background is also more complicated, presumably at least two-dimensional for the higher frequencies and three-dimensional towards longer periods. Therefore natural induction effects will be superimposed onto pipeline distortions. However, this cannot be accounted for by the pipeline-modelling program.

4.4 Summary

During an AMT magnetic variation mapping experiment in southeastern Scotland we observed surprisingly high vertical magnetic field response function values ($|\mathcal{R}e\{Z_H\}| > 2$). The experiment was designed to cross a known conductive boundary (the Southern Upland Fault), with 24 closely spaced sites, arranged along a $2.5km$-profile.

The overall data quality is reasonably good, despite some problems with noise (gas pipeline and electric fences). The vertical magnetic field response functions vary smoothly and consistently over frequency and between sites. The anomaly is clearly resolved in the appropriate frequency range with data from many sites. The 3 MT sites are more affected by noise, particularly in the frequency range between $5\,Hz$ and $0.1\,Hz$.

For the higher frequencies, the general shape of the magnetic variation anomaly is as expected for a two-dimensional geological situtation. The induction arrows are large over resistive Ordovician material and small on the Carboniferous side of the contact. The real induction arrows (Wiese convention) point away from the conductive sediments, the imaginary arrows point anti-parallel to the real ones. Most noticeably on the resistive part, the lengths of the arrows decrease, with increasing distance from the lateral change in conductivity.

However, the size of the Z_H response function values, the existence of a Z_D anomaly, obliquely pointing imaginary arrows and large MT-skews, led us to the conclusion that the data reflect a three-dimensional geological situation; at least for greater penetration depths ($>1\,s$). Using three-dimensional thin sheet modelling, it is possible to reproduce exceptionally large induction arrows with magnitudes of up to 2. These large arrows are caused by strong current channelling into a near-surface conductor. However, the thin sheet models cannot explain why the observed real induction arrows change their directions with increasing skin depths nor the directions of the imaginary arrows at longer periods.

Currents running in a gas pipeline can strongly influence the vertical magnetic field response functions. Hence, the results of some sites near the pipeline might be distorted. For these sites, our data represent a mixture of naturally and artificially produced anomalies, which cannot be separated easily. However, with the exception of two sites (10WW and 10WO), most aspects of the observed anomaly can be explained by geologically motivated models.

Eventually, it is probably safe to conclude that the observed anomaly is predominantly caused by the contact of resistive Ordovician meta-sediments to conductive

Carboniferous sediments. A high density mapping of geomagnetic variations in the audiomagnetotelluric frequency range is an excellent tool for the investigation of such lateral conductivity contrasts.

5 S.P.A.M. MkIII: a new generation of geophysical instrumentation

S.P.A.M. systems are short-period automatic magnetotelluric instruments developed since 1980 by Graham Dawes at the University of Edinburgh. Ever since the mid-eighties, these instruments have been very much the work horses for most of the field work done in the UK. However, since the last upgrade to S.P.A.M. MkIIb in 1986, many electronic devices have been greatly improved in terms of noise, power consumption and size, and also completely new concepts for computational applications have become available. As a result, in 1990 Graham Dawes with support from N.E.R.C. undertook a feasibility study of a transputer based upgrade of S.P.A.M., which has led to the development of a prototype of this new generation of instruments [Dawes, 1990].

Many aspects of the S.P.A.M. MkIII design are completely novel for geophysical instrumentation. This chapter overviews the concepts and main design goals, describes the main instrument components and explains how the various parts operate together.

The major design phase for the prototype started in 1992. An early summary of the ideas behind S.P.A.M. MkIII can be found in Ritter and Dawes, [1992] . The realisation phase, with design and production of the hardware boards, writing of the system control and processing software, making of the cases and cables, started in 1993 and ended in summer 1994 during my second field project. The results from this very first field test of S.P.A.M. MkIII are discussed in chapter 7.

The design, manufacture and testing of hardware components, especially the *Sensor-* and the *Repeater* boxes, form a significant part of D. Nascimento's current research work and his thesis will contain many more details on S.P.A.M. MkIII's hardware.

An explanation of some technical terms is given in appendix A.3.

5.1 Existing instruments and their limitations

Electromagnetic instruments consist of sensors (e.g. magnetometers and electrodes) and data acquisition systems. Data acquisition systems can be divided into two groups: devices which do no more than store the acquired data, and systems which additionally perform real-time data processing. Whether a data logger or a real-time system is used depends mainly on the time for which the instrument is deployed at a particular site.

Historically, MT studies have been concerned with the determination of the electrical resistivity of the Earth's crust or upper mantle on a regional scale. For that purpose, signals in the period range between $100\,s$ and $10000+\,s$ have been recorded with data sampling rates in the order of several seconds to minutes. Accordingly, the recording times for these long period (LMT) data have been in the order of weeks to months at a site.

The amount of data that could be collected was greatly dependent on the progress

in data storage technology. In the 1950's and 1960's, analogue data were recorded on photographic film or paper chart recorders and digitized manually at a later stage. From the 1970's digital data were stored directly, however on modified analogue audio-cassette recorders [Valiant, 1976]. In the 1980's, with the arrival of digital tape and floppy disks, a new era of purely digital recording systems began, and the most advanced LMT systems today use credit card sized RAM boards to store several megabytes of data [NERC Datataker, manual in preparation]. Because of their long deployment times, data loggers must have good long term stability, they must operate very reliably and have low power consumption. Robustness, compactness and low weight are desirable features for all geophysical instruments.

The invention of the microprocessor in the 1980's opened the field to the exploration of the audiomagnetotelluric (AMT) frequency range. AMT data are natural electromagnetic variation signals, typically in the frequency range $1000\,Hz$ - $0.01\,Hz$. The corresponding electromagnetic fields penetrate only the first hundred meters or first few kilometers of the Earth's crust. Because AMT data are collected at much higher sampling rates, it usually takes only several minutes to a day to gather enough data at a site. The fast sampling rates require high performance A/D-converter devices which in the 1980's were available with relatively low resolution and high power consumption. The AMT signal strength varies enormously over the frequency range. Artificially generated signals from the mains power supplies or electric railways exceed the natural signals by several magnitudes. To eliminate these monochromatic noise forms AMT instruments are equipped with special hardware filters (notches). In the frequency range of the *dead band* around $1\,Hz$, the natural signal activity is at a minimum. Hence, recording in narrow frequency bands is necessary to ensure optimum dynamic range of the signals, while LMT data are usually recorded in one broad frequency band.

Because a large volume of data is produced in a relatively short time, most AMT instruments are designed as real-time systems. Short, non-continuous segments of time series data are processed on-the-fly, enabling on-line quality control of the stacked results. In the AMT case, only some of the better quality events are usually kept, while it is very important to store complete data sets in LMT recordings. In some AMT systems the additional hardware requirements involve cumbersome additional equipment such as bulky computers, large batteries or petrol operated power generators and possibly an additional vehicle or trailer. AMT magnetic sensors are normally induction coils instead of fluxgate magnetometers.

Publications on geophysical equipment and in-field processing techniques are often difficult to find. Many instruments are produced by commercial companies, whose main concern is to protect their interests. Although research institutions have always been involved in instrument developments, their results rarely seem to get published in major geophysical journals, but appear in internal reports or as parts of theses. A source with a good record of instrumentation related contributions is the *Protokoll Elektromagnetische Tiefenforschung.* Useful for further reading on AMT instruments are: Schnegg and Fischer, 1980; Liebig and Schreier, 1984; Ritter and Dawes, 1992. More information on logging systems can be found in: Beblo and

Liebig, 1986; Beblo and Hofer, 1986; Wehmeier, 1988; Steveling and Leven, 1992; Donner and Miersch, 1992.

Today AMT and LMT instrument types merge as both benefit from improvements in memory and CPU technology. It is possible to achieve higher sampling rates with data loggers, whereas real time systems become increasingly more portable and continue to require less power. On the other hand, since it may be necessary to leave an instrument at the same place for a few days or some weeks for the longer period soundings, the two different kinds of instruments have a complementary role to play with ideally both being deployed in many studies. For these very practical reasons, the distinction between the AMT and LMT frequency bands will remain.

5.2 S.P.A.M. MkIII overview and design goals

The main design goals for S.P.A.M. MkIII are:

- Improved connectivity for geophysical sensors.
- Low power consumption and low noise.
- High portability: compactness and low weight.
- Time series data logging and real time processing, concurrently.
- Modular design of hardware components.
- Accurate timing (synchronization).
- Support for mixed geophysical methods.

More flexiblity to set up geophysical sensors is particularly important, as existing AMT instruments are very restrictive in that aspect. Some AMT instruments are limited to 5-channel standard MT configurations, while others, like S.P.A.M. MkIIb, offer two additional magnetic or telluric channels to connect sensors from a nearby (e.g. $100 - 200m$) reference site. However, it is becoming increasingly important in AMT projects to work along profiles or grids with very dense site/sensor spacings, to understand local features and prevent side-effects from *geological noise* on interpretations of regional studies.

S.P.A.M. MkIII is therefore designed as a networked instrument. This network consists of sensors with distributed analogue and digital processing and control units. Networks can be very simple, e.g. a standard 5-component AMT configuration, or very complex, limited only by the availability of S.P.A.M. MkIII-modules and the imagination of the researcher (see chapter 5.10).

The network communication is based on digital data transfers, and all devices on the network are synchronized. Because digitally transmitted signals do not deteriorate with distance, reference fields from remote sites can be recorded together with signals from local sites. Remote reference fields are useful to improve the data

processing (chapter 3.3). Furthermore, the application of mixed geophysical methods becomes possible; e.g. a combination of seismics and electromagnetics, which may be useful in geothermal areas or possibly for earthquake prediction.

Microprocessors and data storage media have been improved tremendously over the last decade. More computational power allows parts of the analogue signal processing to be replaced by digital signal processing. Consequently, the design of the analogue sections becomes simpler, which means improved reliability and better noise figures. The computational heart of S.P.A.M. MkIII is the transputer, a microprocessor with built in parallel processing and network support. Parallel execution of processes allows all S.P.A.M. MkIII frequency bands to be generated digitally and concurrently. This is an important improvement over existing instruments as it results in shorter recording times. Until now, different frequency bands had to be recorded sequentially.

All parts of the instrument are built in a highly modular fashion, to allow test facilities, modifications, replacements or enhancements of parts of the system, without having to change everything. Despite of all the additional features, the overall power consumption is greatly impoved over S.P.A.M. MkIIb, mainly because new low power devices could be used throughout the system.

Generally, a S.P.A.M. MkIII network consists of five major nodes:

- The sensor node (*Sensor*): is used to connect various geophysical sensors (e.g. induction coil magnetometers, electrodes, seismometers, etc.). All necessary signal preconditioning and power supplies are included. The sensor node uses one channel board of the correct type for each sensor.

- The remote node (*Remote*): Analogue signals from the sensor node(s) are captured, further band-pass filtered, notch filtered, and amplified using automatic, software-controlled gain ranging. Finally, the analogue signals are converted to digital data. Subsequently, digital data processing is performed. The data are decimated and digitally filtered, to generate several (overlapping) frequency bands in parallel. The filtered time series data are buffered and finally subjected to FFT. Time series data and/or Fourier coefficients are distributed towards the base node using digital high speed serial communication.

- The base node (*Base*): The *Base* controls the entire network and only one *Base* per network is permitted. All control registers (switches, gains, filters, multiplexers, overloads, etc.) in all remote and sensor nodes are set and/or read from the *Base*. The *Base* collects all time and/or frequency domain data sent over the network from the *Remotes* and performs real-time data processing.

  The time series data and the stacked results can be stored on hard disk and/or be transferred to a laptop PC. The PC is utilized as the front-end for user-interaction and as a graphics terminal. The EMERALD database (chapter 6.1) can be used to retrieve or create additional information on hardware calibration, site layouts, default system settings and to organize the raw data.

- The repeater node (*Repeater*): used to refresh the digital signals, if they are attenuated or otherwise weakend by the communication media (e.g long copper cables).

- The branch node: A device to increase the number of communication branches for complex network topologies. A base node can communicate with 2 remote nodes, each *Remote* can communicate with a *Base* and/or one additional *Remote*. A branch node provides two additional digital communication channels.

5.3 The transputer

The computational heart of S.P.A.M. MkIII is the transputer, a family of single-chip, fast RISC microprocessors. The concept of the transputer was developed in Europe by INMOS (UK) which today is part of the SGS/Thompson group (F). The transputer family includes the following types [INMOS, 1992]:

- T200: 16-bit integer CPU, 4Kbytes internal memory (not used in S.P.A.M. MkIII).

- T400: 32-bit integer CPU, 4Kbytes internal memory. TMS425-30MHz peak rate: 30 MIPS.

- T800: 32-bit integer CPU + 64-bit FPU, 4Kbytes internal memory. TMS805-25MHz peak rates: 25 MIPS, 4.3Mflops.

Integrated in the hardware of the transputer are 2 programmable timers and 4 high speed serial links. Different types of transputer can communicate with each other through these bi-directional links at transfer rates selectable between 5/10/20 Mbits/s. The CPU, FPU, links and timers all work independently from each other. This enhances system throughput and allows concurrent task execution. For example, while an operation is being executed by the FPU, data for the next operation are simultaneously being prepared by the CPU and the 4 links are transferring data to other transputer under DMA.

This readiness for parallel computing built into the transputer – without the need for complex operating systems with all their overheads – makes them ideal for instrumentation requirements. Transputer can furthermore be programmed very efficiently in high level languages, such as OCCAM[21] which was specifically designed for the transputer, FORTRAN and C. The FORTRAN and C language standards are extended to support concurrent task execution and link communication.

On a transputer a program (better described as a *process*) is defined as a piece of code that starts, performs a number of actions and may or may not stop. A process is the standard building block for both hardware and software. Many processes may

[21]The founding principle of OCCAM is a minimalist approach which avoids unnecessary duplication of language mechanisms, and is named after the 14th century philosopher William of Occam who proposed that invented entities should not be duplicated beyond necessity. This proposition has become known as "Occam's razor" [INMOS, 1988].

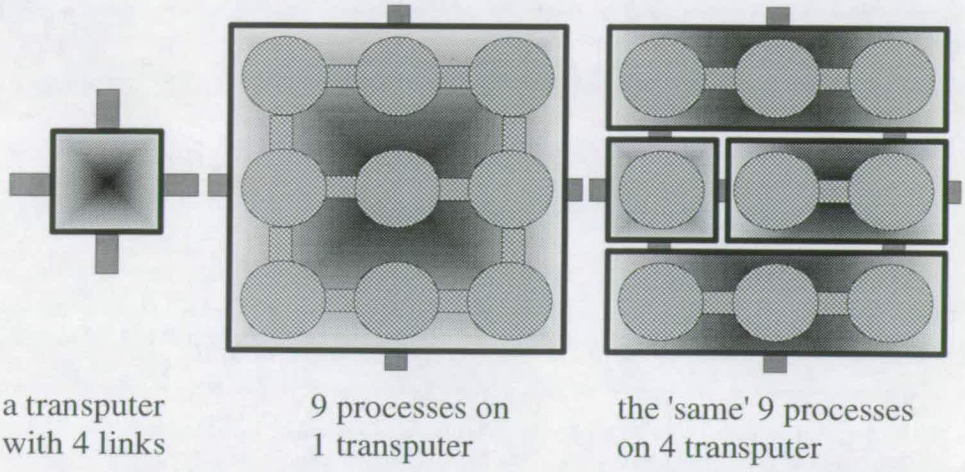

Figure 22: *From the programmer's viewpoint, hardware and software channels look the same. The actual number of transputer is specified at run time with a configuration file.*

run in parallel or concurrently. This is achieved at the programming level where no distinctions are drawn between a number of concurrent processes on one transputer and the same processes on an arbitrary number of transputer. This is because all processes communicate with each other by channels and only at the final program configuration stage these channels are defined as being either (see figure 22)

- soft(ware) channels or
- hard(ware) channels, physical links between transputer.

Internally, they are supported in the same way by the instruction set for concurrent processing within a transputer.

While it is perfectly possible to run applications (e.g. FFT) solely in the transputer's internal memory at full processor speed, large programs can use up to 4 Gb external memory in a linear address space. The overall memory can consist of different types: registers, EPROM, SRAM and DRAM. The power consumption of the transputer depends on the type; typical operational values are 400mW for a T425 and 600mW for a T805.

Although the transputer is no longer considered first choice to construct massive parallel super computers, various transputer modules (TRAM standard) for many computing and controlling tasks are still being developed and are commercially available.

5.4 The sensor node

As mentioned earlier, S.P.A.M. MkIII supports at least 3 different types of sensors: electrodes, magnetometers and seismometers. Because these can be of different

makes, the sensor node is constructed as a generic signal preconditioning device, versatile enough to cope with most geophysical input devices. Generally, the sensor node consists of a power supply with voltage regulation, several sensor boards with options for active or passive sensors, and a control logic (fig. 23).

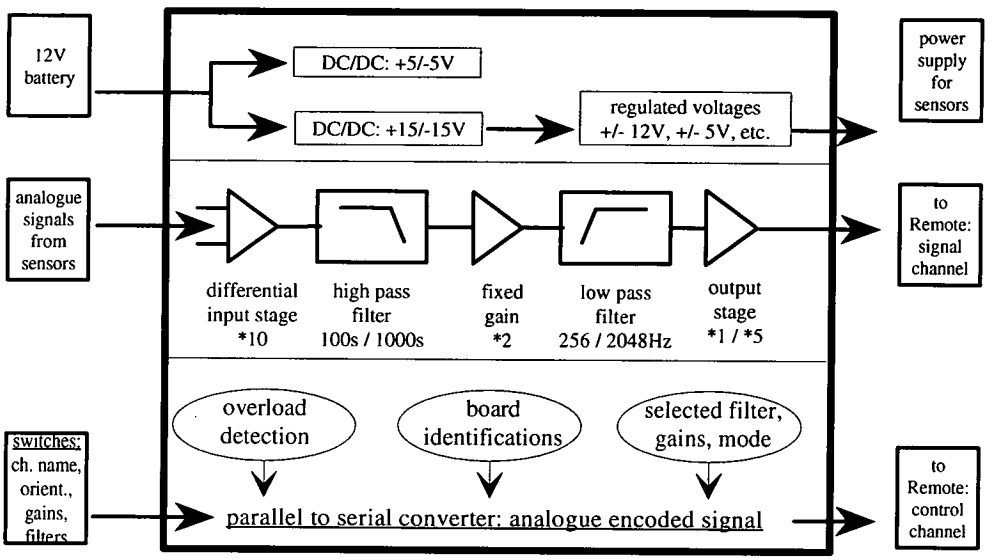

Figure 23: *Sensor node schematic: A sensor box consists (from top to bottom) of a power supply unit with voltage regulation, sensor boards with options for active or passive sensors, and a control logic unit.*

The amount of necessary analogue signal processing depends on the type of sensor connected. Electrodes are usually passive devices, whereas induction coils have active components (band-pass filter, amplifiers) built in. In the case of an induction coil it is sufficient to provide power and to buffer the signals, while for a telluric channel, the sensor node must provide the complete signal preconditioning circuits.

As indicated in figure 23, the telluric input- signals are amplified differentially for common noise reduction. Optionally, shielded cables can be used to suppress high frequency noise pick up. In the next stage, the signals are sent through a passive high-pass filter section to remove DC offsets. The filter cut-off frequencies can be set to $100\,s$ or $1000\,s$. The high-pass filter section is followed by an amplifier and impedance converter, with a signal amplification factor of 2, which is followed by a passive low-pass filter, with cut-off frequencies selectable at $256\,Hz$ or $2048\,Hz$. Finally, the signals are post-amplified, with gains of 1 or 5, into an amplitude range of $\pm 3V$ or less. The last amplifier is furthermore capable of driving shielded signal cables of at least $200m$ length. The total signal amplification for a telluric channel is 20 or 100.

However, any one of the above stages can also be by-passed, if not required, by setting appropriate jumpers on the *Sensor*-boards. Depending on how a sensor is equipped, it might be sufficient to populate the boards only partly; e.g. in order to

support a CM11E induction coil only the output stage is required.

Noise generated at the pre-amplification stages is multiplied through the whole system. It is therefore essential to design a very low noise input stage. One must compromise, though, as low noise amplifiers have high power consumption. Currently, the S.P.A.M. MkIII input amplifier is based on the LT1013 which has very low input current noise, low input voltage noise and a CMR of $> 100db$. Low input current noise is important, because we are usually dealing with low impedance electrodes.

A separate channel board is provided for each connected active or passive sensor and each one of these boards can be identified by a unique hard-wired number (8-Bit). The type of a channel (electric, magnetic or seismic) and its orientation (north/south, east/west or other) can be set with switches. On the outside of the *Sensor*-box are LED-indicators for possible signal overloads. The states of internal or external controls are sampled continuously by the *Sensor*-control logic and sent repeatedly, as a stream of analogue encoded serial data to the *Remote*. It is planned to extend the usage of that control line for bi-directional signal transfer, to feed a test signal through the whole network into the *Sensor*-boards and possibly into the coils.

The principle source of power is $12V$ DC from normal or sealed lead-acid batteries. However, in order to operate all kind of analogue and digital components it is necessary to create several other voltages, too. The main supply voltages of $\pm 5V$ and $\pm 15V$ are derived directly from the battery using DC/DC converter devices. The $\pm 5V$ source is necessary to supply the digital circuits and to generate the analogue encoded signals. The $\pm 15V$ analogue supply voltage can be regulated (stabilized) in variable steps in a range between $\pm 12V$ and $\pm 5V$. $\pm 12V$ are used internally to operate the sensor node. ECA CM11E induction coils, for example, are also operated at $\pm 12V$, while a Metronix GMS05 coil must be supplied with $\pm 15V$.

5.5 The remote node

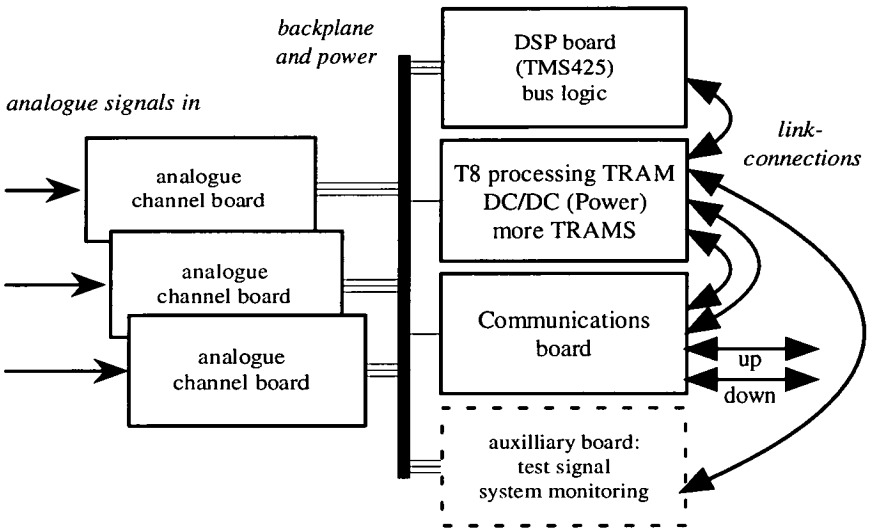

Figure 24: *The building blocks of a Remote: The analogue signals of each channel are filtered, amplified and finally digitized. Further digital signal processing is applied using transputer modules: oversampling decimation, variable band-pass filter and FFT. Digital data can be sent to the Base through the communications board.*

The *Remote* is the primary analogue and digital signal processing unit of S.P.A.M. MkIII. Its components are shown in figure 24. Up to 12 channel boards per *Remote* capture the analogue signals from up to 6 *Sensor*-boxes. Separately for each channel, the analogue signals are fed through a band-pass filter, notch filter and several amplification stages, before they are finally digitized. The complete analogue section for a channel is mounted onto standard Eurocard-sized boards[22].

The DSP-board software activates channel boards and reads and writes various system information: A/D converter outputs, gain and filter settings, etc. The main use of the TMS425 transputer on the DSP-board, however, is to apply low-pass filter and oversampling decimation to the stream of continuously sampled digital data. From here, the decimated data are transferred to the T8 processing TRAM, where digital frequency bands are computed. Several of these frequency bands can be executed in parallel, with variable high-pass and low-pass corner frequencies. Finally, segments of filtered time series data can be transformed into the frequency domain (FFT). The time- and/or frequency domain data are sent to the communications board which provides special hardware to use the transputer link protocol over long distances. Further data handling and processing procedures are then applied at the *Base*.

[22]size: $160x100mm$; Eurocard-sized boards are used throughout the system.

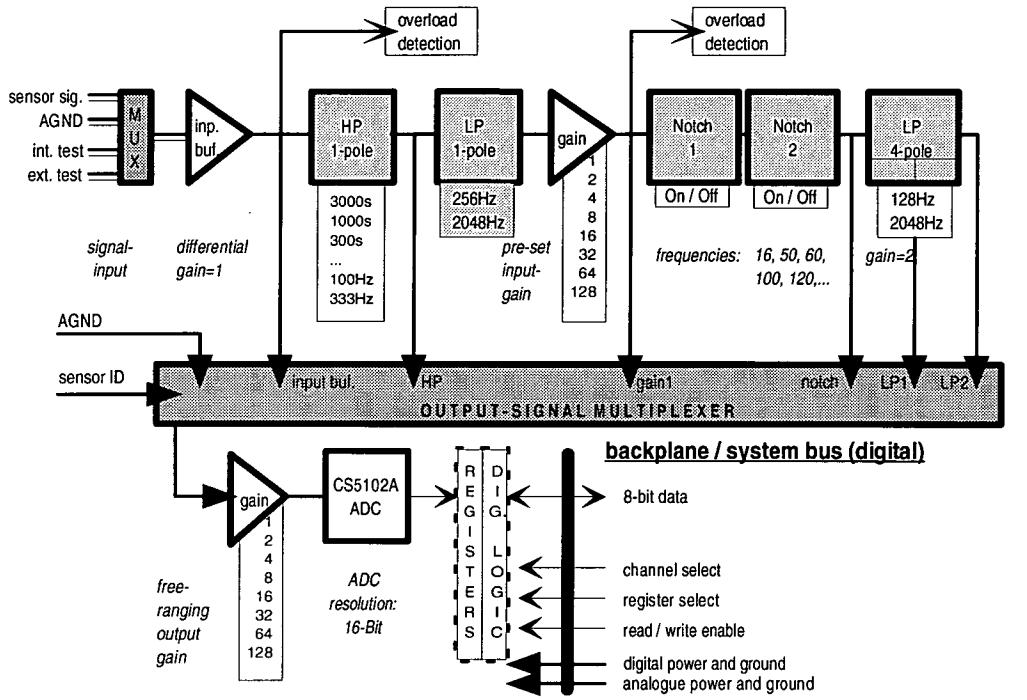

Figure 25: *Schematic of the Remote's analogue channel boards: All stages of the analogue section can be tested by setting input- and output multiplexer accordingly. It is possible to keep the analogue hardware relatively simple, as much of the signal processing is accomplished digitally.*

The involvement of extensive digital signal processing facilitates a relatively simple design of the analogue section. In analogue circuits, noise is introduced in many - often inevitable - ways: production tolerances and temperature drifts of electronic components, signal cross talk from neighboured channels or through ground planes, etc. Tolerances in hardware components make an accurate design of active filters with many poles more difficult, especially, as it is furthermore required that all channels have matched response function characteristics. It is therefore desirable to keep the analogue section simple, in order to minimize distortion of the signals. The schematic of S.P.A.M. MkIII's analogue section in figure 25 reveals only a two-stage 5-pole low-pass filter[23] which can be made very stable, low noise, and cost efficient. However, an active 5-pole low-pass filter, in combination with a 4-times digital oversampling filter, results effectively in a 15-pole filter, with $\approx 90db$ signal reduction at the decimated Nyquist frequency. The oversampling filter consists of a specially designed FIR low-pass filter with 20 coefficients.

If things go wrong, the instrument is usually blamed first. Therefore, various test and calibration facilities are incorporated into S.P.A.M. MkIII (figure 25). The input

[23]with Butterworth characteristic; it is more a $4\frac{1}{2}$-pole filter for the $128\,Hz$ low-pass.

signal multiplexer (MUX) can be directed to short the inputs (AGND) or to feed test signals into the analogue section, instead of the normal sensor signals, in order to confirm system functionality. The output signal multiplexer can pick up signals at various stages of the analogue signal processing. If, for example, the output-signals appear to be saturated, the source of the problem can easily be tracked down by feeding the signals through fewer and fewer parts of the whole system. (To check the overload detection indicators would be a first choice, though!) Alternatively, the output multiplexer can select the *Sensor*-box identification information which is encoded into an analogue signal. The contents of the *Sensor*-box identification is decoded by the DSP software.

S.P.A.M. MkIII's analogue section provides two software-controlled amplification stages with variable gains. The first stage just before the notches is used to raise the signal levels as much as possible, without causing overloads. The maximum gain is usually determined by the $50\,Hz$-signals which have much higher amplitudes than any other signals. But depending on the high-pass filter setting, long period signals or drifts are to be considered, too. This first gain remains fixed during normal operation, because following each gain range, all subsequent filters must settle in again. The gain setting of the second amplifier behind the filters, however, is modified frequently to ensure that the full dynamic range of the ADC converters are used.

Figure 26 shows the frequency domain responses of a 10-channel *Remote* operated in the laboratory. The input multiplexer of all analogue channel boards are set to $AGND$ (shorted inputs). To demonstrate the effects of a faulty channel, one of the input amplifiers is set to unity gain, whereas the others have input gain settings of 32; $50\,Hz$ notches were used for all channels. The *noisy* channel can easily be identified as the one with larger amplitude spectra over the whole frequency range[24] Obviously, this result demonstrates the very reason for having the input gain. The gain settings should be as high as possible during operation, in order to improve the signal to noise ratio.

This first version of S.P.A.M. MkIII operates in the so-called short period band, but analogue boards for long period or high frequency operation can be built, if the needs arise. The short period band is divided into two operating modes: continuous or windowed. In the continuous mode, the low-pass corner frequency is set to $128\,Hz$ and all analogue channels are continuously sampled and converted into *endless* streams of time series data. In the windowed mode, with a low-pass filter setting of $2048\,Hz$, signals with a higher frequency contents can be recorded, but the sampling operation must be interrupted for the data processing. The actual ADC sampling rates are $2048\,Hz$ and $16192\,Hz$ for the continuous and windowed modes, respectively.

The frequency bands are limited by 1-pole high-pass filters. The high-pass corner frequencies can be set in a wide range between $333\,Hz$ and $1000\,s$. To reduce the effects of the mains power supplies and their harmonics, up to two notch filter modules can be activated. Each of which can be selected from a wide range of

[24]the scale of the vertical axes is $1\mu V/cm$ input-referred.

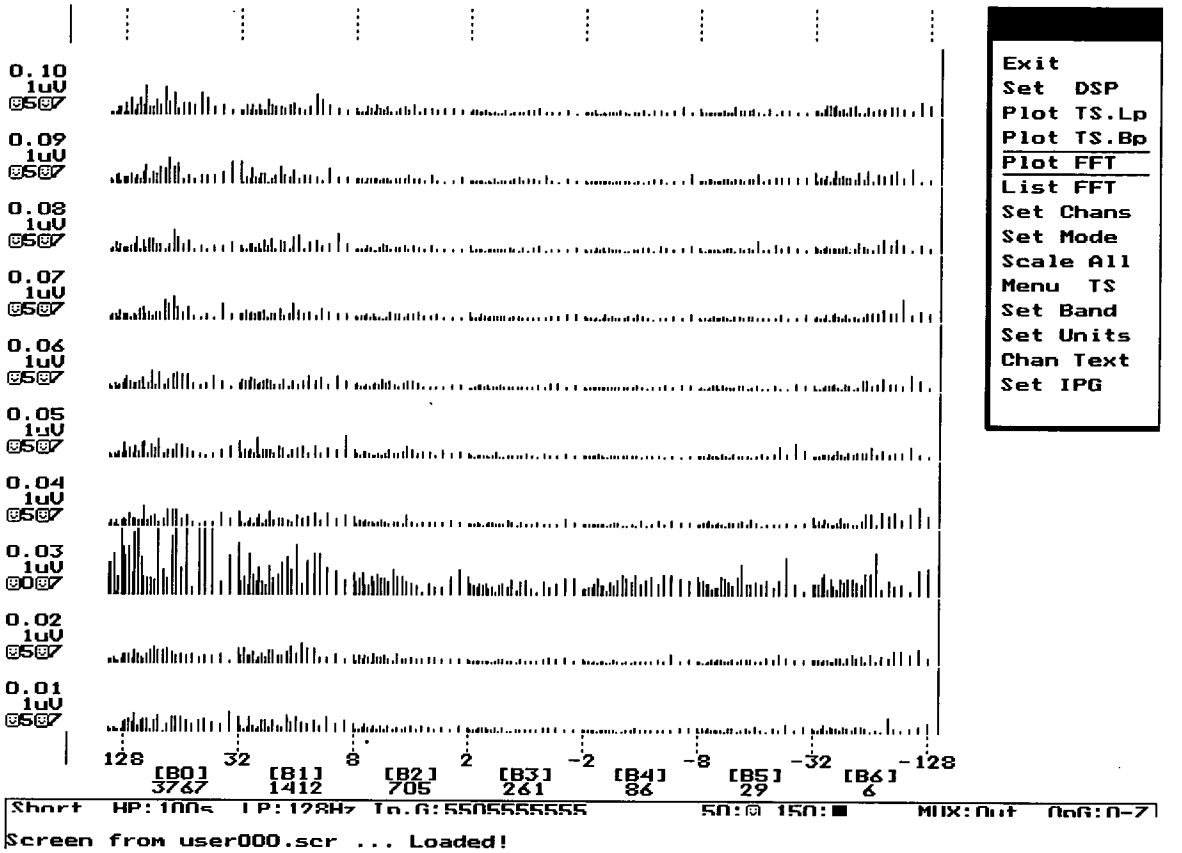

Figure 26: *Example of the Remote's test facilities. Displayed are frequency responses of channels with shorted inputs. One of the channels appears to be noisier because it's input amplifier is set to a lower gain.*

frequencies ($16\frac{2}{3}\,Hz \ldots 250\,Hz$) by changing the filter's resistor section on tiny plug-in modules. The filter characteristics (*Q-factors*) of the notches can either be steep and narrow or less steep, but affecting a wider frequency band.

Generally, it is advisable to examine high frequency electromagnetic data in narrow frequency bands, as signal to noise ratios of the AMT signals vary greatly over the frequency range. Because of S.P.A.M. MkIII's improved analogue sections, however, it is simply not necessary to realize these frequency bands in hardware. The dynamic range of the analogue channels is in the order of $20 - 22$ bits[25] and with all the additional computational power available, other frequency bands are generated using digital filter techniques.

Figure 27 shows a diagram of S.P.A.M. MkIII's binary decimation and processing scheme. Input to the procedure are the *raw* time series from the DSP board (LP_0). As all S.P.A.M. MkIII sampling rates are generated in octaves (power of 2), the time series are continuously low-pass filtered and decimated in steps of 2 ($LP_1, \ldots, LP_n$). The low-pass filtered time series are subsequently high-pass filtered, to generate band-pass filtered data streams. Again, the high-pass corner frequency settings are

[25] or $120 - 132\,db$ ([16 bits: ADC] + [2 – 3 bits: auto-gain] + [2 – 4 bits: digital decimation]).

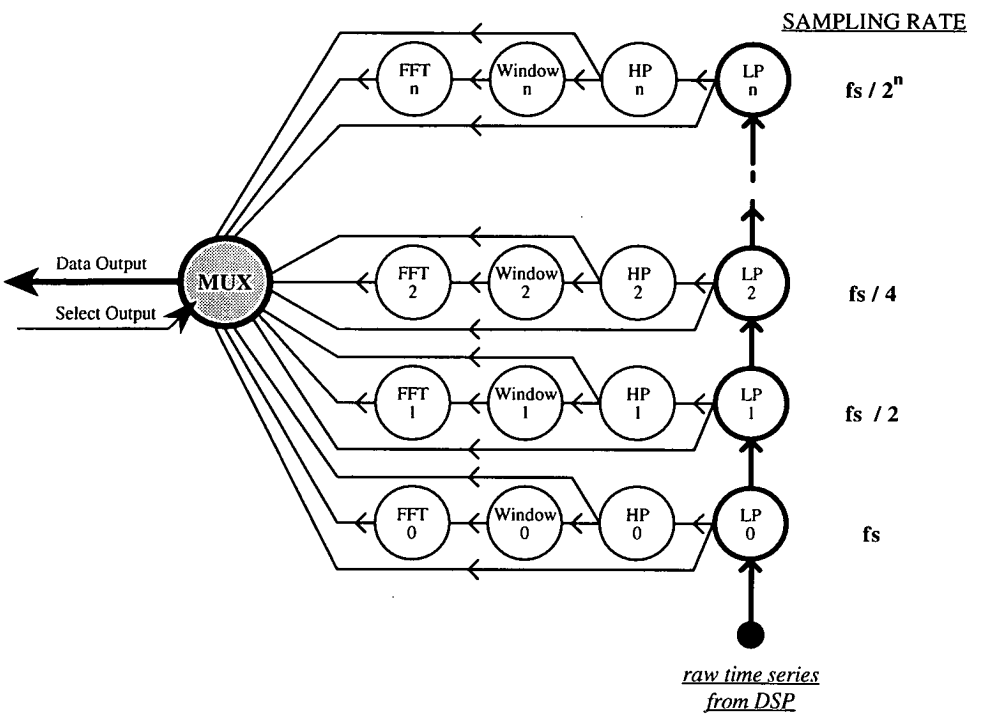

Figure 27: *Diagram of the Remote processing scheme. The raw time series from the DSP board (LP_0) are continuously filtered and decimated in steps of 2 ($LP_1, \ldots, LP_n$). Eventually, any kind of time or frequency domain data can be transferred to the Base.*

variable in octave steps. Next, adjacent or overlapping time segments are chosen and prepared for the FFT ($Window_0, \ldots$). The freqency domain data (Fourier spectra) are corrected for the instrument response functions.

From the *Remote*, data can be forwarded either, as original time series, as decimated and low-pass filtered time series, as band pass filtered time series or as frequency domain data. Any mixture is possible and all time series are continuous streams of data which can be stored and/or further processed at the *Base*.

The window length or the number of samples of a time series segment and hence the length of it's Fourier transform depends on the band-pass filter settings (figure 28). The number of samples is calculated using the formula: $2^{(5+n)}$, where n is the width of the frequency band in octaves. Band 0 in figure 26, for example, has low-pass and high-pass filter corner frequency settings of 128 Hz and 16 Hz, respectively. The bandwidth is 3 octaves, which results in time series of 256 samples.

The design of the digital low-pass FIR filter is based on a Kaiser window, with 27 coefficients and a 96db cut-off at the Nyquist frequency. The high-pass is a 4-pole Butterworth IIR filter which gives 72db attenuation at the fundamental frequency. The IIR filter must be computed using 64-bit arithmetic to avoid filter instabilities. Since FFTs are also computationally expensive, the T8 processing TRAM (see figure 24) contains a TMS805 transputer with integrated floating point unit. The execution

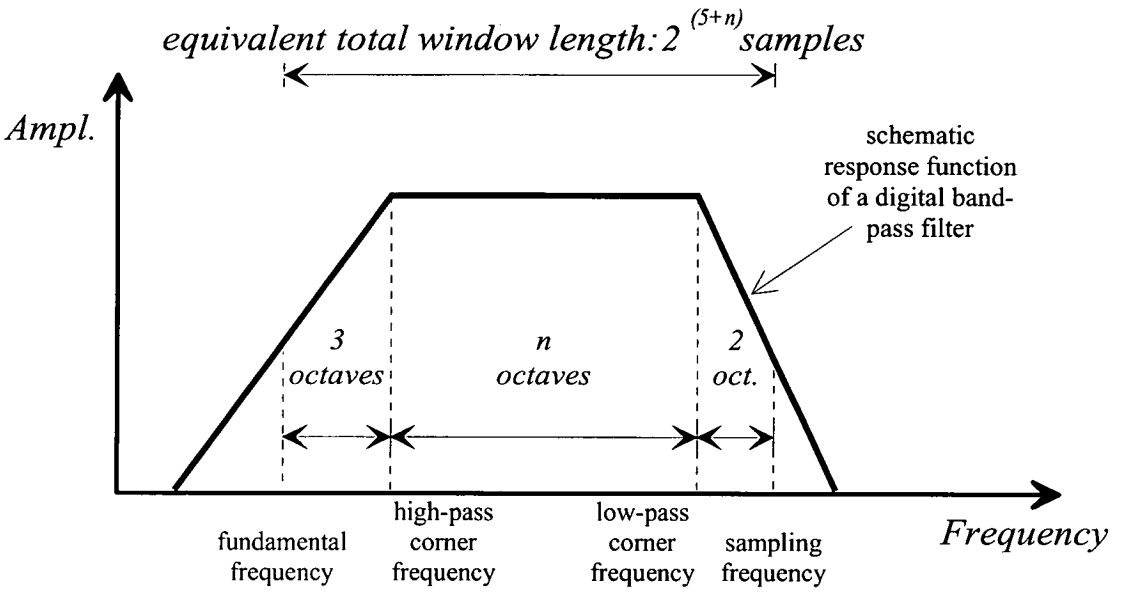

Figure 28: *The length of a time series segment depends on the band-pass filter settings. The number of samples is:* $2^{(5+n)}$, *where n is the width of the frequency band in octaves.*

time of a transputer FFT is approximately $7n \cdot \log_2(n)\,[\mu s]$, where n is the number of samples.

The data decimation scheme in figure 27 can also demonstrate how parallel computing can support the design of S.P.A.M. MkIII. At first, the decimation procedure appears to be a serial operation, because only upon the arrival of the LP_{n-1} samples can the LP_n time series be created. However, the low-pass filter and eventually the high-pass filter operations are processes that can be executed in parallel, if correct data handling is applied. The implementation and execution of parallelized procedures is very efficiently supported by the transputer hardware. All concurrently started processes receive their input data and send their results through channels (software links). The programmer associates these channels with (arrays of) data streams and connects the according processing procedures.

To program, for example, the low-pass filter scheme in figure 27 one would proceed as follows: The main process is started and runs indefinitely. It contains the low-pass filter code in an infinite loop. This loop is duplicated in parallel, simply by preceding the loop instruction with the Occam PAR construct. Each of these parallel low-pass filters contains instructions to wait for data from channel $i-1$ and only if the required data have arrived, will subsequent instructions be executed. The transputer hardware itself takes care of an optimized performance, as it handles all necessary queuing and task switching.

The importance of the transputer for the S.P.A.M. MkIII concept is obvious. Parallel or concurrently started processes are implemented everywhere in the system software, not only for data processing purposes, but also to control the hardware, transport and store data, assure prompt user interaction, etc.

5.6 The base node

The *Base* controls the entire network of *Remotes* and sensor nodes and is used to perform high-level data processing. The software running in the *Base* transputer collects data from all attached *Remotes*, optionally stores the time series on hard disk and computes cross-spectral analysis of the frequency domain data. Various channel combinations can be selected for the analysis, as all data over the network are sampled synchronously. Currently, the data stacking and rejection criteria operate similar as in S.P.A.M. MkIIb (chapter 4.1.2), but other algorithms are likely to be implemented in the future.

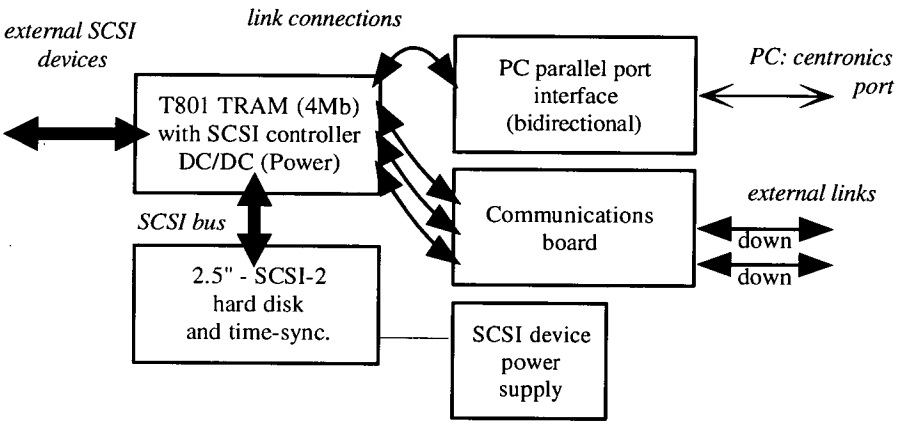

Figure 29: *Block diagram of the Base: The T801 TRAM provides processing power and a SCSI interface for data storage. The PC must be equipped with a bi-directional printer port to enable fast, byte-wide data transfers.*

Figure 29 shows a block diagram of the *Base*. Its most important component is the SCSI-transputer module, a highly integrated, commercial TRAM[26] containing a TMS805 ($25MHz$) transputer, 4Mbytes DRAM, and a very powerful fast SCSI-2 controller chip[27]. The SCSI controller is an *intelligent* device on its own, which shares RAM with the transputer. Therefore, disk operations consume only a small portion of the TMS805 computational power and all the data processing and system monitoring can still be done on the same transputer in parallel. The SCSI transputer module conforms to the TRAM standard and is therefore compatible with our T8 processing board, which is also used in the *Remotes*. It provides slots for up to two TRAMs and their power supplies. If more computational power is required – for example to run 2D inversions in the background – more TRAMs or T8-boards can simply be added to achieve an instant gain in performance.

Built into the S.P.A.M. MkIII prototype is a 2.5″ hard disk[28] with a capacity of 170 $Mbytes$. However, any SCSI-2 hard disk can be attached to the *Base* and disks

[26]C.O.R.A.L. HPT04, double TRAM: length 93mm, width 53mm, power typ.: 2.5W.
[27]type: NCR 53C710.
[28]Quantum GoDrive, power: active 2W, standby 0.2W.

with even higher capacities will become available in the future. Part of the SCSI TRAM package is an OCCAM/C library to initialize, read and write the disk. All disk commands are executed in parallel. Eventually, recorded data can be dumped onto an external SCSI-hard disk. Both, internal and external disks are compatible with the standard PC file system (DOS), which ensures easy access to the data. The sustained data transfer rate between disk and transputer exceeds $2Mbytes/s$.

Initially, we anticipated to use the SCSI bus also to communicate with the laptop PC, but the idea had to be abandoned. Instead, we had to design our own interface, making use of the bi-directional parallel port which nowadays can be found in most laptop computers[29]. INMOS provides a special software - called *iserver* - for communication with transputer subsystems which is available for many computers and operating systems. The original *iserver* is designed to support INMOS PC-boards with add-on TRAMs, but because the C source code is available to the public, I was able to modify it to support the parallel port instead. *iserver* provides the following functionality:

- Reset: issued by the PC, to reset the transputer subsystem. After a reset, the (main) transputer awaits executable code to arrive on one of it's links.
- Boot: issued by the PC after a reset, to load the subsystem with a transputer binary file. After successful reception of the complete boot sequence, the boot-code is executed on the transputer. In a complex environment, the first transputer boots the rest of the transputer network. The transputer takes now control over *iserver*.
- I/O requests: issued by the transputer, to use the PC as the standard input/output system. This includes screen, keyboard, file system and the PC timer.
- Connect: issued by the PC, to connect to a transputer with an already running process, without prior booting the transputer. We use this feature to temporarily disconnect (and then re-connect) the PC from S.P.A.M. MkIII; this is useful for over-night runs, etc.
- Abort program: issued by the PC to re-gain control over the system.

I furthermore extended *iserver* with graphics routines, which can be used by the transputer programs to display results from MT data processing, etc. on the PC screen. Because our modified *iserver* is compatible with the original, S.P.A.M. MkIII can directly be used with àll transputer development kits (compiler, linker, etc.), to create and run transputer programs.

It should be readily comprehensible now, how S.P.A.M. MkIII is operated: When all the network components (*Sensors*, *Remotes*, *Base*) are inter-connected and powered up, the laptop PC is attached to the *Base*. The *iserver* program is started on the

[29]the original PC printer port was used only for output.

PC to reset and boot the entire transputer network. All transputer software including data processing and digital signal processing code, system software, calibration data, transputer network configuration files, and scripts for default operations is loaded from the PC disk into the transputer network. After succesful booting, the PC serves merely as a terminal for user interaction. Usually, the user will first perform various system checks and inform the processing software about site names, electrode spacings, etc. Eventually, the frequency bands of interest are selected and the data recording and processing is started. The user can check the data quality on-line or leave the instrument unattended for automatic data recording.

It is planned for the future, to include 1D and 2D modelling and inversion procedures, which could be implemented on an additional *Base* TRAM. Furthermore, we intend to specify an interface for general user supplied applications, for example seismics processing or robust statistics.

5.7 Digital data communication

The S.P.A.M. MkIII communications boards provide the hardware to interface an external data transmission method with the transputer link protocol. Transputer-links are TTL compatible and intended to be used in electrically quiet environments, between devices on a single printed circuit board or between two boards via a backplane. Direct connection may be made between devices separated by a distance of less than $300\,mm$ [INMOS, 1992, p424]. This restriction is necessary, because if high frequency signals (e.g. link speeds of 10 or 20 $Mbaud$) are sent over very long cables, they arrive mis-shaped and attenuated at the other end.

Consequently, the hardware of the communications boards provides:

- link speed reduction
- RS422/485 drivers/receivers.

The RS422/485 standard is designed specifically to transmit signals in electrically noisy environments over long distances. One-chip solutions to implement the hardware are readily available. INMOS provides so-called link adaptor devices (IMSC011) which are specified for use as programmable I/O (link to parallel port conversion), as inter-family microprocessor interfaces, and for inter-connection of different link speeds. A reduction of the nominal C011 clock frequency ($5\,MHz$) results in an equivalent reduction of the associated link speeds. If two C011 devices are connected back to back via their parallel ports (handshaken byte-wide interfaces), they can be used as frequency changers between any two different link speeds. It is therefore only necessary to reduce the clock frequencies by the same amount on two *output*-C011s (e.g. between *Base* and *Remote*), until an error-free communication is established. Every completely transferred byte is acknowleged by the transputer link protocol. The received data are then forwarded to the respective *input*-C011s and sent to/from other transputer using the internal links at full speed.

Hence, the *output*-link speeds determine the total data transfer rates between S.P.A.M. MkIII nodes. Cable segments $< 400m$ can be operated at $2.5\,MHz$ (approximately $100kbytes/s$), while $1.25\,MHz$ is the maximum for $400m$-cables. $400m$ is currently also the maximum length for copper cables. However, many $400m$ cable segmemts can be inter-connected, if the signals are refreshed at the joints (chapter 5.8). Internally, a 'digital cable' consists of 4 twisted pair cables and a shield. The cable must provide lines for serial data transfer, reset and synchronisation. Twisted pair cables provide a separate ground for each signal line to reduce noise pick-up.

So far, only copper cables are supported as communication media by S.P.A.M. MkIII. However, telemetry or fibre optics (or others) can be supported by replacing the respective communications boards. With telemetry links data from very distant and quiet sites could be included on-line to improve the processing of a local site. Unfortunately, telemetry systems provide only limited data transfer rates, and often, they are required to be operated in a line of sight between transmitter and receiver. With fibre optics cables data transfer rates at full link speeds can be achieved, but they are expensive and very difficult to repair under field conditions.

5.8 The repeater node

A *Repeater*-node is a device to re-create *degenerated* digital signal information. Because copper cables have a certain resistance and a capacitance proportional to their length, they behave like a filter which affects any frequency-dependent signal. Phase shifts and line delays caused by reflection of high frequency signals are additional problems.

By definition, digital signals are either in low or high state (e.g.$\pm 8V$ for RS422) with clearly defined sharp transitions between the two. A smoothing effect on the signals is very dangerous, because the timing of a transition from one logic state to the other becomes increasingly uncertain. Signal-attenuation can cause the amplitudes to fall under the minimum requirements for a logical high or low state. Hence, the *Repeater* hardware picks up such distorted – but still valid – digital signals and restores their original shape. The re-generated signals are buffered and, using the RS422/485 specifications, another long cable segment can be driven.

Internally, the *Repeater*-box is powered by a $6V$ battery which lasts for two or three days. The power consumption of $\approx 400mW$ is mainly determined by the active line terminations which are necessary to reduce high frequency signal reflection problems. The internal battery can be recharged during operation with an external $12V$- battery or a solar panel. Located on the outside of the *Repeater*-box are LEDs for battery charge condition, link speed, and indication of activity on the lines.

5.9 Synchronization and timing

Timing and synchronization of a S.P.A.M. MkIII network is controlled from the *Base*. The *Base* requests absolute time and date from the laptop PC, initializes its

internal timer and transfers the information to the *Remotes*. Furthermore, synchronization pulses with a one second period and a pulse width of $1\mu s$ are generated using the *Base*'s clock. These synchronization signals are sent through the digital cables to the *Remote*(s).

In the *Remote*, the internal timers of the DSP-transputer are set to generate the principal ADC sampling rates of $2048\,Hz$ in the continuous mode and $16192\,Hz$ in the windowed mode. The transputer timers are programmable and the response time (*latency time*) to activate an event on a timer interrupt is less than $1\mu s$. The synchronization pulses from the *Base* signal an external interupt on the DSP-transputer, which subsequently is used to correct timing inaccuracies.

The *Base* clock can easily be replaced by similarly generated external synchronisation signals. Sockets for this purpose are provided on the outside of the *Remote* box. PC clocks, however, are very inaccurate and they cannot be regarded as absolute timing devices. Therefore, we intend to use a high accuracy external timing device, possibly a GPS-system, in the future. Such precission timing would also be necessary to synchronize separated S.P.A.M. MkIII-networks.

5.10 Putting it all together, configuration examples

Figure 30 shows a typical configuration of S.P.A.M. MkIII units for a standard 5-channel set-up with two horizontal remote reference magnetic sensors. The *Base* communicates digitally with the *Remotes* which act as local nodes for sensor inputs. *Sensor*-boxes and *Remotes* are connected via analogue signal cables. Each cable can carry signals of up to 8 channels. The length should not exceed $200m$ and shorter cables are preferrable. Because *Remote- Base* data transfer is digital, cable links (with repeaters) can be used over ranges of more than $1km$. A PC compatible portable computer is attached to the *Base* in order to initialize the entire instrument network, and it serves as a graphics terminal.

All S.P.A.M. MkIII units are usually powered individually, by sealed $12V$ batteries. The *Base* and a 10 channel-*Remote* box use approximately $5W$ each, allowing 48 hours operation from $25Ah$ batteries (half the capacity of a car battery). The power consumption of the *Sensor*-boxes depends mainly on the sensors; a configuration with two telluric channels and 3 CME11 induction coils consumes approximately $2W$.

Figure 31 demonstrates how S.P.A.M. MkIII might be used for experiments in the future. The set-up consists of two independently operated S.P.A.M. MkIII-networks which are synchronized by GPS clocks. Both networks communicate by telemetry. Thereby, at least some of the data from the observatory site are transferred to the main experiment to enhance the data processing. This feature is particularly interesting at locations with high cultural noise levels (e.g. anywhere in Europe).

The local 'site' consists of a complex S.P.A.M. MkIII network with an attached telluric array. This configuration could help to determine the effects of small scale near-surface features (geological noise) which cause so much trouble when it comes to data interpretation. Existing aproaches to tackle the problem (decomposition

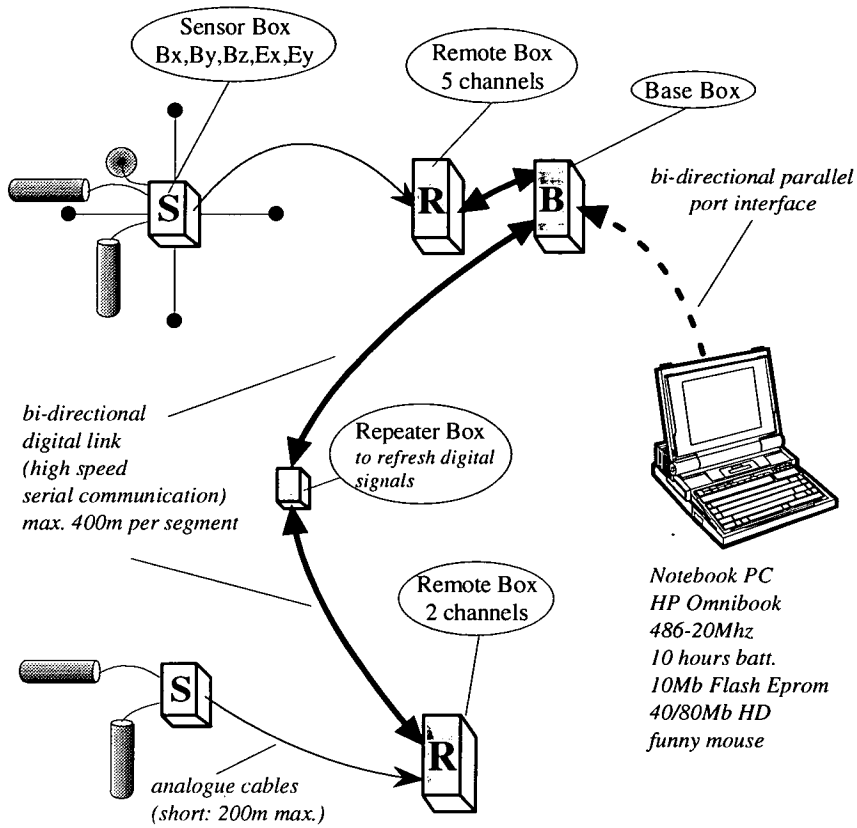

Figure 30: *A simple arrangement of S.P.A.M. MkIII which simulates the present Remote Reference technique. The configuration has been tested up to a maximum distance of* $1.6km$ *between reference and base sites.*

methods) make no use of the spatial stucture of the electric field because it is unknown. It must be preferable to actually measure the electric field around the MT site and use the information contained in the spatial structure to obtain the most representative estimate of the impedance. If the local structure is 1D with small-scale local inhomogeneities superimposed, we would expect that the magnitude and direction of the electric field in the measurement grid would fluctuate around some mean value. In this case, some form of spatial filtering technique could separate and remove the short wavelength features associated with the distortion. However, the electric field may cross a significant geological boundary, in which case we would probably wish to reject observations from one side or the other, and stack the rest.

Clearly, there are numerous other ways to built S.P.A.M. MkIII networks. Measurements of electromagnetic data on dense arrays become feasable which are essential for three-dimensional data interpretations. The inclusion of seismometers in a joint electromagnetic on-line data processing could open completely new fields for geophysical applications. Very comprehensive instruments could be assembled in cooperation with other research institutions, if S.P.A.M. MkIII compatible compo-

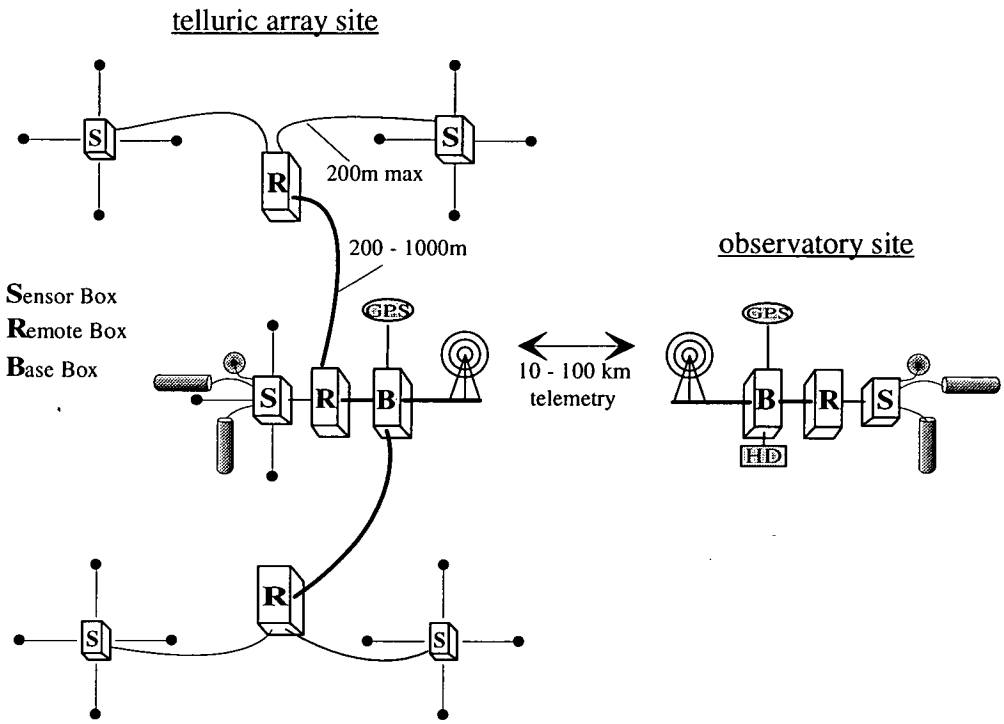

Figure 31: *Possible set-up of S.P.A.M. MkIII for a telluric array experiment with a telemetry link to a remote, noise-free observatory site.*

nents become more widely used.

6 Handling of large, multi-channel, multi-site, synchronous data sets

The extended facilities to connect sensors to the new S.P.A.M. MkIII (chapter 5) are advantageous for many geophysical applications. But it also means that data handling becomes more complicated and often existing data handling procedures are no longer applicable. For further data processing or re-processing, all necessary information on employed hardware, site locations and instrument configurations must be accessible together with the actual time series data. To keep all acquired data efficiently organized is an extremely difficult but very important task.

Most existing data formats are tailored to be used with one particular type of instrument with a fixed or limited number of channels. It is usually assumed that the instrument is deployed to record data at one site, perhaps with some additional *local* remote reference channels. S.P.A.M. MkIII on the other hand can be used as a networked instrument to record synchronous data from several sites with a variable number of channels and sensors. Several of these networks can be set-up in different configurations at the same time. The type of connected sensors is totally variable, as different methods like EM and seismics could be used at the same time.

The hardware composition of a S.P.A.M. MkIII-network is recognized by the system itself, because every sensor-preconditioning and *Remote* analogue board can be identified by a hard-wired number (chapter 5). External and internal calibration facilities are an integral part of the S.P.A.M. MkIII design. Hence, instrument response function corrections can be generated very accurately and kept up-to-date. If the influence of instrument response functions is not taken into account, all processing results will be biased systematically. It is therefore important to keep calibration data well organized, to ensure that a calibration data set can always reliably be associated with a particular time series data file.

The amount of time series data produced by the new instrument can be enormous. It is perfectly normal to fill the internal hard disk of $150Mb$ during an overnight run with several activated frequency bands. Despite S.P.A.M. MkIII's real time processing facilities, the recording of time series data is often desirable, for instance, to try a different data processing technique or to combine synchronous data from separated instruments. Consequently, data files must provide fast access to data records and the data presentation should be compact to ensure efficient use of data storage media.

The only existing file standard for electromagnetic data is defined by the SEG[30]. A file conforming to this format is commonly referred to as an 'EDI' (Electrical Data Interchange) file. The EDI-file format is mainly used to import stacked spectra and impedance tensor estimates into the *Geotools* software package [Geotools, 1993]. *Geotools* has found wide acceptance in the research community and so has the file standard. Specifications to store time series data in EDI-files exist, but since many of the above specifications are missing, this option is of limited use only.

[30]Society of Exploration Geophysicists.

Thus, we felt it was necessary to find a new method to organize our data, especially with respect to the new facilities of S.P.A.M. MkIII. The results are overviewed in this chapter. However, the task is intricate and while new ideas and problems continue to arise, some of the work is still on-going.

6.1 EMERALD, the Electro- Magnetic Equipment, Raw-data And Locations Database

The following list summarizes the desired functionality for the new data handling scheme:

- Organization of time series data. The file structure must be suitable for data processing applications and permanent storage of data files.
- Complete description of all employed hardware components, inclusive calibration data. Up-to-date calibration results must be accessible together with previous results for re-processing of old data sets.
- Storage of auxilliary information about projects, site locations, sensor layouts, etc.
- Definition of software interfaces to access data files in conventional programming languages (e.g. FORTRAN and C).
- Instrument-independent data storage to facilitate an integrative processing of data sets recorded with different instruments.
- Implementation of an interface to S.P.A.M. MkIII, to support users during their field work.
- User-friendly software for maintanance, control and modification of all relevant data structures. Support for data archiving.

The most promising way to achieve these goals was to base the new data handling scheme on a mixture of conventional data files and special database-files; with both, data files and database-files being organized in a hierarchical directory-tree structure. The directory tree is expanded when additional data are incorporated. Information on instruments, projects, site locations, sensor associations, etc. is stored in database-files, while conventional data files are used to hold time series and calibration data. Figure 32 shows the EMERALD root directory and four sub-directories, labelled: *User*, *Inst*, *Misc*, and *Proj*.

The optional *User*-directory contains only one database-file. This file holds information about EMERALD users and their passwords. Access to this directory can be prevented or restricted in a multi-user environment.

The *Inst*-directory sub-tree contains calibration data of the instruments. All available hardware is classified as different categories and the categories are split

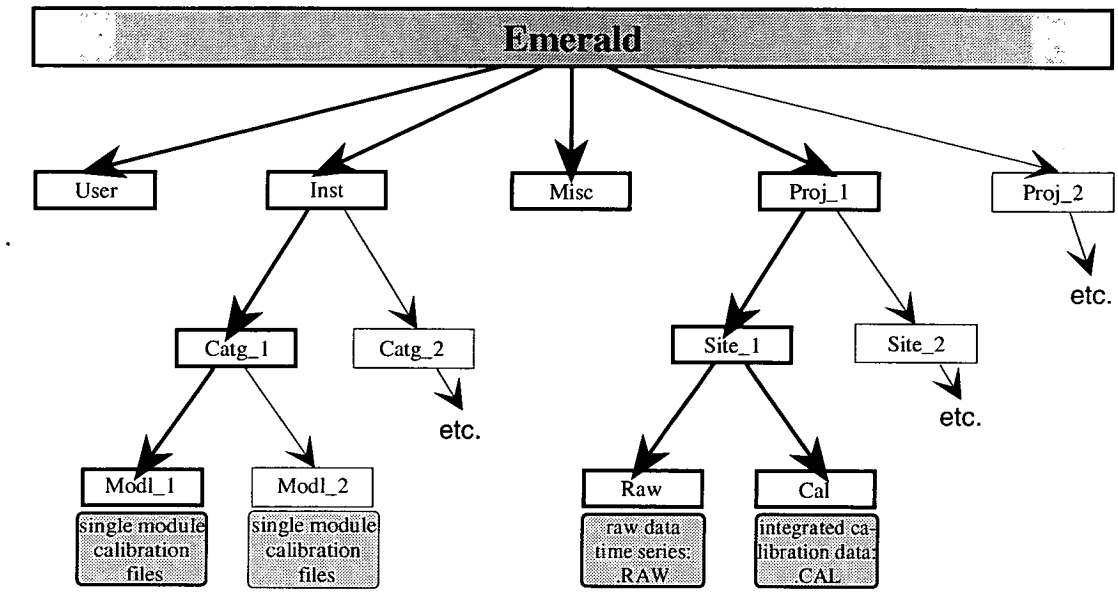

Figure 32: *The directory tree to store the EMERALD data files and database-files.*

further into modules. This is indicated by the *Catg* and *Modl*-directory branches in figure 32. Instrument categories describe all those parts of the equipment, which are usually calibrated separately: induction coil magnetometers, fluxgate magnetometers, sensor preconditioning units, main analogue units, etc. A module, on the other hand, identifies one particular hardware component of that category, e.g. a CM11E induction coil (category) with serial number 47 (module). Usually, each analogue channel of an instrument is described as a composition of several category-module combinations.

The *Catg* and *Modl* directory sub-tree in figure 32 is expanded in accordance to the number of instrument parts that need to be defined. Hence, the *Inst* and all *Catg*-directories contain solely database-files to identify the diverse instrument parts. Calibration results for modules are imported to EMERALD as simple ASCII files. These files contain amplitude and phase differences relative to a calibration signal for the frequency range of interest. Each *Modl*-directory consists of calibration data files for a particular hardware module, together with a database-file which contains a record of the calibration history for that module.

All files in the *Misc*-directory are database-files. They provide auxillary information to help users navigate through EMERALD. These database-files contain information on: projects, valid channel names, frequency bands, the applied geophysical method, instrument set-ups, etc.

The most important role of the database-files is to establish the relation between instruments and sites. Instruments consist of channels which record the data. These channels are composed of hardware modules and each channel is associated with a signal from an electromagnetic field component. For geophysical applications, however, we think in terms of sites. Each site is characterized by its earth response function which is derived from the linear relations between the electromagnetic field

components. Many sites can be covered by one instrument and/or one site can be covered by many instruments. The structure of the database-files guarantees that each channel of an instrument is assigned to exactly one channel of a site and that each channel type (e.g. B_x) is used only once per site. Site-assigned instrument channels have the following information attached: physical units, sensor rotation- and tilt angles, telluric line lengths and a static scaling or conversion factor. Furthermore, a pointer is defined for each hardware module of this channel, in order to locate all its calibration data in the EMERALD *Inst-* directory tree (figure 32).

A new *Proj-* directory sub-tree is created, for each new field project. The *Proj* directories contain the site definition database-files and a separate *Site*-subdirectory is created for each new site. The database-files in the *Site*-subdirectories contain the name and number of a site, its coordinates, and an alias name. Every site consists of one or many layouts. New layouts are generated if the instrument configuration changes, e.g. if a defect sensor needs replacement, if the length of telluric line has changed, or if another method is applied at the same site. The site-layout database-files establish also the relation of a site set-up to an instrument configuration.

Each *Site*-directory holds a database-file containing a log of the time series recorded and imported to EMERALD for that particular site. The actual data files reside in the *Raw*-subdirectories (figure 32). If a file contains synchronous data from several sites, the file physically exists in one of the sites' *Raw*-direcories, only. Together with each raw data file, a calibration data file is stored in the accompanying *Cal*-directories. These calibration data files contain integrated calibration results, compiled for all modules and channels over the whole frequency range. They are composed of the single module calibration data files from the *Inst*-part of EMERALD. They are valid for that specific set of raw data, only.

6.2 EMERALD database files, database extract files and data files

EMERALD database files are accessed by a program called `EMdbw`. `EMdbw` provides a user-friendly interface to enter, read, and modify database records. It creates and alters the EMERALD-directory structure and helps to assign hardware modules to instruments and instrument channels to sites (see figure 33). No limits exist for the number of channels and modules of instruments nor for the number of sites and their layouts.

`EMdbw` is furthermore used to import and export time series- and single module calibration data and it automatically compiles integrated calibration data files. External data formats can be converted into the EMERALD format. Single data files or whole projects can be compressed to free up storage space. The program also generates and interprets so called database extract files.

Database extract files provide a way for bi-directional communication between EMERALD and external sources. As such, extract files can be regarded as a buffered file-based command language to access the database, for example to establish an interface to S.P.A.M. MkIII. Although the contents of the database are distributed

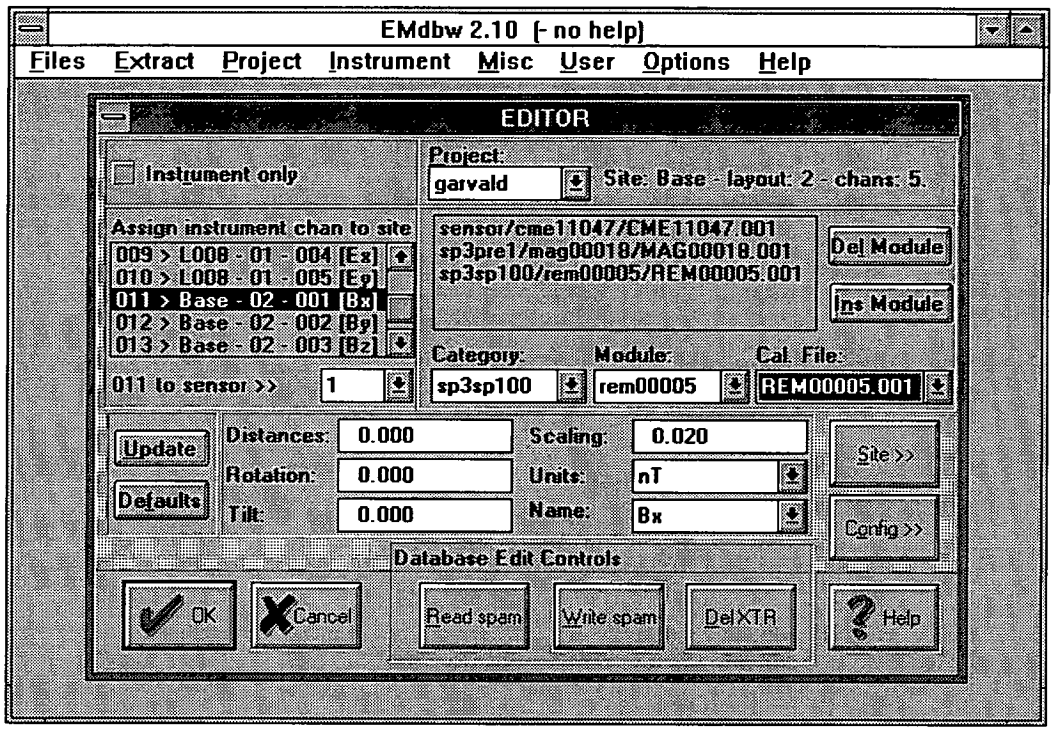

Figure 33: *Screen shot of the database front-end program* `EMdbw`. *The database-Editor is used to assign sites to instruments, to add or remove hardware modules, to enter the telluric line lengths, sensor rotations, and scaling factors. The Site- and Config- buttons open dialogs to create or modify site and instrument information, respectively.*

over several files in different directories, all the information associated with a particular data file can be retrieved as one database extract file. A database extract file in connection with the according data file completely defines a data set and both files can always be reproduced from the database.

Extract files are structured ASCII files which contain information about instruments, sites, data files and the internal structure of EMERALD. However, the degree of completeness of the information supplied depends on the files' originators. `EMdbw` can interpret incomplete extract files and subsequently prompt for missing information. (Re-)processing packages will read extract files as an extension to data files. Therefore, extract files for data processing or for data exchange will be generated differently by `EMdbw`. If extract files contain the complete database information including all single module calibration data, they can be used to move data files between different installations of EMERALD.

High data throughput, fast access time, and easy integration in existing software are the most important criteria for EMERALD data files. Best performances are achieved if the data are stored in the binary presentation of the computer where they are generated. EMERALD-type data files consist of three principal components:

- The general header contains information about the general file structure, such as word length or number of data items per record.

- The event header contains information that is specific for a subsequent block of data. It provides information such as an event's start and end times or the number of records stored for that event.

- The data section contains data in the form of rows and columns of data items. Any integer, real, complex or constant character string matrix of data can be stored (e.g. time series, fourier spectra, cross spectra, etc.).

Each EMERALD data file consists of fixed length records. The record length is calculated as the word length in bytes times the number of data items per column (e.g. the number of channels). Different data files can have different record lengths, but all data in one file are of the same type and word length. Each data file contains one general header, but one or many event headers. General header and event header can extend over one or several records; they are always written as ASCII strings. Event headers are succeded by data sections.

Subroutines to integrate EMERALD data files and extract files in existing data processing procedures have been developed in FORTRAN and C. Both file types are extensively used in my data processing package (see chapter 6.3). Data files are used to store time series, calibration data, Fourier coefficients and single event cross- and auto spectra.

6.3 Overview: data processing software

Figure 34 overviews the EMERALD data processing programs which I have developed in this context. The programs are written in FORTRAN and C; the graphics are based on GKS[31] standard. The package consists of three parts: database application, data processing routines and utility programs. While the database front-end `EMdbw` has already been discussed, it will be useful to introduce briefly the remaining programs:

- **EMTD** is the time domain data processing module. It reads raw data time series information (.RAW) together with the database extract files (.XTR) in order to correct static gains and telluric line lengths. The time series are partitioned into fixed length events suitable for the FFT. It is planned to include additional time domain filtering in the future (e.g. delay-line notch filter).

- **EMFD** reads in the scaled time domain data (.TD) and creates single event cross- and autospectra (.SP). The evaluation frequencies are specified in a frequency-layout file (.FRQ). The instrument response functions are corrected (.CAL) and optionally, raw-frequency spectra can be written to a file (.FD).

[31] Graphics Kernel System.

- **EMSEPP** defines what is to be computed from the single event spectra: e.g. remote reference/single site, impedance tensor/vertical magnetic fields, impedance or admittance, etc. It is furthermore used to combine the results from separate runs for a joint stacking.

- **EMROB** is based on Andreas Junge's robust stacking procedure (see chapter 3). Results are stacked cross- and autospectra and Earth response function estimates.

- **EMPROG** is used to evaluate the final results. Various parameters can be plotted frequency- or location-dependent, including: apparent resistiviy and phases, induction vectors, Bahr's tensor decomposition, Schmucker's $\rho^* - z^*$, etc.

- **EMFRQ** is used to generate a suitable frequency layout. It is usually desired to compute response function estimates on an equi-distant distribution on a logarithmic scale.

- **EM2EDI:** to convert EMERALD stacked spectra files into Geotools *EDI*-format.

- **EMSYN** can generate synthetic time series to test and calibrate the data processing routines. The synthetic time series can be contaminated with various degrees of artificial noise.

database:

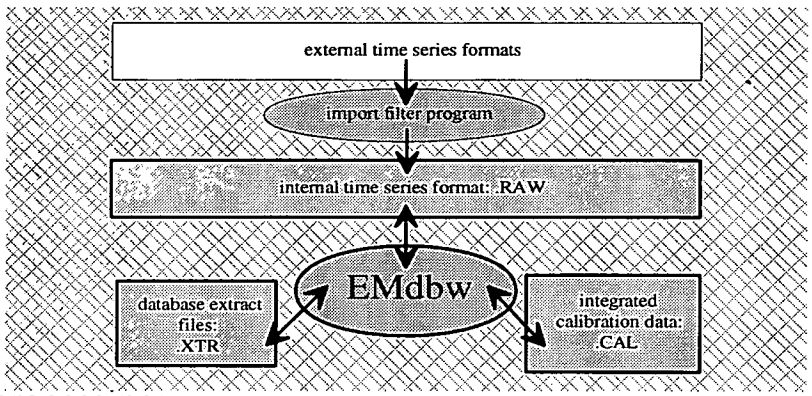

data processing:

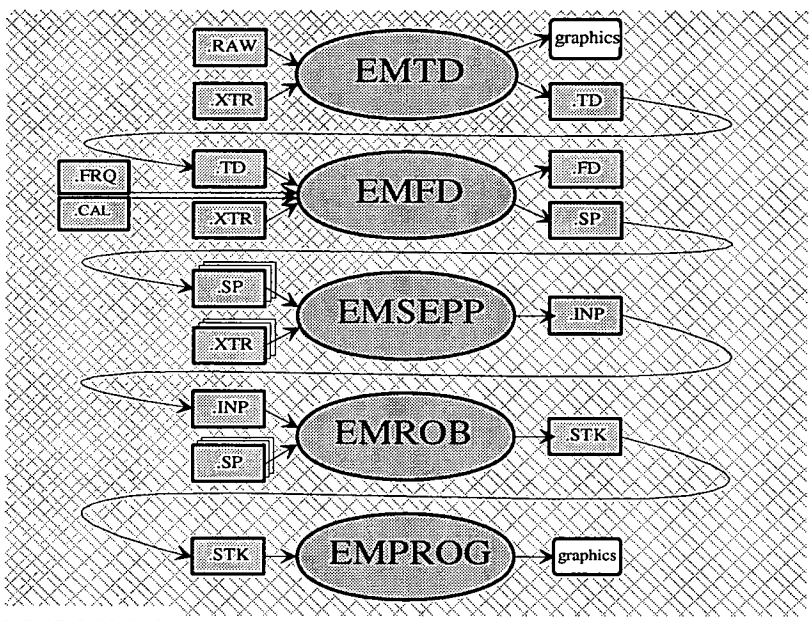

utility programs:

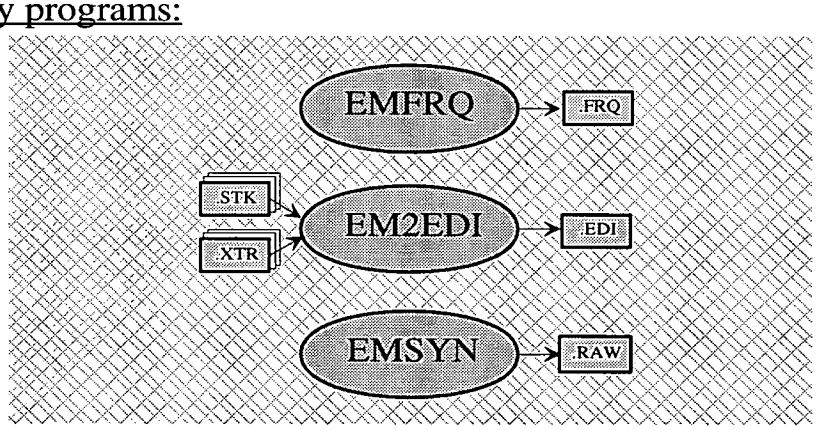

Figure 34: *Schematic of the off-line data processing software.*

7 A second investigation of the Southern Upland Fault using S.P.A.M. MkIII

The MVM mapping experiment at Middleton in chapter 4 revealed a strong vertical magnetic field anomaly. We concluded that the anomaly is associated with the contact of conductive Carboniferous sediments to resistive Ordovician meta-sediments in the vicinity of the Southern Upland Fault. However, the data quality was reduced by noise from electric fences, and a gas pipeline running on top of the assumed fault line made an interpretation of the results difficult.

It was therefore desirable to test the area again, and this chapter is about a second field experiment to cross the Southern Upland Fault – more accurately, the Lammermuir Fault. Clearly, we hoped for a site with less noise and intended to make best use of the new S.P.A.M. MkIII with its multi-channel data acquisition facilites (chapter 5).

Geologically, it was particularly interesting to find out if a vertical magnetic field anomaly could again be associated with the fault and/or the conductive boundary. Furthermore, we wanted to investigate if anomalous fields were more likely to be caused by a shallow conductivity contrast or if deeper structural features would be involved.

7.1 Site location, geological background and instrument configuration

Figure 35 shows the outline geological map of the Southern Uplands [Floyd, 1994] and the locations of the two field experiments near the villages of Middleton and Garvald. The new profile crosses the Lammermuir Fault (LF) $35km$ southeast of Edinburgh. The figure also shows a series of southwest/northeast running, approximately parallel fault lines which separate the Midland Valley (MV) from the Southern Uplands (SU); this is indicated in the detail in the upper left corner of figure 35. The Southern Upland Fault differs from the other faults in that it delineates a distinct and widely recognized terrain boundary. Floyd stresses furthermore, that in its original definition, the Southern Upland Fault is restricted to the central portion of the line, approximately from Straiton (southwest) to Leadburn (northeast).

At its northeastern end, the Lammermuir Fault is often labelled as the eastern segment of the Southern Upland Fault, while there have been alternative suggestions that the Southern Upland Fault continues on towards the northeast beyond Leadburn and is represented by the Crossgatehall Fault (CGF) at the surface. In its effect of separating Upper and Lower Paleozoic strata along fractures with a downthrow towards the northwest, the Lammermuir Fault has certainly some of the character of the Southern Uplands Fault. A northerly downthrow across the Lammermuir Fault of up to $300m$ is suggested by Davies et al. [1986], though Walton [1983] reports that the vertical throw on the fault near Dunbar appears to be small, with slickensides indicating predominantly horizontal movement. As mentioned earlier, gravity data suggest that the throw varies along the fault from $200 - 2000m$ [Lagios, 1979].

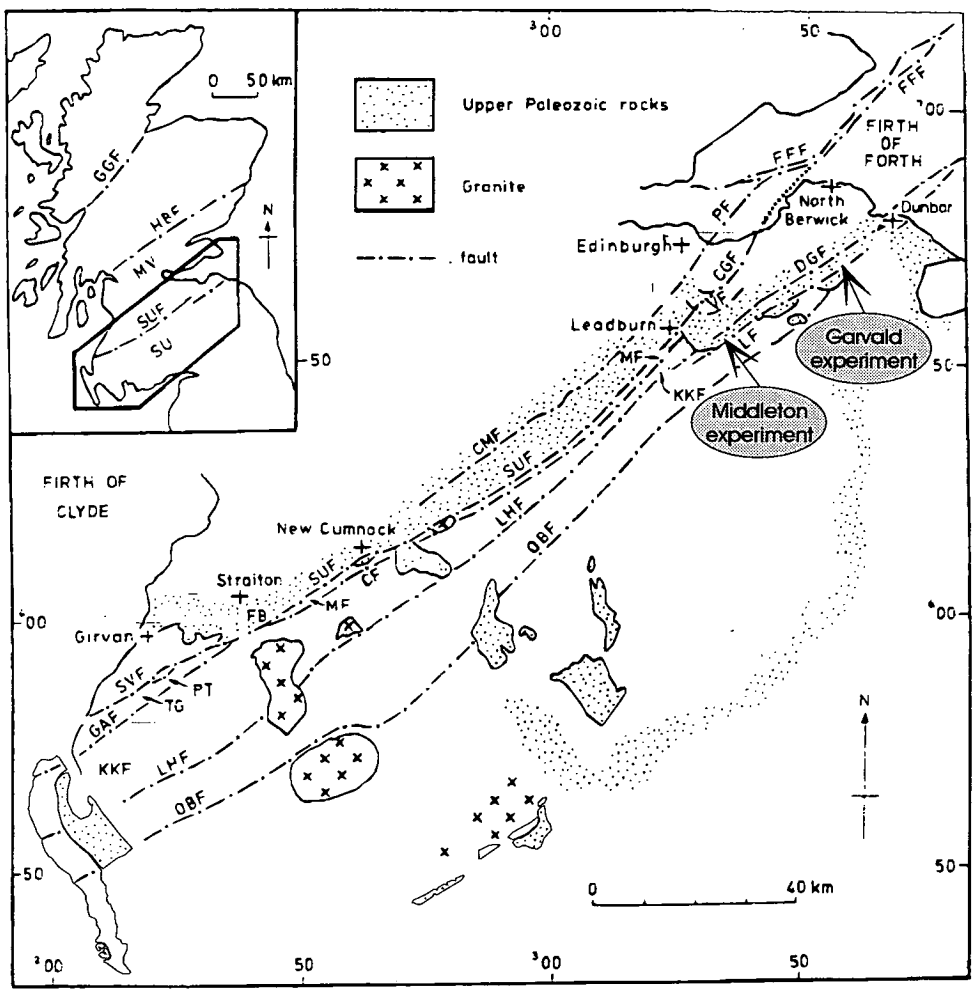

Figure 35: *Outline geological map of the Southern Uplands [Floyd, 1994]. Abbreviations for the fault lines are: CF, Carcow Fault; CGF, Crossgatehall Fault; CMF, Carmichael Fault; DGF, Dunbar-Gifford Fault; FFF Firth of Forth Fault; GAF, Glen App Fault; GGF, Great Glen Fault; HBF, Highland Boundary Fault; LF, Lammermuir Fault; LHF, Leadhills Fault; OBF, Orlock Bridge Fault; PF, Pentland Fault; PT, Pyet Thrust; SUF, Southern Upland Fault; SVF, Stinchar Valley Fault; VF, Vogrie Fault. Geological units/localities: FB, Fore Burn Igneous Complex; KKF, Kirkcolm Formation; MF, Marchburn Formation; MV, Midland Valley; SU Southern Uplands; TG, Tappins Group.*

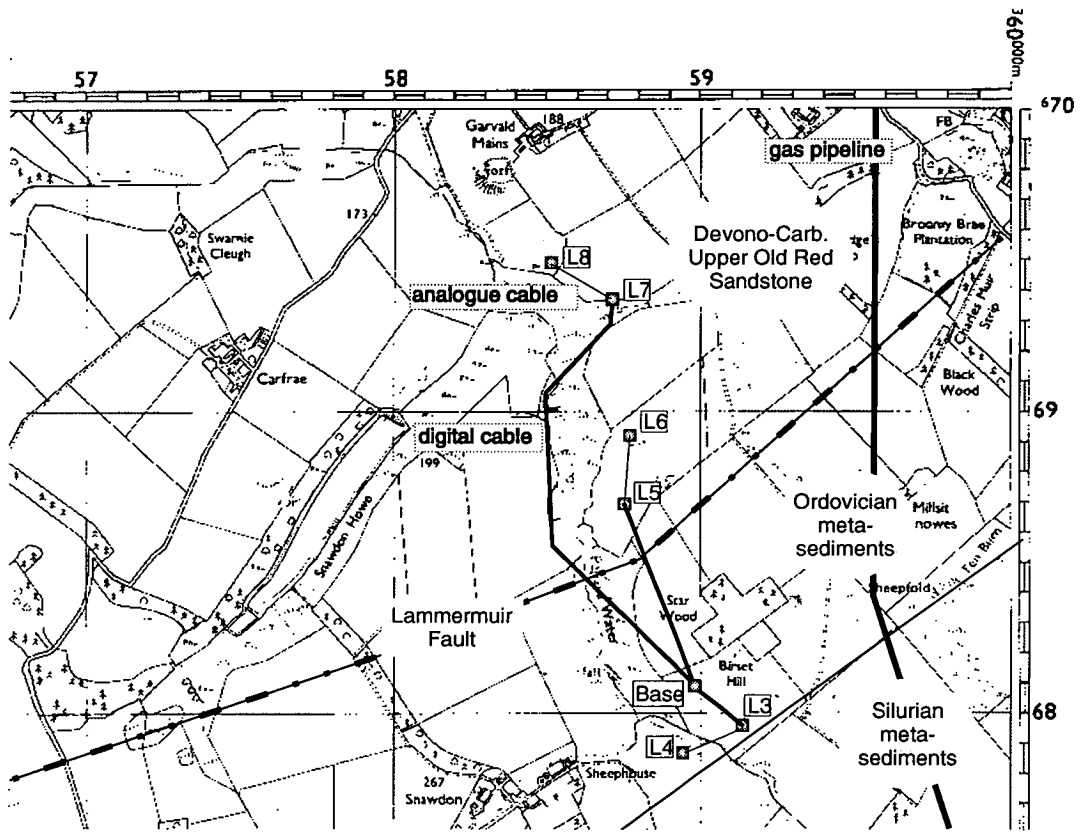

Figure 36: *Site map of the Garvald field project. Always three sites are measured simultaneously. The* BASE*-site remains fixed, the other sites are recorded in pairs. The grid spacing is* $1km$.

In contrast to the site near Middleton where the fault separates directly Carboniferous sediments from Ordovician meta-sediments, the new location near Garvald shows an enclosure of the Ordovician meta-sediments sandwiched between Silurian meta-sediments and the Devono-Carboniferous Upper Old Red Sandstone. Silurian and Ordovician meta-sediments consist mainly of graywacke and shale. Figure 36 shows a detailed site map with the line of the Lammermuir Fault and the contact of the Old Red Sandstone as suggested by the geological map [BGS, 1983a]. Figure 36 shows also the locations of the MT-observations; the exact site coordinates are given in appendix A.2.

In total, we measured electromagnetic data at 7 sites with standard 5-component MT configurations. However, using the new facilities of S.P.A.M. MkIII, three sites were always recorded simultaneously. During the survey, the location of the BASE-site remained fixed while the other sites were recorded in pairs, at varying distances

from the reference point.

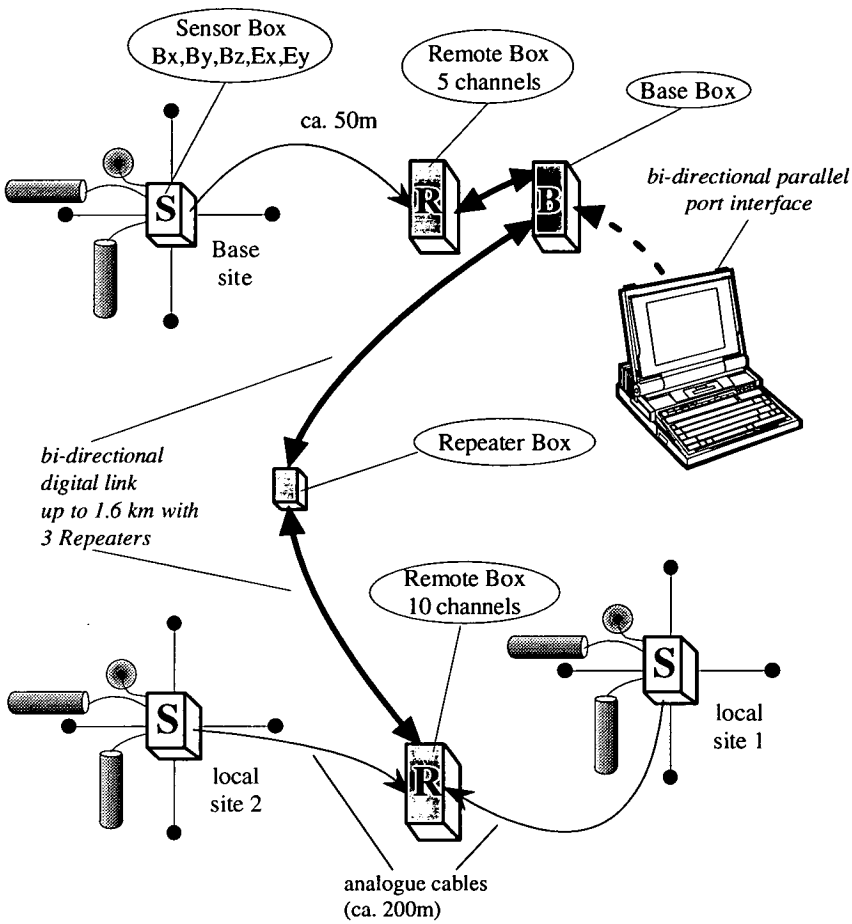

Figure 37: *The configuration of S.P.A.M. MkIII for the experiment near Garvald. Three sites are always recorded synchronously.*

The S.P.A.M. MkIII configuration is shown in figure 37. The entire network consists of a *Base*, two *Remotes* and three *Sensor*-boxes. The BASE-site comprises a 5-channel *Remote* and a 5-channel *Sensor*- box. The *Sensor*-box collects analogue signals from vertical and two horizontal induction coil magnetometers and east/west- and north/south- orientated electrodes lines. Connected to the *Base*-box is a second *Remote* with 10 channels and two *Sensor*-boxes to record the local sites. The distance between local sites is limited to ca. $400m$, since the signals to the *Remotes* are in analogue form. *Base* and *Remote*, however, use digital data communication and hence, longer distances can be achieved, when several $400m$ cable segments are joined with *Repeater*-boxes.

It should be mentioned, that we had considerable difficulties in finishing the new instrument in time for this experiment. The main reason for the delay was problems with the interface between the *Base* and a laptop computer. The company that had promised to provide us with a solution based on the SCSI bus failed to do so, and

rather unexpectedly, we had to find an alternative solution. The process of designing and making the parallel port interface (see chapter 5) was very time consuming, and during that period, the development of other S.P.A.M. MkIII components was put on hold. In the end, time and money for this project were running out fast. The result was that when we went to do the experiment, S.P.A.M. MkIII had never been tested under field conditions, and only parts of the processing software were implemented.

Quite naturally, we had some problems with the new hardware at the beginning, and eventually, the number of sites we succeeded in acquiring was less than we had hoped for. Nevertheless, we successfully installed a 15-channel S.P.A.M. MkIII network, with base and remote sites separated by up to $1.6km$, and in the 10 days of effective recording time we gathered more than 1 *Gigabyte* of time series data.

7.2 Results and data evaluation

7.2.1 Time series

In the short period mode, S.P.A.M. MkIII records all time series data in one broad frequency band with an effective sampling rate of $512\,Hz$. The overall frequency range is limited by the induction coil magnetometers to the band between $100\,Hz$ and $100\,s$. For the data processing, the continuous stream of high frequency data is digitally decimated into separate time series corresponding to narrower frequency bands. A typical frequency band structure that we used for the experiment is shown in table 4.

	low pass	high pass	sampling rate	duration (256 samples)
Band 0:	128 Hz	16 Hz	512 Hz	0.5 s
Band 1:	16 Hz	4 Hz	64 Hz	4 s
Band 2:	4 Hz	1 Hz	16 Hz	16 s
Band 3:	1 Hz	0.25 Hz	4 Hz	64 s
Band 4:	4 s	16 s	1 s	256 s $(4min\,16s)$
Band 5:	16 s	128 s	4 s	1024 s $(17min\,04s)$

Table 4: *A typical S.P.A.M. MkIII frequency band structure for the Garvald experiment which corresponds to the time series examples shown in figures 38 - 40.*

The next 3 figures give examples of time series for all frequency bands, selected from a combination of sites BASE, L7 and L8, the local sites with the greatest distance to the BASE. It should be noted that the time series examples of all frequency bands originate from the same time interval, between 18:30 and 18:45 on 28 July 1994. For the highest frequency band no data were recorded at that time, though.

For frequency band 0 (highest frequencies) in figure 38, the time series are dominated by strong sinusoidal $100\,Hz$ osciallations. However, in the presence of natural

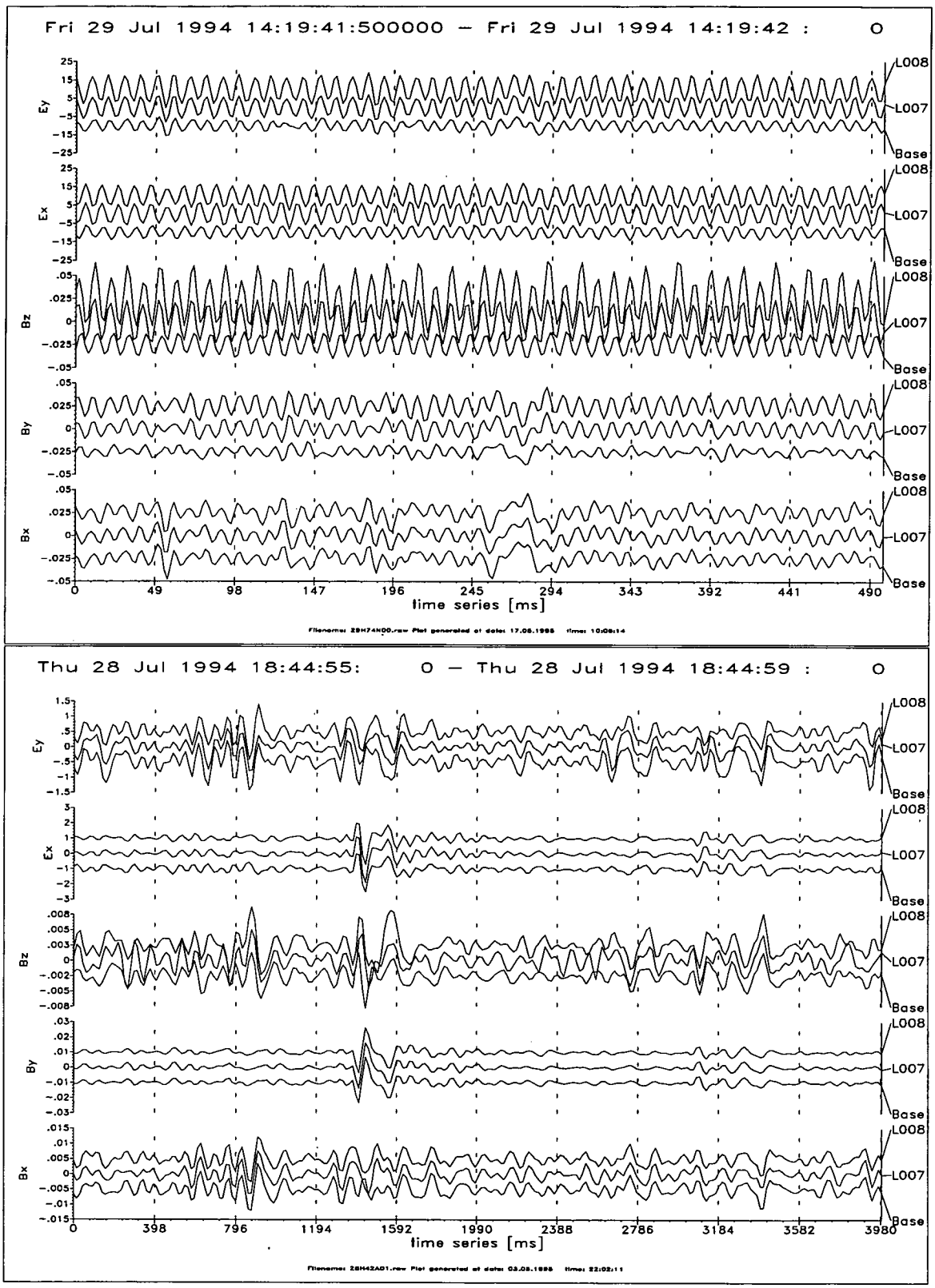

Figure 38: *Time series of bands 0 [128 Hz-16 Hz] and 1 [16 Hz-4 Hz]. The telluric fields are scaled to [mV/km], the magnetic fields to [nT]. The distance between* BASE *and the local sites (*L7 *and* L8*) is* 1.6 *kilometers.*

signal activity the expected correlations between channels B_x , E_y and B_y , E_x can be recognized (e.g. 250ms-300ms). As mentioned earlier, the occurence of 100 Hz-signals is often connected with electric fences. The only obvious electric fence in the area was surrounding sites L7 and L8, but it was battery powered and could be switched off during day time operation. However, the whole surrounding area is farm land, and many items of modern farm equipment are possible sources of electromagnetic noise; the mains power supply ends at the main farm building (Garvald Mains in figure 36). We also identified another gas pipeline which runs approximately north/south, parallel to the profile. The pipeline is between 500m to 1km away from the sites and apparently did not affect the results.

The time series in the bottom half of figure 38 show data of frequency band 1, the first for which all data were stored uninterruptedly. The figure shows all channels very consistently correlated, even though the signal amplitudes are relatively small. The data processing of these time series reveals earth response functions of excellent quality. In fact, any 30 - 50 of the thousands of time series segments recorded are sufficient to generate the same results.

The situation changes, when we look at the other frequency bands. The time series shown in figure 39 are recorded in frequency bands 2 and 3, respectively. The horizontal magnetic fields of band 2 are still very well correlated between the three sites, but both telluric and the vertical magnetic field channels show an increase of uncorrelated signals. The trend continues for band 3, with deteriorating telluric channels. However, only the vertical magnetic field from the BASE-site appears to be noisy, while the B_z-channels of both local sites continue to show good correlation with the horizontal magnetic fields, particularly with B_x. The time series data of the telluric fields of band 4 at the top of figure 40 have almost random appearances, especially when compared between sites. Only the long period data of band 5 on the bottom of figure 40 show an increase in correlated telluric signals, at least for the local sites L7 and L8.

All time series data are perfectly synchronized at the highest frequencies in figure 38. Since all frequency bands are generated from the high frequency data by decimation, always using the same numerical filter, instrumentation problems are unlikely to be the cause for poorly correlated signals. The phenomenon is probably best explained by lack of natural signal activity in combination with high background noise levels.

Figure 41 shows amplitude spectra of the stacked results of site L8. The magnetic field spectra are roughly at a constant level ($< 10^{-3}$) in the frequency range 100 Hz to 1 Hz, but they begin to rise sharply towards longer periods (by a decade in amplitude per decade in frequency). The corresponding vertical magnetic field spectra, which are not shown in the figure, have very similar signal levels over the whole frequency range. The electric fields, on the other hand, show decreasing signal strengths between 100 Hz and 1 Hz. The signal amplitudes stay then at low levels until they eventually begin to rise at 0.1 Hz.

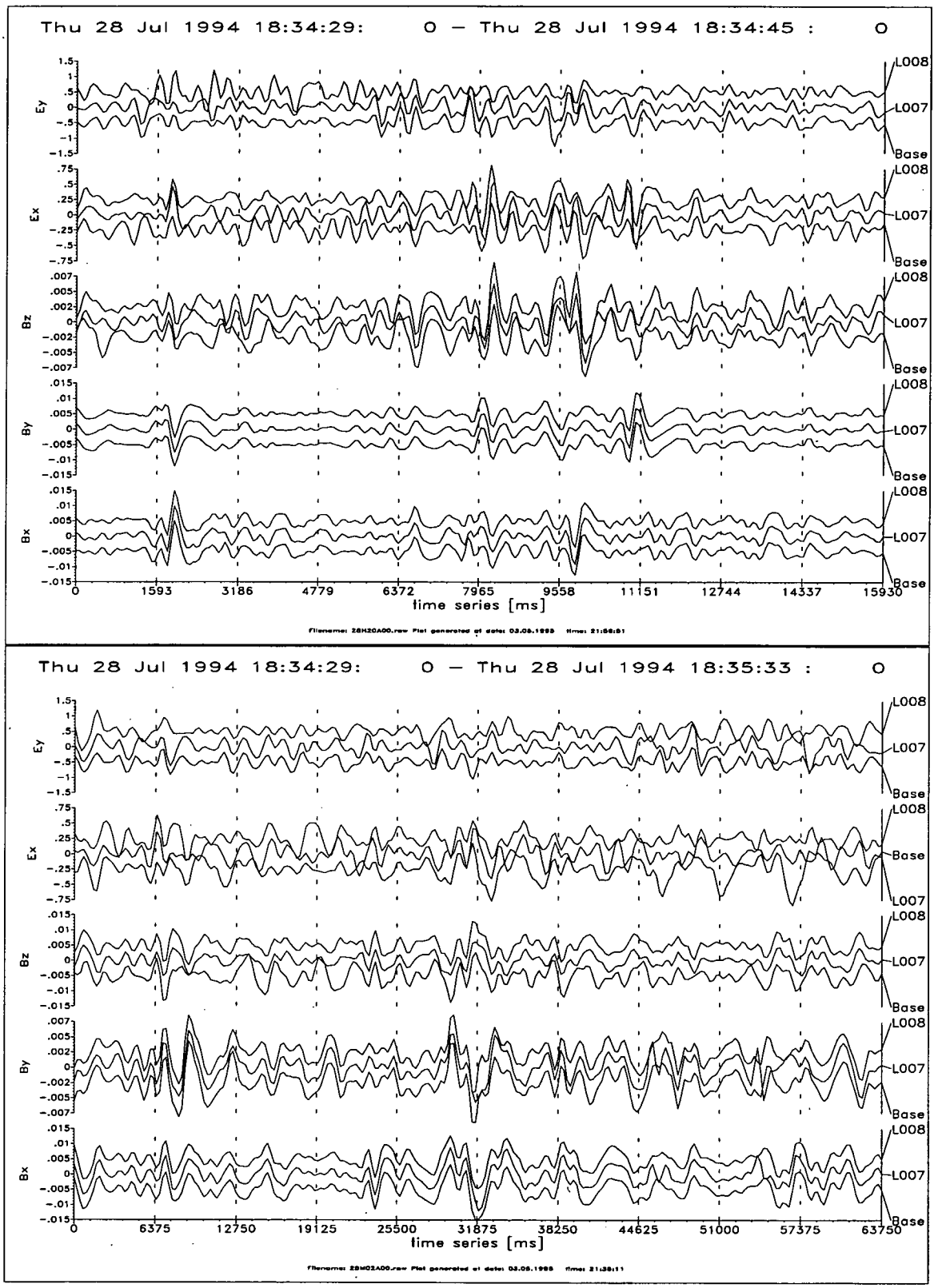

Figure 39: *Time series of bands 2 [4 Hz-1 Hz] and 3 [1 Hz-0.25 Hz].*

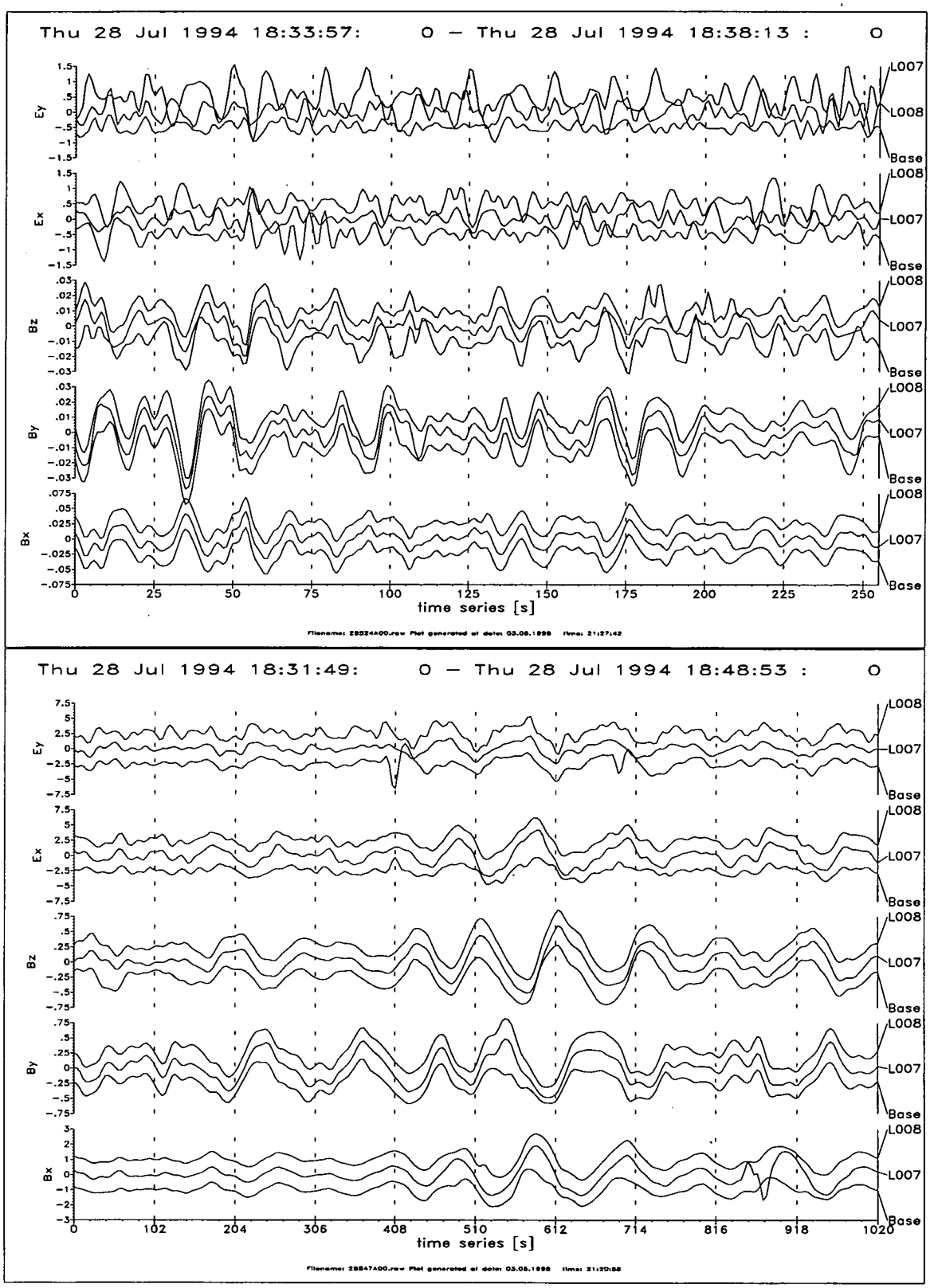

Figure 40: *Time series of bands 4 [4 s - 16 s] and 5 [16 s - 128 s].*

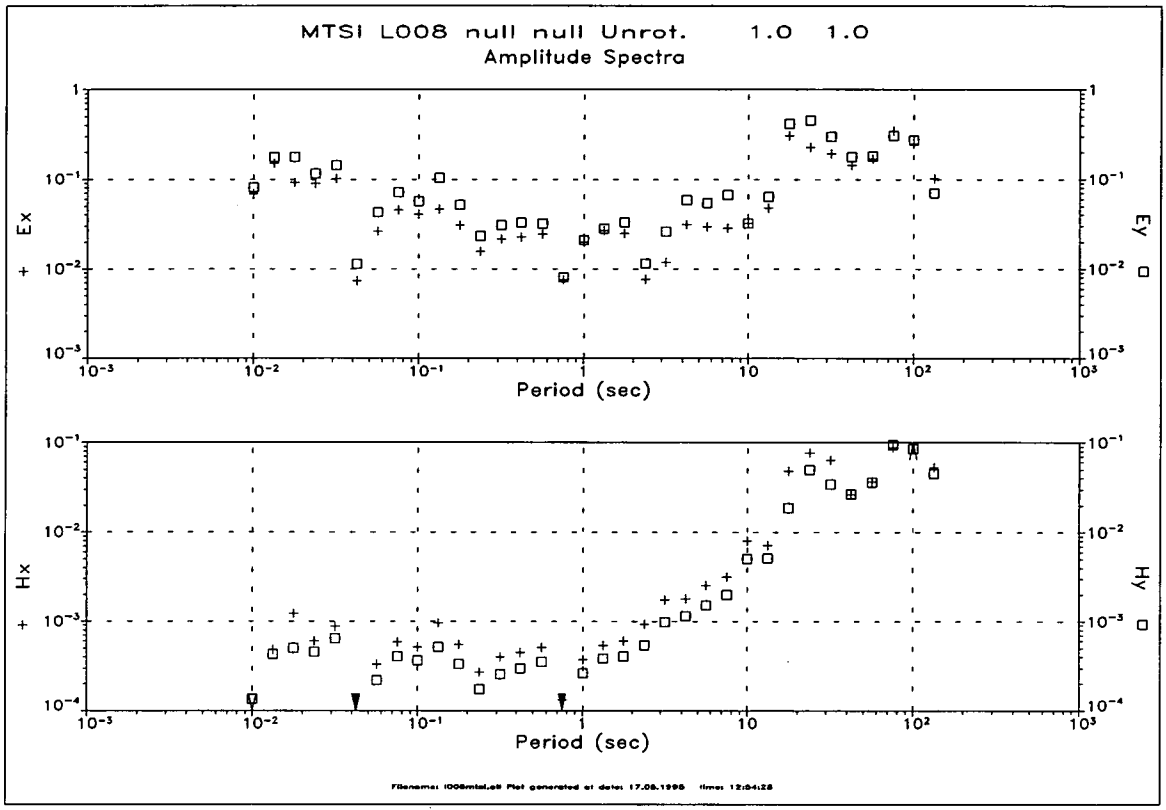

Figure 41: *Amplitude spectra of the stacked results of site* L008. *The spectra are calculated as:* $p = \frac{\sqrt{\langle XX \rangle}}{\mu}$, *where* μ *is the number of degrees of freedom.*

7.2.2 Response functions

As expected, noise affects the results. In particular, the quality of the apparent resistivity and phase curves is disappointing. An example is shown in the top half of figure 42. The period range of the curves is extended with data recorded by Andreas Junge. Within the framework of an LMT survey he undertook in the south of Scotland [Junge, 1995], he generously placed one of his sites (STAR) right next to my BASE-site. The AMT and LMT data overlap at $30\,s$. The figure reveals that seemingly, the apparent resistivity curves are slightly shifted between the two data sets. The gap is not very well defined though, as the AMT data are extremely noisy towards the longer periods (from about $1\,s$). Judging from the outliers in the ρ^* z^*- curves and low bivariate coherencies (bottom half of figure 42), the quality of the LMT data at the short period end ($30\,s$-$500\,s$) is also doubtful. The data were gathered using different types of instruments and data processing procedures, but the shifts in the apparent resistivity curves are most likely to be caused by high noise levels. Over the whole period range – and over the instrumentation boundaries – the coherencies vary systematically with frequency and the rotation angles and skews show also consistent variations. Low coherencies indicate that the data quality is reduced over a wide frequency range between $5\,Hz$ and $500\,s$.

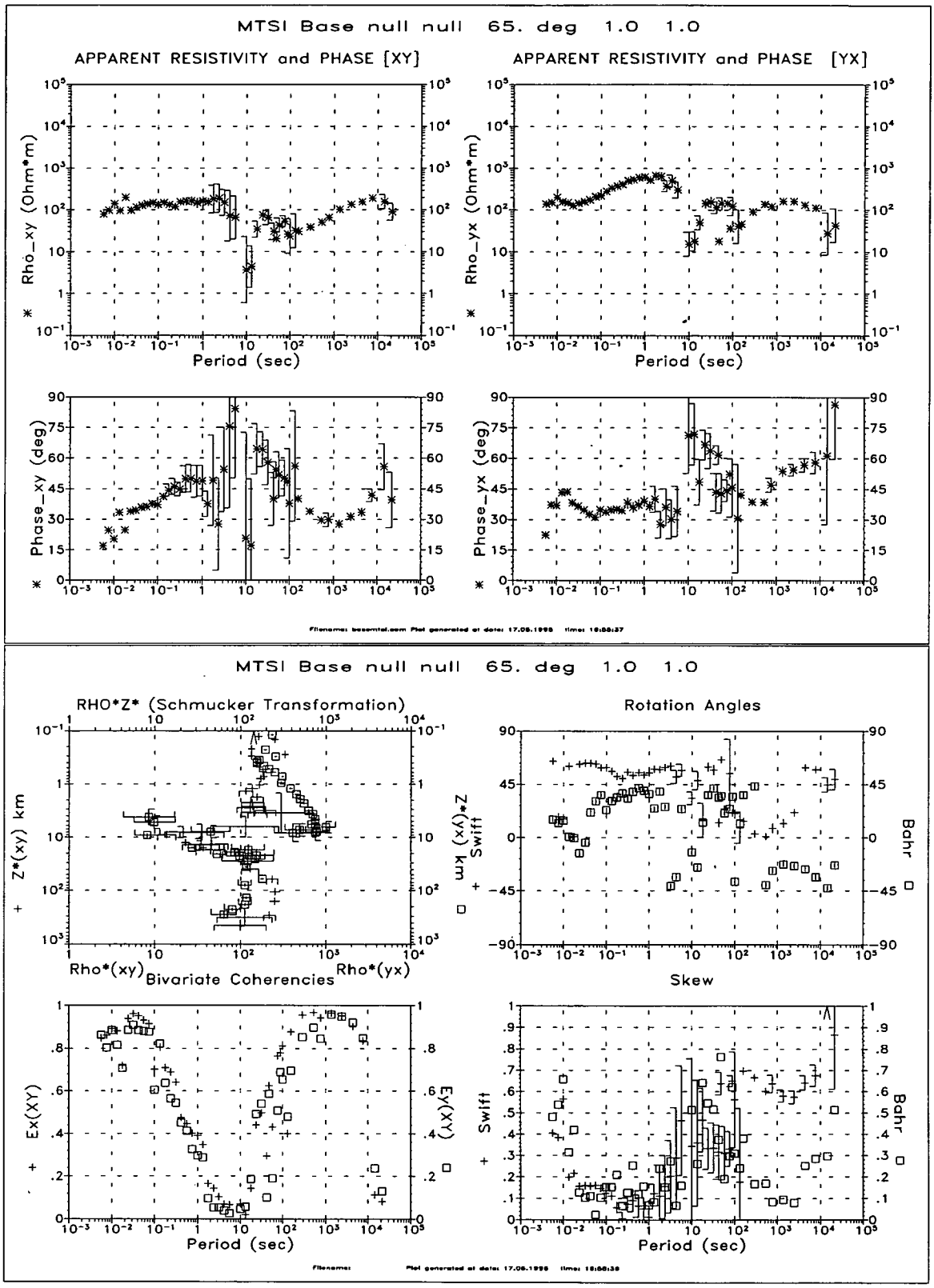

Figure 42: *Combined AMT and LMT apparent resistivity and phase curves at the* BASE*-site. The curves are rotated N65E, which is the direction indicated by Bahr's method for the long periods.*

For the high frequencies ($100\,Hz$ - $1\,Hz$), both Bahr's and Swift's rotation angles vary around 45°[32]. The intermediate period range is dominated by noise, but towards the longest periods (>$750\,s$), we observe fairly stable Bahr angles of ca. $-25°$, while the Swift angles vary greatly. For the same period range, Swift's skews rise from values below 0.2 to 0.6, thereby indicating a strong three dimensional effect. Bahr's rotation-dependent skews, on the other hand, show values significantly lower (0.2 - 0.3). This indicates that the impedances at the long periods seem to represent a regional two-dimensional structure. The impedance values are distorted by local 3D features, though. A more detailed examination of these aspects is beyond the realms of this thesis, but they are discussed extensively by Junge [1995].

Looking at the vertical magnetic field response functions in figure 43 we find an almost perfect match between S.P.A.M. MkIII and the LMT data. The diagrams show a combination of the BASE-site with L3, which are separated by $150m$. The time series plots in the last section have suggested already that the AMT vertical magnetic field component at the BASE was noisy and therefore – and because the vertical magnetic field response functions are not known to be affected by small scale static shift problems – I present the better quality L3-data together with the LMT data.

The quality of the combined data set appears to be excellent over the whole period range. For the AMT data, the coherencies are consistenly close to 1, although they are less homogeneous for the LMT data. This can probably be explained by relatively poor performance of the fluxgate magnetometers at periods less than $300\,s$ and the influence of source field effects towards the longest periods. All in all, however, the smoothness of the response fuctions is very convincing and clearly, they indicate a rather complicated geological situation.

The vertical magnetic field response function curves show maximum anomalous values of approximately -0.7 in the frequency range between $5\,Hz$ and $1\,Hz$ for both, $\mathcal{R}e\{Z_H\}$ and $\mathcal{R}e\{Z_D\}$. Both imaginary parts start with positive values at high frequencies. They reach 0-values at the frequencies where the real parts are maximum and then become negative. The negative anomaly of $\mathcal{R}e\{Z_H\}$ stretches over 5 decades ($10^{-2}\,s$ - $10^{+3}\,s$), while it is much narrower for Z_D. However, the $\mathcal{R}e\{Z_D\}$-values form another negative anomaly of -0.3 at a period of $1000\,s$, suggesting the presence of more than one conductivity contrast. This second minimum is also reflected in the imaginary parts of Z_D. The diagrams of tipper strike and skew[33] in the bottom half of figure 43 give further evidence that the data set shows a three-dimensional situation. The tipper strike angles vary greatly with frequency, indicating that there is no preferred (two-dimensional) strike direction; although in sections, the strike angles are fairly constant.

One of the main interests in the design of this second field experiment was to record synchronous channels in order to enhance the data processing. The top of

[32]by definition, with a ±90° uncertainty.

[33]The tipper strike is calculated in analogy to the Swift angle, in order to find a coordinate system in which Z_D is minimized. Similar to the tensor skew, the tipper skew is an indicator for the dimensionality of the data; it is computed as: $\frac{2[\mathcal{R}e\{Z_H\}\mathcal{I}m\{Z_D\}-\mathcal{I}m\{Z_H\}\mathcal{R}e\{Z_D\}]}{|Z_H|^2+|Z_D|^2}$.

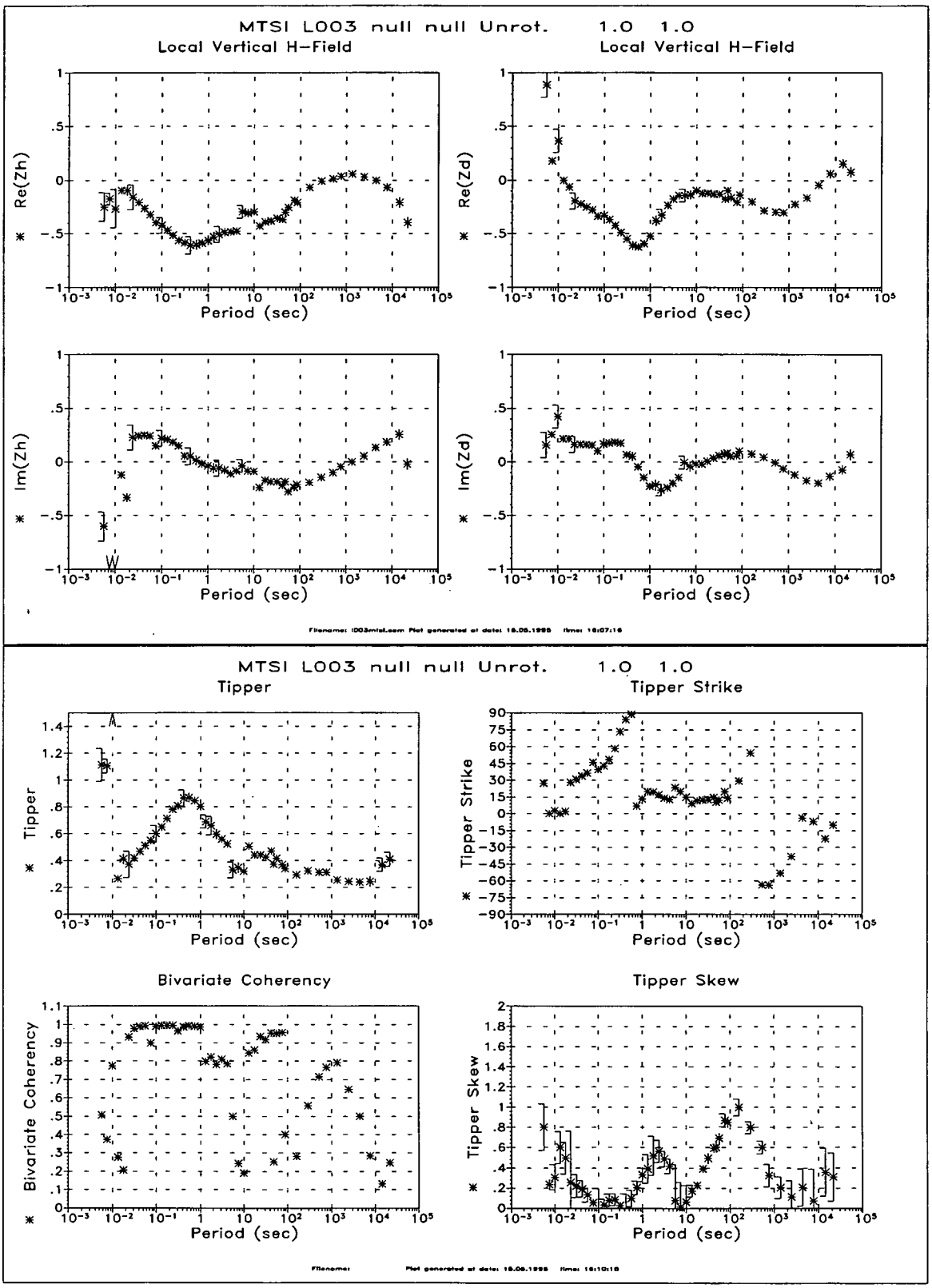

Figure 43: *Combined AMT* (L3) *and LMT* (BASE) *vertical magnetic field response functions.*

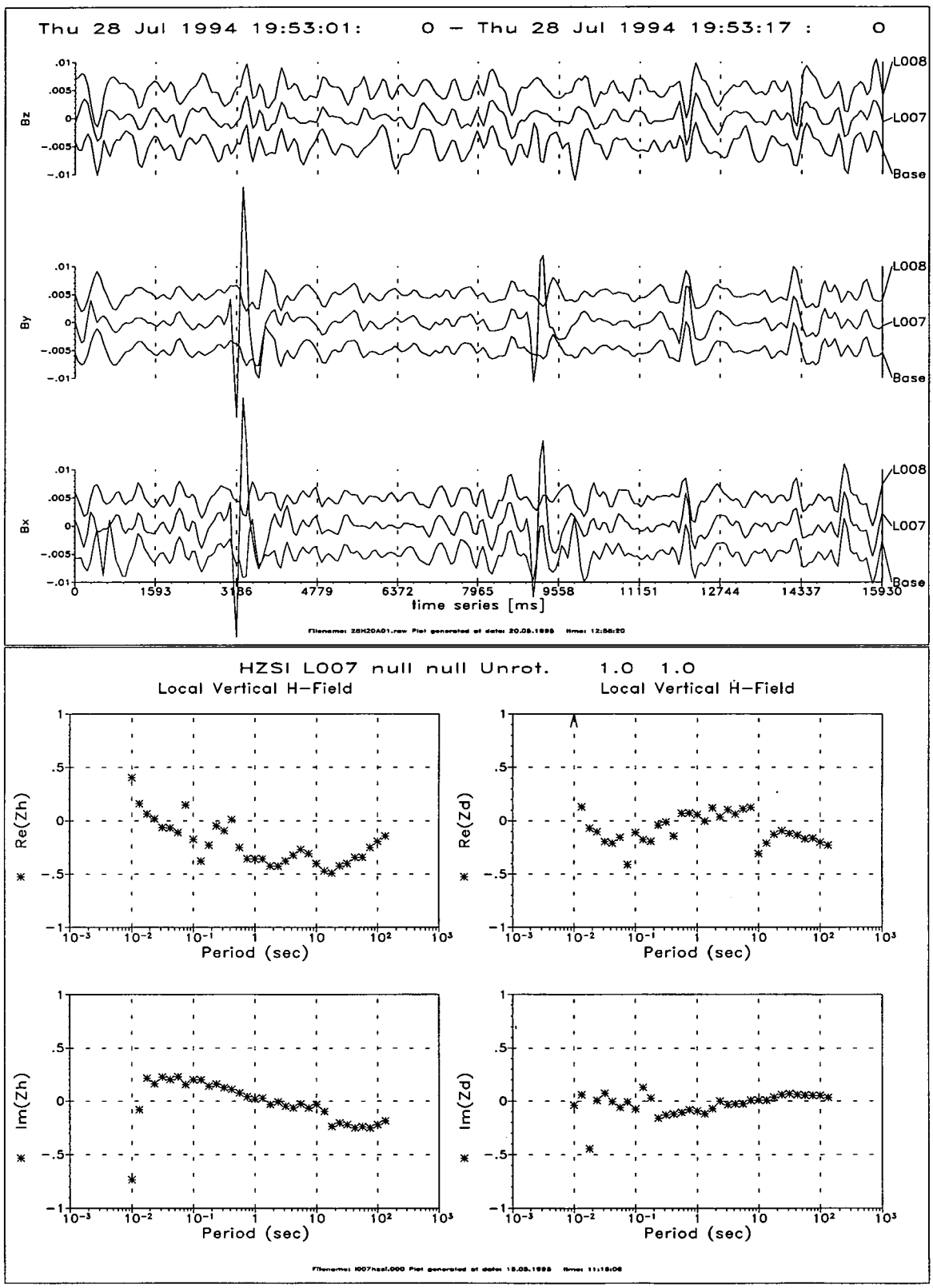

Figure 44: *Top: Time series example (band 2: [4 Hz-1 Hz]) of sites* L7, L8 *and* BASE. *The horizontal magnetic fields of* L7 *are severely distorted. Bottom: The corresponding vertical magnetic field response functions of* L7.

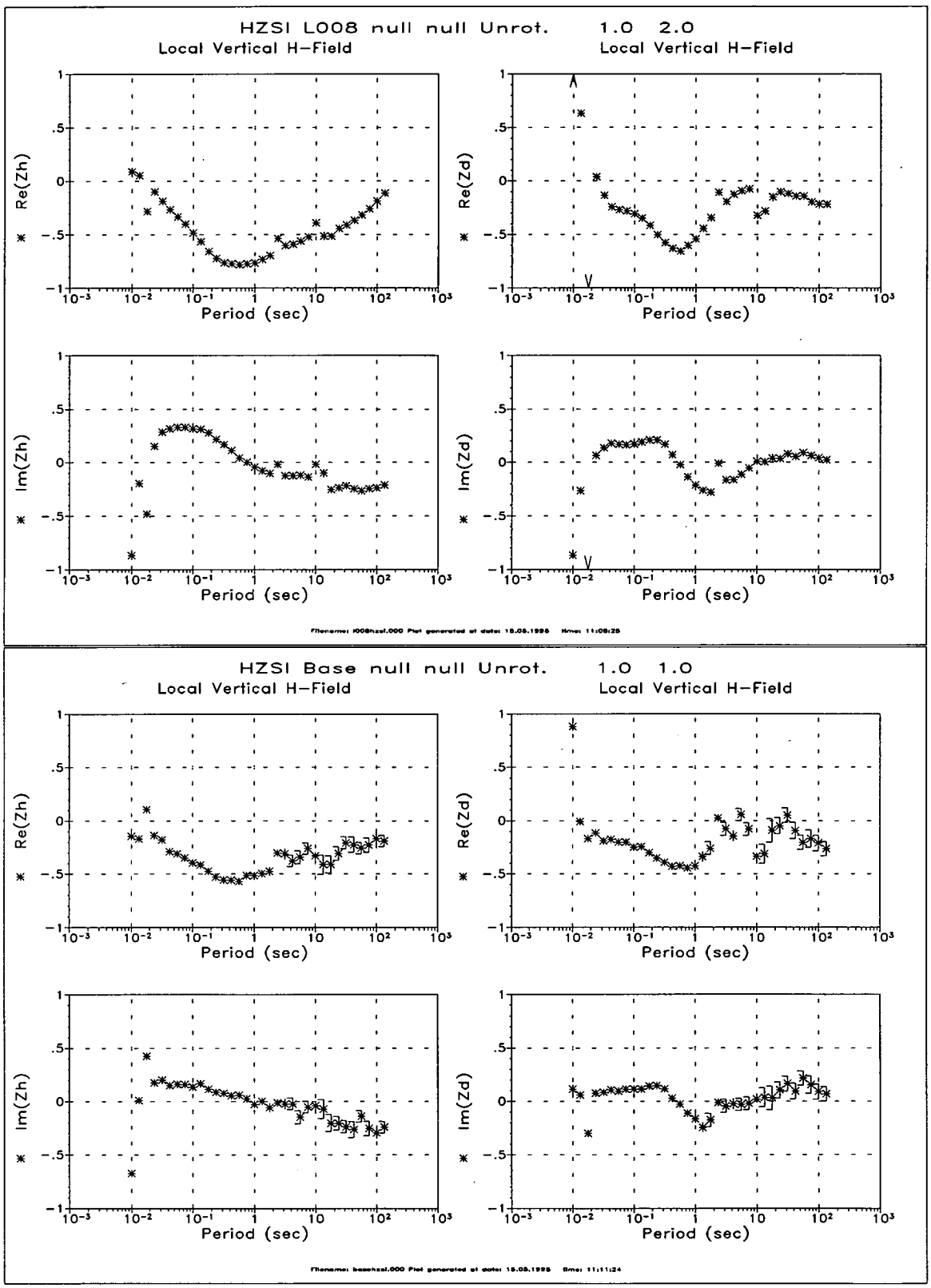

Figure 45: *Top: vertical magnetic field response functions of site* L8. *The data are of excellent quality over the whole frequency range. Bottom: the response functions of the* BASE*-site are noisy towards the long periods.*

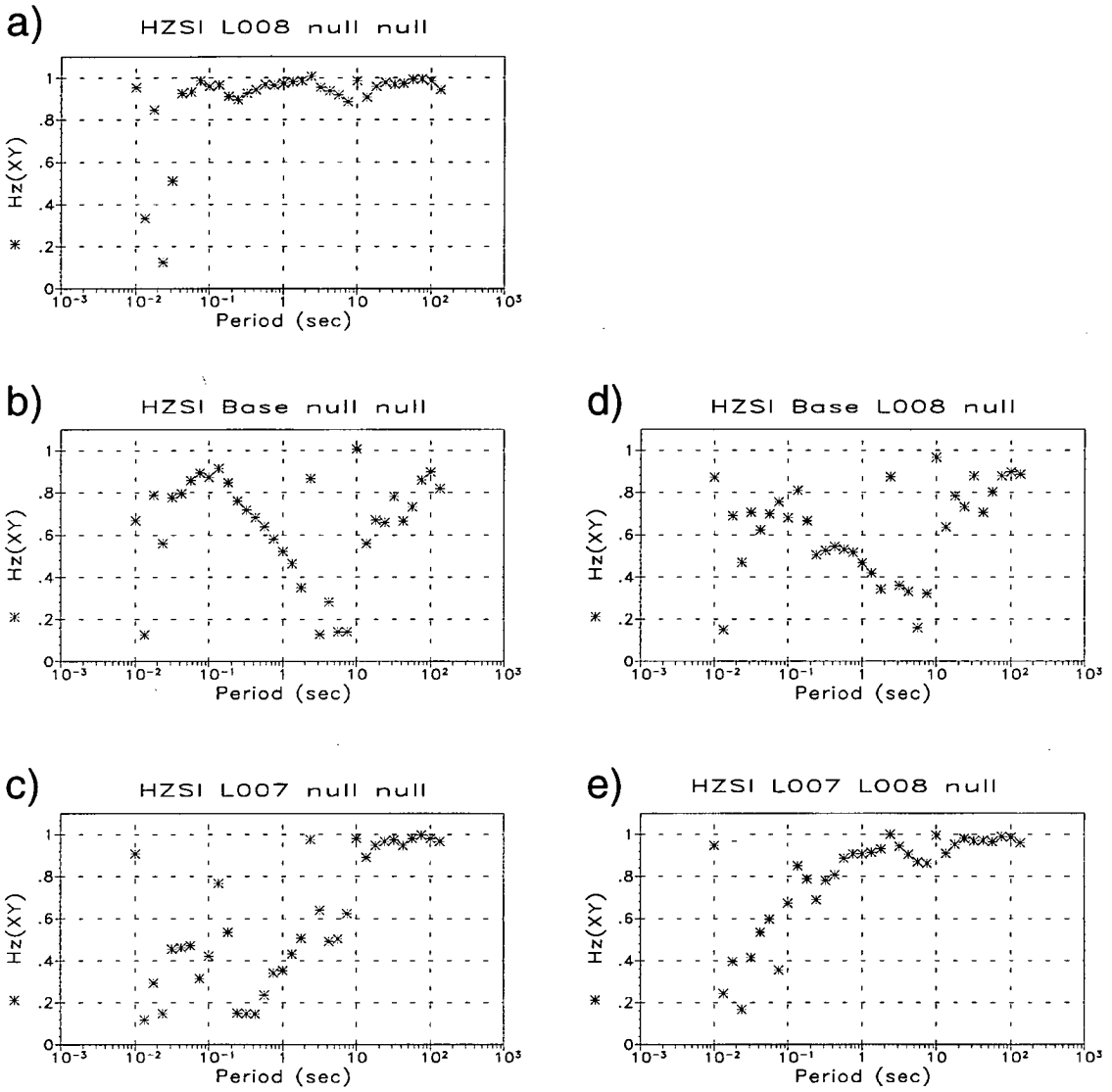

Figure 46: *Comparison of coherencies for single site (a-c) and pseudo remote reference processing (d-e). The use of the horizontal magnetic fields from site* L8 *instead of those from sites* BASE *and* L7 *can improve the coherencies significantly.*

figure 44 shows time series, which again originate from the set of sites BASE, L7 and L8. The examples are frequency band 2 data. They show that site L7 is distorted by impulse-type noise on both horizontal magnetic field channels (e.g. at $3200ms$ and $9500ms$). What causes these spikes is unclear, as they appear at random (but repeatedly) and affect only the horizontal magnetic fields of L7. Neither the BASE-site nor L8 are troubled by spikes, but the BASE appears to be generally noisy (there is an indication of noise at the start of the time series in channel B_x). For site L8, on the other hand, we observe mostly well-correlated signals without any obvious noise interference.

The processing results for these three sites are plotted at the bottom of figure 44 (site L7) and at the top and bottom of figure 45 for sites L8 and BASE, respectively. Obviously, the quality of the vertical magnetic field response funcions of site L8 are by far superior than those of the other sites. This result is expressed more quantitatively in the coherencies on the left side of figure 46. While we observe coherencies close to 1 over the whole frequency range for site L8 (fig. 46a), they are clearly at lower levels for the BASE-site (fig. 46b) and devastating (< 0.5) for site L7 (fig. 46c). It is very interesting that the L7 - response function estimates appear to be biased, when compared with the results from site L8, but the *random* error estimates are clearly ineffective in detecting it.

Figure 47 presents the results of the same sites, using the same data sets, after *pseudo remote reference* processing. For the pseudo remote reference processing the horizontal fields of the local sites (BASE and L7) are simply substituted by those from site L8 as in equation 56. This is different from true remote reference processing, where the reference magnetic fields are used in addition to the local fields to eliminate the effects of noise bias in the horizontal magnetic fields (chapter 3.3, eqn. 40). Obviously, the pseudo remote reference technique relies on the calculation of auto power spectra, and hence, the results will generally be biased in the same way as those of the normal, single site processing. The bias, however, will be small if the amount of noise in the source fields is small.

The method can improve the data significantly. This can be concluded from the quality of the geomagnetic response functions in figure 47 and from the improved coherencies on the right hand side of figure 46. The improvement is more distictive for site L7, for which all four vertical magnetic field response function appear reshaped. From $10\,Hz$ on, most coherencies are better than > 0.8 after reprocessing. Comparison of figures 46c and 46e confirms the achieved improvement. Reduced effects at the BASE-site are quite understandable, though. There, the problems are mainly caused by a noisy vertical magnetic field component, while the source fields are damaged at L7.

Pseudo remote reference processing can also improve the magnetotelluric data, at least in the case of site L7. The MT results for single site processing are shown in the top of figure 48, the data after pseudo remote reference processing are plotted in the bottom half. Clearly, the high frequency parts of the apparent resistivity and phase curves are converted from being almost useless into workable looking data sets. This result is also reflected in the corresponding coherency values (not shown),

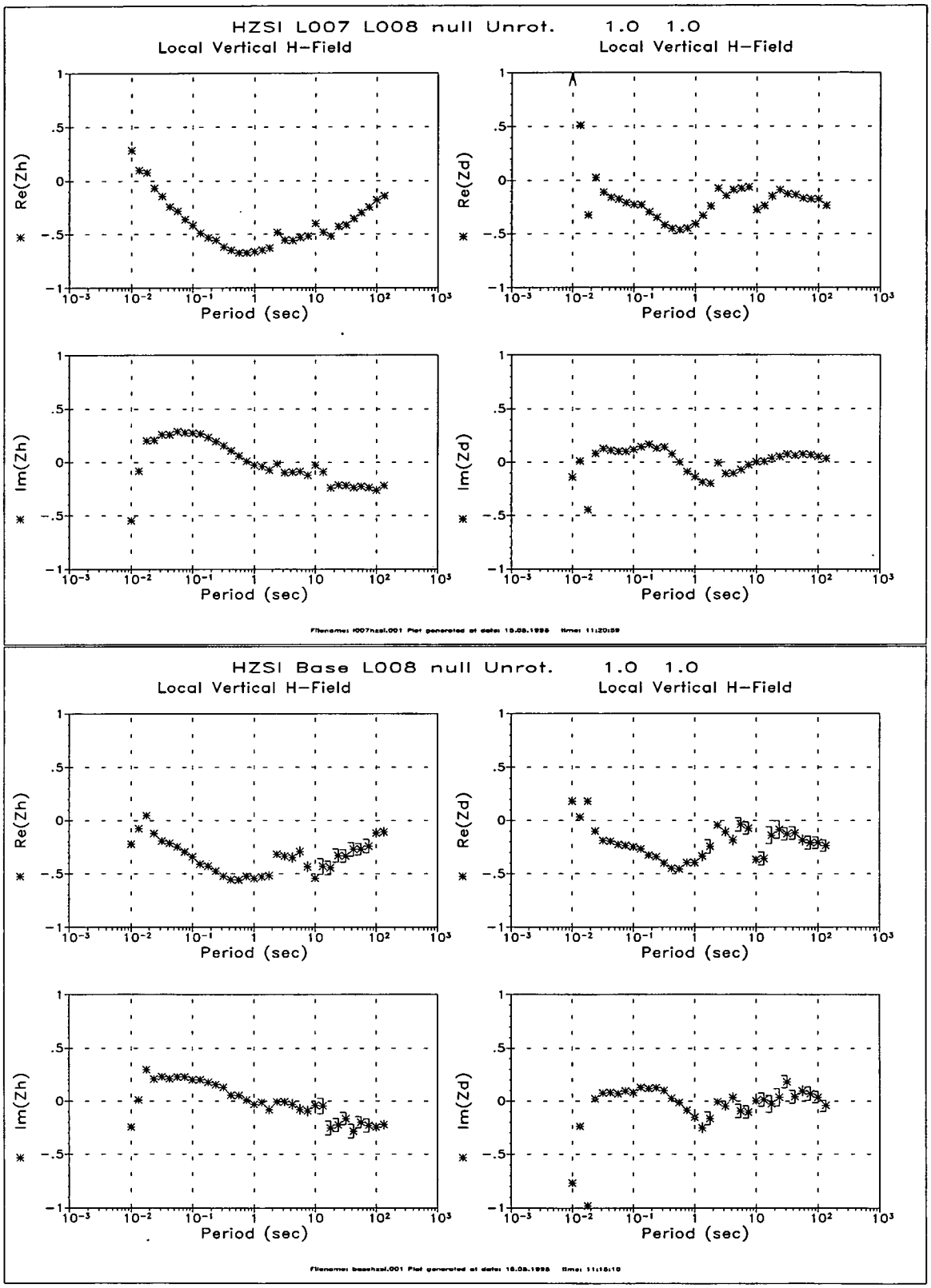

Figure 47: *A simple substitution of the local horizontal magnetic fields (pseudo remote reference processing) can improve the data quality. This is particularly evident at site* L7 *(top), while most of the problems at the* BASE*-site (bottom) are caused by a noisy vertical magnetic field component.*

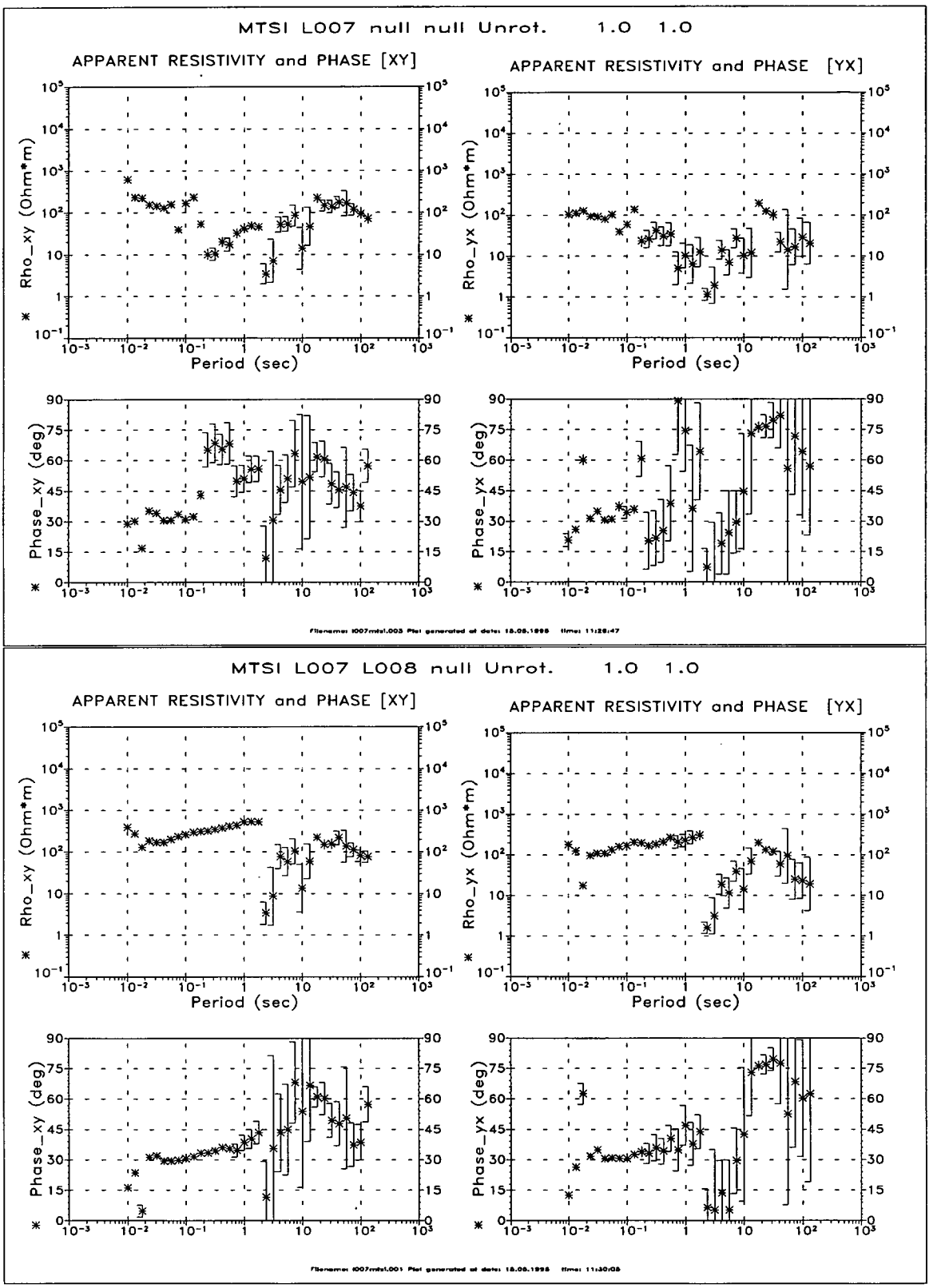

Figure 48: *Standard single site processing of site* L7 *results in very poor quality apparent resistivity and phase curves (top). These data can be also be improved considerably if pseudo remote reference processing is applied.*

which rise from values of below 0.3 to levels of 0.8 and above. However, for periods of $1\,s$ and longer, only a small amount of information can be extracted from these data. In particular the apparent phase curves, which are very important for the data interpretation, are scattered and the data points have very large error bars. The problem, however, is not caused by noisy horizontal magnetic fields but by poorly correlated telluric signals, which is clearly expressed in the time series at all sites throughout the survey.

The final illustrations compare the pseudo remote reference processing technique with the true remote reference method. Remote reference processing results for site L7 are presented in figure 49; the vertical magnetic field response functions are at the top, the apparent resistivity and phase curves at the bottom. For both results, the horizontal magnetic fields of site L8 were used as reference fields in combination with the local fields of site L7. While a considerable improvement over the single site results in figure 44 can be noticed, the quality lags behind the outcome of the pseudo remote reference processing. Obviously, the effects of noisy L7-horizontal fields can not be suppressed effectively by the remote reference method.

The remote reference method is aimed at reducing bias in response function estimates; it does not necessarily improve their precision. That depends on having *i)* low noise reference fields and *ii)* low noise output components $(\mathbf{E}, B_z)$. Hence, successful application of the remote reference technique requires high quality source fields at both local and reference sites, as the results of my last re-processing experiment suggest. The curves in figure 50 are generated using the vertical magnetic field component of site L7 together with the horizontal magnetic fields of sites BASE and L8. The curves at the top of figure 50 are generated using site BASE as the local reference and L8 as the remote reference. Local- and remote reference are swapped for the figure at the bottom. Now, only cross-spectra are used to compute the response function estimates, and consequently the results are un-biased. Although the results appear to be improved over the outcome of the L7/L8-remote reference processing in figure 49, they seem worse than the pseudo remote reference results in figure 47. Obviously, noise on the horizontal magnetic fields of the BASE-site is responsible for this worsening.

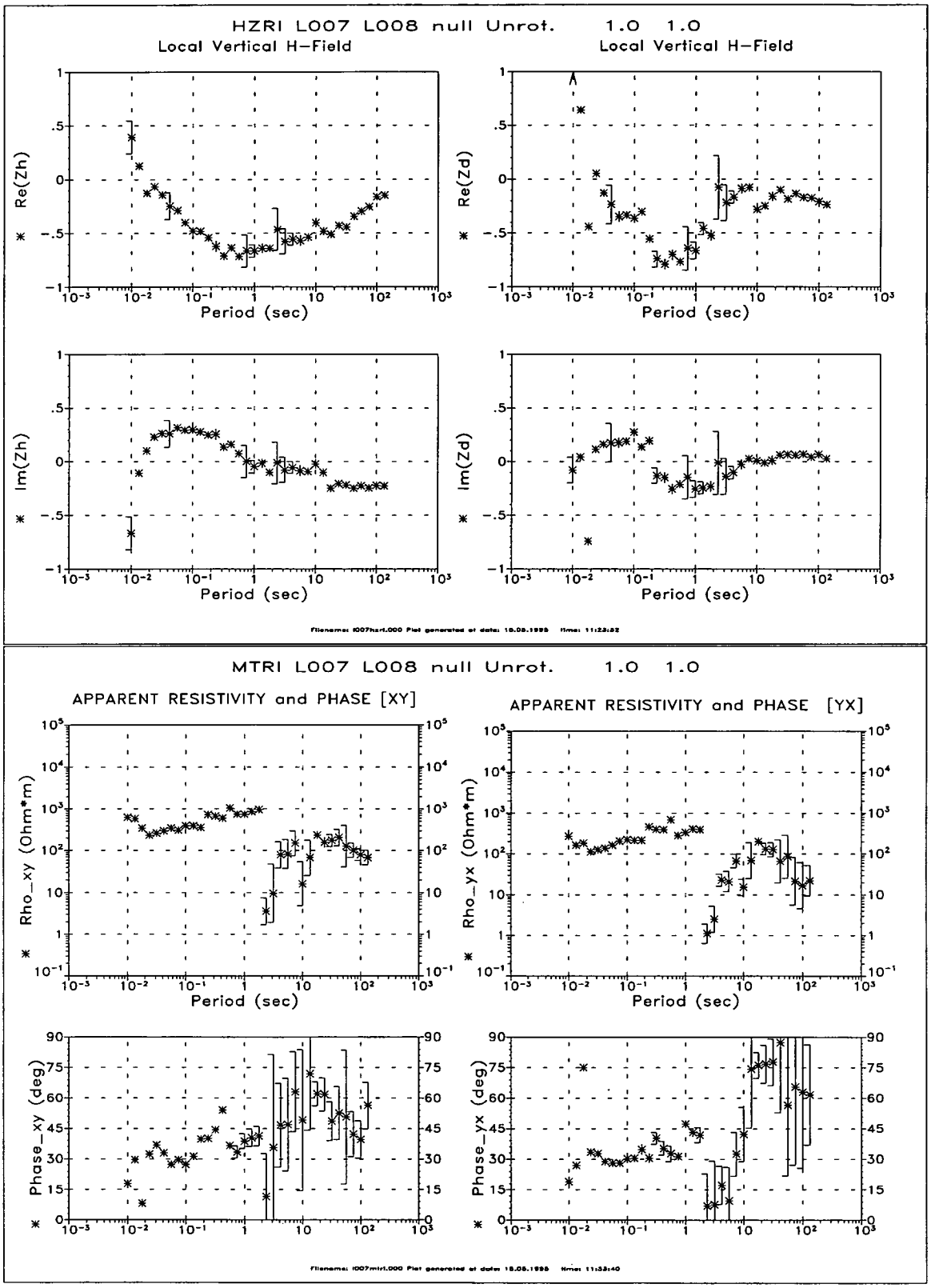

Figure 49: *The remote reference technique can improve the results from standard data processing (top: vertical magnetic fields, bottom: magnetotellurics). However, the curves appear more scattered than in the pseudo-remote reference example.*

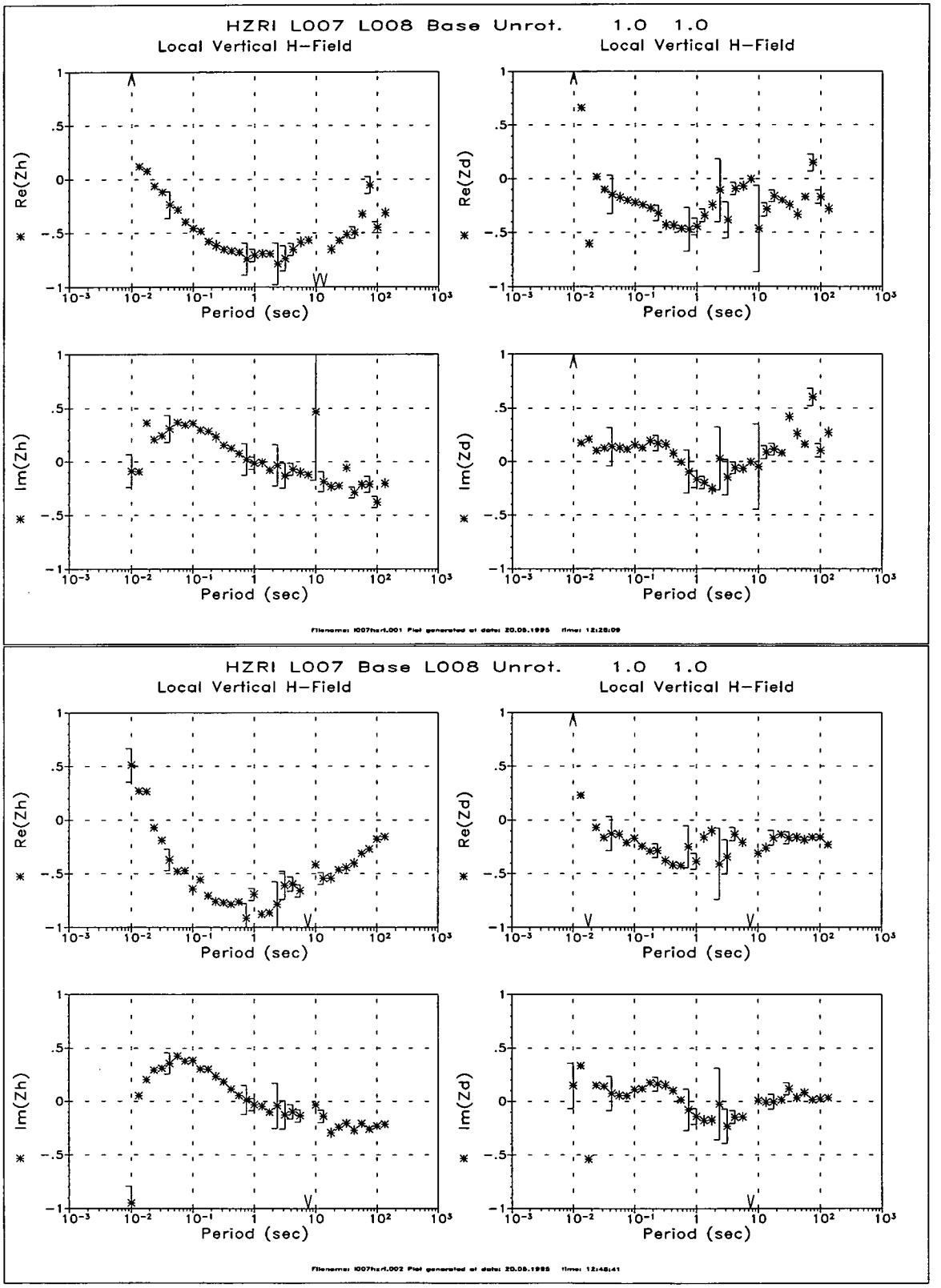

Figure 50: *The combination of pseudo remote reference processing and the remote reference technique can improve the results from standard remote reference processing. Presented are the vertical magnetic field response function of site* L7. *Top: local reference:* BASE, *remote reference:* L8; *bottom: local reference:* L8, *remote reference:* BASE.

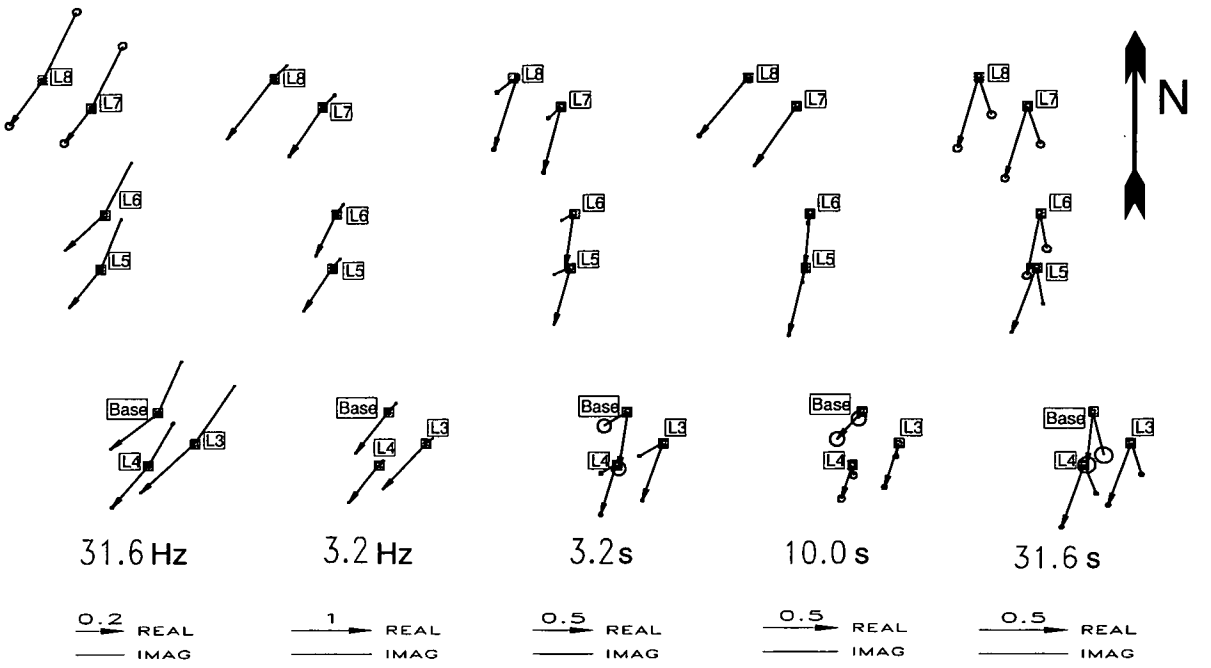

Figure 51: *Wiese induction arrows in the frequency-period range* $32\,Hz$ - $32\,s$.

7.3 Three-dimensional modelling of the results

Depicted in figure 51 are Wiese induction arrows of all sites in the AMT frequency range. Comparison with the site-map in figure 36 shows that sites BASE, L3 and L4 are situated on the Ordovician meta-sediments, to the north of the contact with the Silurian meta-sediments, while the other sites are located on the Devono-Carboniferous sediments. Sites L5 and L6 are close to the Lammermuir fault. The induction arrows are plotted with decreasing frequencies (and varying scales!) from left to right in figure 51.

The real parts of the induction arrows show consistently southwesterly directions, more or less over the whole frequency range. The imaginary arrows point at 180° away from the real arrows at the highest frequency ($32\,Hz$) and they become very small at $3.2\,Hz$. So far, this behaviour of the induction arrows is typically two-dimensional. The directions of the arrows indicate a lateral conductivity contrast somewhere in the north, striking at about 45°-60° from the northwest to the southeast. These results are consistent with the strike angles estimated from the MT data at the high frequencies in figure 42. However, at about $3.2\,s$ we observe imaginary induction arrows which point obliquely to the real arrows towards the west. The imaginary arrows become very small at $10\,s$, but we observe southeastwards pointing imaginary arrows at $32\,s$. Again, the imaginary arrows point obliquely to the real ones.

Figure 52 shows the vertical magnetic field response functions of all sites plotted on top of each other. The curves are plotted in an unrotated north/south orientated coordinate system. The $\mathcal{R}e\{Z_H\}$ curves indicate a trend of continuously decreasing

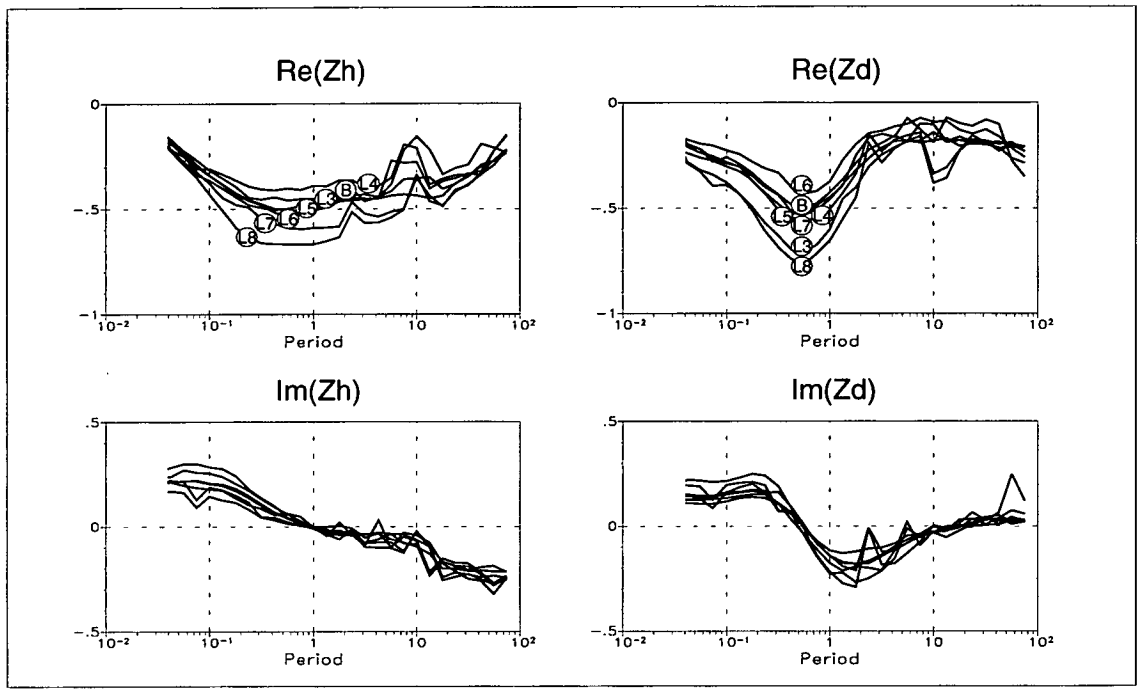

Figure 52: *The vertical magnetic field response functions of all sites plotted on top of each other.*

minimum negative values with increasing distance of the sites from the Ordovician meta-sediments. The $\mathcal{I}m\{Z_H\}$ data, on the other hand, show increasing maximum positive values with increasing distance from the same boundary at $10\,Hz$. The situation is less clear for the $\mathcal{R}e\{Z_D\}$ and $\mathcal{I}m\{Z_D\}$ values, for which the minima of the sites appear unordered. Surprisingly, however, none of the sites close to the fault line or near the contact to the more resistive meta-sediments is particularily distinguished from the others at the higher frequencies.

While the absolute values of the minima in Z_H and Z_D differ slightly, it seems that the curves represent the same geophysical situation. We certainly do not see reversed curves such as we observed in the Middleton experiment in chapter 4. Therefore, all observations must have been made on the same side of a conductive boundary. Because the largest negative values are found at the sites furthest to the north, one would have to look further north for this boundary. As an immediate result, however, one would be inclined to conclude that the Lammermuir fault at Garvald is of negligible electromagnetic significance.

For the modelling, it seems plausible to combine the vertical magnetic field response function of all sites to an averaged curve which represents the whole area. Therefore, I compare the modelling results with the S.P.A.M. MkIII and LMT vertical magnetic field response functions in figure 43. Since the presentation as induction arrows is more illustrative, I concentrate on their modelling over the whole frequency range.

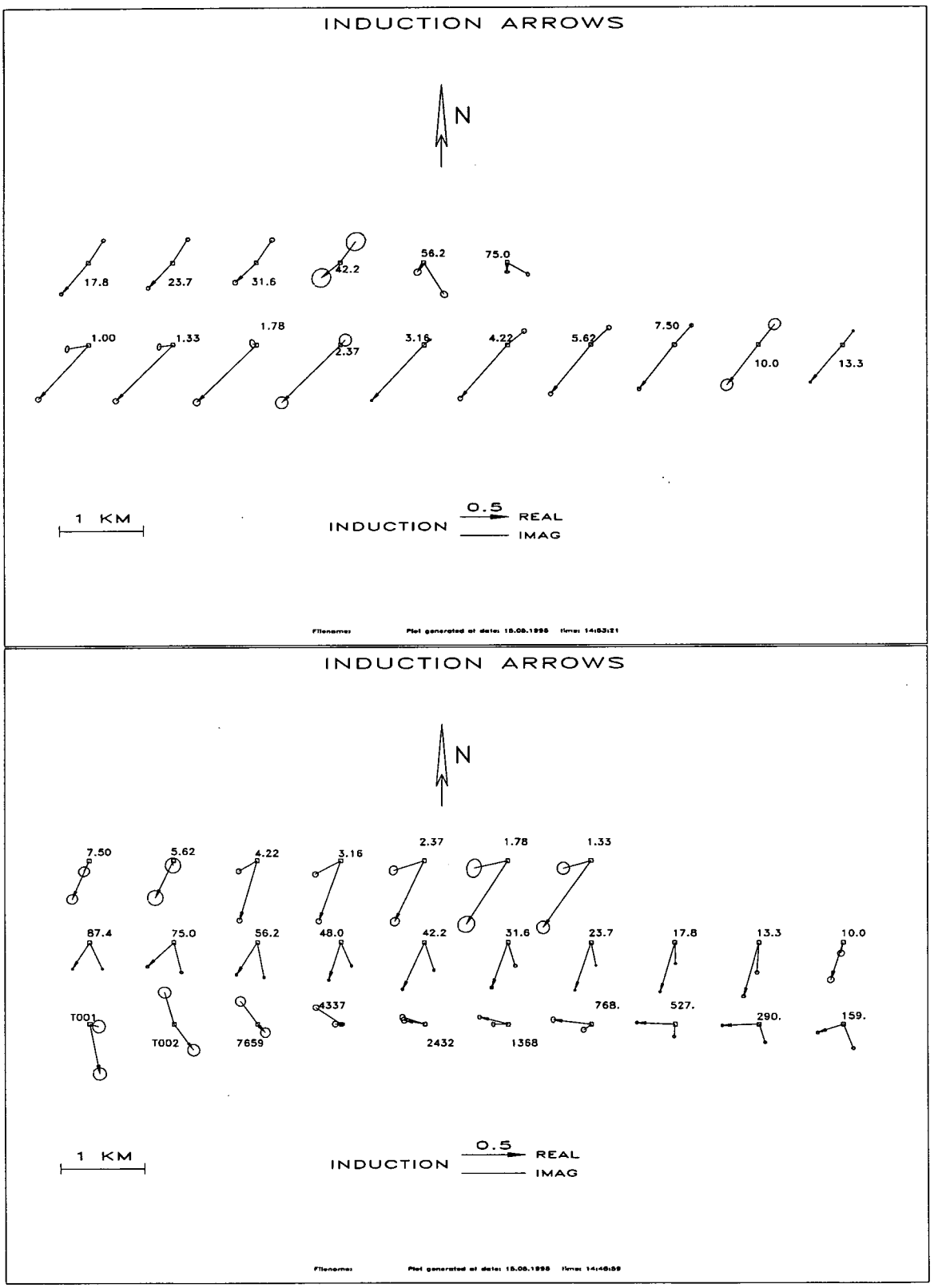

Figure 53: *The induction arrows of the* BASE*-site over the frequency range. Top: induction arrows are labeled with frequency values in Hz; bottom: labels are period values in s. The labels T001 and T002 represent periods of* 14400 s *and* 21600 s*, respectively.*

Figure 53 shows the frequency variation of the Wiese induction arrows at the BASE site. The long period induction arrows are plotted in the lower half of figure 53. The top half of the figure shows the high frequency arrows which have frequency values attached. The induction arrow of the highest frequency ($75\,Hz$) is plotted in the upper right corner of the figure.

I intend to model these induction arrows at 6 selected frequencies in an extended AMT frequency range between $100\,Hz$ to $300\,s$. Each of these frequencies represents a group of induction arrows with similar characteristics (see figure 53):

1. $32\,Hz$: Real and imaginary parts of the induction arrows are anti-parallel; the real arrows point at $-150°$ to the southwest.

2. $1.0\,Hz$: The real arrows reach maximum amplitudes of approximately 1.3, whilst the imaginary arrows disappear.

3. $3.2\,s$: A zone of relatively small imaginary arrows pointing to the west, obliquely to the real parts which are slightly more southwards orientated.

4. $10\,s$: Another part with very small imaginary arrows.

5. $31.6\,s$: The real arrows continue to point towards the southwest, but now, the imaginary arrows point to the southeast. The imaginary arrows also become larger, reaching the size of the real arrows.

6. $290\,s$: Eventually, the real arrows change their directions to point westwards. The imaginary arrows are almost perpendicular, pointing south.

There are more interesting variations in the response functions at longer periods ($>500\,s$). But the attempt to explain everything from the surface of the Earth to the mantle would involve models of unmanageable size. In three dimensions, it is almost impossible to fit all the data, even if the data set is restricted to one site. The number of equivalent models – all those which explain the data to the same extent – must be tremendous and there are just too many cells that can be altered. It is therefore essential to keep the models relatively simple and concentrate on the modelling of some aspects of the whole problem.

In chapter 4.3 I found by thin sheet modelling that very large induction arrows can be explained by strong current channelling into conductive zones at the surface. However, I was unable to explain the variations in the directions of the induction arrows, especially those of the imaginary parts. Having to fulfill the thin sheet conditions in combination with very limited cell sizes meant strict limits on the range of valid models. The inclusion of Randy Mackie's 3D code [Mackie et al., 1994] into the Geotools package came therefore just in time for this project to overcome these problems.

RM3D computes forward solutions for models with three-dimensional inner cores and two dimensional boundaries. For this study, I created a core of 32x16 cells in the horizontal directions and 15 slices vertically. Horizontally, all cells are generated

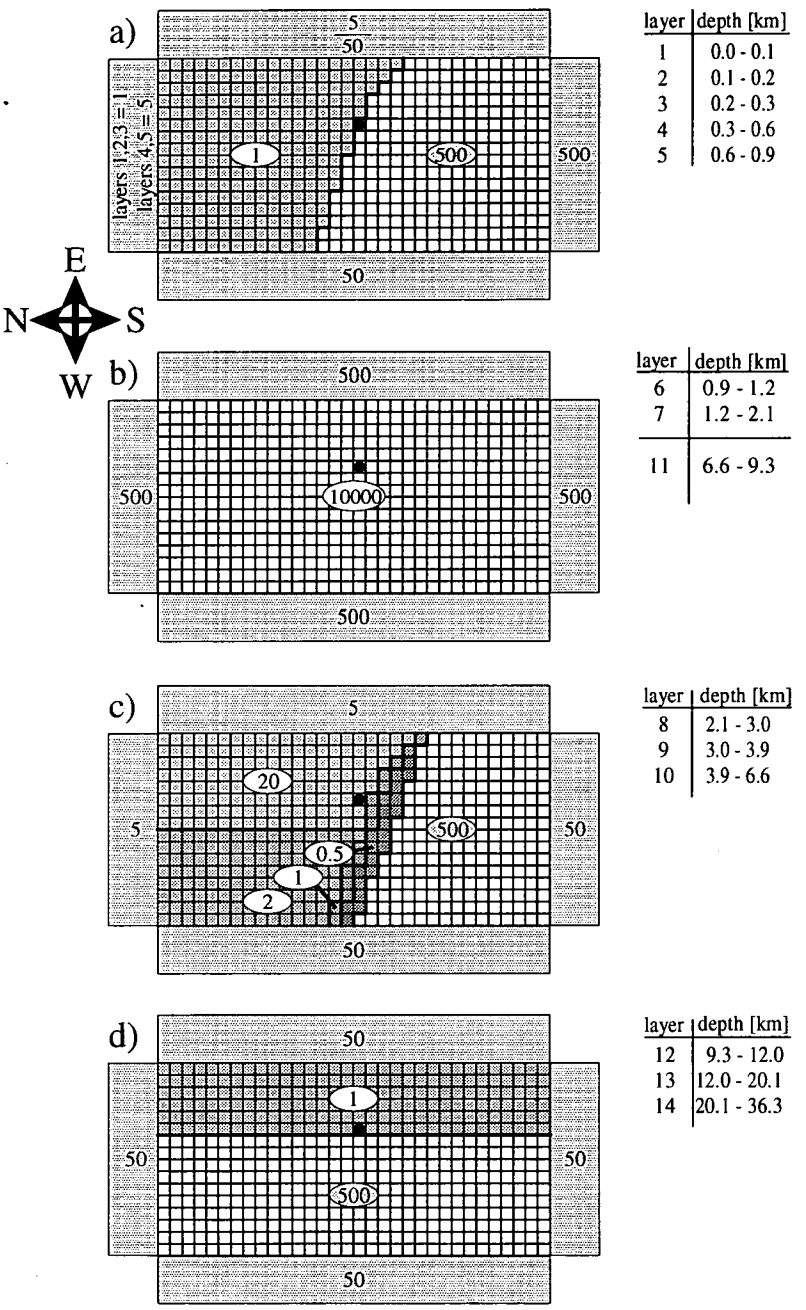

Figure 54: *Vertical slices through a 3D model which is* 32×16 *cells wide. The model consist of* 15 *vertical slices with varying thicknesses. The mesh spacing is* $2km$. *The numbers are resistivities in* Ωm. *The grey areas beyond the grid cells represent the 2D extensions of the model. The black circle shows the area of the experiment in relation to the model.*

$2km$ wide[34]. The vertical extensions of the cells depend on the thickness of the first layer; by default, the thickness of the cells is tripled every third layer. I chose $100m$ for the initial layer thickness, which results in a total depth of more than $30km$ for a 15-slices-model.

The final model is constructed as shown in figure 54. The grid cells at the top (fig. 54a) explain the situation of the 5 layers at the surface. All slices show cells of $1\,\Omega m$ in contact with cells of $500\,\Omega m$ in their inner parts. The contact forms a feature which strikes 45° to 60° from northwest to southeast. The grey areas beyond the grid cells in the figure represent the 2D extensions of the model. Geotools allows several cells for each of these extended areas, but I avoided resistivity variations in order to concentrate on the effects of the inner parts. For the surface layers, the 2D boundary-models extend the conductive and resistive parts of the inner core towards the north and south, respectively. The western and eastern 2D extensions show intermediate resistivies of $5\,\Omega m$ - $50\,\Omega m$. Layers 4 and 5 are thicker than the first three and also have slightly different 2D extensions in order to smooth the resistivity contrast to the insulating layer which follows beneath.

Figure 55 shows modelling results as Wiese induction arrows, at frequencies of $32\,Hz$ and $3.2\,Hz$. The penetration depths at these high frequencies correspond approximately to the thickness of the first 5 slices of the model. The arrows reflect the expected 2D situation at the surface, with real and imaginary arrows of similar lengths reversing across the contact of conductive to resistive cells. This is followed by a zone of maximum real arrows and minimum imaginary arrows at $3.2\,Hz$ on the bottom of figure 55.

Layers 6 and 7 in figure 54b contain highly resistive cells of $10000\,\Omega m$ and also fairly resistive 2D extensions. The insulating layer is not necessarily introduced for geological reasons but to separate the surface layers electrically from the more complicated structures that follow beneath. Without the insulator, the effects of the subsequent layers are expressed less clearly and appear weakened in strength.

The 3 layers in figure 54c show a continuation of the conductive structure at the surface towards the south, underneath the more resistive cells. The general feature seems to be well documented in the data as its inclusion into the model is essential to generate imaginary arrows which point in southwestern directions. The effects can be seen in the modelling results in figure 56. In the upper half of the figure, at a period of $1\,s$, we observe a clear splitting up of real and imaginary arrows. However, the layers also feature horizontal and vertical resistivity gradients. Horizontally, the conductive parts are divided into zones of $20\,\Omega m$- material and zones of $2\,\Omega m$, $1\,\Omega m$, and $0.5\,\Omega m$ for layers 8,9, and 10, respectively. Both horizontal and vertical resistivity contrasts are introduced to generate imaginary arrows with larger amplitudes and more distinguished angles to the real arrows. The influence of this strong three-dimensional feature is indicated by complicated induction arrows at $3.2\,s$ in the bottom of figure 56. Especially, the arrows near the center of the model show great variations with significant changes between neighbouring cells.

Layer 11 is another insulator which separates the predominantly northwest/south-

[34]By default, all cells at the edges have doubled widths, e.g. $4km$.

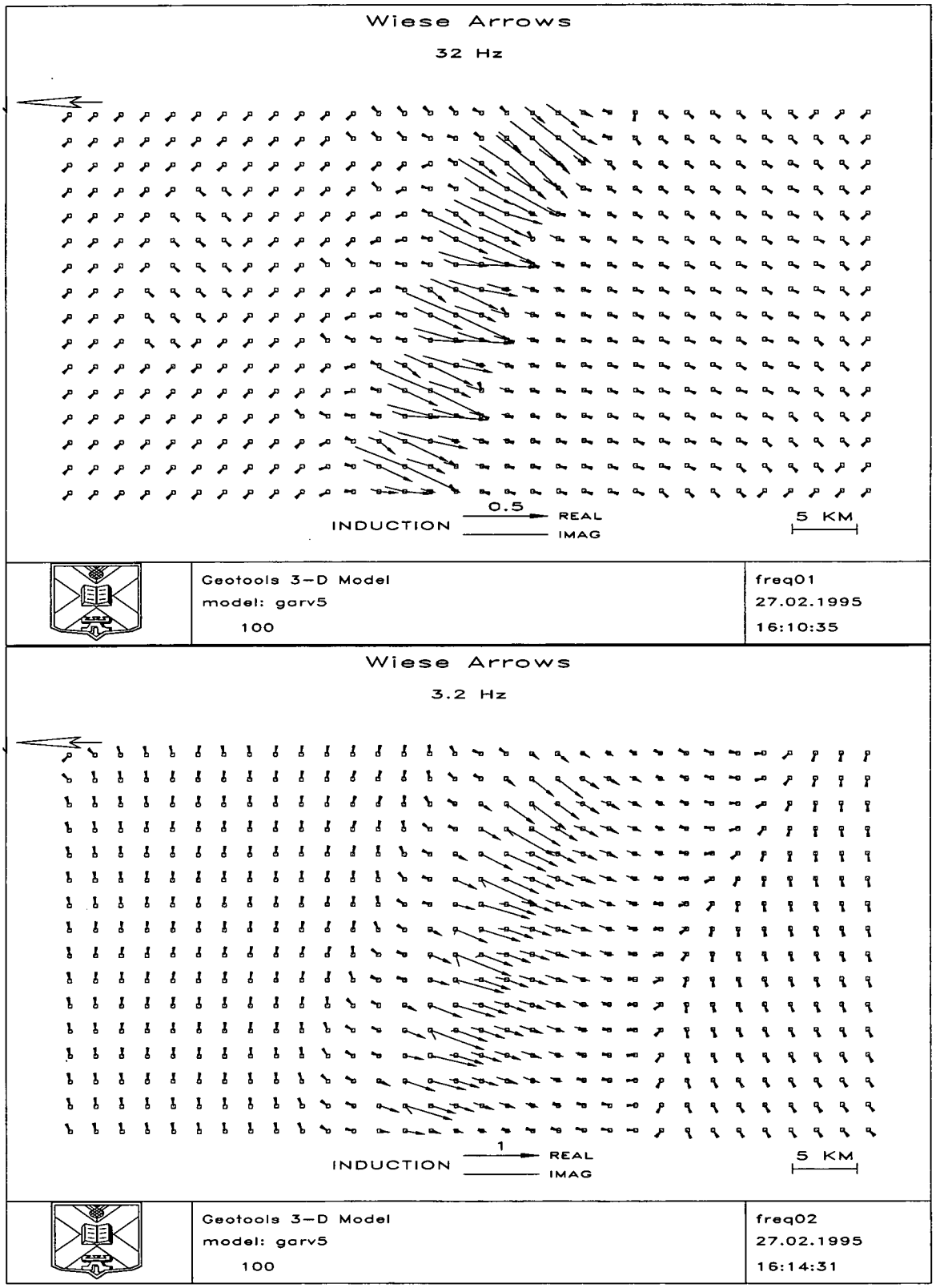

Figure 55: *3D modelling induction arrows at 32 Hz (top) and 3 Hz (bottom).*

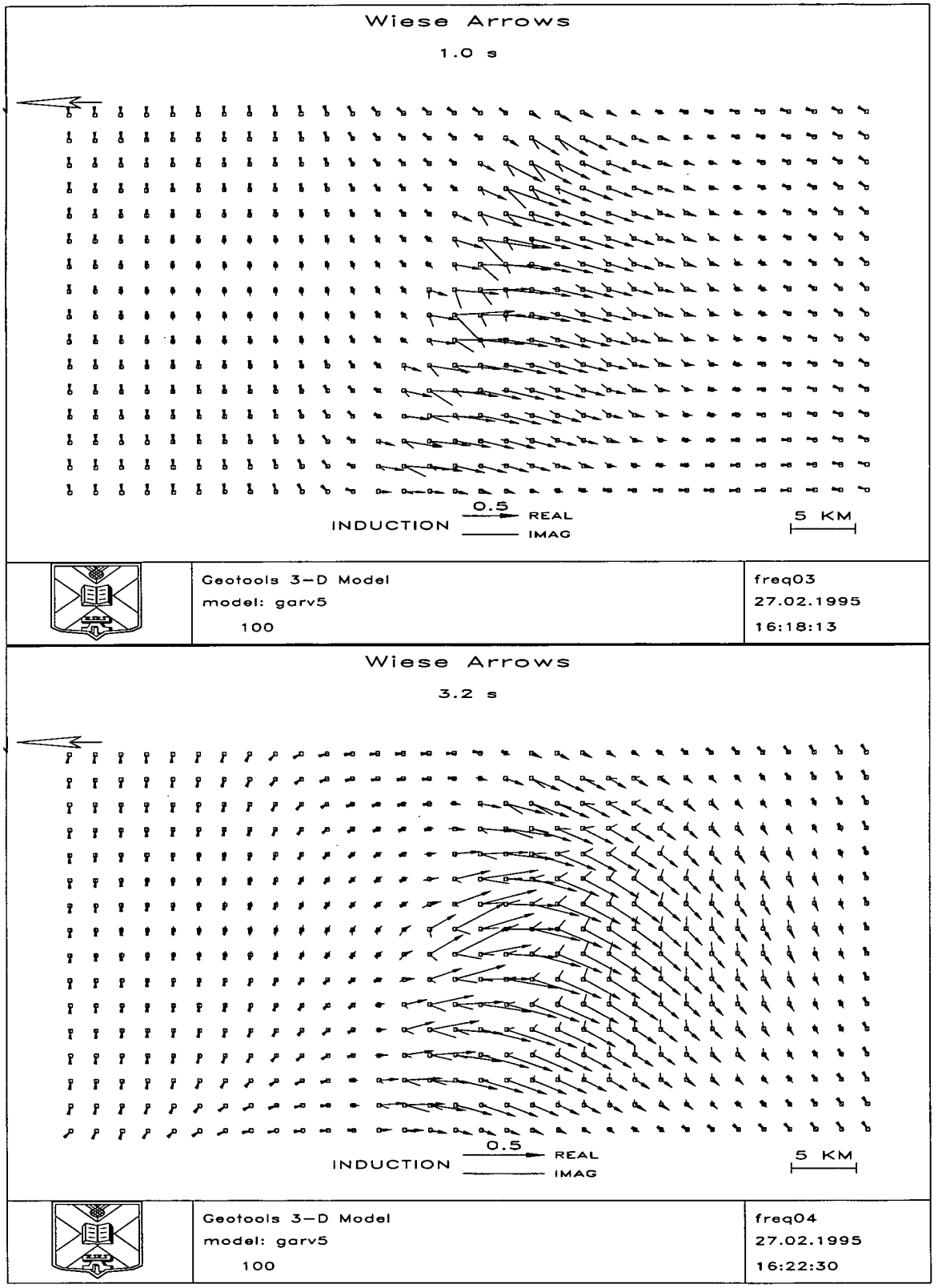

Figure 56: *3D modelling induction arrows at 1 s (top) and 3.2 s (bottom).*

east striking conductive features of the upper $5km$ from the north/south striking features of the deepest parts of the model. Layers 12, 13 and 14 are shown in figure 54d. Layer 15 which is not shown in the figure, consists of homogeneous $50\,\Omega m$ material.

The influence of the deep structure is visible in the induction arrows at periods of $10\,s$, $32\,s$, and $320\,s$ in figures 57 and 58. At $10\,s$, for cells near the contact of conductive to resistive material, the real arrows point at ca. 45° towards the southwest, while the imaginary arrows point to the southeast. The arrows further north are located over more conductive cells and, at that period, are still influenced by horizontal conductivity contrast of the previous layers. The induction arrows of figure 57 are significantly smaller than those of figure 56, as the scales have changed. With increasing periods ($32\,s$ in figure 57), the real arrows continue to point towards the southwest. The imaginary arrows point at cells of the resistive site of the contact almost south in parallel to the strike of the deep structure. They point towards the east, for cells located on the more conductive side.

At $320\,s$ in figure 58, we see parallel pointing real and imaginary arrows. This is the expected pattern for a deep two-dimensional structure, when current scattering and not induction is the dominant physical process (see figure 9 in chapter 4.2). Surprisingly, however, the induction arrows are still greatly influenced by the obliquely stiking features of the previous layers, as they continue to point towards the southwest; this is most distinct at cells near the center of the model.

Figure 59 allows a better comparison of the observed induction arrows with the modelled results. The location of the model-site is indicated by the circle in the grid cells in figure 54; the *'site'* corresponds to cell (16,11) for an origin in the lower left corner in figures 55 - 58. The observed induction arrows in figure 59 are plotted in the top row, easily recognized by the error ellipses. For the whole period range, the modelled induction arrows are too small in comparison with the observations. To explain the lengths of the arrows, however, is not the aim of this study. Our main concern is to understand the principal directions of both, real and imaginary arrows.

At $32\,Hz$, modelled and observed arrows are in very good agreement. Real and imaginary arrows are of similar size and point anti-parallel. At $3.2\,Hz$, the match is still good. The arrows show a zone of maximum real arrows and small imaginary arrows; for the observations this maximum is reached only at $1.78\,Hz$ (cf. figure 53). As I have discussed already, the westwards pointing imaginary arrows at $1\,s$ and $3.2\,s$ can be modelled by a southwards continuation of the conductive material in greater depth. The modelled arrows have slightly narrower difference angles, but the ratios between real and imaginary parts are in good correspondence.

At $10\,s$ the observations show another zone of minimum imaginary arrows. With longer periods ($32\,s$) they grow larger again and point into easterly directions. A zone of very small imaginary arrows is not particularly well resolved by the model for $10\,s$. However, southeastwards pointing imaginary arrows can be picked up at $32\,s$; more clearly though, at cells further to the west in figure 57. There is a disparity between observation and modelling results at the longest period of $320\,s$. More work (and more data) would be necessary to establish a better model for the long periods

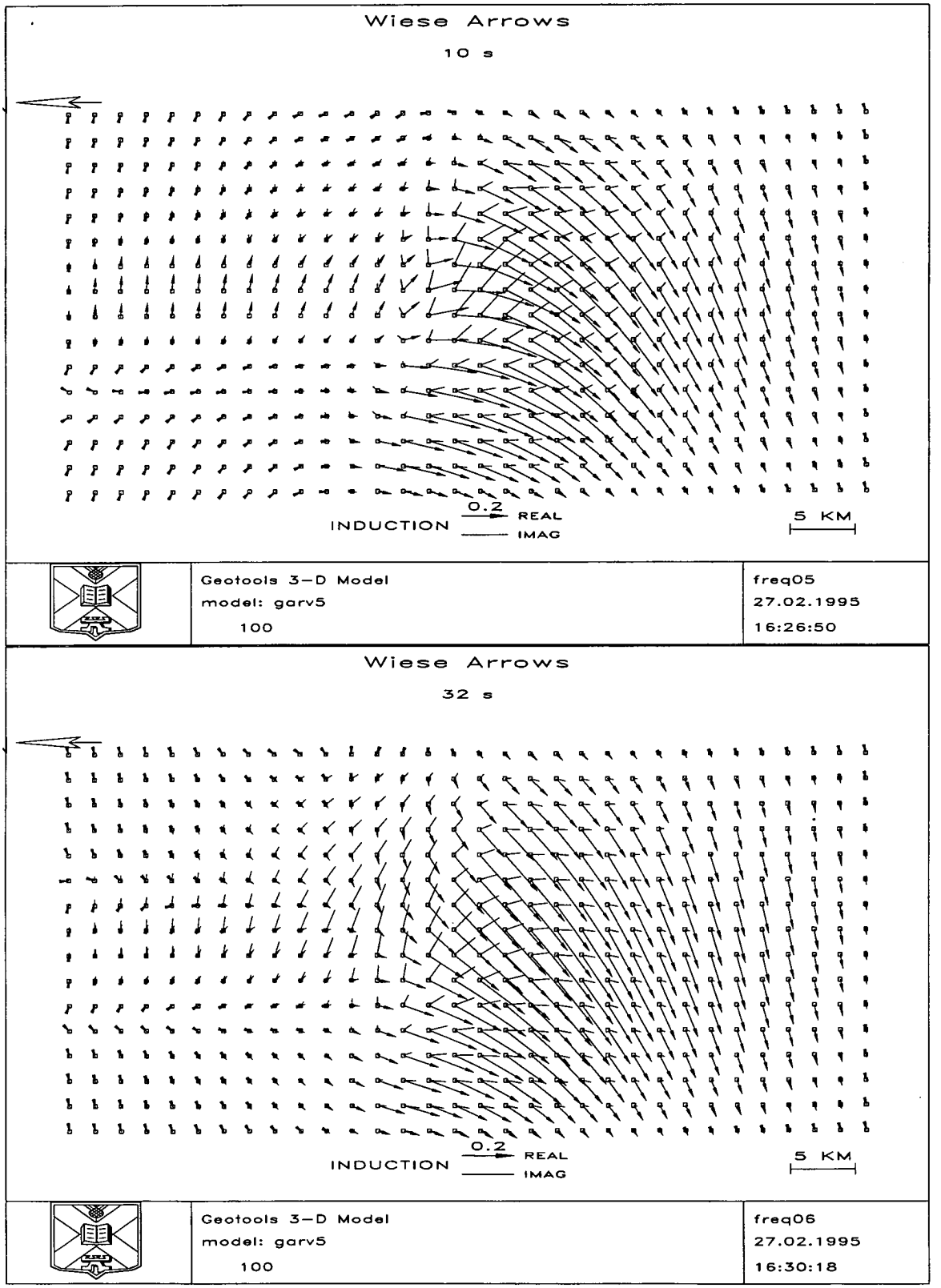

Figure 57: *3D modelling induction arrows at 10 s (top) and 32 s (bottom).*

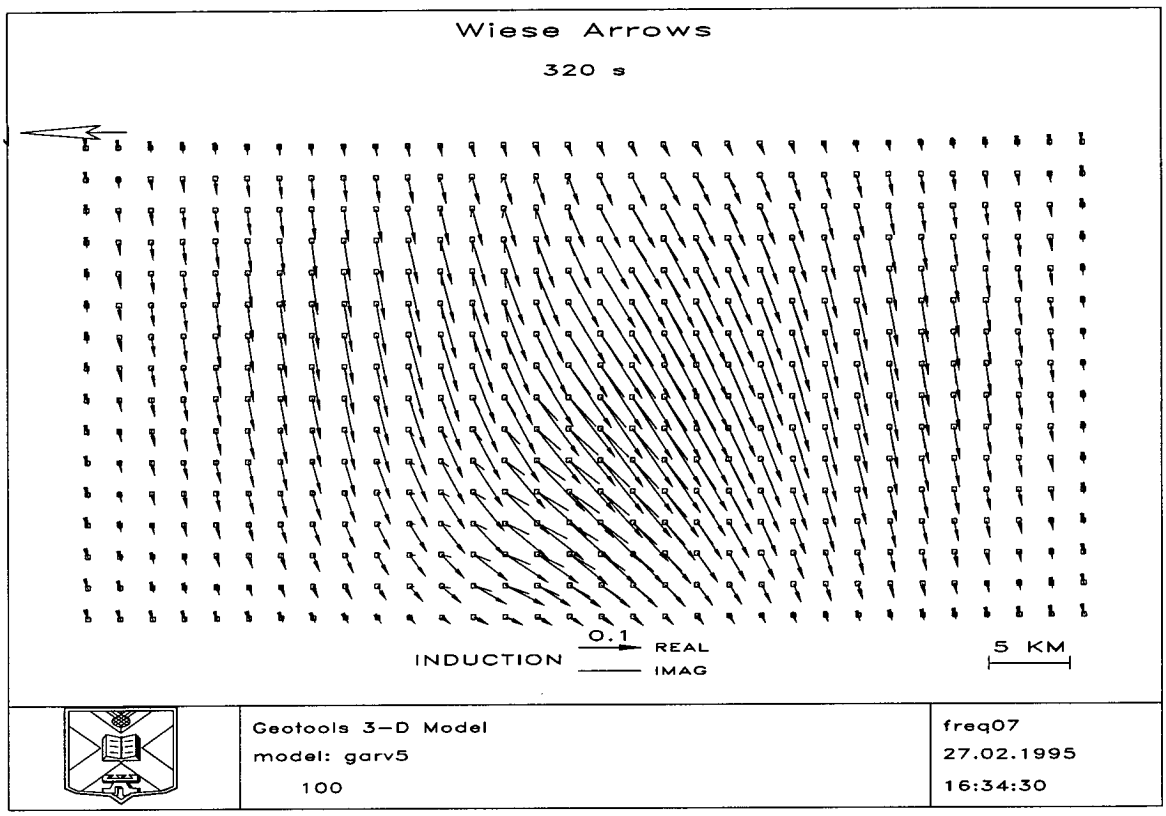

Figure 58: *3D modelling induction arrows at* 320 *s*

(cf. figure 53). However, it will become increasingly difficult to incorporate more features into a single model.

7.4 Summary

In a second field project to cross the Lammermuir Fault (Southern Upland Fault), we recorded data at 7 AMT sites near the village of Garvald, 35 km SSE of Edinburgh. For the experiment – and for the first time ever – the new S.P.A.M. MkIII could be used. With the new system we managed to install a network of three simultaneously running AMT sites, with a maximum distance of 1.6km between reference and local sites.

The quality of the AMT data is usually excellent in the high frequency range (100 Hz - 1 Hz), but at the longer periods (1 s-30 s) high background noise levels in combination with little natural signal energy spoil the data. While the telluric fields are particularily affected, noise is less evident on most of the magnetic channels. Nevertheless, I found that the data quality of some noisy sites can be improved considerably if remote reference processing is used. However, for the successful application of the remote reference technique both low-noise remote and local horizontal magnetic fields are essential. In the case of contaminated local magnetic fields, better results can be achieved if the local horizontal magnetic fields are sim-

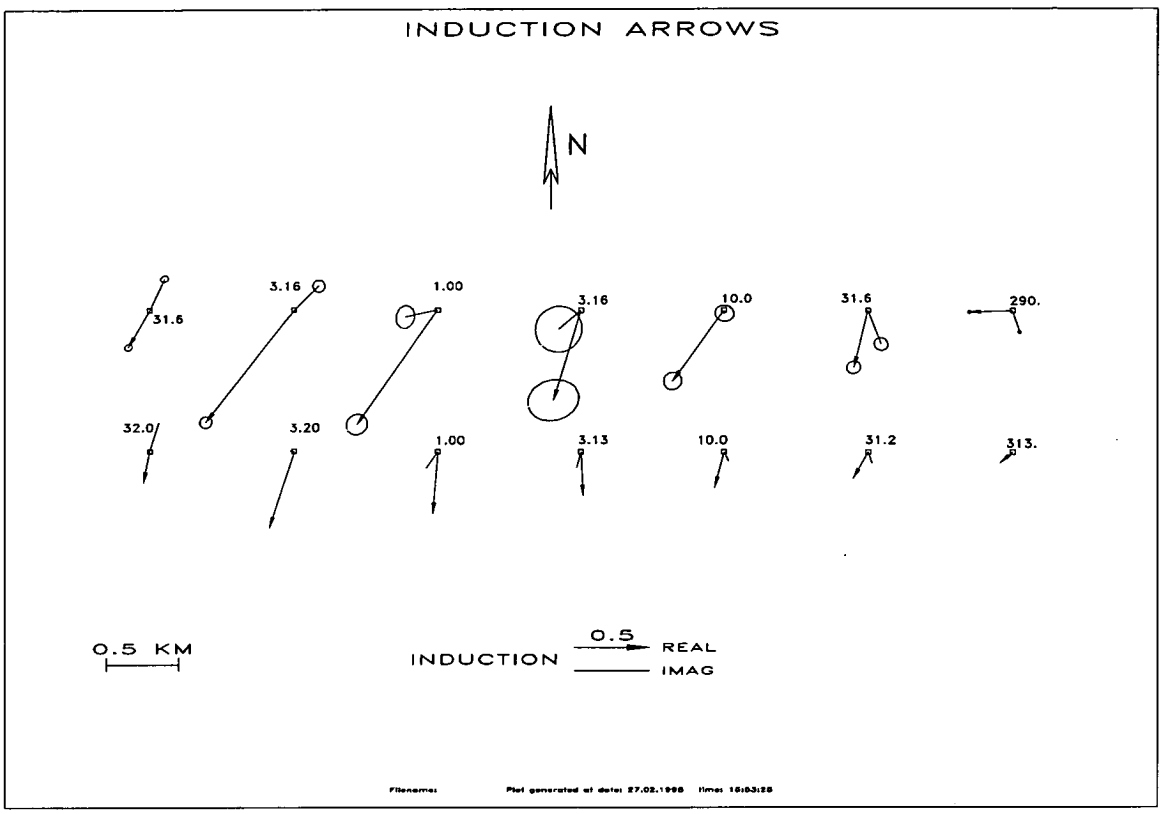

Figure 59: *Comparison of the observed induction arrows with those of a grid-cell near the center of the model. Top row - experimental, bottom row - theory.*

ply replaced by the remote fields (pseudo remote reference). Results from pseudo remote reference processing will be biased though, if the reference fields are noisy.

The obtained vertical magnetic field response functions are generally of very good quality over the whole AMT frequency range. However, the vertical fields differ only slightly between sites and this leads one to assume that the Lammermuir Fault is only a minor feature in an electromagnetic context. Nonetheless, the combined AMT and LMT vertical magnetic field response function show a strong three-dimensional anomaly which is marvellously resolved over 7 decades ($10^{-2}\ s$ - $10^{5}\ s$).

The observed induction arrows can in essence be explained by three-dimensional forward modelling. The results suggest that a northwest/southeast striking conductive feature at the surface is duplicated at greater depth and dips towards the south. Best fitting results are achieved if the two conductors are separated by an insulating layer. At the longest periods (from $300\ s$ onwards), the induction arrows indicate a different strike angle of the conductor. The conductor appears to be more north/south orientated, but this feature is not very clearly resolved by the model.

While the model found is capable to explain many of the features of the magnetic variation data, it is quite independent of any geological constraints. A more detailed interpretation, however, with the emphasis on integrating all geological and geophysical information available, would be beyond the scope of this thesis.

Summary and conclusions

The study of geomagnetic variations at high frequencies and to determine their feasibility for electromagnetic investigations is a key objective for this thesis. My research work in this context involved field experiments with novel sensor configurations (chapters 4 and 7), participation in the development of a new generation of geophysical equipment (chapter 5), writing of new data processing and file handling software (chapters 3 and 6), its application to field data and three-dimensional electromagnetic modelling to interpret the results (chapters 4 and 7).

In order to test the high frequency magnetic variation method, I carried out two field experiments in southeastern Scotland in the vicinity of the Southern Upland Fault complex, more specifically the Lammermuir Fault. The ENE-WSW trending Southern Upland Fault separates the Midland Valley and the Southern Uplands in the South of Scotland. The geophysical significance of the Lammermuir Fault is uncertain. In its effect of separating Ordovician meta-sediments from Carboniferous sediments, the Lammermuir Fault has certainly some of the character of the Southern Uplands Fault as a terrain boundary. It is unclear however, whether it can be seen as the eastern segment of the Southern Upland Fault. Alternative suggestions indicate that the Southern Upland Fault continues on towards the northeast and is represented by the Crossgatehall Fault at the surface (cf. figure 35). However, results from previous electromagnetic investigations suggested that the Carboniferous sediments are in the order of ten times more conductive than the Ordovician meta-sediments. A lateral change in conductivity of that order at the fault is required to generate a distinct effect in the vertical magnetic field response functions.

The magnetic varation mapping experiment near Middleton, 15 km SSE of Edinburgh, revealed exceptionally high anomalous vertical magnetic field response functions ($|\mathcal{R}e\{Z_H\}| > 2$). The anomaly is well resolved, with 24 closely spaced sites, arranged along a $2.5km$-profile. Forced by our logistics requirements, we had to settle for a location which was disturbed by artificial electromagnetic sources, most visibly, electric fences and a gas pipeline running in parallel with the presumed fault line. The effects of noise could not always be reduced efficiently by robust data processing procedures. Particularly affected are the electric fields, and hence the results of the magnetotelluric measurements. The vertical magnetic field response functions, however, are of very reasonable quality at most sites. They vary consistently with frequency and between sites.

The general pattern of the vertical magnetic field anomaly is consistent with a two-dimensional lateral conductivity contrast, which we had anticipated originally. We observe large inductions arrows for the resistive Ordovician meta-sediments, the largest ones nearest to the contact with the conductive Carboniferous sediments; on the conductive side of the profile the induction arrows become rapidly very small. However, the sheer size of the anomaly, expressed in Z_H and Z_D and large MT - skew values, hints at a more complicated, three-dimensional geological setting. Three-dimensional thin sheet modelling shows that strong current channelling into a surface conductor can explain the lengths of the induction arrows. However, the thin

sheet models cannot account for the varying directions with increasing penetration depths of the real arrows, nor for the behaviour of the imaginary arrows.

For the second field project we recorded 7 AMT sites near the village of Garvald, 35 km SSE of Edinburgh and approximately 25 km northeast of Middleton (cf. figure 35). The data were collected using the new S.P.A.M. MkIII in a network of three simultaneous AMT sites, with a maximum distance of 1.6km between reference and local sites. The geological situation at Garvald differs in that Carboniferous sediments are not directly in contact with Ordovician meta-sediments. Instead, at the new location a wedge of the Old Red Sandstone is sandwiched between the two formations. Problems with electromagnetic noise from farming equipment persist at the new location, although less perceptible. Again, the telluric fields are affected more severely, while most of the vertical magnetic response functions are of good or excellent quality. A remarkable set of data exists for the BASE-site, where the AMT data are complemented with long period observations from A. Junge. The combined long and short period vertical magnetic field response function curves are perfectly matched when plotted together, although different recording hardware and processing software were used to obtain them. The data sets cover a huge period range of 7 decades, from $10^{-2}\,s$ to $10^{5}\,s$.

A first surprising result reveals that none of the features from the surface geology – neither the contact between the different geological formations nor the fault line – can be detected in the induction arrows. Apparently, the results from the BASE-site are representative of the whole area, as there is little variation in the induction arrows between the sites. Nonetheless, the vertical magnetic response functions display a strong three-dimensional anomaly with maximum $|\mathcal{R}e\{Z_H\}|$-values of 0.8. The main characteristics of the anomaly can essentially be explained with three-dimensional forward modelling. The modelling results in figure 54 suggest that a 45°-60° SE/NW striking conductive feature at the surface ($0km \ldots 1km$) is duplicated at greater depth ($2km \ldots 6.5km$), where it dips towards the south. Best fitting results are achieved if the two conductors are separated by an insulating layer. For the longest AMT periods (>30 s), the conductor appears to be more north/south orientated. However, this is not very clearly resolved by the model. The modelling results do explain the varying directions of the observed real- and imaginary arrows but not altogether the variations in their lengths.

Although the model was designed to fit the Garvald data, it can also improve our understanding of the results from Middleton, at least for the longer periods (>1 s). At Middleton, we observe southeastwards pointing real induction arrows at the highest frequencies (cf. figure 20, 68.1 Hz), which indicate a SW/NE trending conductivity contrast at the surface. This feature does not exist or is unresolved in the Garvald data. With increasing penetration depths, however, the induction arrows behave similarly to those at Garvald. The real arrows point into southern directions, even the period range of maximum real and minimum imaginary arrows is comparable, at approximately 1 s. Southwestwards pointing imaginary arrows, on the other hand, are less perceptible for Middleton in the period range between 1 s and 10 s. Because of these imaginary arrows we introduced a dipping second

conductor into the Garvald model. This could mean that the second conductor in Middleton has the same orientation as at Garvald, but a dip is probably not required. For the longest AMT periods ($30\,s$), real and imaginary arrows are not pointing in parallel directions but very similar at both locations. For these periods, the model suggests a change in the direction of the deep conductor, more into a north/south orientation.

The motivation for the construction of the models and the original design of the field experiments was primarily to achieve a better understandig of the underlying electromagnetic processes. Consequently, the models are fairly abstract and probably difficult to use in a geological sense. In fact, the geological map in figure 35 shows all the fault lines in the area running SW/NE, almost perpendicular to the directions suggested by the 3D model. Obviously, the whole geological situation of the area is very complex and a lot more work is necessary in order to draw more detailed geological conclusions. These measurements and model experiments suggest that we are only at the beginning of a process of attempting to understand the detailed behaviour of very wide band electromagnetic fields.

To improve our models we require more information. We need magnetotelluric data (electric fields) of higher quality and, since the Earth's crust is 3D, higher observation density. In the past and at the present day, many AMT surveys have been hindered by noise, especially in the period range $1\,s$ - $10\,s$. Noise is usually tackled by frequent repetition of the experiments and application of sophisticated statistical (robust) methods. The processing works successfully if the recordings represent a linear (bivariate) system, if the level of noise is less than that of signals, and it affects only the outputs of the linear system. In practice, however, we find all conditions violated. Noise from near-field sources is added coherently onto the natural electric- and magnetic fields, thereby modifying the linear relation between them. Because the natural signal activity is generally low in this critical period range, the combined signals of noise and data are more often than not dominated by noise.

The new S.P.A.M. MkIII is an important step forward in the development of electromagnetic instrumentation. This highly portable, low-power real time AMT system is operated as a network of arbitrarily distributed geophysical sensors. Installed networks can become very large because the processing power of the instrument increases with the number of network nodes. The new instrument was used for the first time ever during the field experiment near Garvald. Although at that time S.P.A.M. MkIII was not equipped with all features – particularly the real time response function estimation was still missing – its application was extremely important for the success of the field work. It was very surprising to learn how difficult it is to install and operate three simultaneous AMT sites. Many problems we experienced with electrodes, cables, and induction coils could not have been detected with ordinary, single site equipment, as faulty channels become obvious only if the incoming signals can be compared between neighbouring sites.

S.P.A.M. MkIII certainly is suitable and probably necessary for future field experiments with very dense site/sensor spacing to investigate the three-dimensional

nature of the Earth's crust. This is not only because the data can be collected at many sites simultaneously, which is necessary to ensure adequate work progress, but also because the quality of the incoming data can be controlled on-line. Simultaneous recordings of the magnetic time variations would have been very helpful for the Middleton experiment to investigate the effects of anomalous horzontal magnetic fields. Conventional instruments provide very limited multi-sensor support (5 . . . 10), and the distance between sites is usually restricted to only a few hundred meters. S.P.A.M. MkIII-sites, on the other hand, can be separated by a few kilometers, because all network nodes are inter-connected using digital data communication.

The newly developed off-line data processing package is very useful for the analysis and organisation of huge volumes of data. It is geared to S.P.A.M. MkIII as an arbitrary number of channels can be processed. In my experience, robust processing consistently produces better results than on-line procedures. The software package provides a framework to integrate all relevant information on time series, instrument calibration data and site configuration information into a common database. Complete data sets can be retrieved from the database later, e.g.for re-processing of the data to try new methods or simply to correct mistakes.

Eventually, however, further improvements in both data acquisition and data processing are necessary. New processing methods could be based on the inclusion of a priori information which would help filter out unrealistic events [e.g.Parr, 1991]. New field projects should be planned with higher observation density to improve the processing results with redundant information from neighboured sites. The remote reference method can help improve the situation, but only if the recorded reference magnetic fields are truly undisturbed. Many AMT instruments allow distances of only a few hundred meters between local and reference sites. However, the results from Garvald show that a distance of $1.5km$ might not be sufficient in the critical period range. More research is urgently required to investigate the coherence lengths of both natural and noise signals. As it seems necessary to bridge even larger distances between local and remote sites in order to obtain clean reference fields, S.P.A.M. MkIII should (and could) be extended accordingly.

Under no circumstances should the geomagnetic variation field be neglected in AMT surveys, in the way it has been. Vertical magnetic field anomalies can be detected over the whole AMT frequency range and I found the vertical magnetic fields to be more robust against noise than the electric fields. The coherencies are generally higher than those of the respective telluric fields, especially in the critical frequncy range of the *dead band*. In both experiments, the vertical magnetic field anomalies are spatially very consistent between neighbouring sites, and hence the geomagnetic variation field is a very suitable quantity for such dense mappings. Even though the results of my work are surprising – the size of the anomaly at Middleton must be a world record – and not fully understood yet, a further development of the method is highly recommended for the future.

Acknowledgements

I wish to sincerely thank Dr. R.J. Banks and G.J.K. Dawes for their advice and encouragement throughout the course of this investigation. Their competence in a wide area of research was essential for the successful outcome of this work. I am particularly thankful to Dr. Banks for carefully reading the manuscript of this thesis and for many very helpful suggestions he made.

Without Dr. V.R.S. Hutton's strong support, this project would not have been initiated. Her hospitality helped me and my family greatly to settle into our new environment. I thank Dr. A. Junge for his profound comments and stimulation, and for reading large parts of this thesis.

Fieldwork was a very important aspect of my research and I am particularly thankful for the unselfish help I received from G.J.K. Dawes, D. Nascimento, A. Jackson, K. MacDonnald and Dr. A. Junge. My thanks go again to G.J.K. Dawes and D. Nascimento for working literally day and night in order to finish S.P.A.M. MkIII in time for the field project at Garvald.

I am very grateful to everyone who participated actively in our departmental electromagnetic working group. Especially our fortnightly MT meetings provided me with many new ideas and insight into the previously unknown. My sincere thanks go to everyone mentioned already and to Dr. B.A. Hobbs, Prof. K. Whaler, Dr. D. Livelybrooks, T. Volti, Dr. P. Jones, C. Dumitrescu, A.J.K. Wilson and D. Bailey.

Extremely useful for a better understanding of my rather complicated data sets were discussions with my German colleagues. In this respect, I wish to thank Prof. V. Haak, Prof. P. Weidelt, Dr. H. Jödicke and Dr. K. Bahr. I am very thankful to T. Hanstein for the extension of his pipeline model to the MT case. I am furthermore grateful to V. Rath and U. Kalberkamp for their enthusiastic help with my field work during a visit to Edinburgh. I like to thank M. Eisel for making Geotools available to the European electromagnetic research community.

Above all, I wish to thank Patricia for her support during field work, her patience in reading the draft versions of all chapters, her assistance in the preparation of conference papers and generally, for many useful comments and inspirations during the whole duration of this course.

I am much obliged to those responsible within the EEC for providing Patricia and me with this unique opportunity to concentrate on our research, without jeopardising the well-being of our children. I wish to thank particularly E. Staroste who helped at several occasions in administrative matters.

S. Voss and I. Chisholm are thanked for their excellent organisation of the departmental computing facilities. Furthermore, I wish to thank M. Valiant and the NERC - GEP team for their support and well maintained equipment; G. Waugh for his rare gift to make bureaucracy look easy.

For their hospitality I am grateful to the farmers of Falahill, Western Middleton and Garvald Mains.

References

Bahr, K. [1988]. Interpretation of the magnetotelluric impedance tensor: Regional induction and local telluric distortion. *J. Geophys.*, 62:119–127.

Bahr, K. [1991]. Geological noise in magnetotelluric data: a classification of distortion types. *Phys. Earth. Planet. Int.* , 66:24–38.

Banks, R. J. [1969]. Geomagnetic variations and the electrical conductivity of the Upper Mantle. *Geophys. J. R. astr. Soc.* , 17:457–487.

Banks, R. J. [1986]. The interpretation of the Northumberland Trough Geomagnetic Variation Anomaly using two-dimensional current models. *Geophys. J. R. astr. Soc.* , 87:595–616.

Banks, R. J., Beamish, D., and Geake, M. [1983]. Magnetic variation anomalies in northern England and southern Scotland. *Nature*, 303:516–518.

Banks, R. J., Irving, A. A. K., and Livelybrooks, D. W. [1993]. The simulation of magnetic variation anomalies using single-station data. *Phys. Earth. Planet. Int.* , 81:85–97.

Beamish, D. [1986]. Deep crustal structure beneath the Northumberland Basin. *Geophys. J. R. astr. Soc.* , 84:619–640.

Beamish, D. and Smythe, D. [1986]. Geophysical images of the deep crust: the Iapetus suture. *J. Geol. Soc. London*, 143:489–497.

Beaton, A. and Tukey, J. [1974]. The fitting of power series, meaning polynomials, illustrated on band-spectroscopic data. *Technometrics*, 16:147–185.

Beblo, M. [1982]. Die Dielektizitätskonstante ε_r der Minerale und Gesteine. *in Landolt - Börnstein, Zahlenwerte und Funktionen aus Naturwissenschaften und Technik, Neue Serie, (Hg. G. Angenheister), Springer Verlag, Berlin - Heidelberg - New York*, V1b.

Beblo, M. and Hofer, S. [1986]. Überlegungen und Versuche auf dem Weg zum neuen 'Münchener Elektrographen'. *Protokoll Kolloquium Elektromagnetische Tiefenforschung (Hg. V. Haak und H. Homilius)*, Lerbach bei Köln.

Beblo, M. and Liebig, V. [1986]. Mobile Datenerfassung mit CMOS Halbleiterspeichern. *Protokoll Kolloquium Elektromagnetische Tiefenforschung (Hg. V. Haak und H. Homilius)*, Lerbach bei Köln.

BGS [1983a]. *Geological maps of Scotland, Dunbar: Scotland Sheet 33E.* 1:50000, Solid Edition, BGS Edinburgh.

BGS [1983b]. *Geological maps of Scotland, Haddington: Scotland Sheet 33W & Part of 41.* 1:50000, Solid Edition, BGS Edinburgh.

Brasse, H. [1993]. *Audiomagnetische Tiefensondierungen in Nordost-Afrika.* Doktorarbeit, Technische Universität Berlin.

Brewitt-Taylor, C. R. and Weaver, J. T. [1977]. Numerical solutions of two-dimensional induction problems. *Acta Geodaet.,Geophys. et Montanist. Acad. Sci. Hung.* , 12:241–245.

Bronstein, I. N. and Semendjajew, K. A. [1981]. *Taschenbuch der Mathematik.* 20. Auflage herausgegeben von G. Groschke und V. Ziegler, Verlag Harri Deutsch, Thun und Frankfurt/Main.

Cagniard, L. [1953]. Basic theory of the magneto-telluric method of geophysical prospecting. *Geophysics*, 18:605–635.

Chapman, S. [1919]. The solar and diurnal variation of terrestrial magnetism. *Phil. Trans. Roy. Soc. Cond.*, A218:1–118.

Chave, A. D. and Smith, J. T. [1994]. On electric and magnetic galvanic distortion tensor decompositions. *J. Geophys. Res.* , 99 B3:4669–4682.

Chave, A. D., Thomson, D. J., and Ander, M. E. [1987]. On the robust estimation of power spectra, coherencies, and transfer functions. *J. Geophys. Res.* , 92(B1):633–648.

Cocks, L. and Fortey, R. [1982]. Faunal evidence for oceanic separations in the palaeozoic in Britain. *J. Geol. Soc. London*, 139:465–478.

Coggon, J. H. [1971]. Electromagnetic and electrical modeling by the finite element method. *Geophysics*, 36:132–155.

Constable, S. [1993a]. Conduction by mantle hydrogen. *Nature*, 362:704.

Constable, S. [1993b]. Constraints on mantle electrical-conductivity from field and laboratory measurements. *J. Geomagn. Geoelectr.* , 45(9):707–728.

Davies, A., McAdam, A. D., and Cameron, I. B. [1986]. Carboniferous rocks of the Dunbar district: Sheet 33e and part of sheet 41. *Memoir of the British Geological Survey.*

Dawes, G. J. K. [1984]. Short period automatic magnetotelluric (S.P.A.M.) system in a broadband tensorial magnetotelluric study in the Travale - Radicondoli geothermal field (Hutton et. al.). *EEC Final Report (Contract No. EG-A2-031-UK).*

Dawes, G. J. K. [1987]. S.P.A.M. MkIIb user manual. *Univ. of Edinburgh, internal publication.*

Dawes, G. J. K. [1990]. Feasibility study for a transputer-based upgrade of the Short-Period Automatic Magnetotelluric (S.P.A.M.) system. *Univ. of Edinburgh, N.E.R.C. report F3/G6/S43.*

Dawson, T. W. and Weaver, J. T. [1979]. Three-dimensional induction in a non-uniform thin sheet at the surface of a uniformly conducting Earth. *Geophys. J. R. astr. Soc.* , 59:445–462.

Donner, F. and Miersch, G. [1992]. Magneto-Tellurik-Apparatur der Bergakademie Freiberg. *Protokoll Kolloquium Elektromagnetische Tiefenforschung (Hg. V. Haak und H. Rodemann)*, Borkheide.

Duba, A. [1977]. Electrical conductivity of coal and coal char. *Fuel*, 56:441–443.

Egbert, G. D. [1989]. Multivariate analysis of geomagnetic array data: 2. random source models. *J. Geophys. Res.* , 94(B10):14249–14265.

Egbert, G. D. and Booker, J. R. [1986]. Robust estimation of geomagnetic transfer functions. *Geophys. J. R. astr. Soc.* , 87:173–194.

Eisel, M. and Bahr, K. [1993]. Electrical anisotropy in the lower crust of British-Columbia - an interpretation of a magnetotelluric profile after tensor decomposition. *J. Geomag. Geoelect.* , 45(9):1115–1126.

Floyd, J. D. [1994]. The derivation and definition of the 'Southern Uplands Fault': a review of the Midland Valley - Southern Uplands terrane boundary. *Scottish Journal of Geology*, 30:51–62.

Fontes, S. L., Harinarayana, T., Dawes, G. J. K., and Hutton, V. R. S. [1988]. Processing of noisy magnetotelluric data using digital filters and additional data selection criteria. *Phys. Earth. Planet. Int.* , 52:30–40.

Gamble, T. D., Goubau, W. M., and Clarke, J. [1979a]. Error analysis for remote reference magnetotellurics. *Geophysics*, 44:959–968.

Gamble, T. D., Goubau, W. M., and Clarke, J. [1979b]. Magnetotellurics with a remote reference. *Geophysics*, 44:53–68.

Geotools [1993]. *Geotools MT user's guide, Release 6.5.* Geotools corporation, Austin TX.

Goubau, W. M., Gamble, T. D., and Clarke, J. [1978]. Magnetotelluric data analysis: Removal of bias. *Geophysics*, 43:1157–1166.

Greig, D. C. [1971]. *British regional geology: The South of Scotland / D.C. Greig / with chapters by G.A. Goodlet, G.I. Lansden, W. Tulloch.* 3rd. edition (David Cunningham), H.M.S.O., Edinburgh.

Groom, R. W. and Bailey, R. C. [1989]. Decomposition of magnetotelluric impedance tensors in presence of local three-dimensional galvanic distortion. *J. Geophys. Res.* , 94(B2):1913–1925.

Haak, V. [1978]. Interpretationsverfahren für die Magnetotellurik unter besonderer Berücksichtigung lateral variierender Leitfähigkeit im Erdinnern und eines räumlich inhomogenen Magnetfeldes. *Bayer. Akad. Wiss. Math.-Nat. Klasse, Muenchen*, 158.

Haak, V., Ritter, O., and Ritter, P. [1989]. Mapping the geothermal anomaly on the island of Milos by Magnetotellurics. *Geothermics*, 18(4):533–546.

Hampel, F. R., Ronchetti, E. M., Rousseeuw, P. J., and Stahel, W. J. [1986]. *Robust statistics.* Wiley, New York.

Hanstein, T. [1994]. Effekte von Gasleitungen auf MT und VLF-R Sondierungen. *Protokoll Kolloquium Elektromagnetische Tiefenforschung (Hg. K. Bahr und A. Junge)*, Hoechst.

Hobbs, B. A. [1971]. The calculation of geophysical induction effects using surface integrals. *Geophys. J. R. astr. Soc.* , 25:481–509.

Hobbs, B. A. [1992]. Terminology and symbols for use in studies of electromagnetic induction in the Earth. *Surveys in Geophysics*, 13:489–515.

Hohmann, G. W. [1975]. Three-dimensional induced polarisation and electromagnetic modelling. *Geophysics*, 40:309–324.

Huber, P. J. [1981]. *Robust statistics.* Wiley, New York.

Hutton, V. R. S., Galanopoulos, D., Dawes, G. J. K., and Pickup, G. E. [1989]. A high resolution magnetotelluric survey of the Milos geothermal prospect. *Geothermics*, 18(4):521–532.

Hutton, V. R. S., Ingham, M. R., and Mbipom, E. W. [1980]. An electrical model of the crust and upper mantle in Scotland. *Nature*, 287:30–33.

Hutton, V. R. S. and Jones, A. [1980]. Magnetovariation and magnetotelluric investigations in S. Scotland. *J. Geomag. Geoelect.* , 32:141–149.

Hutton, V. R. S., Sik, J. M., and Gough, D. I. [1979]. Electrical conductivity and tectonics of Scotland. *Nature*, 266:617–620.

INMOS [1988]. *Occam 2 reference manual.* Prentice Hall, INMOS document number: 72 occ 45 02.

INMOS [1992]. *INMOS Databook Series, Transputer Databook, third edition 1992.* Prentice Hall, INMOS document number: 72 TRN 203 02.

Jenkins, G. M. and Watts, D. G. [1968]. *Spectral analysis and its applications.* Holden-Day, San Francisco.

Jödicke, H. [1991]. *Zonen hoher elektrischer Krustenleitfähigkeit im Rhenoherzynikum und seinem nördlichen Vorland.* Hochschulschriften Bd.24, Lit Verlag, Münster.

Jones, A. G. [1977]. *Geomagnetic induction studies in Southern Scotland.* PhD thesis, Univ. of Edinburgh.

Jones, A. G., Chave, A. D., Egbert, G., Auld, D., and Bahr, K. [1989]. A comparison of techniques for magnetotelluric response function estimation. *J. Geophys. Res.* , 94(B10):14201–14213.

Jones, F. W. [1973]. Induction in laterally non-uniform conductors: theory and numerical models. *Phys. Earth. Planet. Int.* , 7:282–293.

Jones, F. W. and Price, A. T. [1970]. The perturbations of alternating geomagnetic fields by conductivity anomalies. *Geophys. J. R. astr. Soc.* , 20:317–334.

Jones, P. C. [1992]. *An Electromagnetic Induction Study of South Cornwall, England.* PhD thesis, Univ. of Edinburgh.

Junge, A. [1988]. A telluric field in Northern Germany induced by tidal motion in the North Sea. *Geophysical Journal*, 95:523–533.

Junge, A. [1990]. Robuste Schätzung bivariater Übertragungsfunktionen. *Protokoll Kolloquium Elektromagnetische Tiefenforschung (Hg. V. Haak und H. Homilius)*, Hornburg.

Junge, A. [1992]. Zur Schätzung der effektiven Anzahl der Freiheitsgrade bei der Bestimmung magnetotellurischer Übertragungsfunktionen. *Protokoll Kolloquium Elektromagnetische Tiefenforschung (Hg. V. Haak und H. Rodemann)*, Borkheide.

Junge, A. [1994]. *Induzierte erdelektrische Felder - neue Beobachtungen in Norddeutschland und im Bramwald.* Habil., math.-nat. Fachb., Universität Göttingen.

Junge, A. [1995]. Magnetotellurics in the long period range. *Final Report, EEC Human Capital and Mobility Scheme, prop. nb. ERB 4001 GT 930152.*

Keller, G. V. and Frischknecht, F. C. [1966]. *Electrical Methods in Geophysical Prospecting.* Pergamon Press, Oxford.

Lagios, E. [1979]. *Gravity and other geophysical studies relating to crustal structure of Southeast Scotland.* PhD thesis, Univ. of Edinburgh.

Lahiri, B. N. and Price, A. T. [1939]. Electromagnetic induction in nonuniform conductors, and the determination of the conductivity of the Earth from terrestrial magnetic variations. *Phil.Trans.R.Soc.Lond.*, A237:509–540.

Larsen, J. C. [1975]. Low frequency (0.1-0.6 cpd) electromagnetic study of deep mantle electrical conductivity beneath the Hawaiian islands. *Geophys. J. R. astr. Soc.* , 43:17–46.

Larsen, J. C. [1977]. Removal of local surface conductivity effects from low frequency mantle response curves. *Acta Geodaet.,Geophys. et Montanist. Acad. Sci. Hung.* , 12:183–186.

Larsen, J. C. [1989]. Transfer functions: smooth robust estimates by least-squares and remote reference methods. *Geophys. J. Int.* , 99:645–663.

Leggett, J., McKerrow, W., and Soper, N. [1983]. A model for the crustal evolution of southern Scotland. *Tectonics*, 83:187–210.

Liebig, V. and Schreier, G. [1984]. Aufbau einer mikroprozessor-gesteuerten, mobilen Audio-Magnetotellurik Apparatur. *Protokoll Kolloquium Elektromagnetische Tiefenforschung (Hg. V. Haak und H. Homilius)*, Grafrath/Oberbayern.

Livelybrooks, D., Banks, R. J., Parr, R. S., and Hutton, V. R. S. [1993]. Inversion of electromagnetic induction data for the Iapetus Suture Zone in the UK. *Phys. Earth. Planet. Int.* , 81:67–84.

MacGregor, M. and MacGregor, A. G. [1948]. *British regional geology: The Midland Valley of Scotland.* H.M.S.O., Edinburgh.

Mackie, R. L., Smith, J. T., and Madden, T. R. [1994]. Three-dimensional electromagnetic modeling using finite difference equations: The magnetotelluric example. *Radio Science*, 29(4):923–935.

McKerrow, W. and Cocks, L. [1988]. Oceans, island arcs and olistostromes: the use of fossils in distinguishing sutures, terranes and environments around Iapetus ocean. *J. Geol. Soc. London*, 143:185–191.

McKirdy, D. M., Weaver, J. T., and Dawson, T. W. [1985]. Induction in a thin sheet of variable conductance at the surface of a stratified Earth - II. Three-dimensional theory. *Geophys. J. R. astr. Soc.* , 80:177–194.

Olhoeft, G. R. [1985]. *Electrical Properties of Rocks and Minerals.* Short Course Notes, Golden, Colorado.

Olsen, N. [1991]. *Untersuchung von tagesperiodischen Variationen des Erdmagnetfeldes mit neueren statistischen Methoden.* Doktorarbeit, Universität Göttingen.

Papoulis, A. [1987]. *Signal Analysis.* McGraw Hill, New York, 3rd edition.

Parkinson, W. D. [1959]. Directions of rapid geomagnetic fluctuations. *Geophys. J.*, 2,No1:1–14.

Parr, R. S. [1991]. *Development of Magnetotelluric Processing and Modelling Procedures - Application to Northern England.* PhD thesis, Univ. of Edinburgh.

Parr, R. S. and Hutton, V. R. S. [1993]. Magnetotelluric studies in and adjacent to the Northumberland Basin, Northern England. *Phys. Earth. Planet. Int.* , 81:43–66.

Press, W. H., Flannery, B. P., Teukolsky, S. A., and Vetterling, W. T. [1988]. *Numerical Recipes in C.* Cambridge University Press.

Price, A. T. [1949]. The induction of electric currents in thin sheets and sheels. *Q. J. Mech. appl. Math.*, 2:283–310.

Qian, W. and Boerner, D. E. [1995]. Electromagnetic modelling of buried line conductors using an integral equation. *Geophys. J. Int.* , 121:203 – 214.

Reddy, I. K. and Rankin, D. [1971]. Magnetotelluric effect of dipping anisotropies. *Geophys. Prospecting*, 19:84–97.

Ritter, O. [1988]. Auswertung von Audiomagnetotellurik-Registrierungen auf der Insel Milos. Diplomarbeit, Freie Universität Berlin.

Ritter, O. and Dawes, G. [1992]. A transputer-based multi-station multi-technique geophysical data acquisition system – S.P.A.M.Mk III. *Protokoll Kolloquium Elektromagnetische Tiefenforschung (Hg. V. Haak und H. Rodemann)*, Borkheide.

Ritter, P. [1995]. *Separation of Local and Regional Information in GDS.* PhD thesis, University of Edinburgh (in preparation).

Ritter, P. and Ritter, O. [1995]. The BC87 dataset: Application of hypothetical event analysis on distorted GDS response functions and some thinsheet modelling studies of the deep crustal conductor. *J. Geomagn. Geoelectr.* , submitted.

Rokitiansky, I. I. [1982]. *Geoelectromagnetic Investigation of the Earth's Crust and Mantle.* Springer-Verlag, Berlin - Heidelberg - New York.

Schmucker, U. [1970]. Anomalies of geomagnetic variations in the southwestern United States. *Bull. Scripps. Inst. Oceanogr.*, 13.

Schmucker, U. [1971]. Neue Rechenmethoden zur Tiefensondierung. *Protokoll Kolloquium Elektromagnetische Tiefenforschung*, Rothenberge:1 – 39.

Schmucker, U. [1987]. Substitute conductors for electromagnetic response estimates. *PAGEOPH*, 125.

Schmucker, U. and Weidelt, P. [1975]. *Electromagnetic Induction in the Earth.* Lecture Notes (not published), Aarhus.

Schnegg, P. A. and Fischer, G. [1980]. On-line determination of apparent resistivity in magnetotelluric soundings. *Protokoll Kolloquium Elektromagnetische Tiefenforschung (Hg. V. Haak und H. Homilius)*, Berlin-Lichtenrade.

Schultz, A. and Larsen, J. C. [1983]. Analysis of zonal field morphology and data quality for a global set of magnetic observationary daily mean values. *J. Geomagn. Geoelectr.* , 35:835 – 846.

Schultz, A. and Larsen, J. C. [1987]. On the electrical conductivity of the earth's interior I: mid-mantle response function computation. *Geophys. J. R. astr. Soc.* , 88:733 – 761.

Siemon, B. [1991]. *Ein Interpretationsverfahren für induktiv schwach gekoppelte Leitfähigkeitsanomalien, dargestellt am Beispiel des Salzstockes Wesendorf im Giffhorner Trog.* Doktorarbeit, Universität Göttingen.

Sims, W., Bostick, F., and Smith, H. [1971]. The estimation of magnetotelluric impedance tensor elements from measured data. *Geophysics*, 37(5):938–942.

Steveling, E. and Leven, M. [1992]. Ein Datenlogger für niederfrequente geophysikalische Messungen. *Protokoll Kolloquium Elektromagnetische Tiefenforschung (Hg. V. Haak und H. Rodemann)*, Borkheide.

Strangway, D. W., Swift, C. M., and Holmer, R. C. [1973]. The application of audio-frequency Magnetotellurics (AMT) to mineral exploration. *Geophysics*, 38(6):1159 – 1175.

Sule, P. O. [1985]. *A broadband magnetotelluric investigation in Southeast Scotland.* PhD thesis, Univ. of Edinburgh.

Sule, P. O., Hutton, V. R. S., and Dumitrescu, C. [1993]. Subsurface structure of SE Scotland from broadband magnetotelluric measurements. *Phys. Earth. Planet. Int.* , 81:9–24.

Swift, C. M. [1986]. A magnetotelluric investigation of an electrical conductivity anomaly in the Southwestern United States. *in Magnetotelluric Methods, Society of Exploration Geophysicists, Edited by K. Vozoff*, series no. 5:156–166.

Takasugi, S., Tanaka, K., Kawakami, N., and Muramatsu, S. [1992a]. Effectiveness of spatially dense MT measurements for a study of fine resistivity structure - a case study at Hohi Sugawara, Japan. *J. Geomagn. Geoelectr.* , 44(3):223–242.

Takasugi, S., Tanaka, K., Kawakami, N., and Muramatsu, S. [1992b]. High spatial resolution of the resistivity structure revealed by a dense network MT measurement - a case study in the Minamikayabe Area, Hokkaido, Japan. *J. Geomagn. Geoelectr.* , 44(4):289–308.

Telford, W. M., Geldart, L. P., Sheriff, R. E., and Keys, D. A. [1976]. *Applied Geophysics.* University Press Cambridge, Cambridge - London - New York - Melbourne.

Tikhonov, A. N. [1950]. On determining electrical characteristics of the deep layers of Earth's crust (in Russian). *Dokl. Akad. Nauk. SSSR*, 73:295 – 297.

Valiant, M. J. [1976]. NERC geologger technical handbook. *NERC Geomagnetic Equipment Pool, internal publication.*

Vasseur, G. and Weidelt, P. [1977]. Bimodal electromagnetic induction in non-uniform thin sheets with application to the northern Pyrenean induction anomaly. *Geophys. J. R. astr. Soc.* , 51:669–690.

Volland, H. [1986]. *Atmospheric electrodynamics.* Springer-Verlag, Berlin.

Walden, A. T. [1986]. Estimating confidence intervals for the gain and phase of frequency response functions. *Geophys. J. R. astr. Soc.* , 87:519 – 537.

Walton, E. K. [1983]. In Craig, G.Y. (ed.) Geology of Scotland (2nd edition). *Scottish Academic Press, Edinburgh.*

Wannamaker, P. E., Stodt, J. A., and Rijo, L. [1987]. A stable finite element solution for two-dimensional magnetotelluric modelling. *Geophys. J. R. astr. Soc.* , 51:2131–2144.

Weaver, J. [1994]. *Mathematical Methods for Geo-Electromagnetic Induction.* Research Studies Press, Taunton, England.

Weaver, J. T. [1973]. Induction in a layered plane Earth by uniform and non-uniform source fields. *Phys. Earth. Planet. Int.* , 7:266–281.

Weaver, J. T. [1990]. On the addition of induction vectors. *Protokoll Kolloquium Elektromagnetische Tiefenforschung (Hg. V. Haak und H. Homilius)*, Hornburg.

Wehmeier, M. [1988]. Ein Modularkonzept für die Analogelektronik registrierender geophysikalischer Messgeräte - universelles Interface zwischen Sensor und Datenaufzeichnung. *Protokoll Kolloquium Elektromagnetische Tiefenforschung (Hg. V. Haak und H. Homilius)*, Königstein im Taunus.

Weidelt, P. [1972]. The inverse problem of geomagnetic induction. *Zeitschrift für Geophysik*, 38:257–289.

Weidelt, P. [1975]. Electromagnetic induction in three-dimensional structures. *J. Geophys.*, 41:85–109.

Weidelt, P. [1978]. *Entwicklung und Erprobung eines Verfahrens zur Inversion zweidimensionaler Leitfähigkeitskontraste in E-Polarisation.* Habil. math.-nat.Fak., Universität Göttingen.

Wiese, H. [1962]. Die Streichrichtung der Untergrundstrukturen des elektrischen Widerstandes, erschlossen aus geomagnetischen Variationen. *PAGEOPH*, 52:83–103.

Zhang, P., Chouteau, M., Mareschal, M., Kurtz, R., and Hubert, C. [1995]. High-frequency magnetotelluric investigation of crustal structure in north-central Abitibi, Quebec, Canada. *Geophys. J. Int.*, 120:406–418.

Zhang, P., Pedersen, L. B., Mareschal, M., and Chouteau, M. [1993]. Channelling contribution to tipper vectors: a magnetic equivalent to electrical distortion. *Geophys. J. Int.* , 113:693 – 700.

A Appendices

A.1 Site details of the Middleton field experiment

MVM - sites									
Site		records / freq. band				site coordinates			
set	no.	B0	B1	B2	B3	latitude	longitude	easting	north.
50	OR	221	177	50	19	03:00:39.39	55:48:14.09	336688	657138
	EO	221	177	50	19	03:00:37.96	55:48:10.85	336713	657038
	EE	120	57	0	0	03:00:37.27	55:48:07.19	336725	656925
30	WW	100	150	163	37	03:00:37.27	55:48:07.19	336725	656925
	WO	100	50	52	0	03:00:35.09	55:48:03.95	336763	656825
	OR	100	150	163	37	03:00:30.09	55:48:02.33	336850	656775
	EO	100	50	52	0	03:00:27.91	55:47:59.90	336888	656700
	EE	100	50	52	0	03:00:25.61	55:47:57.57	336938	656625
10	WW	200	200	188	399	03:00:11.42	55:47:48.18	337175	656338
	WO	200	200	188	204	03:00:07.80	55:47:45.33	337238	656250
	OR	300	250	350	568	03:00:04.93	55:47:43.10	337288	656181
	EO	200	200	188	399	02:59:59.19	55:47:41.71	337388	656138
	EE	200	200	188	399	02:59:52.75	55:47:41.28	337500	656125
20	WW	200	200	296	408	02:59:52.75	55:47:41.28	337500	656125
	WO	200	0	0	0	02:59:47.70	55:47:39.67	337588	656075
	OR	200	200	296	408	02:59:42.70	55:47:38.47	337675	656038
	EO	200	200	296	408	02:59:31.90	55:47:38.05	337863	656025
	EE	200	200	204	204	02:59:26.91	55:47:37.24	337950	656000
40	WW	200	200	102	65	02:59:26.91	55:47:37.24	337950	656000
	WO	200	200	102	65	02:59:22.60	55:47:35.62	338025	655950
	OR	200	200	102	65	02:59:18.98	55:47:33.61	338088	655888
	EO	200	200	102	65	02:59:14.67	55:47:31.99	338163	655838
	EE	200	200	102	65	02:59:11.11	55:47:29.40	338225	655758
60	WW	400	300	201	204	02:59:11.11	55:47:29.40	338225	655758
	WO	400	400	201	204	02:59:01.68	55:47:27.52	338300	655700
	OR	604	502	269	449	02:59:01.75	55:47:25.52	338388	655638
	EO	400	400	201	204	02:58:56.75	55:47:25.09	338475	655625
	EE	400	400	201	204	02:58:52.40	55:47:24.71	338550	655613
MT - sites									
50	OR	221	177	50	19	03:00:39.39	55:48:14.09	336688	657138
10	OR	100	50	170	169	03:00:04.93	55:47:43.10	337288	656181
60	OR	204	102	68	245	02:59:01.75	55:47:25.52	338388	655638

Table 5: Site details of the Middleton field experiment.

A.2 Site details of the Garvald field experiment

site	latitude	longitude	easting	north.
Base	02:39:18.02	55:54:17.46	359087	668020
L003	02:39:05.78	55:54:12.91	359275	668037
L004	02:39:12.29	55:54:09.87	359175	667937
L005	02:39:32.53	55:54:34.17	358825	668750
L006	02:39:37.56	55:54:39.11	358737	668900
L007	02:39:33.97	55:54:55.44	358787	669450
L008	02:39:23.13	55:54:58.86	358600	669550

Table 6: Site details of the Garvald field experiment.

A.3 Glossary: technical terms

Term:	Explanation
AC	Alternating Current
A/D	Analogue to Digital; ADC: analogue to digital converter
CISC	Complex Instruction Sets Computer
CMR	Common Mode Rejection
CPU	Central Processing Unit
DC	Direct Current
FFT	Fast Fourier Transform
DMA	Direct Memory Access
DRAM	Dynamic Random Access Memory
DSP	Digital Signal Processing
EPROM	Erasable Programable Read Only Memory
LED	Light Emitting Diode
FIR	Finite Impulse Response (filter)
FPU	Floating Point Unit
GPS	Global Positioning System
IIR	Infinite Impulse Response (filter)
I/O	input/output
MUX	Multiplexer
PC	Personal Computer
RAM	Random Access Memory
RISC	Reduced Instruction Set Computer
SCSI	Small Computer System Interface
SPAM	Short Period Automatic Magnetotelluric
SRAM	Static Random Access Memory
TRAM	Transputer Module
TTL	Transistor Transistor Logic

Table 7: *Glossary: technical terms.*

A.4 Published Papers

The following papers have been published during the course of this study:

- O. Ritter and G. Dawes, [1992], *A Transputer-based Multi-station Multi-technique Geophysical Data Acquisition System – S.P.A.M. MkIII*, Protokoll Kolloquium Elektromagnetische Tiefenforschung (Hg. V. Haak und H. Rodemann), Borkheide.

- O. Ritter, [1994], *Ein AMT Experiment zur hochauflösenden Kartierung von Vertikalfeldvariationen*, Protokoll Kolloquium Elektromagnetische Tiefenforschung (Hg. K. Bahr und A. Junge), Hoechst.

- P. Ritter and O. Ritter, [submitted in 1995], *The BC87 Dataset: Application of Hypothetical Event Analysis on Distorted GDS Response Functions and Some Thinsheet Modelling Studies of the Deep Crustal Conductor*, J. Geomagn. Geoelectr.

Oliver Ritter and Graham Dawes

A Transputer-based Multi-station Multi-technique Geophysical Data Acquisition System - S.P.A.M. Mk III

S.P.A.M. systems are SHORT-PERIOD AUTOMATIC MAGNETOTELLURIC instruments developed since 1980 by Graham Dawes at the University of Edinburgh, with updates as shown below:

revision:	year	note:
Mk I	1980-81	prototype
MK II	1983-84	main design phase
Mk IIa	1986	CPU upgrade
Mk IIb	1988	Data storage and printer upgrade

These instruments have been used in many studies worldwide not only by the University of Edinburgh but through the acquisition of two systems by N.E.R.C (the Natural Environment Research Council) for its general equipment pool by all other U.K. EM Induction researchers. S.P.A.M. systems are also in use in India by the Indian Institute of Geomagnetism (Bombay) and in Canada by the University of Alberta.

Since the last upgrade in the mid eighties many electronic devices have been greatly improved in terms of noise, power consumption and size and also completely new concepts for computational applications have become available. As a result, in 1990 Graham Dawes with support from N.E.R.C. undertook a feasibility study of a Transputer-based upgrade of S.P.A.M. This study (Dawes 1990) has led to a further major development phase with work in progress on a prototype of S.P.A.M. Mk III, a system for the acquisition of time-varying geophysical (not only magnetotelluric) data. This will be completed by October 1993.

Many aspects of the Mk III design are completely novel for geophysical instrumentation as indicated by this article which overviews the concepts and main design goals. Because of the historical association of S.P.A.M. with magnetotellurics the main ideas will be presented with respect to that technique.

Existing MT instrumentation and its deficiences

Historically MT studies were concerned with determination of the electrical resistivity of the Earth's crust or upper mantle on a regional scale. Signals in a period range between 100s and 10000+s were recorded with a typical site spacing of a few kilometres to some 10 kilometres. To collect enough data, recording was undertaken for 2 weeks to one month or even longer at each site. The recording systems for this frequency range were initially paper chart recorders, then data loggers with as little power consumption as possible to maximise battery life. Robustness, small size and weight were also desirable features for these systems. Loggers were primarily or only used to store data - they nor-

mally did not perform any data processing. In the Protokoll Elektromagnetische Tiefenforschung there are several papers illustrating how data loggers have been (and still are being) improved (Beblo, Donner, Steveling, this issue, Beblo&Hofer 1986, Beblo&Liebig 1986, Knödel et al. 1982, Steveling 1982)

Almost from their introduction, audiomagnetotelluric instruments (1000Hz - 10+s) have had very different characteristics, with real time processing being undertaken in the field. In some systems this involved cumbersome additional equipment such as bulky computers, large batteries and probably an additional vehicle or trailer. AMT magnetic sensors are typically induction coils rather than fluxgate magnetometers. Special hardware filters (notches) are incorporated to eliminate mains power frequencies and recording in narrow frequency bands is necessary to cover the whole dynamic range of the signals. (Liebig&Schreier 1984, Micheel 1980, Schnegg&Fischer 1980) Most AMT instruments record short, non continuous time intervals to enable the real time data processing. Typically it only takes between a few hours to one day to gather enough data at a site. Site spacing for an AMT survey is normally much less than for the traditional MT survey, being some hundreds of meters to a few kilometres (Brasse 1988, Drewes 1988) .

Today both instrument types merge as they benefit from improvements in memory and CPU technology. It is possible to achieve higher sampling rates with data loggers while real time systems have become increasingly more portable and continue to require less power. On the other hand, since it may be necessary to leave an instrument at the same place for a few days or some weeks - for the longer period soundings - the two different kinds of instruments have a complementary role to play with ideally both being deployed in many studies.

Flexibility of instruments and main design goals for S.P.A.M.III

The flexibility of instrumentation seems likely to become increasingly important for (A)MT projects in the future. Situations exist where acquisition other than that of standard 5-component-MT and data from very dense profiles or grids are advisable. New experiments with remote magnetic(s) or E- and B-mapping configurations could help to improve our understanding of some geological features. The acquisition of additional parameters, such as the vertical electric field which could be monitored with antennas or in certain active areas, the common registration of seismic and magnetotelluric signals might be interesting. In general, the instrumentation should be highly upgradable to adapt best to the problems posed by the physical, geological, logistical and the local noise conditions. Thus, the main design goals for the new S.P.A.M. have been defined as:

- Flexibility in quantity, type and distribution of sensors: Many kinds or numbers of sensors can be connected to one instrument, remote sensors can be connected by the concept of a distributed, networked instrument with digital data transmission.
- Portability: Low power consumption to allow for battery operation and small size and weight so that operation is not restricted to use from a vehicle.
- Continuous wide band recording with digital sub-banding: Because of a greatly improved dynamic range, data covering the whole frequency range can be recorded in one hardware band. The data are then digitally decimated and filtered into sub-bands.

Thus, short and long period data are recorded simultaneously, reducing the overall recording times.

- Real time processing and stand alone operation: Real time operation enables the evaluation of data quality, noise conditions and best system settings. All inputs, even for distributed systems with remote sensors can be made centrally. 'Stand alone' operation to gather more data (long periods, 'dead band') can be undertaken without further user interaction.
- Up- and down-gradable computational power: As the more powerful computers also have higher power consumption, 16 and 32 bit processors of the same compatible transputer family are used to optimise the overall performance.
- Accurate time synchronisation: This enables applications using the remote reference or difference field techniques (or Seismics).
- Integral calibration facility: This facility is used to test for functioning and accuracy of all or selected devices of the instrument (excluding the sensors).
- Support for mixed methodologies: By common registration , e.g. MT + seismic, on hardware and software level mixed methodologies can be supported.

Instrument overview and principal components

S.P.A.M. is constructed in a highly modular fashion. Since a module is an option, replacing one module by another is equivalent to invoking another option (compare Wehmeier 1988). The principal instrumental components, consisting of many smaller modules, are shown in figure 1 and comprise:

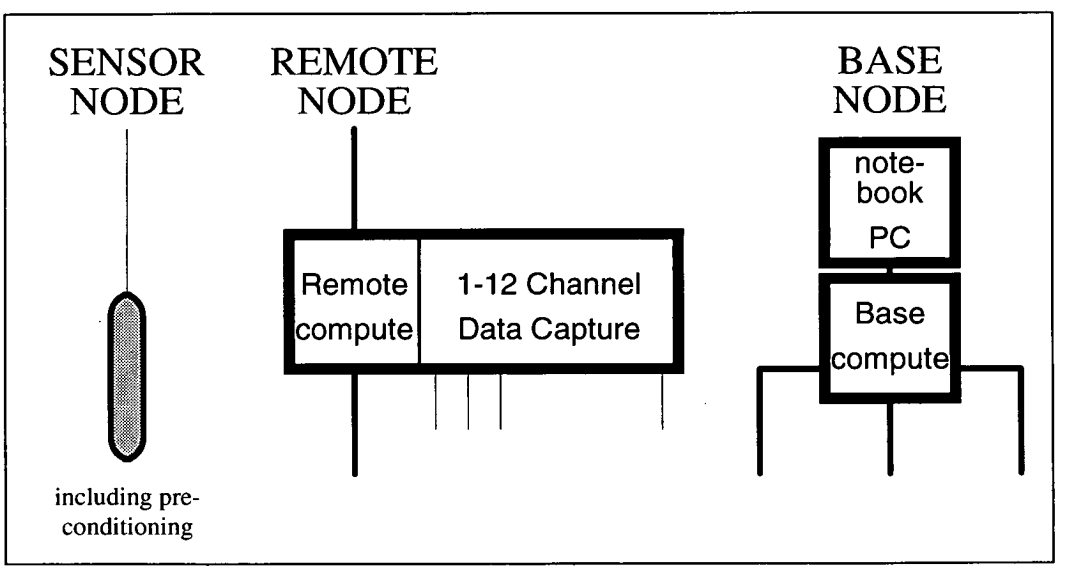

Figure 1: The principal instrument components

- the sensor node: - sensors (e.g. magnetometers, electrodes or seismometers) including signal preconditioning (e.g. preamplifiers, filters)

- the remote node: - data capture, all analogue signal conditioning, like band -pass and notch filtering, signal amplification and finally, analogue to digital conversion. Furthermore the digital data are decimated, digitally filtered, subjected to FFT and distributed to the base node.
- the base node: - collection of data in the time and/or frequency domain from all remote nodes. Performance of real time processing of all time synchronous channels and calculation of all (inter-site) transfer functions. 1D & 2D inversion, contouring and execution of user supplied software dependent on the actual configuration of the sensors. Data transfer to the PC, the integrated hard disk or an optional printer.
- notebook PC: - the user interface to the base node and the whole instrument. Software for instrument set-up, control and testing, graphical data visualisation and data storage. This can be disconnected during stand alone operation.
- the branch node: - a device to increase the number of communication branches by two (not shown in the figure).

In figure 2 the modular concept of S.P.A.M. is illustrated. Analogue signals are fed from the sensors or the calibration signal generator into the analogue signal conditioning modules of a REMOTE. The first transputer module (TRAM) performs data acquisition and oversampling filtering. As the output registers of the analogue to digital converters are directly mapped into the transputer memory, very high sampling rates can be achieved. From the acquisition module, the data are transferred to the REMOTE computer TRAM for digital band pass filtering, prewhitening and transformation of the data to the frequency domain. Corrections for sensor response functions are also performed at this level.

BASE and REMOTEs have three and two channels/branches respectively for long distance digital communication. The communication modules and the attainable data transfer rates may vary, depending on the physical media used (e.g. cable or telemetry). REMOTEs can be connected to each other and a REMOTE or branches of REMOTE(s) can be connected to a BASE. Thus, a networked instrument with virtually any number of channels can be created. This concept is limited by the accumulated bandwidth of the communication media and at the base the computational power of the TRAMs.

Time series and/or frequency domain data are stored on the internal hard disk and processed by the BASE computer module. Time series, frequency spectra and (intermediate) results can be visualised and archived on a standard notebook or laptop PC. Optionally, hard copies may be produced on a fast thermal printer.

As all REMOTEs are usually connected to one BASE, all channels are synchronised with a time signal generated by the BASE. An accuracy better than 5μs is anticipated. With external clocks (e.g. GPS or DCF), higher accuracy or synchronisation of unconnected S.P.A.M.s can be accomplished.

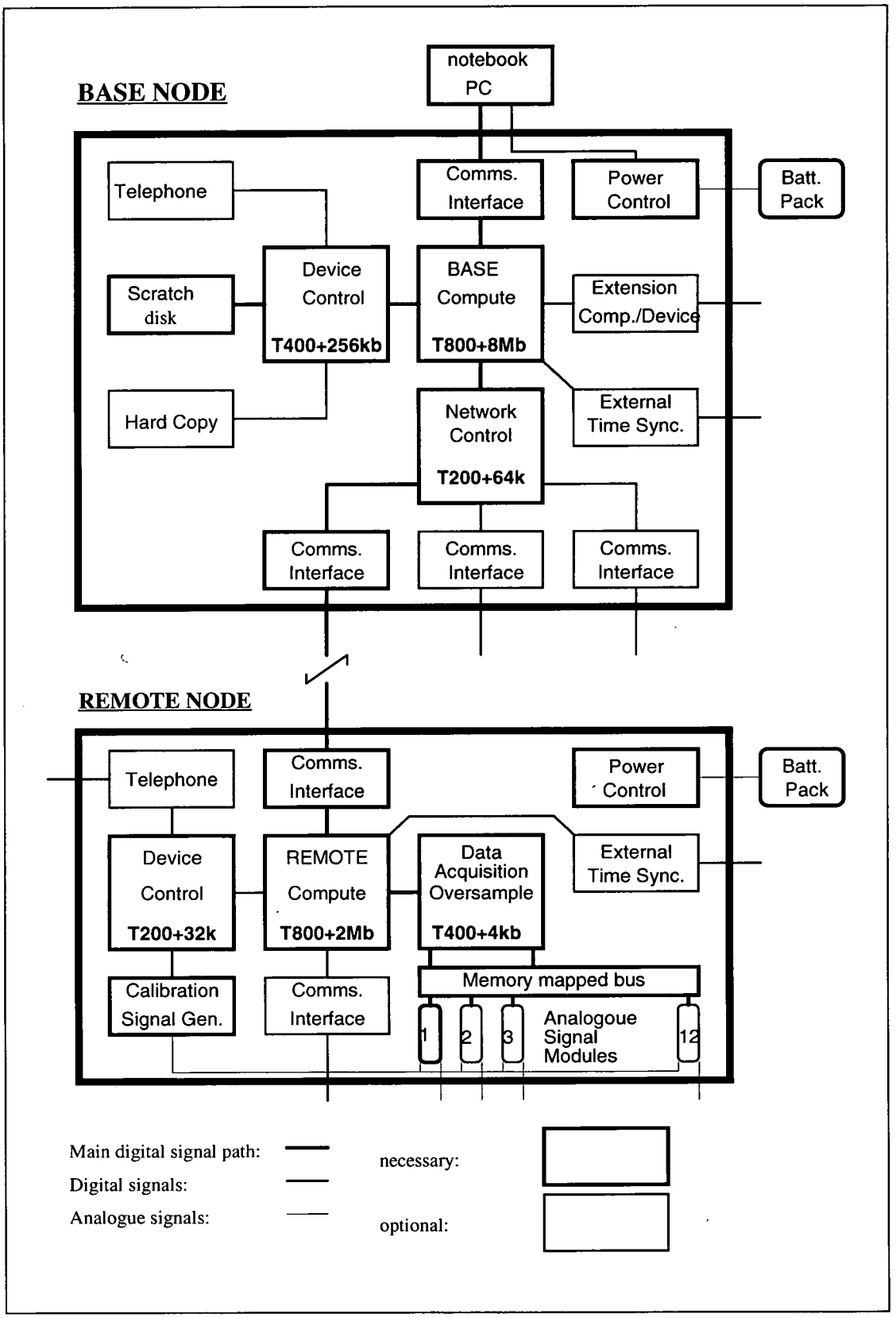

Figure 2: The modular concept of S.P.A.M. III

The need for a telephone may not be obvious, but one would be very helpful in the initial set-up phase, for calibration and maintainance of a working network. As all the high speed digital connections are already available, a telephone could very easily be incorporated into the system.

To save battery life, modules which are not used for some time are switched off by the power control module. If the device is needed at a later stage, it can be re-activated.

The modules

While some of the components shown in figure 2 are optional (e.g. telephone, hard copy or an external time base), others can be replaced by a different type or configuration (e.g. different analogue signal conditioning modules, size of the hard drive or the amount of RAM for a TRAM).

Data acquisition modules

The data acquisition modules operate in three frequency ranges:

- HF (high frequency) band: 8KHz - 1Hz
- SP (short period) band: 128Hz/2kHz (switchable) - 1000s[1]
- LP (long period) band: 1Hz - DC

All modules have fixed low pass filters (two, for the SP board), but the high pass filter corner frequencies are switchable over a wide range. Therefore, the values given above are only examples. The HF and SP boards will contain up to two notch filter modules for which the frequencies can be chosen (e.g. 16.6, 50, 60, 100Hz, etc.). For the HF band the maximum number of channels per REMOTE is 8, while for other bands it is 12. For the low frequency bands the signal are recorded continuously without the need to interrupt the data acquisition for processing the data. In the high frequency mode of the SP band (2kHz - 1Hz) and the HF bands, time windows of a fixed length are recorded and then processed by the same software as for real-time.

To improve signal to noise ratios all channels are oversampled, depending on the frequency band, by factors of 2, (2)4 or 16 respectively The CS5101, CS5102 and CS5505, 16-bit AD converters from CRYSTAL Semiconductor are used for the HF, SP and LP bands, respectively.

The signal amplification is divided into static and dynamic gain sections, which both provide amplification in steps of a power of 2 from 2^0 to 2^7. Initially the signal amplitudes are raised by the static gains, which are normally not changed during recording. After all the analogue filtering is done, the signals are again adjusted by an auto-gain circuit. Their amplification is changed continuously, while data are being recorded. This feature has been used successfully in the earlier S.P.A.M.s with the objective of further enhancing the dynamic range. The overall sample resolution is estimated to be 20-22bits (16Bits:ADC + 2Bits:auto-gain+ 2-4Bits:digital decimation) or 120db-132db. The

---

[1]Only the SP board will be built in the initial design phase.

overall signal amplification is between 2^0 and 2^{14} plus any additional external preamplification (e.g. telluric).

Compared to the previous versions of S.P.A.M., more time domain signal processing can be done digitally, simplifying the design needs for the analogue filters. Very stable and cost efficient 5-pole low pass filters can be built with low noise specifications. An active 5-pole low-pass filter, in combination with a 4-times digital oversampling filter, results effectively in a 15-pole filter, with 90db signal reduction at the Nyquist frequency.

Computer modules

The computational heart of S.P.A.M. III is the transputer, a family of single chip, fast RISC microcomputers, each with its own internal memory, 2 timers and four high speed serial channels, the links. Transputers communicate through these bi-directional links at transfer rates selectable between 5/10/20 Mbaud. Three compatible transputer types coexist in the system:

- T200: 16-Bit-CPU for input/output operation, device control and network control
- T400: 32-Bit-CPU for data acquisition and oversampling filter
- T800: 32-Bit-CPU + 64-Bit-FPU for digital filtering (floating point), FFT and general data processing and interpretation.

The CPU, FPU, links and timers all work independently from each other. For example, while an operation is being executed by the FPU, data for the next operation is simultaneously being prepared by the CPU and the 4 links are transferring data to other transputers under DMA (direct memory access).

Transputers can be programmed by high level languages, such as FORTRAN, C and OCCAM. They provide very efficient, embedded multi-tasking without the need for an operating system. TRAM modules can consist of only internal on-chip-memory (4kb) or up to 4Gb external memory in a linear address space. Different kinds of memory (e.g. register, EPROM, SRAM and DRAM) can be attached at the same time. Typical power consumption is in the range 300mW to 700mW. Ready configured TRAM modules are commercially available and if necessary more powerful devices such as the TMS 320C40 or the new H9000 can be connected via the transputer links.

Digital communication modules

Although the constructors of these transputers probably never considered the requirements of a distributed MT instrument, our tests have shown that for distances of up to 300m, data transfer rates of 100kbyte/s can be achieved with normal cables (see fig. 3). Despite the long distances between single processors they still behave as a normal transputer cluster since they are connected by their standard link interfaces.

However, depending on the distance between BASE and REMOTEs different media and therefore communication modules for data transfer are necessary:

- <300m(-500m) - Dual twisted pair cables,are being used for the initial design.
- <4000m - Cable with repeater boxes or fibre optics: Longer distances can be achieved with normal dual twisted pair cables if the signals are refreshed every 200m by repeater boxes. Fibre optics weigh less than normal cable and provide very high transfer rates (in the order of Mbyte/s) but are very expensive and difficult to repair.
- >4000m - Radio telemetry: Telemetry could be used in applications where REMOTES are too far away to be connected by cable. Typical transfer rates for telemetry systems are in the range of 4kbaud and hence real time operation at higher frequencies would not be possible.

Transputers connected internally, inside a BASE or REMOTE communicate at full speed, e.g. 20 MBit/s. Depending on the peripherals to be attached, ports and software drivers for parallel (CENTRONICS), SCSI and serial (RS232 or RS422) connections can be included.

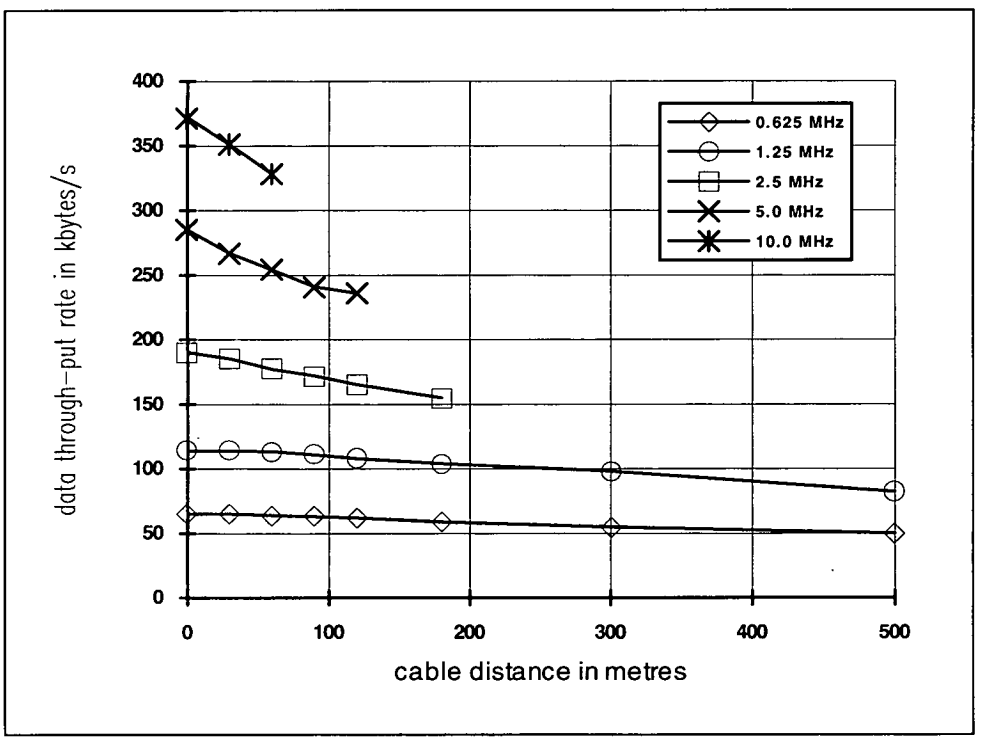

Figure 3: Transmission test results: Data through-put rates at varying cable lengths using RS422 receiver/transmitter devices. The transputer links are operated at frequencies between 0.625 MHz and 10 MHz. For distances of 300m transfer rates of more than 100kbytes/s are achievable.

Peripheral modules

The following peripherals can or must be connected to a S.P.A.M. system:

- internal hard disc drive as a scratch disk for temporary data storage, size e.g. 100Mb
- internal printer: a high speed thermal printer (e.g. 640 dots/line, 200 dotlines/s)

- time synchronisation: e.g. Omega clocks, GPS, DCF (optional)
- inter-node telephone (optional)
- calibration signal generator
- notebook PC (user interaction and data storage)
- external data storage: to dump data e.g. optical disk, exabyte, streamer (optional)

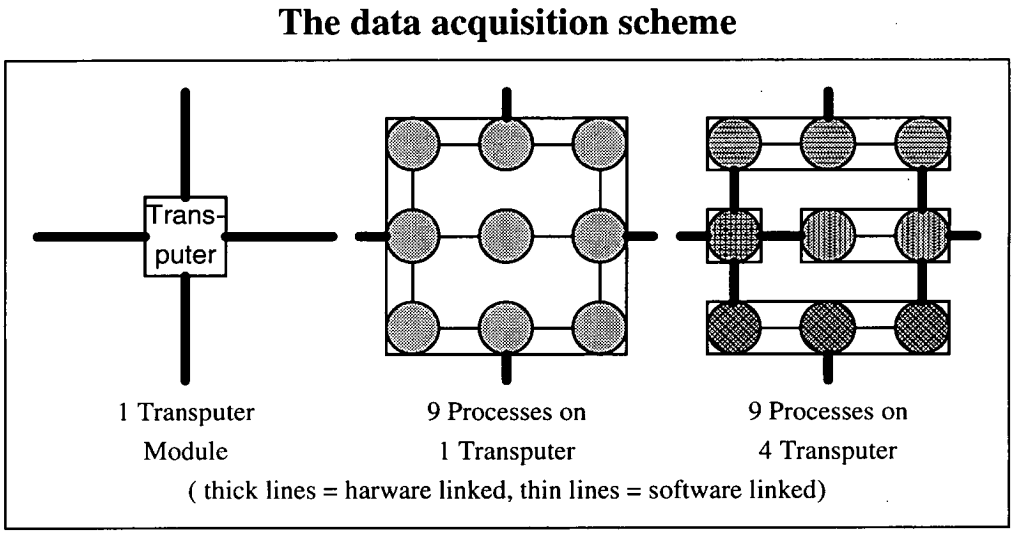

Figure 4: From the programmers viewpoint, hardware and software channels look the same. The actual number of transputers is specified at run time with a configuration file

On a Transputer a programme or better a *process* is defined as a piece of code that starts, performs a number of actions and may or may not stop. Many processes may run in parallel or concurrently. A process is the standard building block for both hardware and software. This is achieved at the programming level where no distinction is drawn between a number of concurrent processes on one transputer and the same processes on an arbitrary number of transputers. This is because all processes communicate with each other by channels and only at the final programme configuration stage these channels are defined as being either (see. figure 4)

- soft(ware) channels or
- hard(ware) channels, physical links between transputers.

Internally they are supported in the same way by the instruction set for concurrent processing within a transputer.

In the current system up to 12 channels can be digitised synchronously and in parallel. Each channel can now be *cascaded* (band pass filtered and decimated) independently from all others. The cascading however must be done sequentially (see figure 5), as the times series with fs/4 (fs=sampling rate) is derived from the fs/2 series which was itself generated from the original time series fs. The processing modules in this data acquisition scheme are low pass filter, high pass filter, prewhitening and fast Fourier transformation. After correct synchronisation of the cascaded signals however, all the processing code can be executed concurrently. Once again, the advantages of the transputer concept

for this task should be obvious. Once the processing modules are written, the problem is reduced to connection of the correct data streams (links). The transputer itself ensures an optimised system performance.

Fig. 5 also shows that the data can be forwarded as the original time series, as decimated and low pass filtered time series, as band pass filtered time series or as time windows, transformed to the frequency domain. Any mixture is possible and all time series are the continuous, non-interrupted streams of data which can be stored and processed at a BASE.

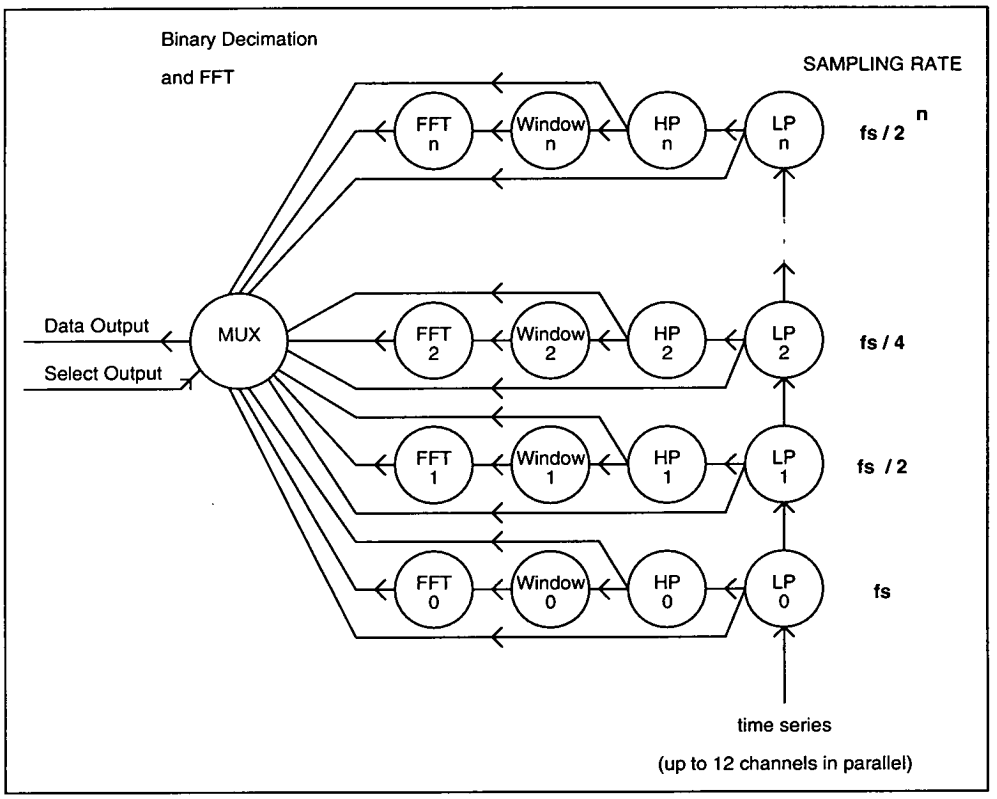

Figure 5: The data acquisition scheme

For this cascade scheme, the frequency bands in which the data are to be processed can be selected dynamically and modified in steps of a power of two.

Decimation	0	1	2	3	4	5	6	7	8	9	10	11	12	13	14	15	16	17
Band-corners	128	64	32	16	8	4	2	1	2	4	8	16	32	64	128	256	512	1024
Band 1	[----------																	
Band 2					[----------													
Band 3							[----------											
Band 4									[----------									
Band 5											[----------							]

Fig. 6: frequency bands can dynamically be selected and modified

In fig 6 for example, 5 overlapping frequency bands (more are possible) in the range 128Hz - 1024s have been selected. Wider bands have been used at both ends of the frequency range but small, narrow frequency bands at around 1Hz. This enables the identi-

fication and isolation of noise sources and derivation of sub-bands with similar signal amplitudes.

As the frequency range has to be divided into sub-bands for processing, this seems to be the most flexible way and it can be implemented painlessly with transputers. The data can be processed in a combination of cascade decimation and conventional methods with the length of the time segments depending on the band width (e.g. 1024 samples). As robust processing methods will also be incorporated good quality results are expected in real-time, and without the need for further main frame processing as is the current practice.

Typical field layouts

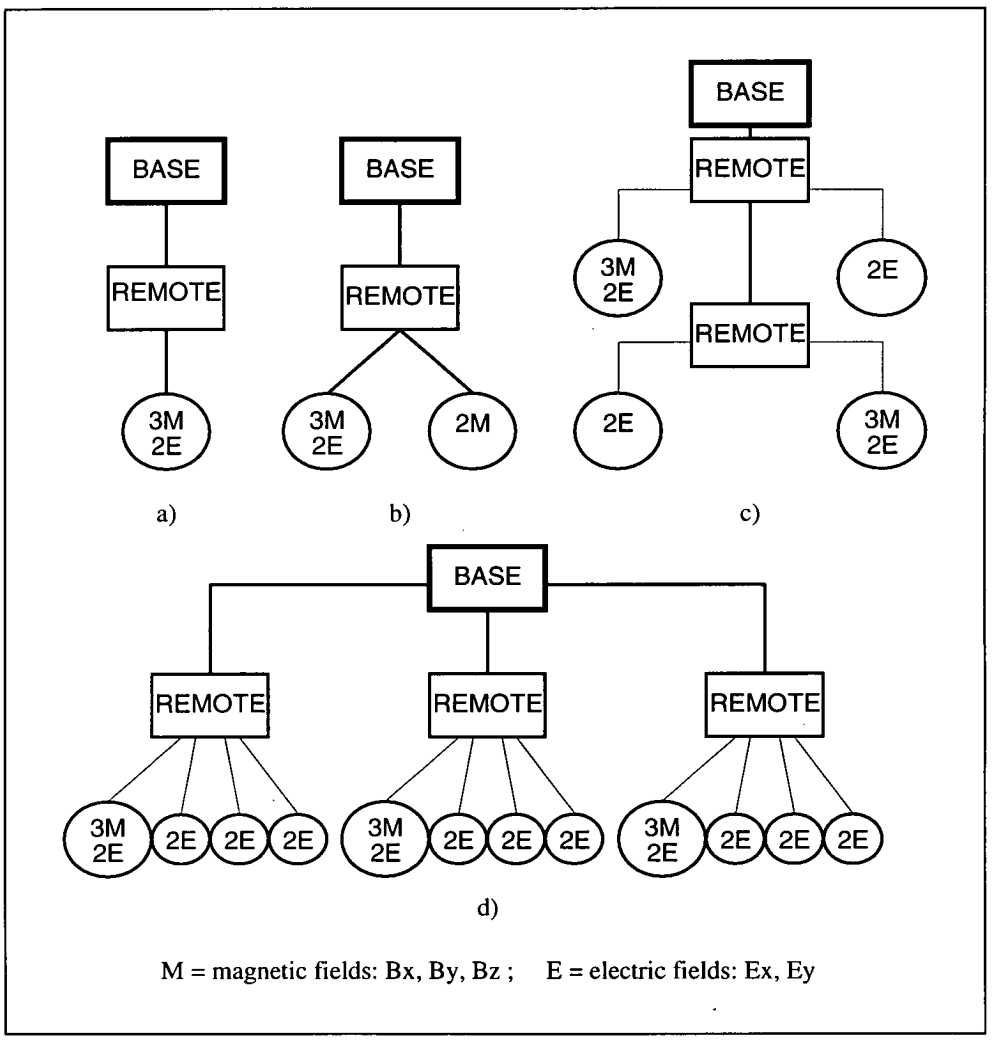

Figure 7 a-d: Example field layouts with S.P.A.M.III

Some field layouts using the S.P.A.M concept are sketched in Fig 7. In 7a and 7b the normal 5 component MT and the Remote Reference cases respectively are shown. In 7c two 5 component MT sites plus two remote telluric sites are set-up on a grid and in 7d a combined MT and E-mapping project on a profile is illustrated.

In general, any tree structure of sensors can be assembled. To increase the number of communication channels for more complex networks, branch nodes can be linked between any two REMOTEs or BASEs, but only one BASE per tree is possible. Computationally, the BASE could be extremely powerful, as the BASE TRAM can consist of a whole cluster of transputers or other processors connected. It can also run as a stand alone compute engine for reprocessing and modelling data in the laboratory.

Software and operation

At the moment this is the most speculative part of the development, but S.P.A.M.III software consists of programs running on the PC and code executed on the transputer network with some communication between the two worlds. A decision has not yet been made as to the nature of the communication between the two, but a bi-directional printer port or a standard SCSI interface could be used. All programs, including the transputer code, will be located on the PC and down loaded to the BASE and REMOTEs:

- Initialisation: A small utility program is executed first, to reset and initialise a whole transputer network and to analyse all link connections to automatically determine the configuration beeing used and to check the processor states.
- Calibration: There are tools to test all devices and connections using the built in signal generator and to calibrate all channels, excluding the sensors.
- Processing and control software containing routines for:
  - Start/stop/programme recording
  - Instrument parameter: to set/reset gains, switches, high pass filters etc.
  - Program parameter: to set/modify frequency bands, stacking parameter, etc.
  - Data storage: Allocation map for internal hard disk, data dump.
  - Data visualisation: time series, frequency spectra, stacking results, transfer functions, etc.
- Database: Since very complex instruments can be created with many sensors and other hardware modules connected, it would be inefficient if the complete system had to be described from scratch in every detail on each deployment. Therefore, a PC based database is being implemented - this will contain the details of all available modules and where specific configurations can be put together, stored and be recalled. This database will also help organise the file handling, as existing file formats are normally unable to deal with instruments that can cover several sites with many sensors in non standard configurations. It is also possible to retrieve information from the data base for off-line data processing, e.g. site co-ordinates, sensor spacing, etc.
- Presentation of results: Programs are available for 1D and 2D inversion or modelling and a contouring package is included
- Optional Packages: Definition of an interface to allow external, user supplied software (PC or transputer based) to be included.

References

Beblo M. und St. Hofer, Überlegungen und Versuche auf dem Weg zum neuen "Münchener Elektrographen", Protokoll Elektromagnetische Tiefenforschung, Ed. V. Haak u. J. Homilius, Lerbach bei Köln, 1986.

Beblo M. und V. Liebig, Mobile Datenerfassung mit CMOS-Halbleiterspeichern, Protokoll Elektromagnetische Tiefenforschung, Ed. V. Haak u. J. Homilius, Lerbach bei Köln, 1986.

Brasse, H., Audiomagnetotellurische Untersuchungen in von künstlichen Feldern freien Gebieten in Südägypten und Nordsudan, Protokoll Elektromagnetische Tiefenforschung, Ed. V. Haak u. J. Homilius, Königstein im Taunus, 1988.

Dawes G.J.K., Feasibility Study a for Transputer-based Upgrade of the Short-Period Automatic Magnetotelluric (S.P.A.M.) System, Univ. of Edinburgh: N.E.R.C. Report F3/G6/S43, 1990.

Drews C., Aktive Audiomagnetotellurik auf Milos (Griechenland) zur Bestimmung der Verteilung der elektrischen Leitfähigkeit und ihrer Korrelation mit geothermischen Anomalien, Protokoll Elektromagnetische Tiefenforschung, Ed. V. Haak u. J. Homilius, Königstein im Taunus, 1988.

Liebig V. und G. Schreier, Aufbau einer mikroprozessor-gesteuerten, mobilen Audio-Magnetotellurik Apparatur. Protokoll Elektromagnetische Tiefenforschung, Ed. V. Haak u. J. Homilius, Grafrath/Oberbayern, 1984.

Micheel, H.J., Eine Audiomagnetotellurik Messaparatur (1Hz - 20kHz) und erste Ergebnisse der Datenanalyse, Protokoll Elektromagnetische Tiefenforschung, Ed. V. Haak u. J. Homilius, Berlin Lichtenrade, 1980.

Knödel K., W. Losecke, W. Müller und H. Rodemann, Das neue Magnetotellurik-Messystem der BGR, Protokoll Elektromagnetische Tiefenforschung, Ed. V. Haak u. J. Homilius, Neustadt/Weinstrasse, 1982.

Schnegg P. A. und G. Fischer, On-line Determination of Apparent Resistivity in Magnetotelluric Soundings, Protokoll Elektromagnetische Tiefenforschung, Ed. V. Haak u. J. Homilius, Berlin Lichtenrade, 1980.

Steveling E,. Analoge Aufzeichnung langperiodischer Tellurik-Signale mit Rustrak-Recordern, Protokoll Elektromagnetische Tiefenforschung, Ed. V. Haak u. J. Homilius, Neustadt/Weinstrasse, 1982.

Wehmeier M., Ein Modularkonzept für die Analogelektronik registrierender geophysikalischer Messgeräte - universelles Interface zwischen Sensor und Datenaufzeichnung, Protokoll Elektromagnetische Tiefenforschung, Ed. V. Haak u. J. Homilius, Königstein im Taunuss, 1988.

Oliver Ritter

Ein AMT Experiment zur hochauflösenden Kartierung von Vertikalfeldvariationen

Einleitung

Die Auswertung von Vertikalfeldvariationen (MVM) ist eines der am längsten erprobten Verfahren der Induktionsmethoden überhaupt. Eine vertikale Komponente der Variationsfelder gibt es nur in Gegenwart von lateralen Änderungen der elektrischen Leitfähigkeit[1] und daher ist deren Kartierung eine sehr geeignete Methode zur Auffindung von anomalen Bereichen im Untergrund.

Magnetische Variationsanomalien wurden dabei typischerweise in einem Periodenbereich zwischen 50s und 10000s vermessen und anomale Felder wurden im gesamten Periodenberich festgestellt. Bei diesen Perioden ist die räumliche Ausdehnung der Anomalien in der Größenordung $10km$ oder mehr, mit Quellen, die mindestes einige Kilometer tief liegen. Bei solchen Messungen war die räumliche Dichte der Meßstationen allerdings kaum ausreichend, um Anomalien mit kürzeren Wellenlängen ausschließen zu können und es ist sehr wahrscheinlich, daß zumindest einige der Anomalien an Grenzschichten erzeugt werden, die an der Oberfläche sichtbar sind, z.B. den gefalteten Rändern von Sedimentbecken.

Wir haben uns daher ein Experiment ausgedacht, indem wir versuchen, die Vertikalfelder mit ausreiched hoher Stationsdichte und bei geeignet hohen Frequenzen zu kartieren, um die gemessenen Anomalien direkt im Vergleich mit der Oberflächengeologie interpretieren zu können.

Lokation und geologischer Hintergrund

Für das Experiment suchten wir ein Gebiet in der Nähe von Edinburgh, mit einem Leitfähigkeitskontrast von 10 : 1 oder mehr, mit der Möglichkeit entlang eines Profils arbeiten zu können, aber - selbstverständlich - ohne elektromagnetische Rauschquellen. Solche Meßgebiete existieren tatsächlich nie in Wirklichkeit, jedoch wußten wir von früheren Messungen, daß das Gebiet um die Southern Uplands Fault (SUF) ein geologisch geeignetes Areal ist.

Die ostnordost-westsüdwest verlaufende SUF ist ein sehr prominenter geologischer Komplex, welcher das Midland Valley und die Southern Uplands im Süden Schottlands voneinander trennt. Tektonisch ist die SUF an die Schließung eines Proto-atlantischen Ozeans im späten Paläozoikum gebunden. Im Frühpaläozoikum trennten mehrere hundert Kilometer tiefer Ozean - der Iapetus - den Norden Schottlands, damals Teil der (amerikanischen) Laurentia Platte, vom Süden Schottlands und dem Norden Englands, die Teil der (europäischen) Avalonia Platte waren. Beginnend im Kambrium und fortwährend bis ins Devon wurde dieser Ozean schließlich durch Subduktion im Norden unter Laurentia aufgezehrt.

Das von uns gewählte Profil kreuzt die SUF etwa 15km SSO von Edinburgh (Abb. 1). An der Störung, die lokal als Lammermuir Fault bekannt ist, grenzen karbonische Sedimente im NW an ordovizische Metasedimente im SO. Von den früheren Untersuchungen her war auch bekannt, daß die karbonischen Sedimente Leitfähigkeiten um die $100\,\Omega m$ aufweisen, während die Metasedimente in der Größenordnung $>1000\,\Omega m$ liegen. Abb. 1 zeigt die gemessenen 24 MVM Stationen (schwarze Punkte) und 3 MT Stationen (Rechtecke); die Gitterlinien auf der Karte entsprechen $1km$ Abständen.

Abbildung 2 zeigt die Projektion dieser Stationen auf ein Profil. Die MVM Daten wurden in sechs Stations-Sets (10-60) im September und Oktober 1992 registriert. Magnetotellurische Daten sind an beiden Enden des Profils (50OR, 60OR) und in der Profilmitte gemessen worden (10OR). Für den überwiegenden Teil des Profils beträgt der Abstand zwischen den Stationen ca. $100m$, allerdings musste das Profil zwischen den Sets 10 und 30 aufgrund einer Landstraße

[1] bei Annahme homogener Quellenfelder

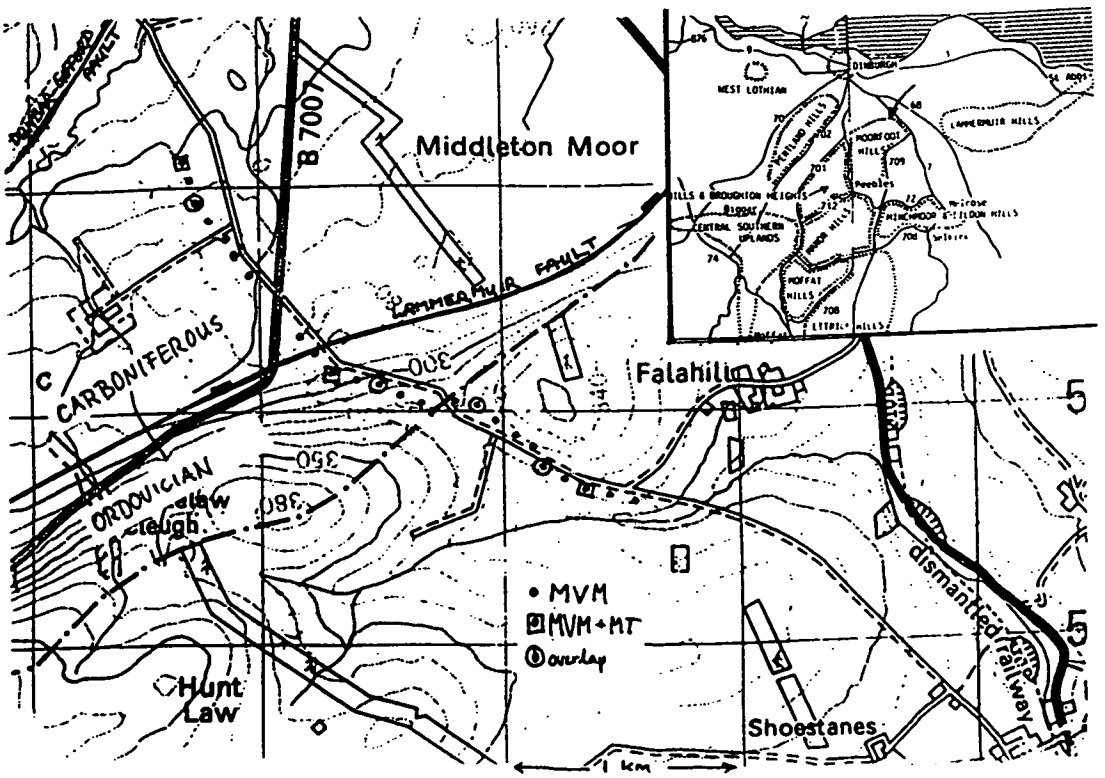

Abbildung 1: Stationskarte

unterbrochen werden. Abb. 2 zeigt auch den angenommen Verlauf der Störung und den praktisch identischen Verlauf einer Gaspipeline.

Instrumentation

In der Vergangenheit scheiterten derartige dichte Kartierungen an den hohen Anforderungen an die Meßgeräte (hohe Abtastraten) und das Fehlen von hochauflösende Magnetometern. In Edinburgh war das Meßgerät in Form des universitätseigenen S.P.A.M. MkIIb vorhanden, während 9 Induktionsspulen von Typ CM11E vom NERC Geophysical Equipment Pool ausgeliehen werden konnten. Diese Hardwarekombination ermöglicht Registrierungen elektromagnetischer Zeitreihen von bis zu 7 Kanälen im Frequenzbereich $100\,Hz$ bis $100\,s$. Für unser Experiment und um die 7 Kanäle voll auszunutzen, verwendeten wir das Gerät wie in Abbildung 3 dargestellt. Jede Gerätekonfiguration besteht aus zwei orthogonalen horizontalen und 5 vertikalen Magnetfeldkomponenten. Die horizontalen Magnetfelder in der Mitte jedes Stationsfünflings werden dabei als Referenzfelder für die jeweils fünf Vertikalfeldstationen registriert. Mit jeder Auslage werden also 5 Stationen und 400 Profilmeter abgedeckt.

S.P.A.M. MkIIb ist eine Real-time Apparatur, die normalerweise für Standard MT Anwendungen eingesezt wird. Alle Daten werden in Form von diskontinuierlichen, kurzen (256 samples) Zeitsegmenten registriert und anhand von on-line Qualitätskriterien wird ein komplettes Datensegment entweder zurückgewiesen oder gestapelt. Aus Zeitmangel konnte die bestehende Registriersoftware nicht an die Besonderheiten dieses Experimentes angepasst werden, so daß ausschließlich die Qualität der jeweils mittleren Station ausschlaggebend für die Akzeptanz der Daten des kompletten Sets war.

Auswertung der Felddaten

Für die Datenanalyse bestimmt man aus den drei Meßgrößen, den Magnetfeldkomponenten

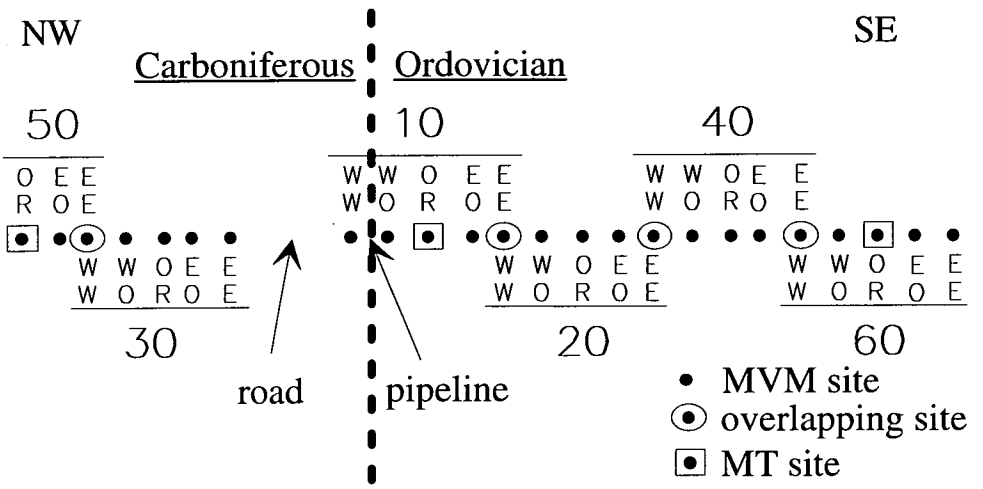

Abbildung 2: Projektion der Stationen auf ein Profil

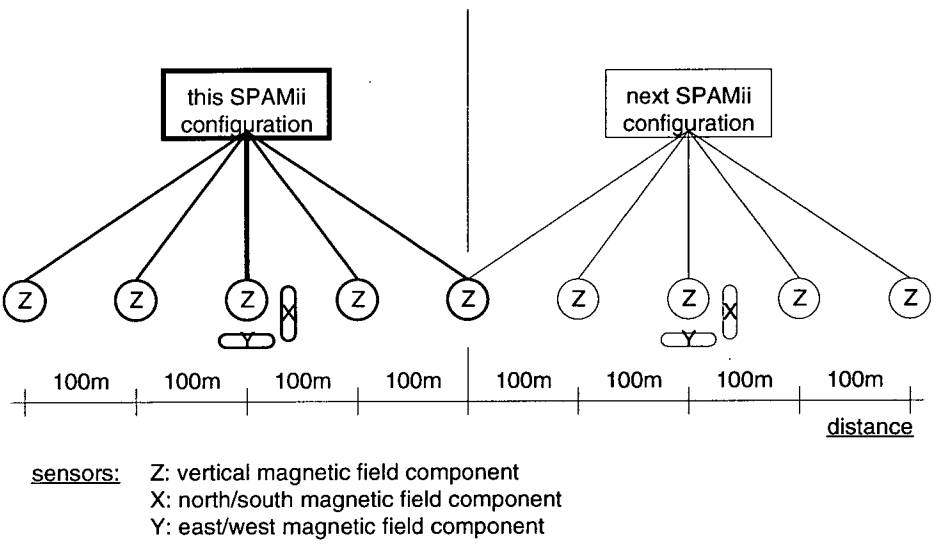

Abbildung 3: S.P.A.M. MkIIb Gerätekonfiguration für das MVM Experiment

B_x, B_y und B_z, die Elemente der vertikalen Übertragungsfunktionen (ÜFs) Z_H und Z_D:

$$B_z(\omega) = Z_H\, B_x(\omega) + Z_D\, B_y(\omega) + \delta B_z(\omega) \tag{1}$$

Bekanntermaßen problematisch ist hierbei die Bestimmung der Rauschkomponente $\delta B_z(\omega)$.

Wie bereits erwähnt verläuft praktisch unmittelbar parallel zum vermuteten geologischen Streichen eine Gaspipeline und zusätzlich waren im gesamten Meßgebiet elektrische Weidezäune im Betrieb, so daß der Einfluß von Noise sicher zu beachten ist. Im Bereich der höchsten Frequenzen sind starke $100\,Hz$ Signale auffällig. Diese überschreiten aber nicht den Bereich der Gerätedynamik und beeinflussen daher nur ein sehr eingeschränktes Frequenzband, welches beim Datenprocessing berücksichtigt werden kann. Schwerwiegender sind die Einflüsse von Störsignalen, wie sie in Abbildung 4 dargestellt[2] sind.

Besonders bei den vertikalen Magnetfeldern (Hz) deutlich erkennbar sind periodisch (alle $11.5s$) einsetzende künstliche Signale. Die horizontalen Magnetfelder scheinen von diesen

[2] Alle Magnetfeldkanäle sind ungefähr auf nT skaliert, lediglich die Einflüsse der bandbegrenzenden Filter sind nicht mitberücksichtigt.

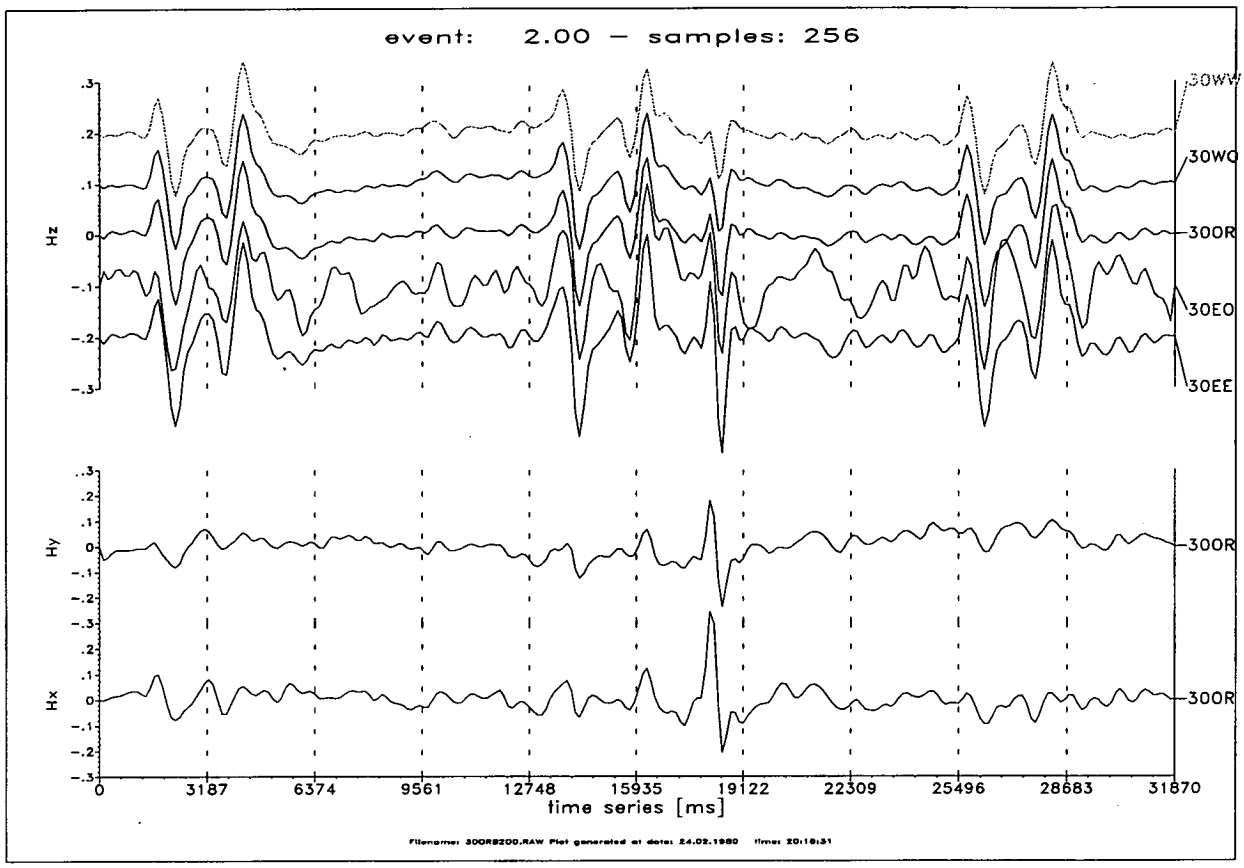

Abbildung 4: Zeitreihenbeispiel mit Störsignalen für Stationen von der nördlichen Profilseite.

Störungen weniger stark beinflußt zu sein. Was man in der Abbildung sieht, dürfte das bandpassgefilterte Resultat eines ursprünglich mehr impulsartig verlaufenden Signals sein. Impulsförmige Signale sind die schädlichsten Rauschformen, da sie weite Teile des Frequenzspektrums beeinträchtigen. Oftmals verfälschen diese Signale alle Komponenten der elektromagnetischen Felder gleichermaßen und können daher nicht von den auf Kohärenz beruhenden (on-line) Processingverfahren unterdrückt werden. Auch durch ein robustes Nachprocessing der Daten[3] können diese Störer nicht immer wirkungsvoll unterdrückt werden.

Bevor wir mit der eigentlichen Diskussion der Ergebnisse beginnen, ist es hilfreich sich mit dem für diese geologische Situation zu erwartenden Resultat vertraut zu machen. Abbildung 5 zeigt dazu als eine erste Approximation an die Geologie ein einfaches 2D Model, welches mit Geotools erstellt worden ist. Das Modell ist im unteren Teil des Bildes geplottet und es besteht aus einer $10\,\Omega m$ gutleitenden, $1km$ dicken Schicht, welche in eine $1000\,\Omega m$ schlechleitende Umgebung eingebettet ist. Das Modell erstreckt sich horizontal über $5km$ und darauf verteilt sind 14 Modellstationen. Für diese Stationen sind in den oberen beiden Graphen die ÜFs der vertikalen Magnetfelder als Isolinienpläne dargestellt.

Die obere linke Abbildung zeigt eine Pseudo-Tiefensektion des Realteils der ÜF[4] Z_H, während die rechte obere Abbildung die Imaginärteile zeigt. Die Realteile schwanken zwischen negativen (dunkel) und Werten um Null (hell). Der Rand der Leitfähigkeitsgrenze wird dabei sichtbar als Übergang von leicht negativen (< -0.4) zu stark negativen Werten (bis -1). Die Anomalie ist deutlich über einen weiten Frequenzbereich ($1000\,Hz$ - $10\,s$) zu erkennen, wobei die laterale Leitfähigkeitsgrenze das ausgeprägteste Merkmal ist. Bei den höchsten Frequenzen ist die hori-

[3] basierend auf A. Junges Verfahren.

[4] In einem geeigneten Koordinatensystem ist im 2D Fall die Z_D Komponente immer 0.

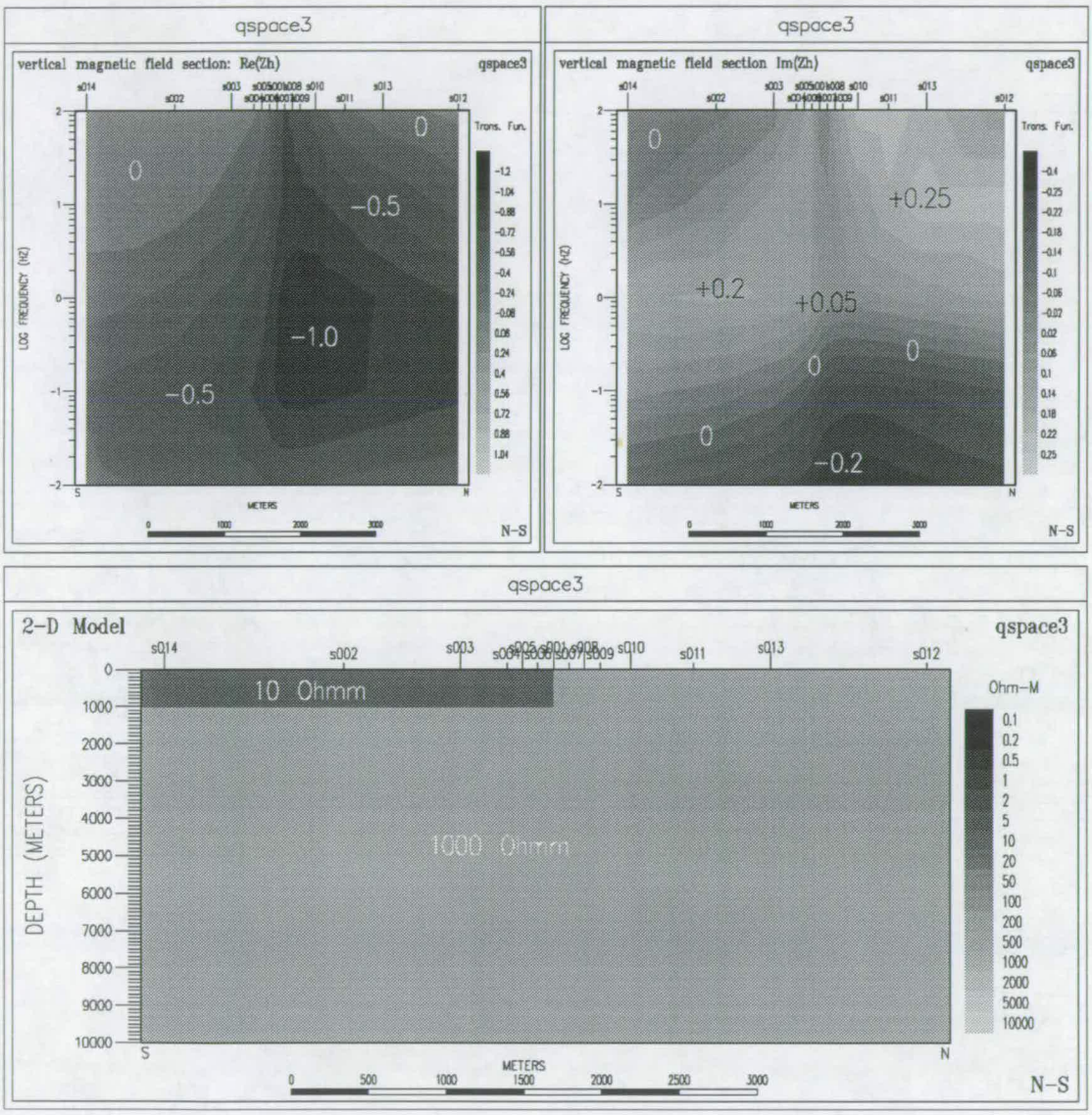

Abbildung 5: 2D Model als eine erste elektromagnetische Approximation an die zu erwartende geologische Situation.

zontale Erstreckung der Anomalie gering, während sie sich zu längeren Perioden hin ausweitet.

Die Anomalie ist auch durch die Imaginärteile angedeutet, allerdings im Vergleich zu den Realteilen mit geringeren Amplituden. Mit zunehmender Eindringtiefe, bei einer Periode von ca. $1\,s$, ändert sich jedoch das Vorzeichen der ÜFs. In der Zone zwischen $1\,s$ und $10\,s$ sind die Imaginärteile minimal und dies korrespondiert mit einer Zone maximaler Realteile. Mit diesem charakteristischen Verhalten der ÜFs werden die zugrundeliegenden physikalischen Prozesse wiedergespiegelt. Für die höchsten Frequenzen (kleine Eindringtiefen) ist Induktion der dominierende Vorgang, die anomalen Ströme werden im guten Leiter durch die Anomalie selbst erzeugt. Die Tiefe der maximalen anomalen Ströme ist dann erreicht, wenn die anomalen Felder gerade in Phase mit den induzierenden Feldern sind. Zu den längeren Perioden hin werden die Ströme außerhalb der Anomalie in viel größerer Tiefe erzeugt und zu dem Oberflächenleiter hin abgelenkt; dieses Phänomen kann also als *Gleichstromverzerrung* betrachtet werden.

Abbildung 6 zeigt als Beispiel für die Ergebnisse der Felddaten ÜFs von den Stationen vom südlichen Teil des Profils. Dargestellt sind die Real- und Imaginärteile von Z_H. Die Stationen 60 stammen vom südlichsten Teil des Profils und sind ca. $1.2km$ von den 10er Stationen entfernt, die über die Störung hinweggehen. Von der letzten 60er-Station (60WW) bis zur ersten 10er-Station (10EE) hat sich das negative Maximum der Anomalie fast verdoppelt (unterschiedliche Achsenskalierung!). Während sich zwischen den 60er-Stationen nur wenig ändert, sind die Unterschiede zwischen den einzelnen Stationen des 10er Sets gewaltig. Zunächst vermerken wir einen moderates aber beständiges Anwachsen der Anomalie zwischen 10EE, 10EO und 10OR, dann aber, bei 10WO, einen enormen Anstieg auf Werte bis zu -8 und nur $100m$ weiter entfernt einen umgekehrten Verlauf der ÜFs.

Mit Ausnahme von 10WW scheinen diese Stationen ein ähnliches Ergebnis anzudeuten wie für das vorher diskutierte Modell. Die Stationen im SO zeigen die schlechter leitende Seite des Profils durch negative Werte an. Maximal negative Werte werden bei den Stationen in der Nähe des Leitfähigkeitskontrastes im Frequenzbereich zwischen $1\,Hz$ und $10\,Hz$ erreicht. Mit zunehmendem Abstand von der Störungslinie flacht die Anomalie langsam nach SO hin ab.

In der nächsten Abblildung (7) sind die ÜFs an diskreten Frequenzen für alle Stationen über dem Profil dargestellt. Dabei wird deutlich wie abrupt die Anomalie im NW abbricht. Überhaupt ist durch die unglückliche Profillücke der Verlauf der Anomalie über den besser leitenden Sedimenten nur sehr schlecht aufgelöst. Ausschließlich an Station 10WW sieht man eindeutig eine Vorzeichenumkehr, während die anderen nördlichen Stationen 30WW-50OR nur neutrale bis leicht positive Werte einnehmen. Die Imaginärteile der Z_H ÜFs zeigen aber das erwartete Muster, mit der Vorzeichenumkehr im Frequenzbereich der maximalen Realteile. Beginnend mit der höchsten Frequenz von $68\,Hz$ bis hin zu $2.2\,Hz$ wachsen die Realteile auf maximal negative Werte an, während die Imaginärteile von leicht positiven zu Werten um 0 wechseln. Es wird aber auch deutlich, wie ungenau die ÜFs im nördlichen Teil des Profils bestimmt sind. Interessant ist, daß sie bei $2.2\,Hz$ positive Werte annehmen und damit einen schlechten Leiter weiter im Norden anzudeuten scheinen. Ein schnelleres Abklingen der Anomalie über den gutleitenden Sedimenten ist hingegen zu erwarten.

Im Vergleich zu den Z_H Resultaten sind die Z_D ÜFs wesentlich kleiner und auch weniger einheitlich. Die Imaginärteile von Z_D scheinen sogar zweimal den Verlauf zu ändern. Bei entsprechenden Versuchen Z_D durch Rotation des Koordinatensystems zu minimieren, konnten keine konsistenten Drehwinkel gefunden werden. Da das Profil bereits in etwa senkrecht zum erwarteten Streichen verläuft, muß bei diesen Daten daher von einer dreidimensionalen Struktur des Untergrundes ausgegangen werden. Dies wird auch durch die Stärke der Anomalie unterstützt, die bei den Felddaten Werte von -2 übersteigt, während mit 2D Modellen auch bei extremen Leitfähigkeitskontrasten nur Maximalwerte um -1 erzielt werden können.

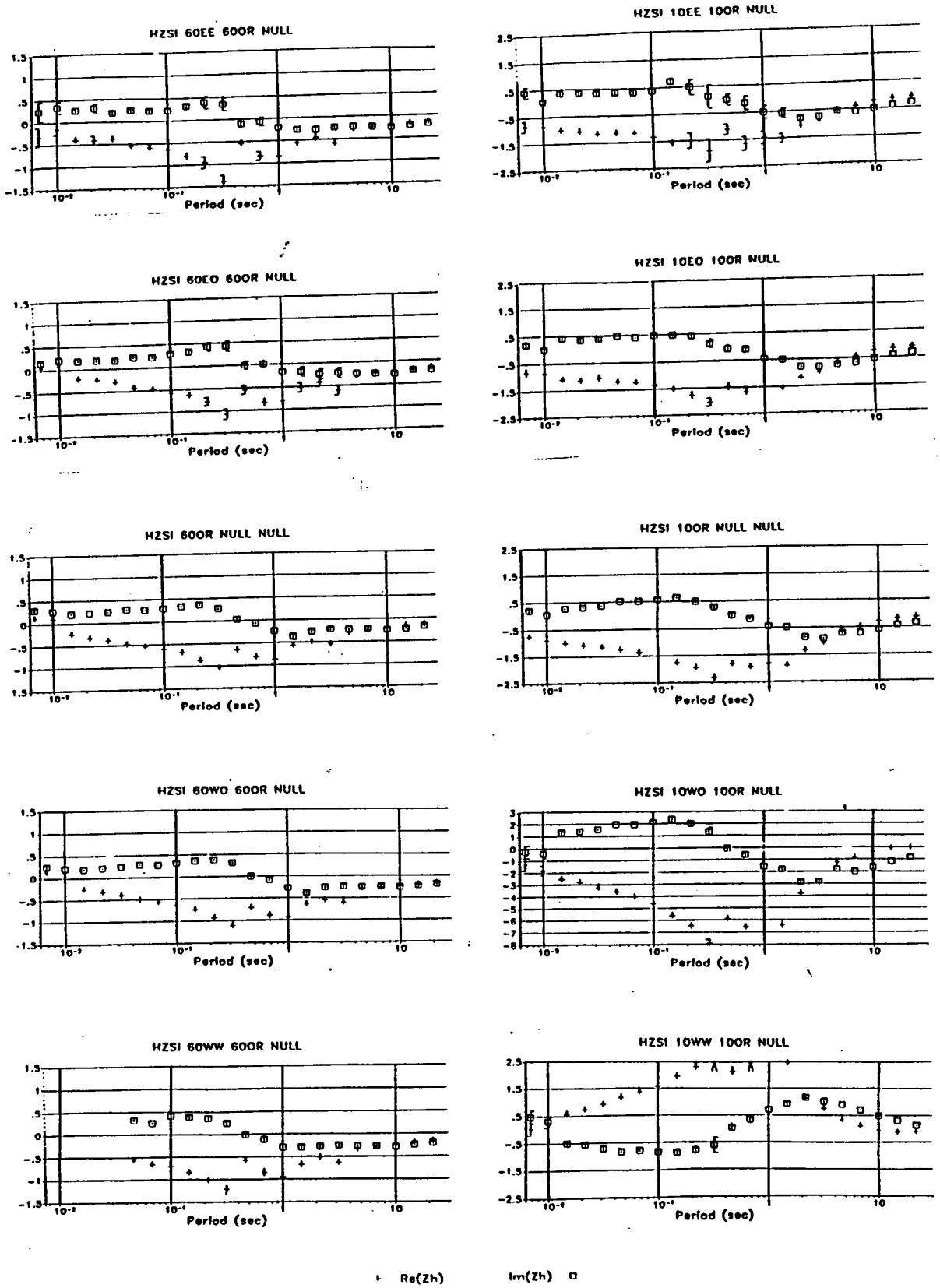

Abbildung 6: Darstellung der Real- und Imaginärteile der Z_H Übertragungsfunktionen über der Frequenz.

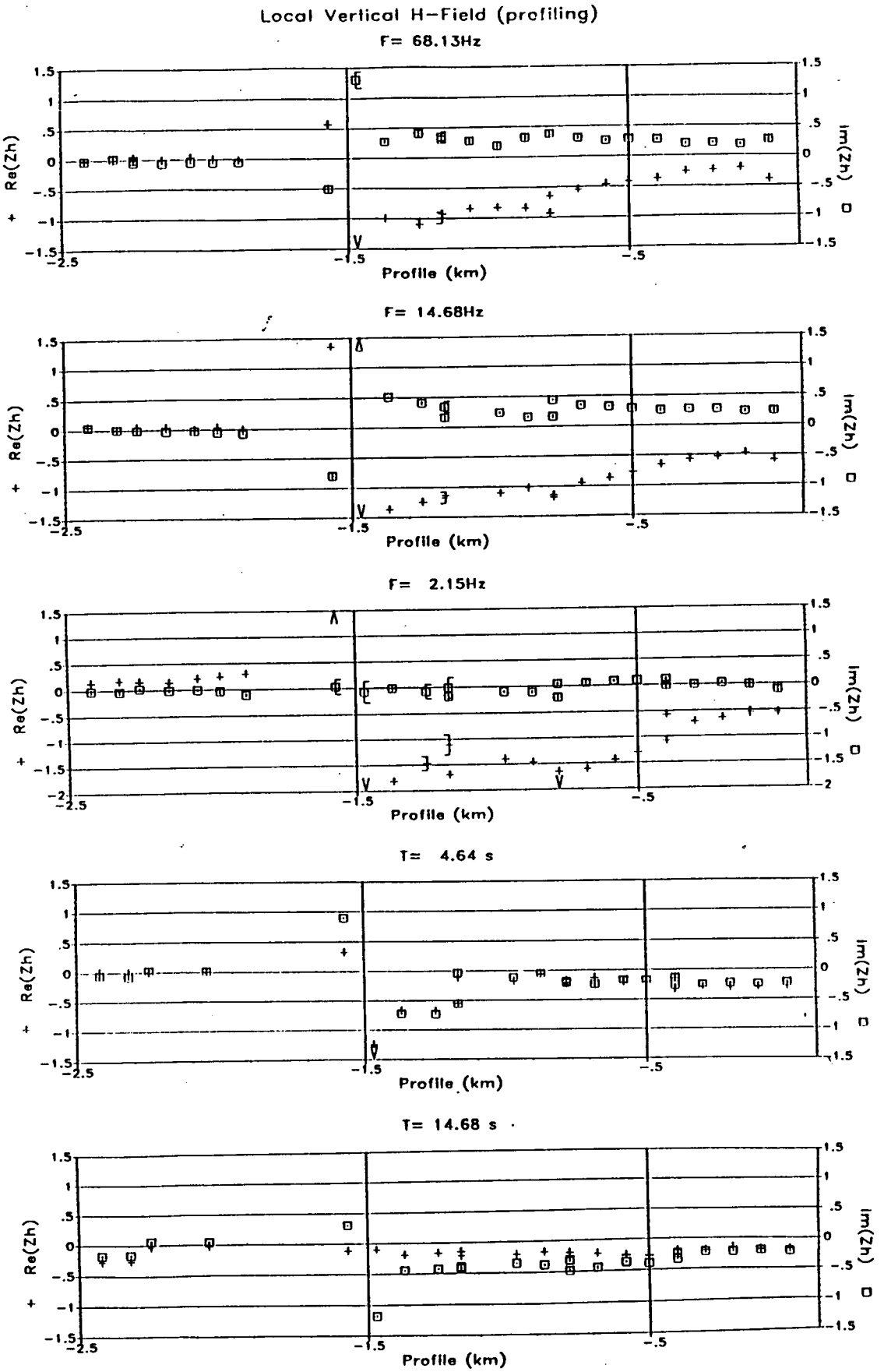

Abbildung 7: Darstellung der Real- und Imaginärteile der Z_H Übertragungsfunktionen an diskreten Frequenzen über dem Profil.

3D dünne Schichten Modellierung

Im letzten Abschnitt haben wir aus der Größe der Anomalie und dem Nichtverschwinden der Z_D-Komponente gefolgert, daß die Daten eine dreidimensionale Situation wiederspiegeln. Die Resultate der 3 MT- Stationen, die auch nach Bahr'scher Dekomposition hohe Skew-Werte aufweisen, bestätigen dieses Ergebnis. Gegenwärtig ist es jedoch kaum möglich, anhand von 3D Modellierungen eine Anpassung an Meßdaten zu erreichen. Die Rechenzeit für die 3D-Vorwärtsrechnung liegt in der Größenordnung von Stunden für jede Frequenz und die Anzahl der Gitterpunkte für die Modelle ist sehr begrenzt. Wir beschränken uns daher auf die Betrachtung eines Teilaspektes, indem wir untersuchen, ob die Maximalwerte der Anomalie ($Z_H > -2$) mit dreidimensionalen Strukturen zu erreichen sind.

Zur Verfügung stand uns hierzu das 3D dünne Schichtenprogramm nach [McKirdy et al., 1985] in einer Implemetation von P. Jones auf einer SUN workstation. Maximal können damit 22x22 Zellen in die dünne Schicht eingebaut werden. Ein solches Eingabemodell ist in Abbildung 8 dargestellt. Wie man sieht, besteht das Modell aus einem $10\,\Omega m$ gutleitenden Kanal, der in

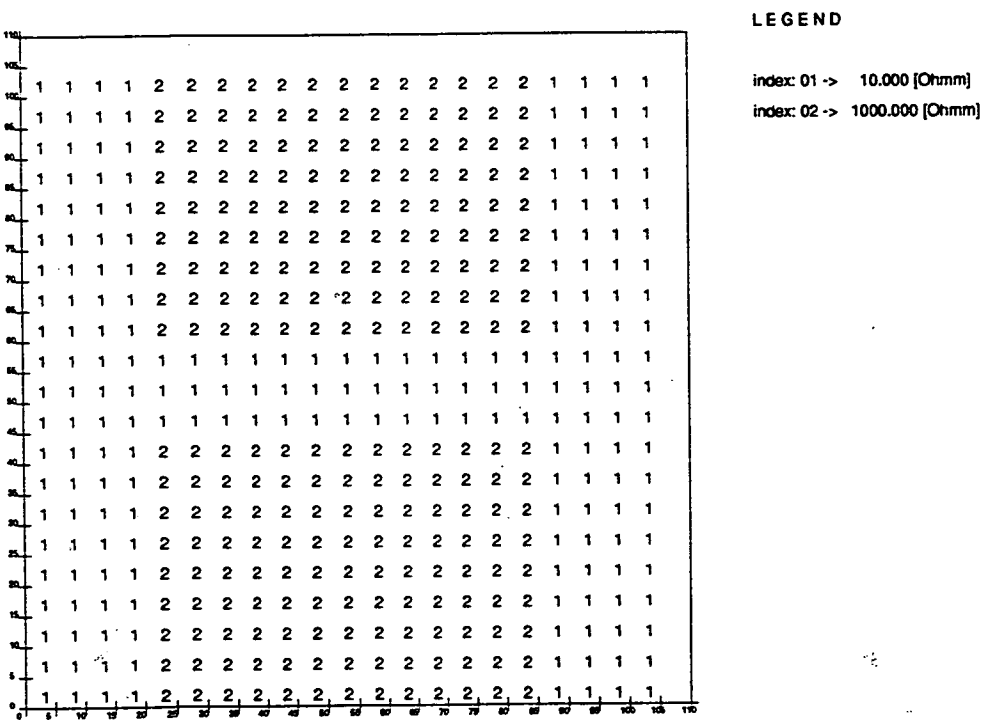

Abbildung 8: Dünne Schicht: Eingabemodell

eine schlechtleitende Umgebung eingebettet ist ($1000\,\Omega m$); die Tiefe der dünnen Schicht beträgt $500m$, die horizontalen Erstreckungen des Modells jeweils $2000m$. Mit einem solchen Modell erreicht man eine starke Bündelung der Ströme in den gutleitfähigen Kanal an der Oberfläche hinein, und die Auswirkungen auf die Parkinson-Induktionspfeile[5] sind in der Abbildungen 9 dargestellt.

Bei der höchsten Frequenz von $10\,Hz$ ist die Anomalie noch wenig ausgeprägt, lediglich die Imaginärpfeile (rechtes oberes Bild in Abb.9) deuten auf die Ränder der Leitfähigkeitsanomalie hin. Einschränkend muß man aber darauf hinweisen, daß die Eindringtiefe der elektomagnetischen Felder für die leitenden Bereiche des Models gerade der Tiefe der dünnen Schicht entspricht

[5]in der Parkinson Konvention zeigen die Realpfeile zum guten Leiter hin, während die Wiesepfeile davon wegdeuten. Die Imaginärpfeile sind in beiden Konventionen einheitlich.

und daher die Voraussetztung für eine solche Betrachtung eigentlich verletzt ist. Bei der nächsten Frequenz ($1\,Hz$) ist die Anomalie deutlich erkennbar. Die Realpfeile erreichen Werte bis zu 1.5, die Imaginärpfeile sind ebenfalls groß und zeigen in die Richtung der Realpfeile. Bei $10\,s$ in Abb. 9 nehmen die Realpfeile Maximalwerte > 1.75 ein, während die Imaginärpfeile auf minimale Werte abfallen. Zu den längsten Perioden hin ($100\,s$) werden die Realpfeile wieder kleiner, die Länge der Imaginärpfeile bleibt in der gleichen Größenordnung, sie sind um 180° gedreht und zeigen entgegengesetzt zu den Realpfeilen.

Zum Vergleich hierzu nun die Induktionspfeile der Meßdaten, die aber in der Wiese Konvention gezeichnet sind (Abb. 10). Real und Imaginärpfeile zeigen deshalb bei der hoechsten Frequenz von $68.1\,Hz$ - in Übereinstimmung mit den Modellergebnissen - um 180° entgegengesetzt. Mit abnehmenden Frequenzen verschwinden die Imaginärpfeile ($2.2\,Hz$), während in der Nähe der Leitfähigkeitgrenze die Realpfeile Maximalwerte um 2 einnehmen. Mit zunehmenden Eindringtiefen wachsen die Imaginärpfeile wieder an und zeigen, wie erwartet, in Richtung der Realpfeile. Das Abdrehen der Induktionspfeile mit zunehmender Periode von SO nach SW und der Winkel zwischen Real- und Imaginärpfeil bei $14.7\,s$ können durch das dünne Schichtenmodell allerdings nicht erklärt werden. Auch die Richtung der Induktionspfeile an Station 10WO kann durch natürliche Ursachen kaum erklärt werden.

In diesem Band befindet sich ein sehr interessanter Beitrag von T. Hanstein, der sich mit dem Einfluß von Pipelines auf MT Ergebnisse befasst. Es wird gezeigt, daß insbesondere die vertikalen ÜFs stark betroffen sind, wenn das Verhältnis der Leitfähigkeiten von Pipeline zur Umgebung 10^9 oder mehr ist. Die künstlich erzeugten Induktionspfeile zeigen dann immer weg von der Pipeline. Ein solcher Effekt scheint sich in den Daten tatsächlich bei $68\,Hz$ in (Abb.10) einzustellen, allerdings zeigen die Induktionspfeile bei längeren Perioden fast senkrecht zur Pipeline.

In dem Beitrag wird die Pipeline als Linienstrom eines unendlich langen Zylinders modelliert. Da Pipelines aber normalerweise elektrisch unterbrochen werden, dürften die Auswirkungen letzlich geringer sein.

Zusammenfassung

In einem Experiment im Südosten Schottlands wurde über eine bekannte geologische Struktur hinweg (Southern Uplands Fault) mit 24 Meßstationen auf einem Profil von ca. $2.5km$ Länge eine dichte Kartierung der Vertikalfeldvariationen durchgeführt. Die Ergebnisse zeigen überraschend hohe anomale Werte (> -2) für die vertikalen magnetischen Übertragungsfunktionen im Bereich des erwarteten Verlaufs der Störung.

Obwohl die Daten sicherlich sehr ungewöhnlich sind und Probleme mit Störsignalen bestehen, ist eine genauere Untersuchung der Ergebnisse interessant. Generell ist die Datenqualität befriedigend. Die Übertragungsfunktionen variieren glatt und konsistent zwischen benachbarten Stationen und über den gesamten Frequenzbereich hinweg. Eine Zone anomaler Leitfähigkeit ist klar erkennbar, belegt mit vielen dicht vermessenen Stationen und im richtig gewählten Frequenzbereich ($100\,Hz$ - $100\,s$).

Extreme Anomaliewerte für die ÜFs des Vertikalfeldes können durch Strombündelung in einem oberflächennahen leitfähigen Kanal erklärt werden. Letztlich handelt es sich bei diesem Datensatz wohl aber um eine nicht trennbare Überlagerung von künstlich und natürlich erzeugten Anomalien, die eine abschließende geologische Interpretation außerordentlich schwierig macht.

Literatur

McKirdy, D. M., Weaver, J. T., and Dawson, T. W. [1985]. Induction in a thin sheet of variable conductance at the surface of a stratified Earth - II. Three-dimensional theory. *Geophys. J. R. astr. Soc.* , 80:177–194.

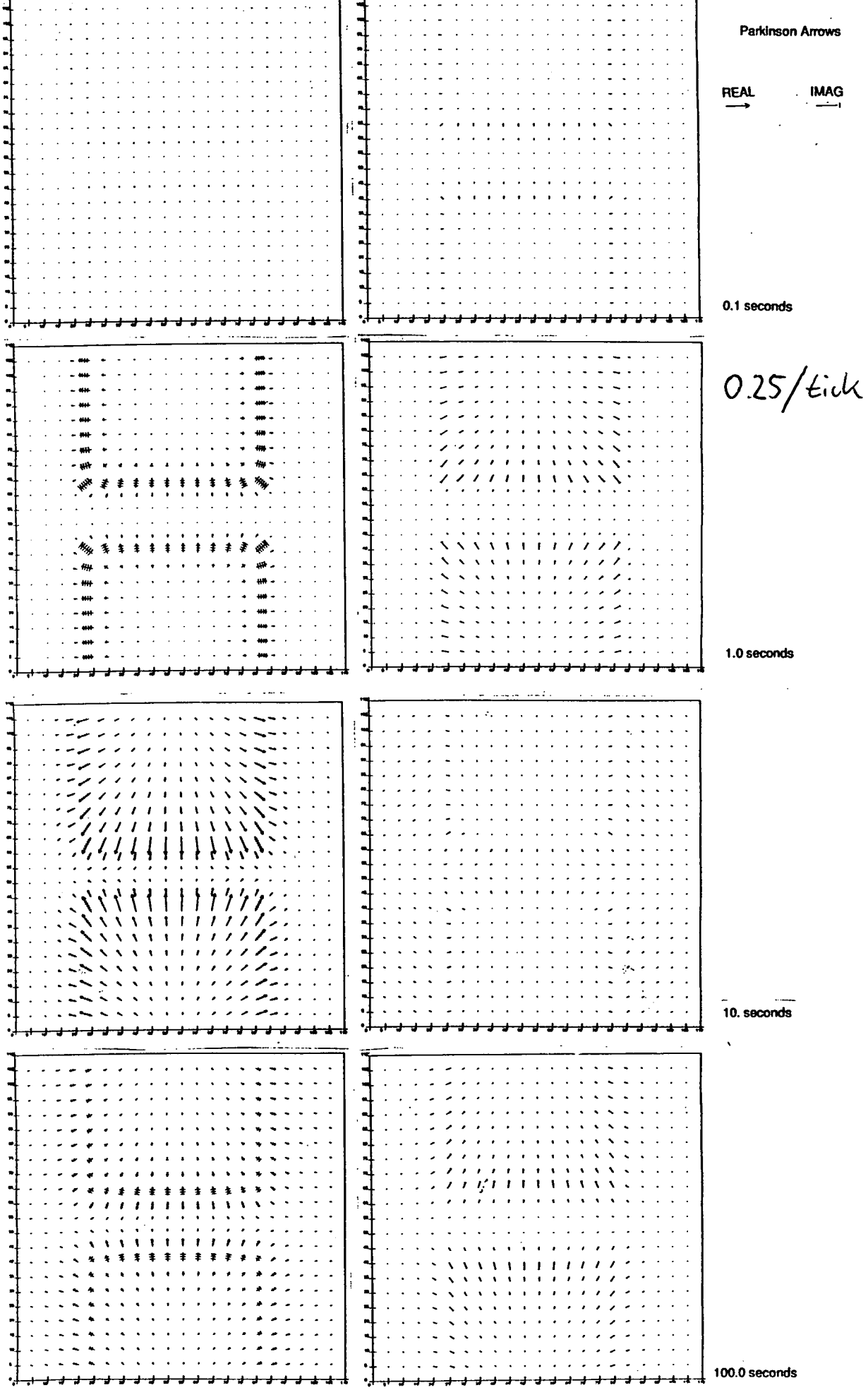

Abbildung 9: Induktionspfeile in Parkinson Konvention für die Frequenzen 10 Hz bis 100 s (Modelldaten).

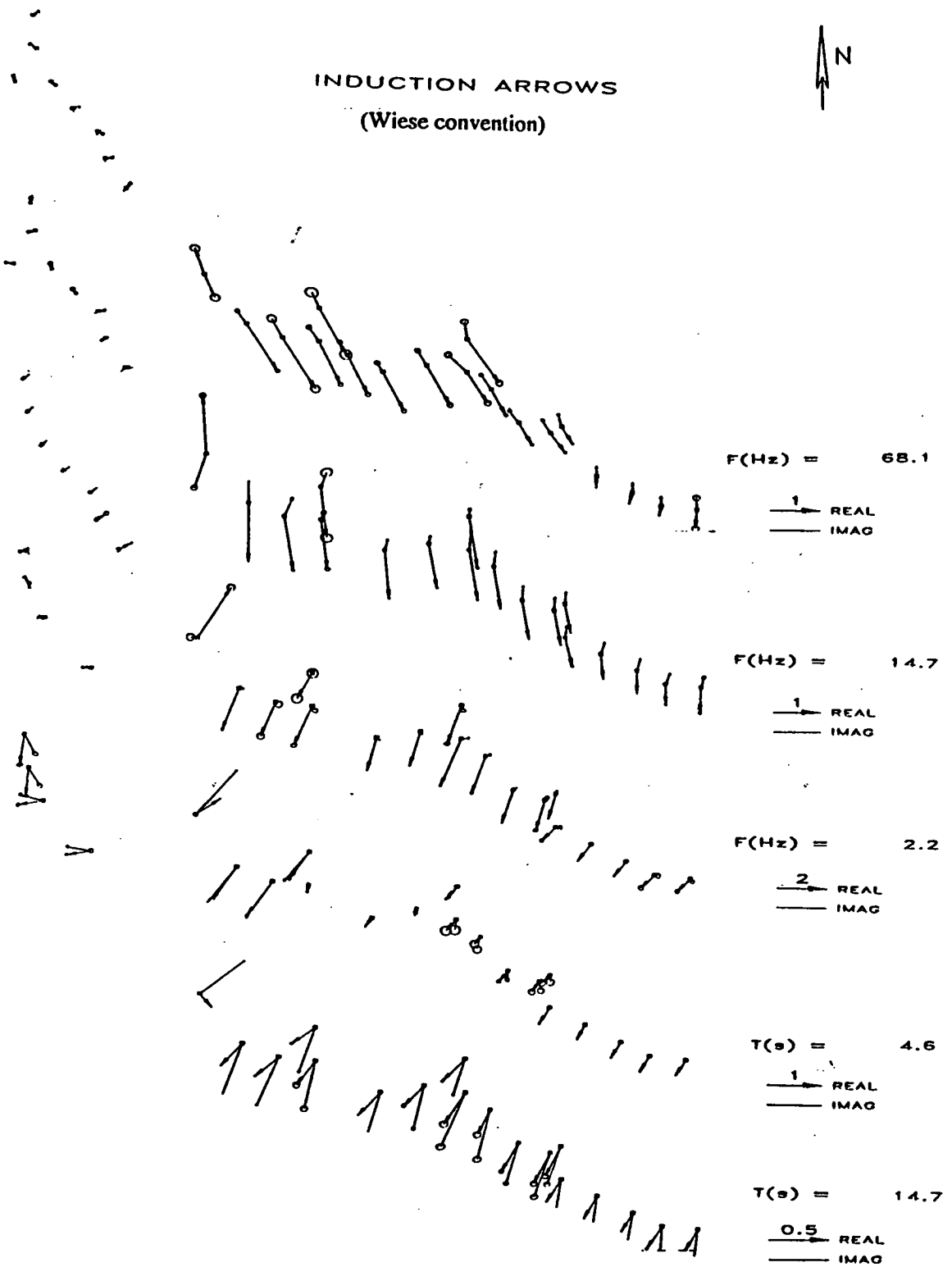

Abbildung 10: Unrotierte Real und Imaginärpfeile der Meßdaten an diskreten Frequenzen.

J. Geomag. Geoelectr., **00**, 000–000, 1995

The BC87 Dataset: Application of Hypothetical Event Analysis on Distorted GDS Response Functions and Some Thinsheet Modelling Studies of the Deep Crustal Conductor

Patricia Ritter and Oliver Ritter

Department of Geology and Geophysics, University of Edinburgh, Edinburgh EH9 3JW, Scotland

(December 1994)

Galvanic distortion was inferred from MT results of the BC87 dataset presented at the MT-DIW1 in 1992. Since perturbation currents also produce an anomalous magnetic field, the GDS response functions were suspected to be distorted in the long period range. In order to reveal the correct regional strike direction, hypothetical event analysis was applied to the data of all sites. With this technique common regional information such as strike and impedance phase can be uncovered from distorted response functions. Although the BC87 GDS data are noisy, the resulting regional strike direction agrees well with the azimuth suggested from previous MT decomposition methods.

Thinsheet modelling studies of the geometry of the deep crustal conductor (L-shaped or oblique) at 1000 s imply, that along the BC87 profile, induction arrows are generally produced by current deviations around the resistive Nelson Batholith. Comparison of the induction arrows with those determined from the BC87 data indicates that the model featuring the oblique, NE striking (SABC) conductor may be favoured.

1. Introduction

At the first Magnetotelluric Data Interpretation Workshop (MT-DIW1) held in Wellington 1992, interpretation of the BC87 dataset was focused mainly on MT results, although GDS data are available for all 27 sites. This seemed to be for two reasons: 1. Data quality is not very good, especially in the long period range; 2. MT observations revealed strong 3-D effects over the whole period range. These effects were interpreted partly as 3-D induction, partly as galvanic distortion, depending on the geometry of the relevant anomalies (Eisel & Bahr, 1993; Jones et al, 1993). Galvanic distortion of the electric field imposes strong effects on the magnetic field components, too. Therefore distortion of the magnetic response functions must also be suspected. This phenomenon is well known in GDS and has been examined with respect to decomposition methods only recently (Groom, 1988; Zhang et al, 1993; Chave & Smith, 1994).

Magnetic distortion due to near-surface conductivity heterogeneities becomes particularly evident when the magnetic response functions are presented as induction arrows: lengths and azimuths may entirely be controlled by the local anomalous magnetic field of the shallow deviations of the regional currents. Nevertheless, one would expect that the response functions also contain information on the regional geology. We can assume that this information is common to all sites of a certain area at long periods. On the other hand, distortion is highly site-dependent. Hence the magnetic distortion problem can be formulated as a combination of site-dependent distortion parameters and contributions from site-independent regional induction processes. Hypothetical event analysis (HEA) as a method for interpreting the output from magnetometer arrays treats the dataset as a unit, and therefore it is most effective in recovering the common information content. If the results from HEA are presented in appropriate diagrams, site-dependent parts of the vertical magnetic field can be isolated. Ritter & Banks (in prep.) show that with noise-free

data and a good spatial coverage of the area, it is possible to determine the regional strike direction and phases of the principal regional impedances with this technique. The response functions of the BC87 dataset do not meet these conditions adequately: they have large error bars at long periods and the sites are arranged along a profile. Nevertheless all sites were submitted to HEA in the suspected period range of distortion at 100 s - 1000 s. The results are consistent throughout the whole decade, confirming a strike angle in the same range as found in previous MT analyses.

Another unsolved problem of the area is the geometrical nature of the deep crustal conductor (Jones, 1993). For the MT-DIW2 we investigated with 3-D thinsheet modelling at 1000 s, whether the form of the conductor may be determined from the induction arrows, if the shallow, resistive Nelson Batholith is also included into the models.

2. Theoretical Background

Magnetic Distortion: Conductivity heterogeneities causing galvanic distortion are generally assumed to be much smaller than the skin depth. Since the anomalous magnetic field $\mathbf{B}^a$ is due to local deflections of otherwise uniform regional currents, it is in phase with the regional electric field $\mathbf{E}^o$. Therefore the parameters describing magnetic distortion are real, frequency-independent quantities. If the regional structure is two-dimensional, but the observation points are well removed from the vertical boundary, we may assume that the vertical magnetic component is due to distortion only (Ritter & Banks, in prep.) :

$$\mathbf{B}_z^a \;=\; (D_{zx}, D_{zy})\,\mathbf{E}^o \;=\; (D_{zx}, D_{zy}) \begin{pmatrix} 0 & Z'_{xy} \\ Z'_{yx} & 0 \end{pmatrix} \begin{pmatrix} B_x^o \\ B_y^o \end{pmatrix} \tag{1}$$

(D_{zx}, D_{zy}) are the vertical magnetic distortion parameters; primes denote the principal impedances in strike coordinates. The product $(D_{zx}, D_{zy})\,\underline{\mathbf{Z}}^o$ corresponds to the magnetic response function $(\mathcal{A}, \mathcal{B})$.

Hypothetical event analysis: We can calculate a predicted value of the vertical field B_z^p that is associated with a certain polarisation $\vartheta^\star$ of the horizontal magnetic field from the observed response function. The horizontal field is supposed to be of unit amplitude over the area of investigation. Using the above expression which includes magnetic distortion, we obtain in observation coordinates:

$$B_z^p \;=\; (D_{zx}, D_{zy})\;\underline{\mathbf{R}}_{-\theta_r}\;\underline{\mathbf{Z}}^{\mathbf{O}}\;\underline{\mathbf{R}}^T_{-\theta_r} \begin{pmatrix} 1\cdot\cos\vartheta^\star \\ 1\cdot\sin\vartheta^\star \end{pmatrix} \tag{2}$$

where $\underline{\mathbf{R}}_{-\theta_r}$ denotes anti-clockwise rotation by the strike angle θ_r. The equation for the predicted value simplifies considerably for two special cases: when the polarisation angle equals the regional strike direction and when it is perpendicular to it.

$$\vartheta^\star = \theta_r : \qquad B_z^p \;=\; Z'_{yx}[-D_{zx}\sin\theta_r + D_{zy}\cos\theta_r] \;=\; \mathcal{A}'(\theta_r) \tag{3}$$

$$\vartheta^\star \perp \theta_r : \qquad B_z^p \;=\; Z'_{xy}[\;D_{zx}\cos\theta_r + D_{zy}\sin\theta_r] \;=\; \mathcal{B}'(\theta_r) \tag{4}$$

In fact the expressions for the predicted vertical field B_z^p for these cases are the same as for the components of the response function in regional strike coordinates $(\mathcal{A}', \mathcal{B}')$. Note that these predicted fields contain only one of the principal impedances. This is an important aspect, because it implies that their phases are equal to the phase of the respective impedance and predicted values at all sites representing the same regional geology should therefore show the same phases. In practice one can find the regional strike angle by gradually varying the polarisation angle $\vartheta^\star$ and plotting the predicted values of all sites at one given period in the complex plane (Argand

diagram). We can determine the regional phase, when the data points fall on a line through the origin, indicating the phase angle. This happens when the magnetic field is polarised in the strike direction of the regional structure (or perpendicular to it).

3. BC87 Dataset

Induction Arrows (Wiese convention): In the short and intermediate period range (T < 10 s) the angular distribution of the azimuths of the real arrows is very scattered along the profile. At longer periods (T > 10 s), however, arrows at most sites follow an overall trend, changing smoothly from $-90°$ to directions around $0°$ ($\pm 30°$) with increasing periods, although in this range magnetic response functions have relatively large errors. At these periods, the imaginary arrows point approximately $-180°$. Lengths and azimuths of the Wiese arrows are shown in fig.1 for periods 450 s and 910 s. Note that Wiese arrows point away from conductive regions.

The arrow directions suggest an eastwest striking structure at some depth to the south of the profile. However, this does not coincide with the strike direction inferred from MT results at 45° to 60°, associated with the upper mantle anisotropy (Eisel & Bahr, 1993; Jones et al, 1993). Since the amplitudes of the response functions show a definite maximum in the intermediate period range between 0.1 s and 1 s at all sites (fig.2), we can assume that induction takes place in the upper parts of the crust (i. e. the conductor at the eastern edge of the resistive Nelson Batholith (Jones 1993)). The large arrows at longer periods are likely to be produced by currents being deflected by these shallow structures and galvanic distortion may be the cause for the vertical magnetic field components observed.

Hypothetical Event Analysis: In order to find a more reliable regional strike direction we applied HEA to all magnetic response functions in the range 10 s - 1000 s. In the case of the BC87 dataset, sites are located along a profile (150 km E-W) with only limited spatial extension (25 km N-S). Hence mapping of the results in contour plots, as it is usually done, may be dominated by interpolation effects rather than providing true images. We found that in this case, a presentation of the values in the complex plane (Argand diagram) is better suited to find common aspects in the data. Since no distinct features could be found in the range 10 s to 100 s, we concentrated our investigations mainly to the decade 100 s to 1000 s. The real and imaginary parts of the predicted values B_z^p of all sites at periods 450 s and 910 s are presented in Argand diagrams (fig.3) for 4 different polarisations of the event.

Varying the polarisation of the hypothetical event moves the points in the complex plane relative to each other, but doesn't rotate them altogether. At a polarisation angle of about $-30°$ the predicted values calculated from the observed response functions arrange roughly on a line through the origin. This happens when the hypothetic magnetic field is polarised parallel to the strike direction of the regional structure or perpendicular to it. The strike angle can therefore be expected at $-30°$ or at 60°. The latter corresponds well to the strike found by MT decomposition methods at 45° - 60°. The slope of the line through the origin was determined by weighted least squares fitting; it dips $-30°$ at 450 s and ca. $-20°$ at 910 s. This line should represent the regional impedance phase, it varies consistently from $-40°$ to $-20°$ from shorter to longer periods. However, the optimum polarisation angle is constantly $-30°$ throughout the investigated decade. Unfortunately the errors of the response functions increase towards the long period end, so that no reliable results can be obtained from data beyond 1000 s.

4. Thinsheet Modelling - The Deep Crustal Conductor

One question that arose from previous MT and GDS interpretations in the area was whether the deep crustal conductor is L-shaped (striking N/S and E/W), or whether it consists of two separate parts: one situated in the west and striking N/S, the other one located further east

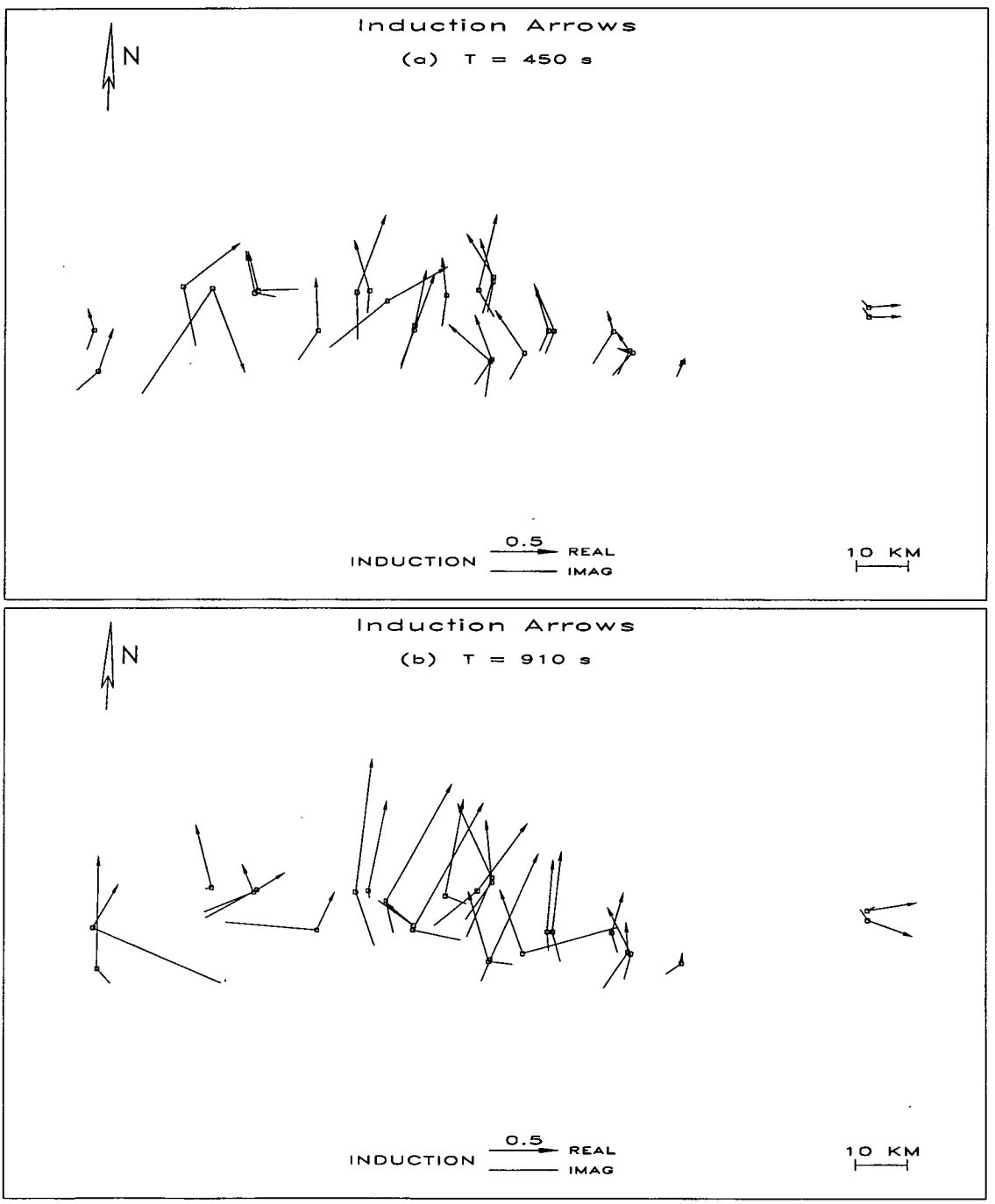

Fig. 1. Induction Arrows (Wiese convention) of all 27 sites at (a) 450 s and (b) 910 s; RE: real arrow, IM: imaginary arrow.

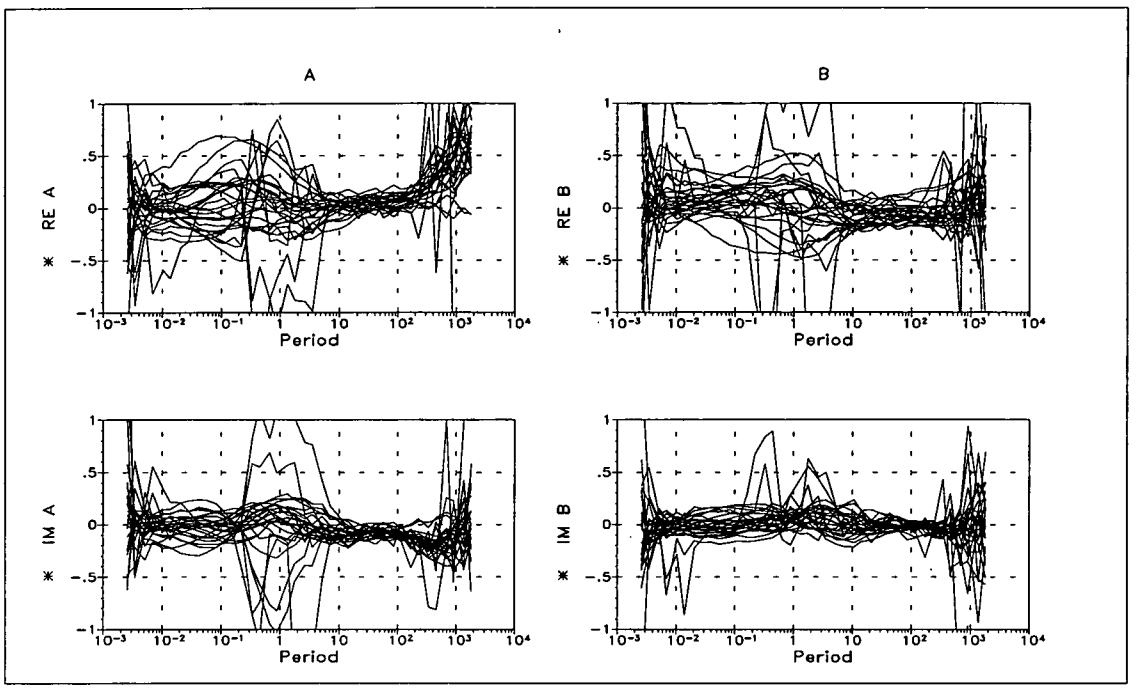

Fig. 2. Magnetic response functions (A, B) of all sites over the whole period range; RE: real part, IM: imaginary part.

and striking NE/SW (the so-called SABC anomaly in Southern Alberta - British Columbia). A detailed description of the general geological situation of the area can be found in Jones (1993). We also included the Nelson Batholith as a resistive feature into our models, and examined the effects of the two cases on the induction arrows in the region of the BC87 profile (fig.4). The models were calculated with the McKirdy & Weaver thinsheet code (McKirdy et al, 1985) for a period of 1000 s. As the emphasis was to study principal effects, resistivity contrasts and sizes are oversimplified.

In both models the induction arrows are attenuated over the centre of the resistive feature. At the south-eastern part of the resistor the arrows are influenced by the form of the conductor. East of the batholith, the real arrows are bented into directions perpendicular to the strike of the 'second' conductor: near the E/W striking structure they point northwards, while arrows near the oblique conductor have a northwest tendency. Across the southern part of the batholith and in the vicinity south of it, however, the arrows point generally towards northeastern direction in both models, although arrows of the SABC model in the southern area are clearly more inclined to the east. The main difference of the models is manifested in the lengths of the real arrows in the region east of the resistor. The arrows decrease towards the center of the SABC conductor and also reverse their sign beyond it, whereas they are of constant lengths along the edge of the L-shaped conductor. The imaginary arrows are generally very small and point at arbitrary angles relative to the real arrows due to the strong three-dimensionality of the studied area.

The azimuth distribution of the BC87 data along the profile shows preferred directions of the real arrows of approximately 10° to 30° from north, although directions of ca −20° occur as well at the more easterly located sites. The lengths of the real arrows decrease towards the east, and at the most eastern sites of the profile they point strictly westwards. Although the observed real

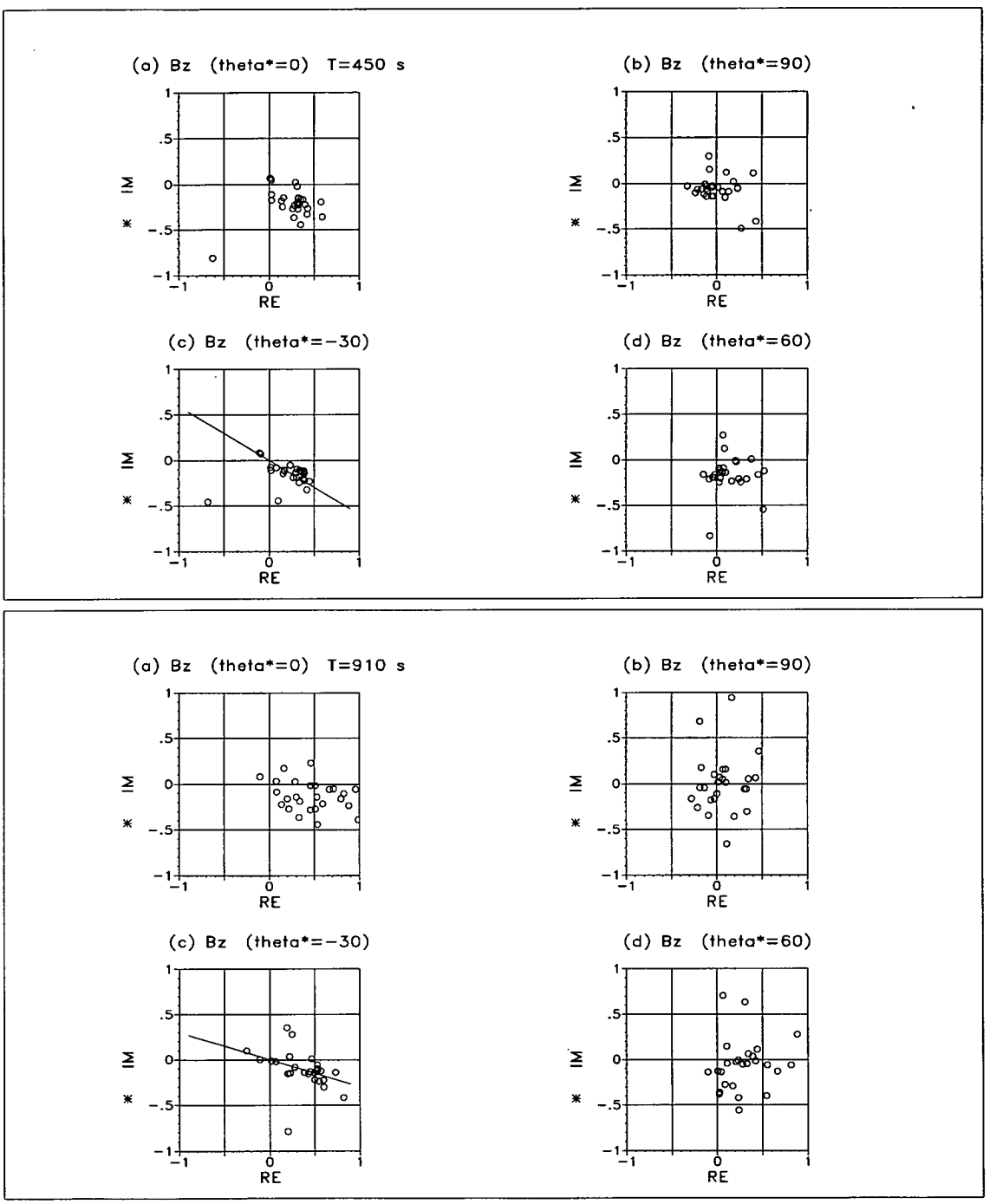

Fig. 3. Hypothetical event analysis, Argand diagram: Predicted values B_z^p of all sites at periods 450 s (upper) and 910 s (lower). RE: real part, IM: imaginary part. (a) Polarisation angle of the hypothetical magnetic field (with amplitude = 1, phase = 0°) : $\vartheta^* = 0°$, (b) $\vartheta^* = 90°$, (c) $\vartheta^* = -30°$, (d) $\vartheta^* = 60°$.

arrows are generally longer than the modelled arrows, the general behaviour of arrow directions and magnitudes supports the oblique model.

5. Conclusion

The GDS response functions of the BC87 dataset at long periods are just as strongly affected by galvanic distortion as the MT impedances. Since the directions of induction arrows are inconsistent with the regional strike directions found by MT decomposition methods, we applied hypothetical event analysis to the data. This technique is capable of recovering information that is common to all sites from the distorted response functions. Although better quality of the data in the examined period range (100 s - 1000 s) would be desirable, the predicted values for the vertical magnetic field at all sites reveal common phase angles for polarisations of around $-30°$. This azimuth corresponds to the strike of the regional conductivity structure or to a direction perpendicular to it.

Due to the geological complexity of the region, the limited spatial coverage, and the deficient data quality at long periods, this dataset might not be appropriate to show the full capability of the method; however the results are in good agreement with the strike direction determined by decomposition of MT impedances at 45° - 60°.

Thinsheet modelling studies of the deep crustal conductor (L-shaped or oblique) at 1000 s confirmed that induction arrows along the BC87 profile may generally be produced by current deviations around the resistive Nelson Batholith. Only sites in the (south-) eastern part of the batholith are affected by the form of the deep crustal conductor. The azimuth distributions and the length variations of the real arrows in the area of the profile at that period indicate that the observed data may rather represent the oblique model (SABC conductor).

The BC87 dataset was made available by D. W. Oldenburg (LITHOPROBE) and A. G. Jones (GSC). This paper was prepared for the second Magnetotelluric Data Interpretation Workshop (MT-DIW2) in Cambridge, preceding the 12th Workshop of Electromagnetic Induction in the Earth held in Brest, France, in August 1994. Adam Schultz and Alan Jones are thanked for their excellent organisation of the pre-workshop workshop, that truely deserved it's name.
LITHOPROBE Publication number xxx.

References

[1] A. D. Chave and J. T. Smith. On electric and magnetic galvanic distortion tensor decompositions. *J. Geophys. Res.*, 99 B3:4669–4682, 1994.

[2] M. Eisel and K. Bahr. Electrical anisotropy in the lower crust of British-Columbia - an interpretation of a magnetotelluric profile after tensor decomposition. *J. Geomagn. Geoelectr.*, 45(9):1115–1126, 1993.

[3] R.W. Groom. The effects of inhomogeneities on magnetotellurics. *PhD thesis, Univ. Toronto*, 1988.

[4] A. G. Jones. The BC87 dataset - tectonic setting, previous EM results, and recorded MT data. *J. Geomagn. Geoelectr.*, 45(9):1089–1105, 1993.

[5] A. G. Jones, R. W. Groom, and R. D. Kurtz. Decomposition and modeling of the BC87 dataset. *J. Geomagn. Geoelectr.*, 45(9):1127–1150, 1993.

[6] D. McA. McKirdy, J. T. Weaver, and T. W. Dawson. Induction in a thin sheet of variable conductance at the surface of a stratified Earth - II. Three-dimensional theory. *Geophys. J. R. astr. Soc.*, 80:177–194, 1985.

[7] P. Ritter and R. J. Banks. Separation of local and regional information in the Iapetus dataset with the help of hypothetical event analysis. *in preparation*, 1995.

[8] P. Zhang, L.B. Pedersen, M. Mareschal, and M. Chouteau. Channelling contribution to tipper vectors: a magnetic equivalent to electrical distortion. *Geophys. J. Int.*, 113:693–700, 1993.

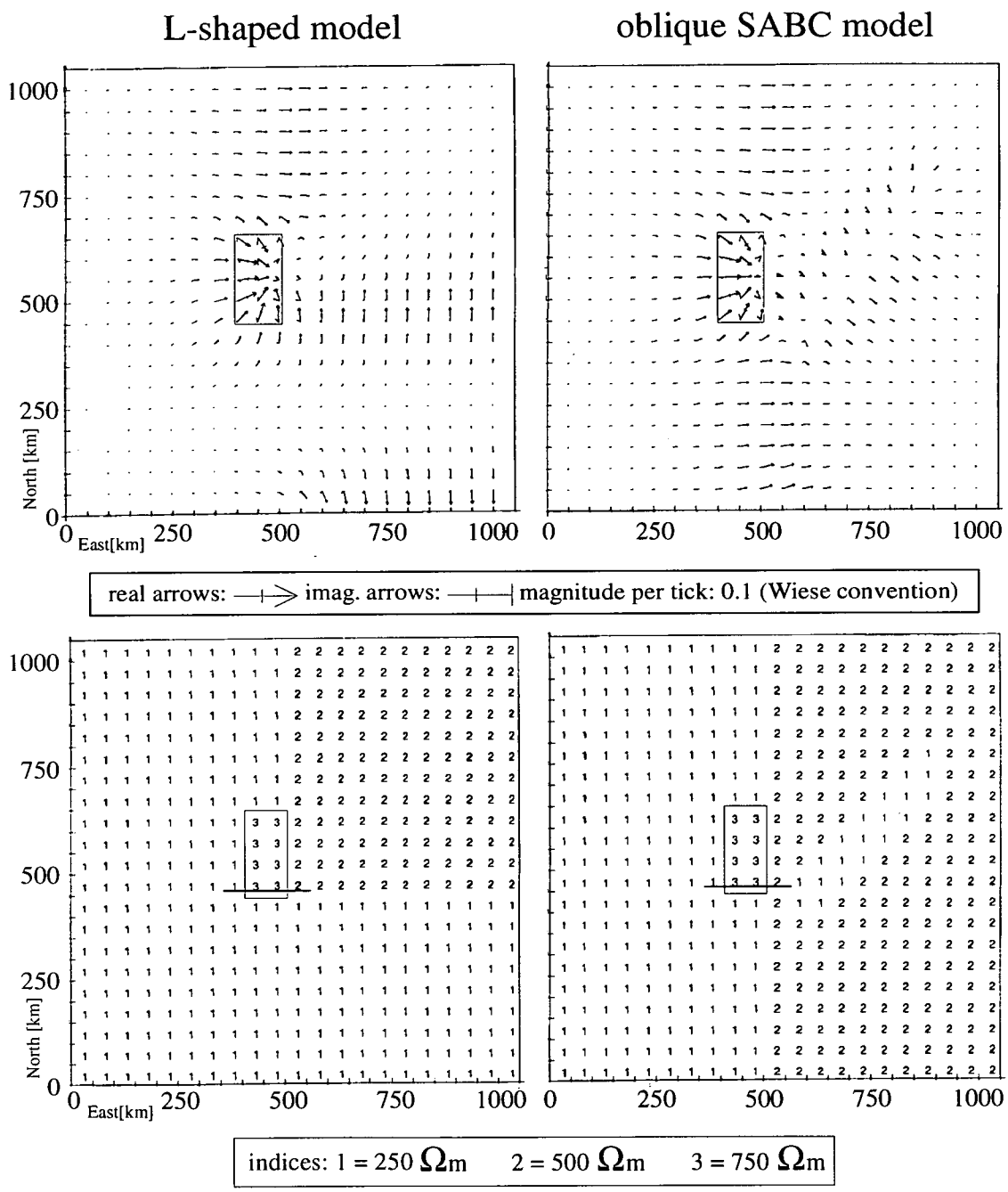

Fig. 4. 3-D thinsheet modelling of the deep crustal conductor: Induction arrows (Wiese convention) for the L-shaped model (left) and the oblique SABC model (right). Marked in the central parts of the figures are the Nelson Batholith and the approximate location of the BC87 profile.
The sheet cells extend to 50 km in each direction. Beneath the thinsheet we placed a resistive layer of 750 Ωm which is followed by a homogenous halfspace (50 Ωm) at a depth of 400 km.